TRIBOLOGY AND INTERFACIAL DELAMINATION OF THIN FILM SYSTEMS

By

HONG TIAN

B. S., Qinghua University, Beijing, China (July, 1983)
M. S. M. E., Massachusetts Institute of Technology (February, 1987)

Submitted in Partial Fulfillment
of the Requirements for the Degree of

DOCTOR OF PHILOSOPHY
IN MECHANICAL ENGINEERING
at the
MASSACHUSETTS INSTITUTE OF TECHNOLOGY
June 1990

Signature of Author _____
Department of Mechanical Engineering
June 15, 1990

Certified by _____
Dr. Nannaji Saka
Department of Mechanical Engineering

Certified by _____
Professor Ernest Rabinowicz
Department of Mechanical Engineering

Accepted by _____
Professor Ain A. Sonin
Chairman, Graduate Committee
Department of Mechanical Engineering

TRIBOLOGY AND INTERFACIAL DELAMINATION OF THIN FILM SYSTEMS

by

Hong Tian

Submitted to the Department of Mechanical Engineering
on June 15, 1990 in partial fulfillment of the requirements
for the degree of Doctor of Philosophy in Mechanical Engineering

Abstract

Thin film contact systems are widely used in modern mechanical and electronic devices. Thus the mechanical reliability of these thin film systems has become a great concern of applied mechanicians and materials scientists. In this thesis, the sliding and fretting failure mechanisms of an electroplated multi-layer system (Au/Ni/Brass) used for electrical connectors are investigated. Experimental observations have shown that the failures of the multi-layer system are due to excessive plastic deformation of the top layer (gold) and interfacial delamination of the interlayer (nickel) from the substrate (brass). The high surface friction is responsible for the plastic deformation and the interfacial failure. The measurement of electrical contact resistance was found to be insensitive for detecting failures of the electroplated gold contacts in the accelerated laboratory tests.

A finite element analysis of an elastic-plastic two-layer half-space with and without an interface crack has been conducted. The contact pressure distributions are bounded by parabolic and elliptic (Hertzian) distributions under the elastic normal loadings, and become flatter in the elastic-plastic regime. The locations of initial yielding strongly depend on the interlayer thickness and the surface friction coefficient. The magnitude of shear stresses and strains along the interfaces increases with the surface friction coefficient. When the interfacial shear strain exceeds a critical value it is likely that debonding or microcracking occurs. For a pre-existing interface crack lying along the nickel-brass interface, the elastic-plastic analysis has shown that size of the plastic zone around crack tips is comparable with the crack length and the layer thicknesses. Thus the use of elasticity theories of interface cracking is limited. Plastic deformation at crack tips expands primarily in two directions as predicted by a slip-line field for a closed interface crack. The crack tip sliding displacement (CTSD) is considered as a valid indicator of the crack growth rate. The surface friction tends to increase the plastic zone size and enhance the relative displacement of crack faces in the sliding direction. The crack face friction, by contrast, considerably reduces the plastic zone size and the values of CTSD. A fatigue model for interface delamination of thin film contact systems was established and the main conclusions of the finite element analysis were validated experimentally.

Thesis Advisor: Dr. Nannaji Saka
Title: Principal Research Scientist and Lecturer

Thesis Advisor: Dr. Ernest Rabinowicz
Title: Professor of Mechanical Engineering

Acknowledgements

About five years ago, I arrived in New York city from Beijing, China. Being in a new country for the first time, I was excited, anxious, and nervous at that time. Just before heading for a graduate school in Ohio, I made a phone call to Dr. Nannaji Saka and asked him if I could come to the MIT with the admission papers but without the entering visa to MIT. Later this phone call turned out to be the beginning of the journey of my graduate study at the MIT.

The first taste of the MIT course I took was 2.800, *Tribology*, taught by Professor Ernest Rabinowicz. I had missed two weeks of classes since I came late, but I managed to catch up with this entrance course of the Tribology Research Program. Every student in the tribology group had his own research project. The first project Dr. Saka assigned me was on boundary lubricated sliding. Still trying to get used to the environment and the "culture" of the tribology group, I started to learn some experimental techniques and gained a lot of computer experience as Dr. Saka gradually furnished the tribology laboratory with microcomputers. My wife joined me from China in the spring of 1987, right after I obtained my M.S.M.E. and passed the qualifying exam. Since then I have worked on scuffing, plasma polymerization, and rolling contact fatigue. Finally, the tribology of electrical contacts was chosen as my doctoral thesis topic. I spent two and a half years on the project, and submitted several papers for publication based on the thesis.

Dr. Saka, my thesis advisor, is a truly extraordinary educator and researcher. The five years I have worked with him have been an experience of learning and maturing, both intellectually and personally. His guidance and support over the years are appreciated. During our numerous afternoon and evening discussions, his physical intuition and academic insight helped me formulate my thesis. I am sure that what I have learned from him will be invaluable to my professional career.

I would like to thank my thesis co-advisor, Professor Rabinowicz, a highly distinguished scholar in the field of tribology. Discussion with him has been fun itself. I am grateful to him for his many helpful suggestions along the way and also for his generosity of providing me with noble metals for testing.

I would also like to thank Professor Nam P. Suh, a distinguished leader in the tribology field, for being on my thesis committee and for his constructive criticism and helpful suggestions as my thesis progressed. Special thanks are due Professor David M. Parks, the other thesis committee member, for helping me set up the

finite element analysis and for keeping me informed of the frontier research of fracture mechanics of bimaterials.

The faculty and students in the tribology group are remarkable people, who are inspirational in their dedication to hard work and creative thinking. I have learned a lot from them. I wish to thank Professor Ming-Kai Tse, Messrs. John Briggs and Penyun Gu for helping me set up the acoustic emission experiments. Thanks are also due Dr. Zhigang Suo of Harvard for teaching me interface fracture mechanics, and Professor T. Erturk of the University of Lowell for his encouragement and remarks regarding looking at things in proper perspective. I also want to extend my thanks to my friends and my fellow graduate students who made my stay at MIT a fulfilling experience. My sincere appreciation is extended to Ms. Dorothy Cavignano for her constant help and care, to late Ms. Georgia Nagle for her help and for that wonderful pool party, to Ms. Leslie Regan for her help on administrative matters, and to Messrs. Fred Coté and Victor Lerman for their help in the workshop throughout the years.

This work was sponsored by the Teradyne Connection Systems, Inc., of Nashua, New Hampshire. Working on an industrial problem brought me not only with something a little closer to the real world, but also to some special people. I wish to thank Messrs. Vasant Gandhi, Dave Gailus, Mark Gailus, Len Johnson, Lou Spiridigliozzi, Phil Stokoe, and David Whitehead of Teradyne for their continued interest in this project and for their constant help during this work.

One-term teaching assistantship of *Thermodynamics* provided by Professors Joseph L. Smith, Jr., Markus I. Flik, and Gilberto Russo is also highly appreciated.

Finally, special thanks are due, as always, my parents whose love and encouragement have been supporting me all these years, and my wife Xiaofang for her enthusiasm, cheerfulness, and everything she has endured on my behalf. I also wish to express my deepest gratitude to Shulan, my mother-in-law, who came a long way from China to take care of our baby boy. I will be spending more time playing with my eighteen month old son, Kevin, after my graduation.

Tribology Laboratory, MIT Hong Tian
June, 1990

Contents

List of Tables

List of Figures

Chapter 1

Statement of the Problem

1.1 Introduction

The Van Nostrand's Scientific Encyclopedia [1] defines thin film systems as layers of any substances that are deposited on planar or curved substrates by vacuum evaporation, cathode sputtering, electroplating, spraying, and by various surface chemical reactions in a controlled atmosphere or electrolyte. The thickness of such supported films ranges from an atomic monolayer to a few micrometers. Due to their unique characteristics, thin film systems are widely used in decorative finishing, mechanical, electronic, magnetic, and optical devices [2]. In tribology, the thin films are often used as protective coatings. For example, soft metallic coatings (copper, gallium, gold, indium, lead, silver, tin, etc.) have been used to reduce friction and wear of gears, bearings, and electrical contacts. Hard coatings, such as nitrides, carbides, and oxides, have greatly improved the tribological behavior of various machine elements and cutting tools.

In electrical connectors in particular, layered metallic surfaces have been of widespread use to satisfy multiple functional requirements, such as high electrical conductivity, solderability, corrosion resistance, and wear resistance [3]. As the computer and telecommunication industries evolve toward smaller and more powerful systems, the need for reliable high-density electrical connectors becomes a great challenge to both design engineers and material scientists. The basic criterion for choosing contact materials is that a connector must be designed to preserve the electrical integrity (high electrical conductivity or low contact resistance) of the contact over the life of the application, i.e., maintaining low contact resistance at the contact spots.

At present an electroplated thin gold coating on copper or a copper-based alloy substrate, with a nickel underplate between the gold coating and the substrate, is the typical structure of low-voltage low-current electrical connectors. Gold does

not react with atmosphere to form oxide and has high electrical and thermal conductivities. No other metal (not even palladium, platinum or rhodium) is as completely free of oxide film as gold. Another advantage of using gold as the top layer is that gold surfaces provide clean and reliable metal-to-metal contact even at a very low normal force. However, gold surfaces are not always good for all contact applications. For example, gold should not be used in arcing contacts because it erodes rapidly and has a strong tendency to weld. Also gold should always be applied as a thin film layer on a substrate instead of a pure solid, because solid gold tends to stick, gall, smear, and wear severely. Nevertheless, gold is now the best contact material for the high-density electrical connectors.

The nickel underplate is used for several reasons. If no nickel underplate is present, the corrosion products (oxides of the base materials such as copper) may build up within a pore which exists due to high porosity of gold plating. These corrosion products may migrate up the walls of the pore and eventually contaminate the contact surfaces. When a nickel underplate is applied, nickel oxide films form at the base of the pore sites. Since nickel oxides have limited migration, the potential corrosion/degradation due to the porosity of gold coating is greatly reduced by using a nickel underplate. Another function of nickel underplate is to be a diffusion barrier. When the connectors are subjected to elevated temperatures (200-500°C) during soldering and brazing, solid state diffusion occurs across the layers. Diffusion of copper through nickel is about two orders of magnitude slower than it is through gold, palladium and silver. Thus the nickel underplate acts as a barrier to prevent the contamination of gold by the diffusion of zinc or copper atoms from a brass substrate. Additionally, sliding and fretting wear resistances can be generally increased by "hardening" the composite thin film system with a nickel underplate.

While connectors provide ease of assembling and disassembling electronic systems, they are also the "weak links" in an otherwise reliable system. The reliability of the advanced expensive electronic systems are totally dependent on the successful operation of the relatively inexpensive connectors. Thus the reliability of electrical connectors is vital to the reliability of modern electronic systems. A failure rate of about 0.001 percent per 1,000 hours of operation is often required for connectors in the modern electronic systems.

In practice connector failures are diverse and elusive. The ultimate failure of connectors is wear-out of the gold coating and exposure of base metals, which leads to high contact electrical resistance due to oxidation and corrosion of the base metals. The frequent assembly and disassembly (insertion and withdrawal) of connectors often lead to sliding failure of the gold contacts. Fretting failure also occurs as a result of vibration and thermal excursion of connectors. A harsh environment (high humidity, high temperature, etc.) often facilitates the corrosion failure of the base metals once the gold plating is worn out.

The various aspects of contact failure have been investigated by many researchers and reported in literature. For example, Antler [4] showed that gold hardened with a small percentage (usually less than 1 percent) of cobalt or nickel provides a great improvement of wear resistance. However, if the gold coating with cobalt or nickel additives is exposed to high temperatures (200 °C) for long periods, the cobalt or nickel may migrate to the contact surface forming an insulating oxide film. Gold plated from an acid cyanide bath contains considerable void volume which is filled with polymeric reaction products of the cyanide. These polymers greatly reduce the adhesive wear of gold without loss of the high conductivity of the gold contact [5]. Lubrication is an effective tool for improving wear life of the connectors. Typical lubricants are polyphenyl ether and microcrystalline wax [6,7]. The microcrystalline wax is widely used in the telecommunication industry. The only concern with its use is that the microcrystalline wax cannot withstand long exposure to high temperatures (above 200°C). Polyphenyl ether, by contrast, has been widely used as a base for high temperature lubricants. Another important issue is the frictional polymer which is formed when organic vapors polymerize on catalytic surfaces. The polymer may adhere to the contact surface causing high contact resistance. The most catalytic materials are platinum group metals and gold is also catalytic but to a much lesser extent. One solution is to use lubricant which prevents the polymer from adhering to the surface. Another way is to simply provide sufficient contact force to displace the polymer.

One of the important aspects of contact failures is that the interfacial bonding between films and substrates must be strong enough to sustain external thermal and mechanical loadings. If bonding is poor at either the gold-nickel interface or the

nickel-substrate interface, debonding or microcracking may take place under cyclic contact loading. Eventually interfacial delamination could cause the fatal failure of electrical connectors. Thus the failure mechanisms (and the tribological behavior) of thin film systems under sliding and fretting contacts need to be carefully examined. Then the critical operation parameters must be identified from the contact mechanics point of view to assure better designs of the thin film contact systems.

1.2 Mechanisms of Friction and Wear

Before presenting the objectives of this study and scope of the thesis, the current understanding of friction and wear phenomena are briefly reviewed with an emphasis on the thin film contact systems. Sliding friction mechanisms have been investigated for the past several decades. Recently Tabor [8] has reviewed the developments over last fifty years in friction and wear. The first study of friction was pioneered by Amontons [9] in 1699 and by other French scientists. Coulomb [10] summarized the laws of friction in 1785. Since then, Coulomb's view that friction is caused by the interlocking of surface asperities had dominated thinking of engineers, and had led to the false notion that smooth surfaces are frictionless until about 60 years ago when the adhesion theory of friction emerged as a dominant theory of friction. The pioneering work on the adhesion theory of friction was done by such distinguished scientists as Tomlinson [11], Bowden [12], Holm [13], and Bowden and Tabor [14]. The adhesion theory of friction states that the adhesion between contacting asperities is the major cause of friction and that the friction force is the product of the shear strength and the area of welded junctions between contacting asperities. Later Rabinowicz [15] incorporated surface energy of contact materials into the adhesion model of friction to explain high friction coefficients observed in the sliding tests of pure metals with very smooth contact surfaces. Recently, other researchers have developed the deformation models [16,17] and the plowing model of friction [18] to account for the discrepancies between experimental data and the predictions of the adhesion theory of friction. Suh and Sin [19] proposed that friction consists of three components: asperity deformation, plowing, and adhesion; but plowing was found to be the predominant mechanism of friction in both dry and boundary lubricated sliding [20].

All those theories, however, were developed for the sliding friction of extended homogeneous materials. Accordingly, they are not strictly applicable for the sliding friction of thin film contact systems. Now the effects of two interfaces, namely, the interface between contact surfaces, and the interface between films and substrates, must be explicitly considered. Bowden and Tabor [14] showed long ago that the friction is a minimum at a critical film thickness. Besides the film thickness, sliding friction also depends on other things such as normal load, sliding velocity, the elastic-plastic property ratios of films and substrates, and most importantly, the interfacial bonding between films and substrates [21-23]. Several researchers have proposed analytical models of friction for thin film contact surfaces. For example, Rabinowicz [21] proposed a theory to explain the effects of film thickness on friction behavior, based on the characteristic junction sizes. Finkin [24] also investigated the effects of film thickness based on contact mechanics. Heilmann and Rigney [25] advanced an energy-based model of friction to the coated surfaces. Recently, Kato et al. [26-28] have developed a protuberance model of friction to study the effects of normal load, film thickness, and film topography. But the correlation between friction behavior and the interface "strength" of film-substrate systems has not been addressed.

Wear is generally classified as adhesive wear, abrasive wear, oxidation wear, delamination wear, and melting wear, as in the Wear-Mechanism Map developed by Lim and Ashby [29]. The first equation of mechanical wear, or adhesive wear, is attributed to Holm [30]. Later Archard [31] gave a theoretical support to that equation. Archard's equation was originally aimed at adhesive wear, but it has also been used to estimate wear rates due to other type of wear mechanisms [32]. For the wear of sliding electrical contacts, Rabinowicz [33] introduced a compatibility chart of noble metals, and provided guidelines for selecting material combinations to obtain low friction and low wear [34]. Antler [35] showed that adhesive wear is more important than abrasive wear and brittle fracture when noble metals such as gold, silver, palladium, and their alloys are used as thin film materials. Prow formation in front of a spherical slider and wear particle transfer between sliding surfaces are claimed to be the main wear processes. Halling [36] developed a wear equation for thin film systems based on Archard's assumption that wear rate is

proportional to some power of contact area. The wear rate was found to be lower for thinner films in that model.

The delamination theory of wear was introduced by Suh [37] in the early 1970s for dry sliding of homogeneous materials. In repeat-pass sliding, cracks initiate at dislocation pile-ups a short distance below the surface, and especially around second-phase inclusions. Delamination occurs when the cracks propagate and emerge at the surface, resulting in thin sheets of wear particles. For the contacts of thin film systems, the interface between the film and the substrate is the likely place for an interface crack to initiate and grow. Delamination can occur right along the interfaces due to poor bonding or low interface strength. Indeed, recent experimental observations have shown that cracks could be readily initiated at interfaces due to residual stresses when thin film systems are quenched to low temperatures. Cracks were found to propagate along the interfaces [38-40]. In sliding and fretting stress fields, however, the stresses are predominantly compressive. Thus the initiation and growth of cracks along interfaces are rather complex. Accordingly, the fundamental aspects of interfacial delamination in sliding and fretting situations need to be addressed.

1.3 Scope of the Thesis

In this thesis, the tribological behavior of electroplated gold film systems used for electrical connectors is investigated. The interfacial delamination of the multi-layer contact systems is emphasized. It is hoped that a basic understanding from contact mechanics point of view will be established for a rational design of thin film systems for electrical connectors. Chapters 2 and 3 are the experimental investigation of sliding and fretting failures of the electroplated gold contacts, respectively. The finite element method (FEM) is used to conduct the stress and strain analyses. Chapter 4 is the FEM analysis of normal contact, Chapter 5 of the sliding contact, and Chapter 6 of the sliding contact with an interface crack. The summary of the thesis and the experimental evaluation compose in Chapter 7. Each chapter is relatively independent, and has its own nomenclature and references. Brief descriptions of the each chapter are as follows.

Chapter 2 Mechanisms of sliding failure

Reciprocating sliding tests, which simulate the operation of insertion and withdrawal of electrical connectors, were conducted with a sphere-on-flat arrangement to investigating the mechanisms of friction and failure of electroplated gold contacts. Brass balls and plates which were electroplated with nickel and gold were used as contact specimens. The friction force, electrical contact resistance and acoustic emission (AE) signals were continuously recorded during the sliding tests. Scanning electron microscopy and Auger electron spectroscopy were used to identify the failure processes. In addition, lubricated sliding tests were conducted with polyphenyl ether as a lubricant for comparison. Implications of these experimental findings for the design of electrical connectors are discussed.

Chapter 3 Mechanisms of fretting failure

Fretting tests, also with a sphere-on-flat arrangement, were carried out to investigate the fretting failure mechanisms of electroplated gold contacts. The minimum fretting amplitude necessary for gross slip was determined experimentally and all fretting tests were conducted at amplitudes larger than the minimum amplitude. The friction force and the electrical contact resistance were continuously recorded during the fretting tests. Lubricated fretting tests were also conducted with mineral oil as a lubricant. Both the ball and plate specimens were examined by a scanning electron microscopy and Auger electron spectroscopy. The failure criterion based on electrical contact resistance, which is commonly used, is carefully examined.

Chapter 4 FEM analysis of normal contact

The contact problem of a rigid cylinder indenting an elastic-plastic two-layer half-space, in particular the Au/Ni/Copper structure used in electrical connectors, is analyzed using the finite element method. The contact pressure, subsurface stresses and strains, interfacial stresses and strains are obtained for various thicknesses of the interlayer (nickel). Both elastic and elastic-plastic loadings are applied on a two-layer half-space. The location of initial yielding is identified for different interlayer

thicknesses. In the light of the finite element results, the mechanisms of crack initiation at interfaces and the interfacial delamination process are qualitatively addressed.

Chapter 5 FEM analysis of sliding contact

It is well known that the effect of friction forces in sliding is more important to the wear of materials than the normal forces. Thus stress analysis of thin film systems subjected to both normal and tangential loadings is necessary to understand the wear processes at contact spots. In this chapter, the stress and strain fields of a elastic-plastic two-layer half-space are determined. A plane strain finite element mesh is set up for the stress analysis. The normal and tangential loadings are applied proportionally and incrementally on the surface. Surface deformation, location of initial yielding, stresses and strains along the interfaces between layers and between layer and substrate are examined. Effects of the surface friction are emphasized. The implications for interface failures are qualitatively addressed.

Chapter 6 Interfacial cracking

In the stress analysis of normal and sliding contacts, perfect bonding between films and substrates is assumed. In reality, however, defects or weakly bonded areas always exist at interfaces. These interface flaws can be treated as pre-existing interface cracks. In this chapter, a plane strain finite element model for the growth of an interface crack in an elastic-plastic two-layer half-space under sliding contact is presented. The elastic theories of interface cracking are briefly reviewed, and the limitations of the elastic solutions to the present problem are discussed based on the finite element calculations. The size of plastic zone around crack tips is compared with the crack length and the coating thicknesses. The stress and strain states around the crack tips are also characterized. The crack sliding displacement (CSD) is calculated at various loading positions. The effects of both the surface friction and the crack face friction on the crack growth are emphasized.

Chapter 7 Experimental evaluation

The main conclusions from the previous chapters are summarized. A fatigue model for interfacial delamination is proposed. The main conclusions from the FEM analysis are validated experimentally. The effects of metallurgical compatibility, the surface roughness, and diffusion annealing on delaying interfacial delamination are investigated. Finally, the limitations of both experimental investigations and the FEM analyses are examined, and the future work is suggested accordingly.

References

[1] *Van Nostrand's Scientific Encyclopedia*, 7th Edition, Van Nostrand Reinhold, New York, 1989.

[2] *Handbook of Thin-Film Deposition Processes and Techniques: Principles, Methods, Equipment and Applications*, ed. by Schuegraf, K. K., Noyes Publications, Park Ridge, New Jersey, 1988.

[3] *Principles of Electronic Packaging*, ed. by D. P. Seraphim, R. Lasky, and C-Y. Li, McGraw-Hill, Inc., New York, 1989.

[4] Antler, M., "Sliding Wear of Metallic Contacts," *IEEE Trans. Circuit, Hybrids and Manufacturing Technology*, Vol. CHMT-4, 1981, pp. 15-29.

[5] Freed, R. L., "Microstructural Characterizations of Thick, Soft and Hard Gold Electrodeposits," *13th Annual Connector Symposium Proceedings*, Oct. 8-9, 1980, pp. 11-20.

[6] Antler, M., "Survey of Contact Fretting in Electrical Connectors," *IEEE Trans. Circuit, Hybrids and Manufacturing Technology*, Vol. CHMT-8, 1985, pp. 87-104.

[7] Messina, F. D., "Evaluation of Microcrystalline Wax Dispersion Contact Lubricants," *Holm Conference on Electrical Contacts*, 1980, pp. 49-52.

[8] Tabor, D., "Friction and Wear -- Developments Over the Last Fifty Years," *Tribology--Friction, Lubrication and Wear, Fifty Years On, Proceedings of the Institution of Mechanical Engineers*, Vol. 1, 1987, Paper C245/87.

[9] Amontons, G., "De La Resistance Causée Dans Les Machines," *Mémoires de L'Académie Royale A*, Vol. 12, 1699, pp 257-282.

[10] Coulomb, C. A., "Théorie des Machines Simples," Mémomires de Mathématique et de Physique de L'Académie Royale, Vol. 10, 1785, pp 161-342.

[11] Tomlinson, G. A., "A Molecular Theory of Friction," Phil. Mag., Vol. 7, 1929, pp 905-939.

[12] Bowden, F. P., *General Discussion on Lubrication, Institution of Mechanical Engineerings*, Vol. 2, 1937, pp 183-184.

[13] Holm, R., *Electric Contacts*, Almqvist & Wikssells, J. Springers Verlag, Berlin, 1946, pp 202-210.

[14] Bowden, F. P. and Tabor, D., "Mechanism of Metallic Friction," *The Friction and Lubrication of Solids*, The Clarendon Press, Oxford, 1950, pp 90-121.

[15] Rabinowicz, E., *Friction and Wear of Materials,* John Wiley & Sons, Inc., New York, 1965, pp 65-67.

[16] Challen, J. M. and Oxley, P. L. B., "An Explanation of the Different Regimes of Friction And Wear Using Asperity Deformation Models," *Wear,* Vol. 53, 1979, pp 229-243.

[17] Johnson, K. L., "Aspects of Friction," *Proc. 7th Leeds -Lyon Symposium on Tribology,* University of Leeds, England, 1980, pp 3-12.

[18] Tzukizoe, T. and Sakamoto, T., "Friction in Scratching without Metal Transfer," *Bull. JSME,* Vol. 18, 1975, pp 65-72.

[19] Suh, N. P. and Sin, H.-C., "The Genesis of Friction," *Wear,* Vol.69, 1981, pp 91-114.

[20] Komvopoulos, K., Saka, N. and Suh, N. P., "The Mechanism of Friction in Boundary Lubrication," *J. Tribology,* Vol. 107, 1985, pp 452-462.

[21] Rabinowicz, E., "Variation of Friction and Wear of Solid Lubricant Films with Film Thickness," *ASLE Trans.,* Vol.10, 1967, pp 1-9.

[22] Sherbiney, M. A. and Halling, J., "Friction and Wear of Ion-Plated Soft Metallic Films," *Wear,* Vol. 45, 1977, pp 211-220.

[23] Halling, J., "The Tribology of Surface Coatings, particularly Ceramics," *Proc. Institution of Mechanical Engineers,* Vol. 200, 1986, pp 31-40.

[24] Finkin, E. F., "A Theory for the Friction of Sulfide and Other Thin Films," *Wear,* Vol. 18, 1971, pp 231-241.

[25] Heilmann, P. and Rigney, D. A., "An Energy-Based Model of Friction and Its Application to Coated Systems," *Wear,* Vol. 72, 1981, pp 195-217.

[26] Kato, S., Yamaguchi, K., Marui, E. and Tachi, K., "Frictional Properties of a Surface Covered with a Soft Metal Film - Part II: Analysis of Friction Between a single Protuberance and a Surface," *J. Lub. Tech.,* Vol. 104, 1982, pp 39-45.

[27] Kato, S., Marui, E. and Tachi, K., "Frictional Properties of a Surface Covered with a Soft Metal Film (Interference Effect of Soft Metal Film Deformation between Two Protuberances)," *J. Tribology,* Vol. 107, 1985, pp 444-451.

[28] Kato, S., Marui, E. and Tachi, K., "Frictional Properties of a Surface Covered with a Soft Metal Film (Surface Topography and Frictional Properties)," *J. Tribology,* Vol. 109, 1987, pp 545-551.

[29] Lim, S. C. and Ashby, M. F., "Wear-Mechanism Maps," *Acta Metall.*, Vol. 35, 1987, pp 1-24.

[30] Holm, R., "Mechanical Wear in Currentless Sliding Contacts," *Electric Contacts*, Almqvist & Wikssells, J. Springers Verlag, Berlin, 1946, pp. 214-221.

[31] Archard, J. F., "Contact and Rubbing of Flat Surfaces," *J. Appl. Phys.*, Vol. 24, 1953, pp 981-988.

[32] Rabinowicz, E., "Wear Coefficients --- Metals," Wear Control Handbook, Eds. by Peterson, M. B. and Winer, W. O., ASME, 1980, pp 475-506.

[33] Rabinowicz, E., "The Influence of Compatibility on Different Tribological Phenomena," *ASLE Trans.*, Vol. 14, 1971, pp 206-212.

[34] Barber, S. A. and Rabinowicz, E., "Material Selection for Noble Metal Slip Rings," *Proc. Holm Conference on Electrical Contacts*, Illinois Inst. of Technology, Chicago, IL, 1980, pp 33-40.

[35] Antler, M., "Sliding Wear of Metallic Contacts," *IEEE Trans. Circuit, Hybrids and Manufacturing Technology*, Vol. CHMT-4, 1981, pp 15-29.

[36] Halling, J., "Toward a Mechanical Wear Equation," *J. Lub. Tech.*, Vol. 105, 1983, pp 213-220.

[37] Suh, N. P., "The Delamination Theory of Wear," *Wear*, Vol. 25, 1973, pp 111-124.

[38] Evans, A. G. and Hutchinson, J. W., "On the Mechanics of Delamination and Spalling in Compressed Films, " *Int. J. Solids Structures*, Vol. 20, 1984, pp 455-466.

[39] Hu, M. S., Thouless, M. D., and Evans, A. G., "The Decohesion of Thin Films from Brittle Substrates," *Acta Metall.*, Vol. 36, 1988, pp 1301-1307.

[40] Cao, H. C., Thouless, M. D., and Evans, A. G., "Residual Stresses and Cracking in Brittle Solids Bonded with a Thin Ductile Layer," *Acta Metall.*, Vol. 36, 1988, pp 2037-2046.

Chapter 2

Friction and Failure of Electroplated Sliding Contacts

Summary

The mechanisms of friction and failure of electroplated gold contacts have been investigated. Brass balls and plates which were electroplated with nickel and gold were used as contact specimens, and reciprocating sliding tests were conducted with a sphere-on-flat arrangement. The friction force, electrical contact resistance and acoustic emission (AE) signals were continuously recorded during the sliding tests. Scanning electron microscopy and Auger electron spectroscopy were used to identify the failure process. In addition, lubricated sliding tests were conducted with polyphenyl ether as a lubricant. Three stages could be distinguished in the sliding tests. In stage I, the friction coefficient increased steadily and prows formed on the ball surface, which then were rubbed off. In stage II, cracks initiated and propagated at the nickel-brass interface of the ball specimen, and eventually emerged to the surface. The friction coefficient was more or less constant in this stage until plate-like wear particles were delaminated from the nickel/brass interface of the ball specimen. In stage III, wear particles continually delaminated from the ball specimen and adhered to the plate surface, resulting in high and fluctuating friction as well as severe wear. The RMS values of the AE signal remained more or less constant in the first two stages, but fluctuated significantly in stage III. Lubrication was very effective in keeping the sliding interface in stage I throughout the test. Implications of these findings for the design of electrical connectors are discussed.

List of Symbols

a = radius of contact or indentation

A = constant

A_r = real area of contact

E = Young's modulus

E_1, E_2 = energy

E_f = Young's modulus of film

f = ratio of shear strength of interface to shear strength of substrate

h = depth of indentation

k = wear coefficient

L = normal load

p = hardness

R = radius of indenter

R_c = electrical contact resistance

r = radial coordinate

s = shear strength

t = film thickness

V = wear volume

W_{ab} = work of adhesion

x = sliding distance

α = asperity slope

γ = surface energy

μ = friction coefficient

ν = Poisson's ratio

ν_f = Poisson's ratio of film

ρ_1, ρ_2 = resistivity

σ_{Mises} = Mises equivalent stress

$\sigma_r, \sigma_\theta, \sigma_z$ = radial, circumferential and axial stresses

σ_{Tresca} = Tresca equivalent stress

2.1 Introduction

In the electrical connector industry, layered metallic surfaces have been of widespread use to satisfy such multiple functional requirements as low contact resistance, wettability and solderability, corrosion resistance, and wear resistance. Thin composite layers comprising gold and nickel are commonly used on copper, brass or phosphor bronze substrates to meet these requirements at low cost. Because gold is a noble metal with good electrical and thermal conductivities, as well as excellent corrosion resistance, it is applied as the surface layer. An underplate layer of nickel is used as a diffusion barrier between the surface layer (gold) and the substrate (copper, brass, or bronze). Sliding and fretting wear lives of the gold plated surfaces are greatly increased by nickel underplating.

The tribological behavior of electrical connectors is vital to the reliability of modern electronic systems. Although these multi-layer connectors perform fairly well, sliding failure due to frequent mating and unmating still remains a major concern. Antler [1] investigated the friction and wear of thick electrodeposited gold using a pin-on-flat apparatus. He found that the dominant wear mechanism of electroplated gold was prow formation, a phenomenon first investigated by Cocks [2]. The prow formation process is closely related to junction growth. A model of junction growth proposed by Greenwood and Tabor [3] suggests that junction growth readily occurs in soft ductile metals whereas hard and low-ductility surface materials limit junction growth. Electroplated nickel-hardened gold was indeed shown to give better wear resistance [4-6]. The wear mechanism changed from severe to mild adhesive wear, and then to "brittle" fracture as the nickel content in the gold was increased. Wear of electroplated gold was also considerably reduced by a hard nickel underplate [7]. Recently, Goodman and Page [8] have studied the wear behaviour of two Au-Co electrodeposits. Whether the sliding failures were associated with catastrophic failure of the plating-substrate interface or with progressive attrition of gold by adhesive wear is unclear.

Nevertheless, once the gold coating is worn out or is delaminated from either contact surface, substrate corrosion causes unacceptable increases in contact resistance. From the reliability point of view, then, it is desirable to determine the failure mechanisms of electroplated contacts. The objective of this study therefore is to

determine the dominant mechanisms of sliding friction and failure of electroplated contacts. Friction, electrical contact resistance, and acoustic emission (AE) signal were measured in sliding tests of electroplated gold contacts with nickel underplating. Auger electron spectroscopy (AES) was also used to determine the wear process. Implications of these findings for the design of electrical connectors are discussed.

2.2 Experimental

2.2.1 Materials and specimens

Figure 2.1a shows the micrograph and Figure 2.1b a schematic longitudinal section of a typical electrical connector. The stationary contact is spherical; the movable contact is flat. A normal force is applied by the spring action of the stationary contact as the movable contact is inserted. To simulate these insertion and withdrawal processes, a sphere-on-flat geometry was chosen for the reciprocating sliding tests. Brass balls, 3.175 mm in diameter, with 1.5 μm electroplated gold over 2.5 μm nickel underplate, and brass plates with 1.5 μm electroplated gold over 5 μm nickel underplate were used as test specimens. The relevant bulk properties of the contact materials are listed in Table 2.1. The hardness of the electroplated gold was measured using a Knoop microhardness tester at a penetration force of 0.1 N.

2.2.2 Apparatus and experimental procedures

A schematic diagram of the sliding test apparatus is shown in Figure 2.2a. The plate specimen was mounted on a platform which was driven back and forth at a frequency of 0.1 Hz by an electric motor. The stroke length was 20 mm. A normal force of 1 N was applied by a deadweight. The ball specimen was held stationary in a stainless steel holder, which was attached to a strain ring. The friction force was measured by the strain gages mounted on the strain ring. Figure 2.2b shows the contact ball/AE sensor assembly. A piezo-electric ceramic AE sensor (Vernitron PZT-5A), which produces a voltage when subjected to a stress pulse, was held between two aluminum blocks which were used as two electrodes for AE outputs. One aluminum block was in contact with the ball specimen, and the other

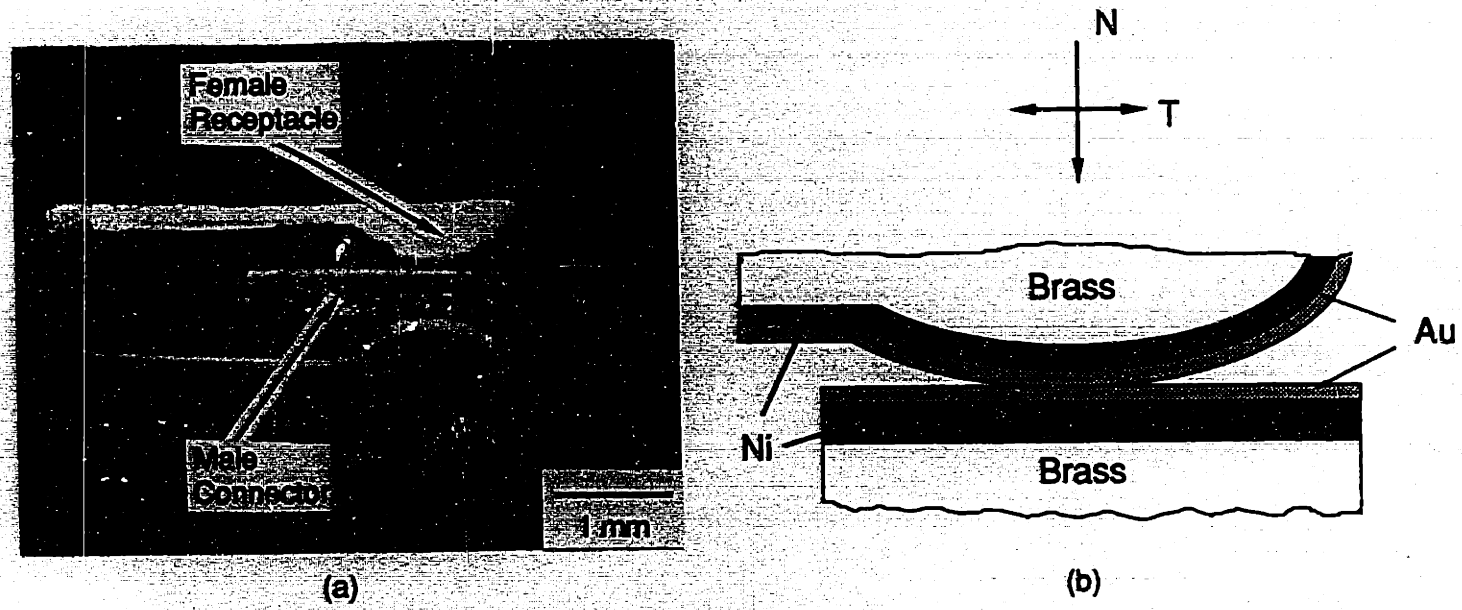

Fig. 2.1 Single electrical connector: (a) micrograph and (b) schematic of longitudinal section

Table 2.1 Properties of Experimental Materials

Materials	Electrical Resistivity ($\Omega m\ 10^{-8}$)	Young's Modulus (GPa)	Poisson's Ratio	Yield Strength (MPa)	Penetration Hardness (MPa)	Surface Energy (J/m^2)
Au + 0.5%Ni	2.24	79	0.32	298	953	1.12
Ni	6.84	204	0.32	815	2548	1.70
Brass (Cu-35%Zn)	7.80	125	0.32	405	1244	0.99*

* $\gamma_{Cu} = 1.10\ J/m^2$, $\gamma_{Zn} = 0.79\ J/m^2$, $\gamma_{Brass} = 0.65\ \gamma_{Cu} + 0.35\ \gamma_{Zn} = 0.99\ J/m^2$

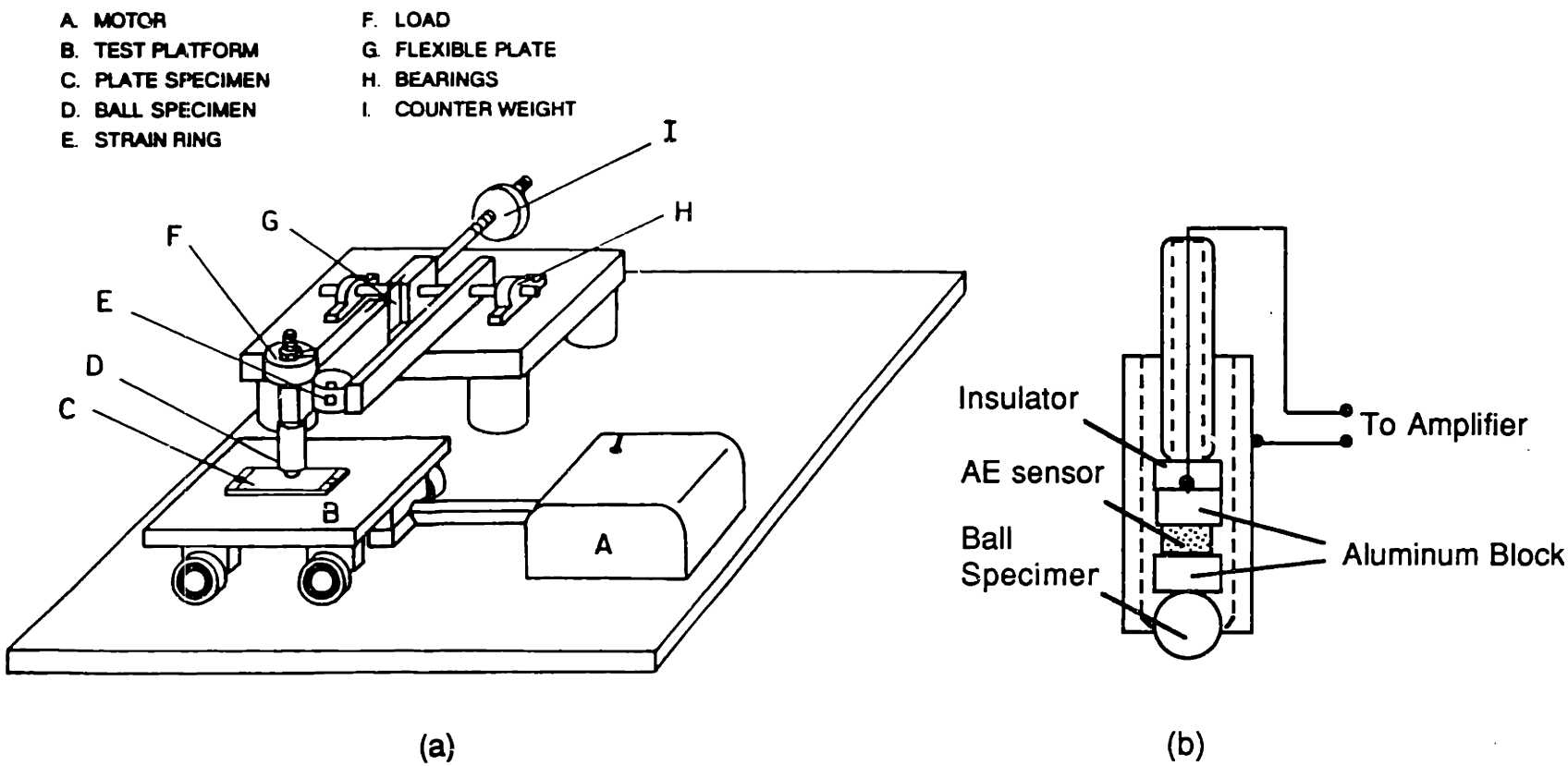

Fig. 2.2 Schematic of apparatus: (a) the sliding tester and (b) the ball holder

was insulated from the ball holder. The whole assembly was lightly tightened by a set screw. One wire soldered to the plate specimen and the other screwed tightly to the ball specimen were connected to a Wheatstone bridge circuit to measure the contact resistance continuously during the sliding test. The contact voltage drop and the current through the contact spots were about 0.2 mV and 12 mA, respectively. Thus any heating effects at the contact spots were ignored.

Figure 2.3 is a block diagram of the instrumentation. The friction force and the contact resistance signals were directly sent to a computer data acquisition system. The output from the AE sensor was first sent to a broad-band differential amplifier (Tektronix AM502), where the AE signals in the frequency range 0.1 Hz - 1 MHz were amplified and filtered to provide a wide-band frequency response. Then the signal was sent to an RMS meter (Hewlett-Packard 3400A), a spectrum analyzer (Hewlett-Packard 3461A), and a high-speed digitizer (Tektronix 7D20). The RMS meter output was connected to the computer data acquisition system. The spectrum analyzer output, which examined frequency responses in the 0 to 100 kHz range, was sent to another computer (Compaq 386) for storage. The digitizer sampled data at a rate of 2 MHz, monitoring frequencies in the 0 to 1 MHz range. Its output was also sent to the computer. A computer program (in C language) was written to perform a Fast Fourier Transform (FFT) of the digitizer output, and the spectral data were stored for later processing.

Before each test, both the ball and the plate specimen were cleaned with acetone in an ultrasonic cleaner for a few minutes and then cleaned with Freon TF solvent. After the specimens were mounted and a dead weight of 1 N was applied on the ball holder, the data acquisition system was activated for one minute to take a trace of the background noise. Then the sliding test was started. The total number of sliding cycles was 500. All tests were conducted at room temperature in a laboratory environment.

2.2.3 Spectral analysis of AE signals

The reason for using an AE sensor is to correlate the changes in AE spectra with the sliding mechanisms of friction and failure. It was found that a single time trace of FFT of the AE signal did not provide a clear representation of changes in

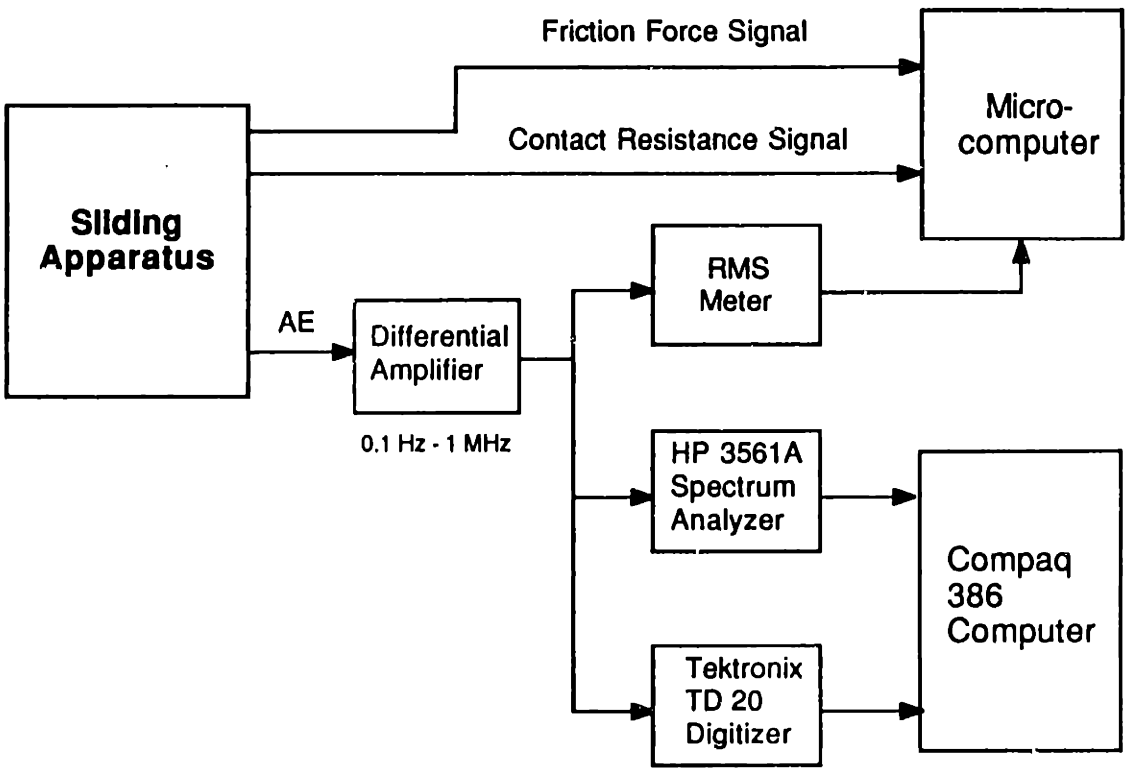

Fig. 2.3 Block diagram of instrumentation

the spectra. Thus averaging the magnitude in the frequency domain was necessary to nullify the short-term fluctuations in the AE spectra. The magnitudes of 100 waveforms of the AE spectra were averaged every minute by the spectrum analyzer, and 30 waveforms by the Tektronix digitizer. That is, an average frequency spectrum was obtained every minute (6 sliding cycles). Although some detail was lost, significant changes in the AE spectra could easily be identified by this averaging process.

In processing the AE spectral data, a normalization scheme was used to further identify the changes in the AE spectra. The AE spectrum at the onset of sliding was taken as a reference spectrum. All other spectral data were divided by the data of the reference spectrum, i.e., by the data of the average spectrum of the first 6 sliding cycles. The typical amplitudes of background noise and the reference spectrum are plotted in Figure 2.4. Compared with the background noise, the amplitude of the first AE signal was large enough to represent the AE spectrum of sliding. No significant differences were found in the AE spectra in the 100 kHz to 1 MHz frequency range. Thus all spectra are plotted only up to 100 kHz.

2.2.4 Auger electron spectroscopy and profilometry

The ball and the plate specimens were analyzed with a PERKIN-ELMER PHI 660 Scanning Auger Multiprobe. A 10 kV beam voltage was chosen to obtain maximum sensitivity for detecting gold. One minute of sputtering was used to reduce carbon peaks in the Auger spectra. The current density for sputtering was 15 mA/cm^2 at 2 kV. Ten Auger survey spectra were averaged at the selected areas. The surface profiles of the ball and the plate specimens were measured using a DEKTAK II profilometer. Profiles were taken in the direction perpendicular to the sliding direction.

2.3 Results

2.3.1 Friction coefficient, contact resistance, and RMS of AE signal

Upon examining the plots of friction coefficient versus the number of cycles of 25 sliding tests it became apparent that the sliding history can be divided into

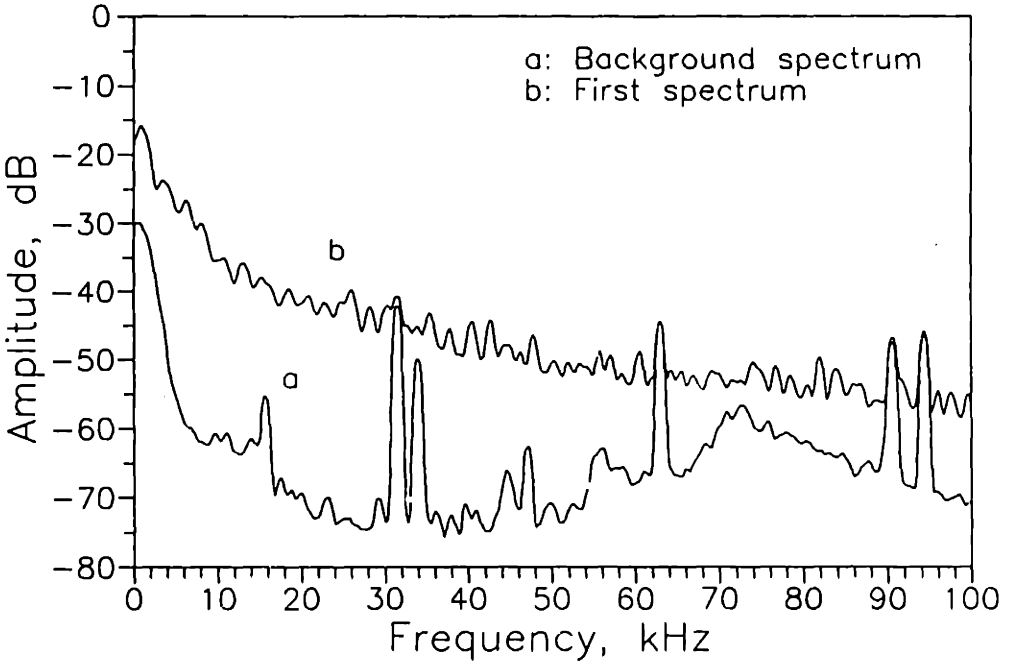

Fig. 2.4 AE spectra of the background and the first sliding cycle

three stages. Figure 2.5 shows the typical plots of the friction coefficient, electrical contact resistance, and RMS values of the AE signal versus sliding cycles. In stage I, the friction coefficient started at a low value, about 0.3, and it increased gradually as sliding continued. After about 90 sliding cycles, the friction coefficient reached a maximum, about 0.8. Then it quickly dropped to 0.4-0.5. In stage II, the friction coefficient quickly reached 0.6-0.7 and stayed at this value until the onset of the stage III (about 200 sliding cycles). The friction coefficient started increasing again in the stage III, fluctuating between 0.6 and 1.2. The contact resistance versus sliding cycles is plotted in Figure 2.5b. The contact resistance was almost constant throughout the sliding test.

Figure 2.5c shows the RMS values of the AE signal versus sliding cycles. RMS of the AE signal was essentially constant in the first stage, except for slightly high values at the end of stage I. In the second stage, the RMS values of the AE signal fluctuated more than those in the first stage. As the friction coefficient increased again at the onset of stage III, the RMS of the AE signal increased drastically and fluctuated as the sliding continued. Notice that a high friction coefficient does not necessarily correspond to a high RMS value of the AE signal.

2.3.2 Auger electron spectral analysis

In order to correlate the friction coefficient, the contact resistance and the RMS values of the AE signal with interactions at the sliding contact spots and to identify the mechanisms of friction and wear in the different stages, step-by-step sliding tests were conducted. Sliding tests were stopped after different number of sliding cycles which delineated different stages. The number of sliding cycles to reach those stages was not exactly the same in each test, but the scatter was within 50 sliding cycles. Auger electron spectroscopy (AES) survey was then conducted on both the ball and the plate specimens.

Figure 2.6 shows the micrographs of the ball and the plate specimens after 47 sliding cycles. As can be seen, a prow has formed on the ball surface. AES survey was taken in two areas on the ball surface, one at the center of the contact and the other on the edge of the prow. The AES spectra of both areas, Figures 2.7a and 2.7b, show only gold. (The appearance of carbon in the spectra is perhaps due to

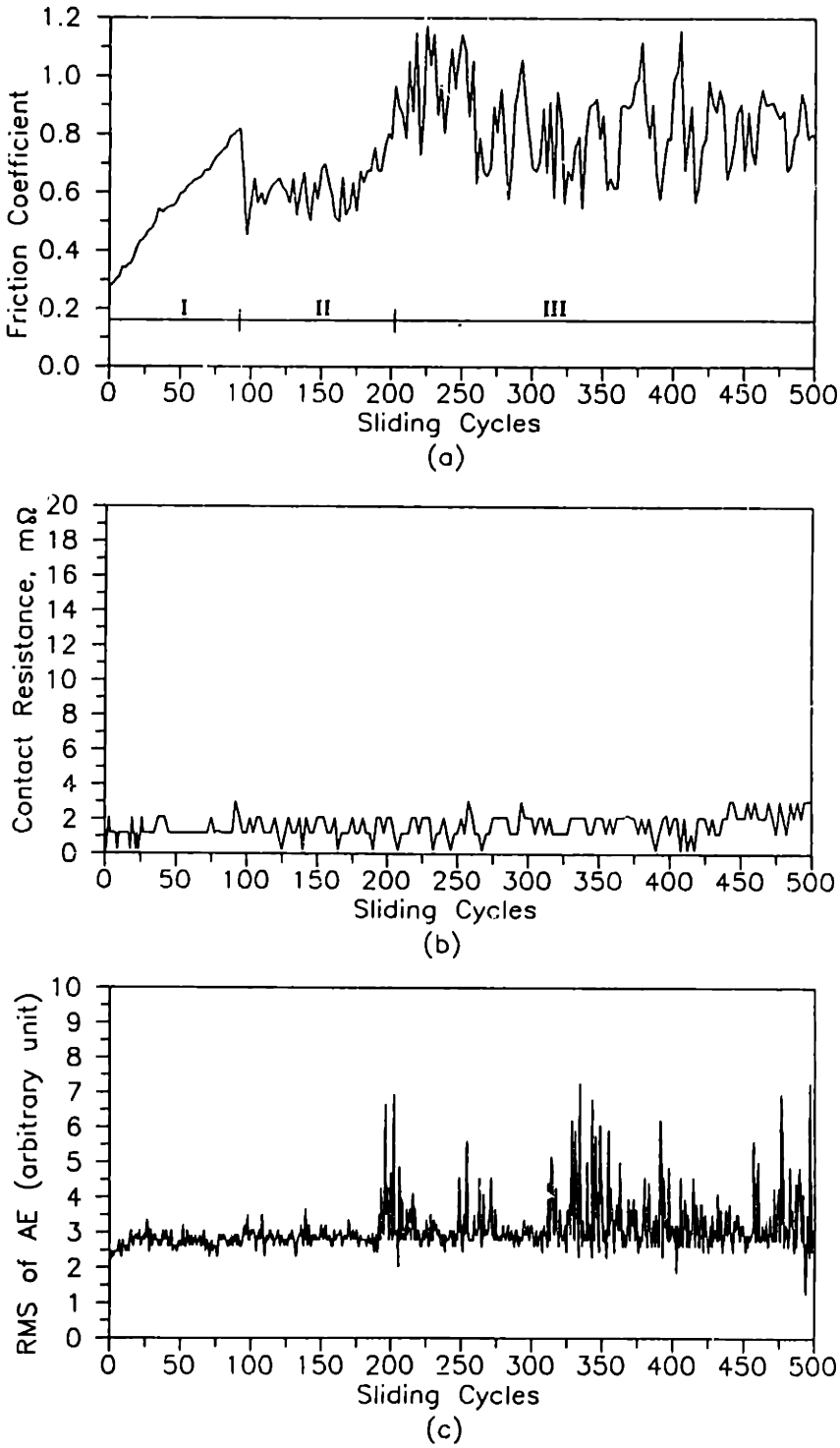

Fig. 2.5 (a) Friction coefficient, (b) contact resistance, and (c) RMS of AE signal versus sliding cycles

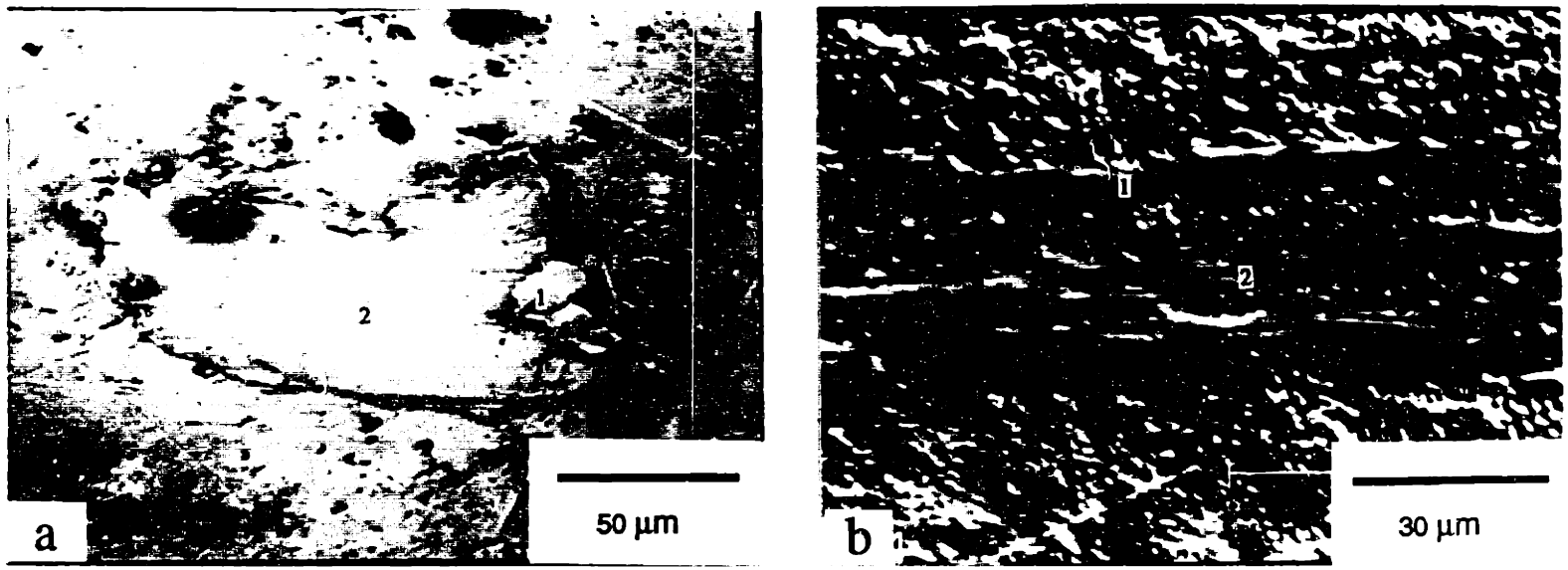

Fig. 2.6 Micrographs of worn surfaces after 47 sliding cycles:
(a) ball specimen and (b) plate specimen

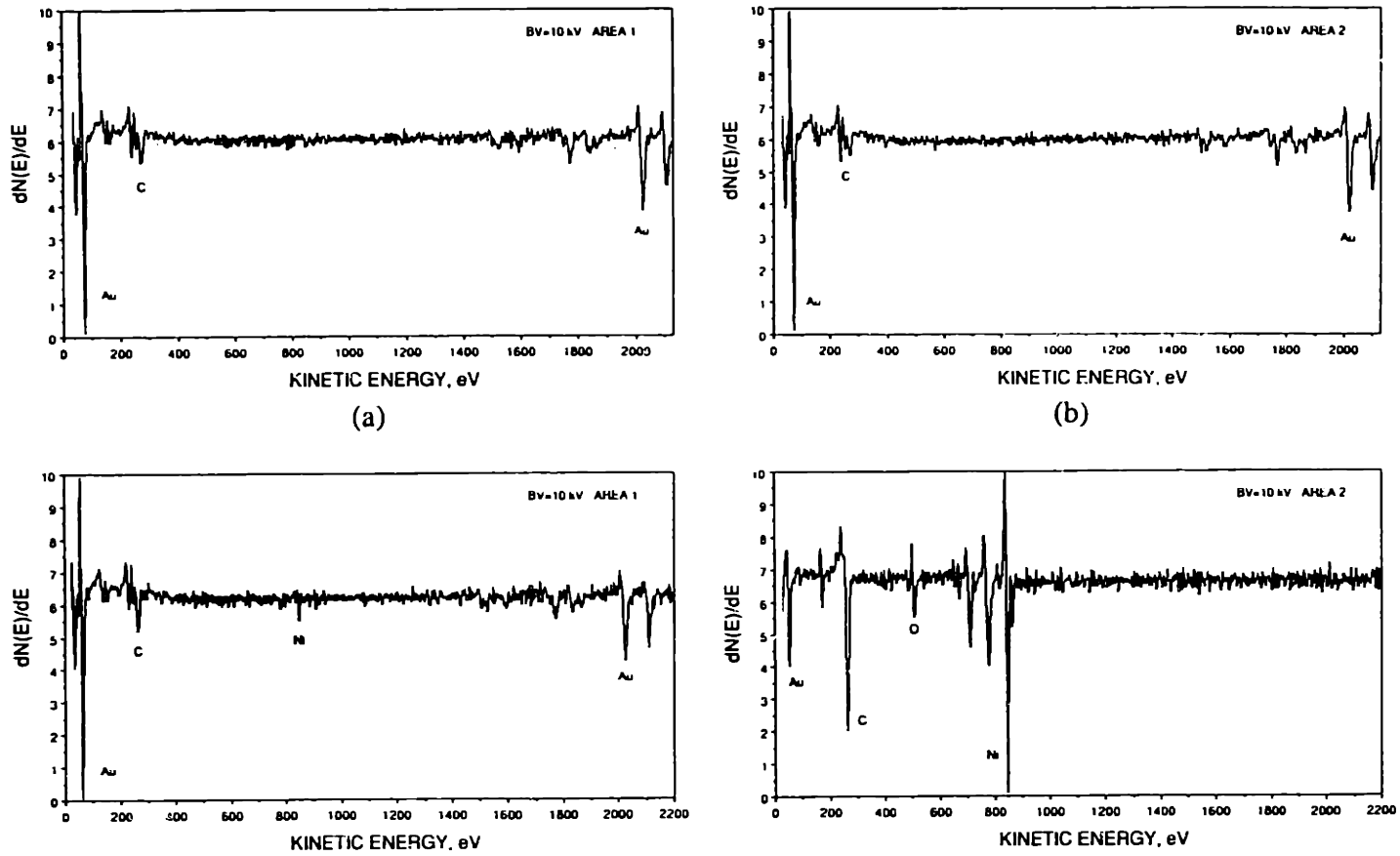

Fig. 2.7 Auger spectra at selected areas: (a) area 1 on the ball surface, (b) area 2 on the ball surface, (c) area 1 on the plate surface, and (d) area 2 on the plate surface.

the exposure of specimens to the atmosphere.) On the surface of the plate specimen, a visible trace of wear track was observed after 47 sliding cycles (Figure 2.6b); some pin holes are also apparent inside the wear track. Two areas were selected for AES survey. The AES spectrum in Figure 2.7c shows only gold inside the wear track (area 1). In the pin holes (area 2), however, nickel was the main component and some oxygen was also detected. Thus gold coatings on both the ball and the plate specimens stayed on up to 50 sliding cycles, although the friction coefficient increased monotonically from 0.3 to 0.6.

After about 100 sliding cycles, the friction coefficient reached a maximum and then quickly dropped to a low value, which marked the end of stage I. Then sliding was stopped and the surface topographies of the ball and the plate specimens were examined (Figure 2.8). The prow-like wear particles seemed to have rubbed off the ball surface. A black circle was found about the contact center. The AES spectrum in the area 1 (Figure 2.9a) which was outside the circle shows that the gold signal was dominant, while some nickel was detectable. The AES spectrum inside the circle (area 2 in Figure 2.9b) shows that only gold was on the surface. The black circle comprises nickel and nickel oxides (area 3 in Figure 2.9c). On the plate surface, plastic deformation was observed, and AES spectrum, Figure 2.9d, shows that gold coating was still on the surface, though some nickel was also detected.

Figure 2.10 shows the micrographs of the ball and the plate surfaces at the end of stage II. The sliding test was monitored by the RMS meter and the AE spectral analyzer. When drastic changes in the RMS value of the AE signal occurred (see Figure 2.5c), the sliding test was stopped and the surfaces were examined. A plate-like wear particle was removed from the surface of the ball specimen. The AES spectrum of the worn region (area 1) shows the presence of Ni, Cu, Zn and O. Spectral analysis of area 2, Figure 2.11b, shows only gold and some nickel. It seems that gold coating and nickel underplate were removed together, and that the brass substrate was exposed and oxidized. On the plate specimen, by contrast, only extensive plastic deformation was observed (Figure 2.10b). The spectrum inside the wear track (in area 1) shows gold and some nickel. A few wear particles were found on the plate surface. The spectrum of area 2 (Figure 2.11d), which was on the top of

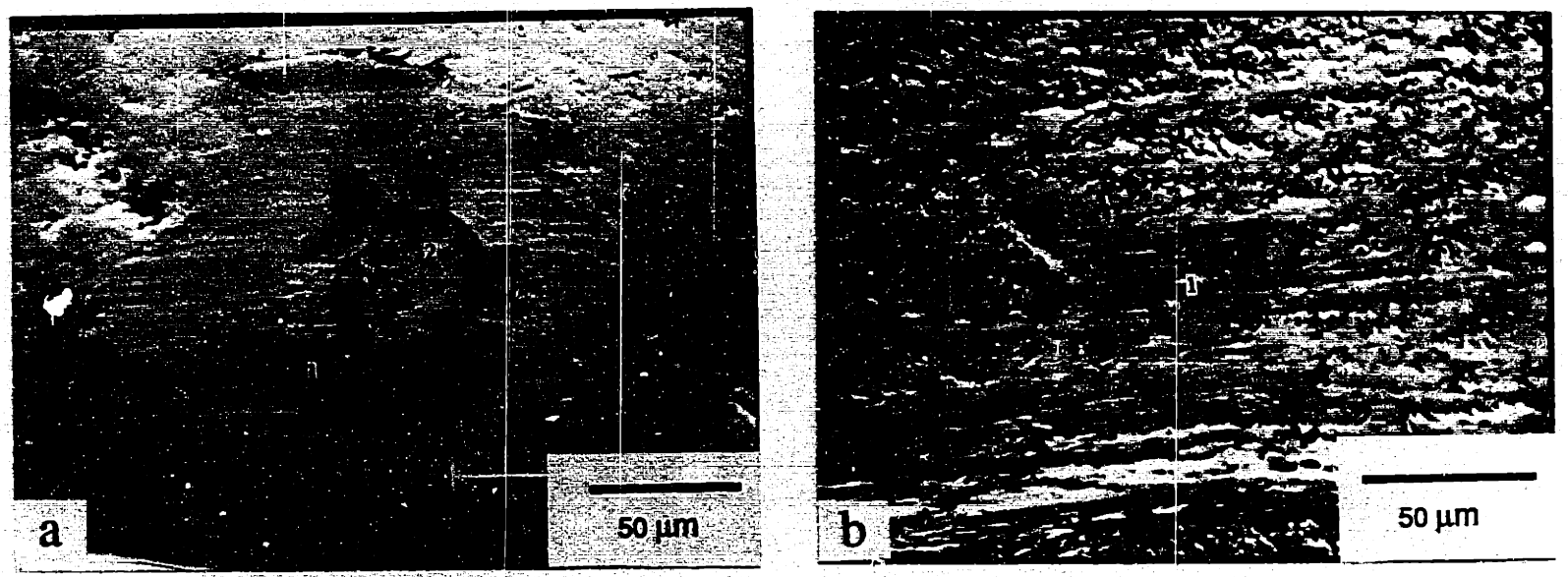

Fig. 2.8 Micrographs of worn surfaces after 95 sliding cycles: (a) ball specimen and (b) plate specimen

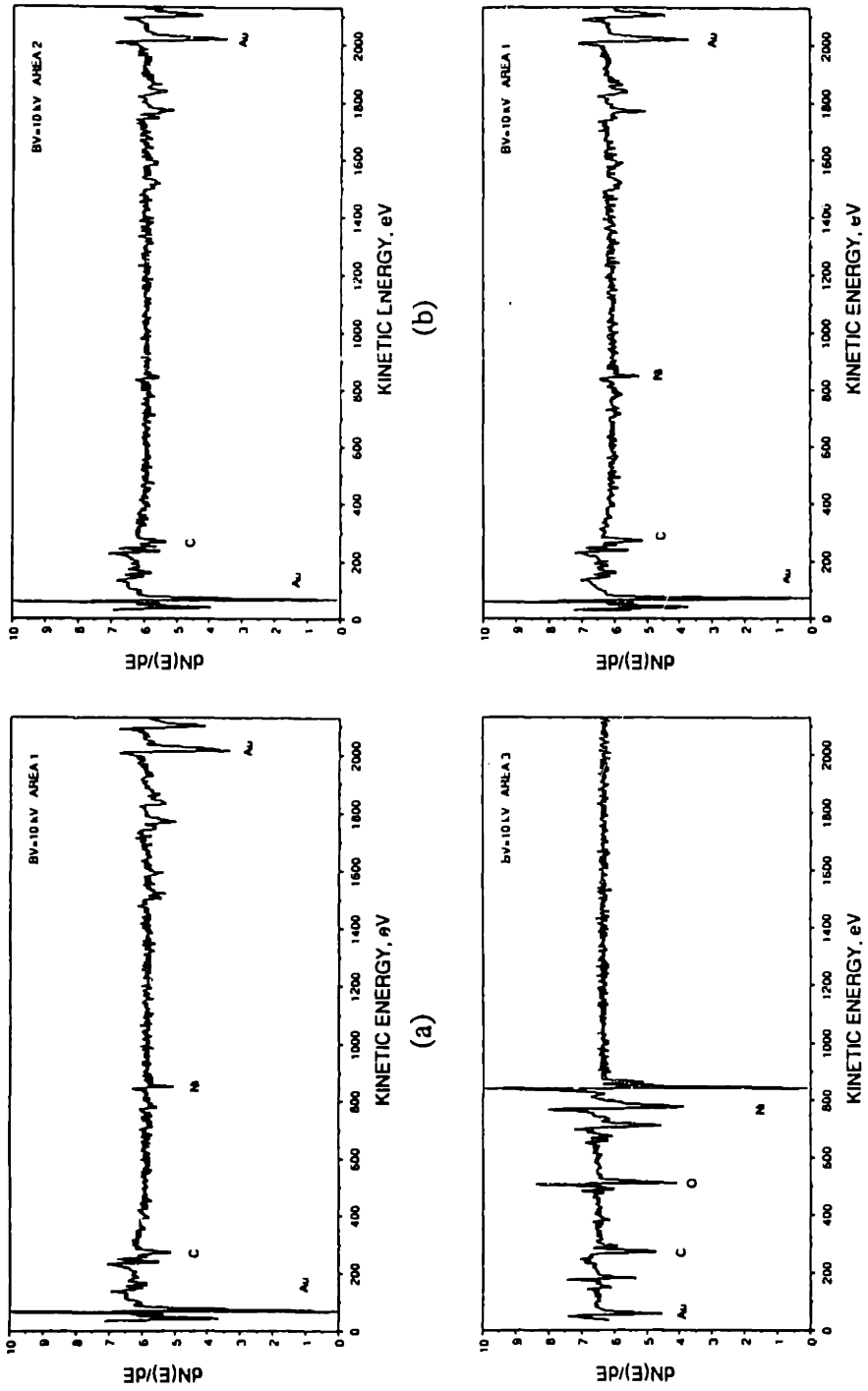

Fig. 2.9 Auger spectra at selected areas: (a) area 1 on the ball surface, (b) area 2 on the ball surface, (c) area 3 on the ball surface, and (d) area 1 on the plate surface.

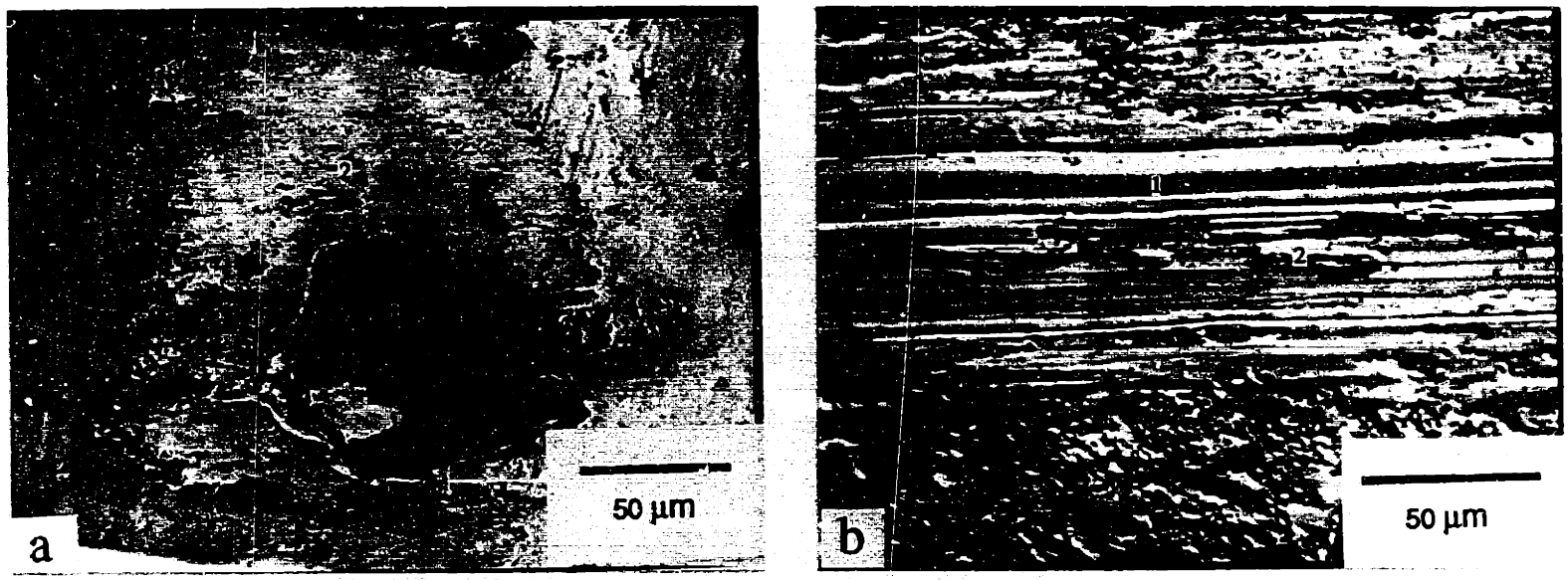

Fig. 2.10 Micrographs of worn surfaces after 197 sliding cycles:
(a) ball specimen and (b) plate specimen

one of these wear particles, shows the strong presence of Ni, Cu, Zn, and O, which is similar to that of area 1 in the ball surface. This indicates that these regions comprise Ni, Cu, Zn and their oxides, which only could happen at nickel-brass interfaces. It is believed thus that these wear particles were delaminated from the nickel-brass interface of the ball specimen. This belief was further confirmed from the surface profiles of the ball and the plate specimens. Figure 2.12b shows that the depth of the worn region on the ball surface was 2.5 μm, which is about the thickness of the nickel underplate. The profile of the plate surface indicates that the surface became relatively rough.

At the onset of stage III, the friction coefficient started increasing and fluctuating. The friction coefficient and the RMS of the AE signals were irregular. Figure 2.13 shows the micrographs of the ball and the plate specimens after 473 sliding cycles. The damage zone was obviously enlarged, and the brass substrate of the ball specimen was almost completely exposed. The AES spectra of the worn area on the ball surface, Figures 2.14a and 2.14b, confirm the exposure of brass substrate. Wear particles were found along the wear track on the plate surface. Figures 2.14c and 2.14d are the Auger spectra of the plate on the wear particle and on the wear track. Again, the gold coating was still on the plate surface, and the spectrum of these wear particles, Figure 2.14d, shows the presence of Ni, Cu, Zn and O. These wear particles were not produced from the plate specimen. Surface profiles were taken across the worn area on the ball surface and across the wear particle on the plate surface (Figure 2.12c). The profiles of the wear particle is above a zero line of the surface, not below the zero line. The height of the wear particle is about 4 μm. The profile of the ball surface shows that the depth of the worn spot is larger than the sum of the gold coating and nickel underplate thicknesses. This implies that the wear particles were delaminated from the nickel/brass interface, and that then the fresh brass substrate was further worn out as sliding continued.

2.3.3 AE spectral analysis

Acoustic emission signals are responses of AE sensors to mechanical interactions at sliding contact spots; for example, asperity deformation, junction formation

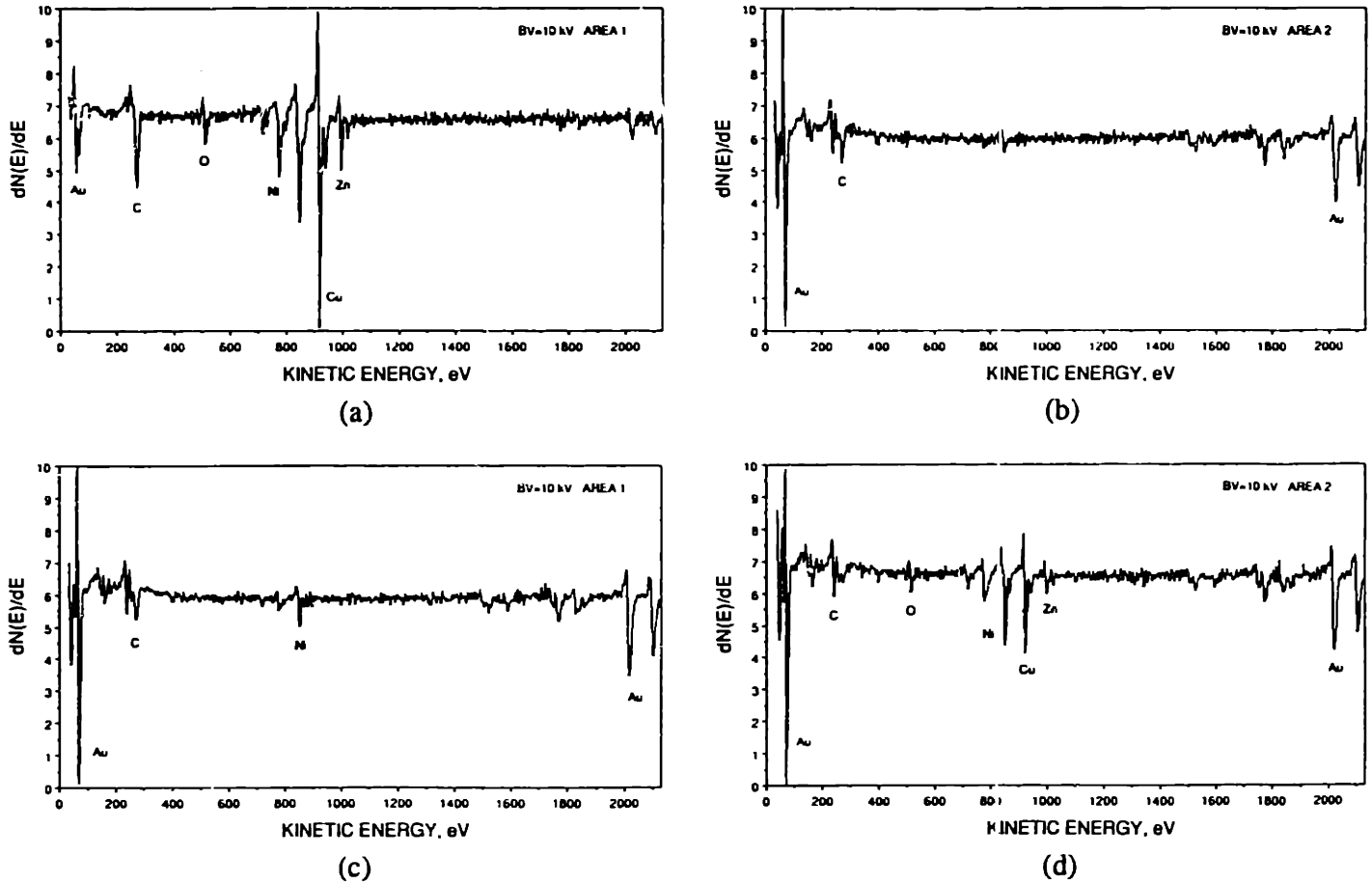

Fig. 2.11 Auger spectra at selected areas: (a) area 1 on the ball surface, (b) area 2 on the ball surface, (c) area 1 on the plate surface, and (d) area 2 on the plate surface.

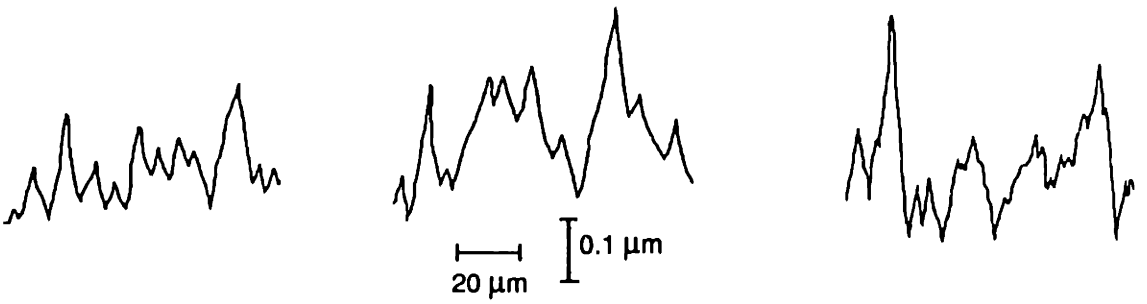

1. The ball surface (perpendicular to fretting direction)

2. The plate surface (perpendicular to fretting direction)

3. The plate surface (along fretting direction)

(a)

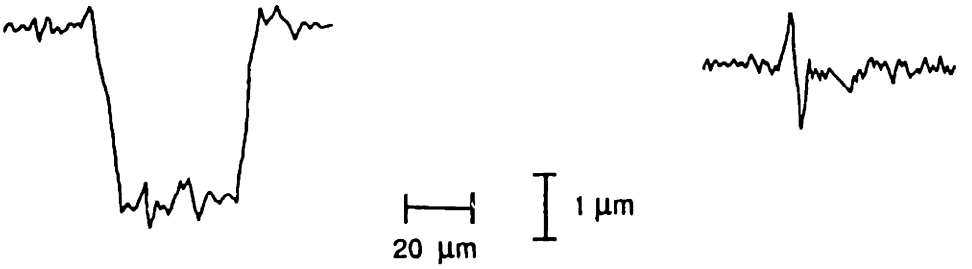

1. The ball surface

2. The plate surface

(b)

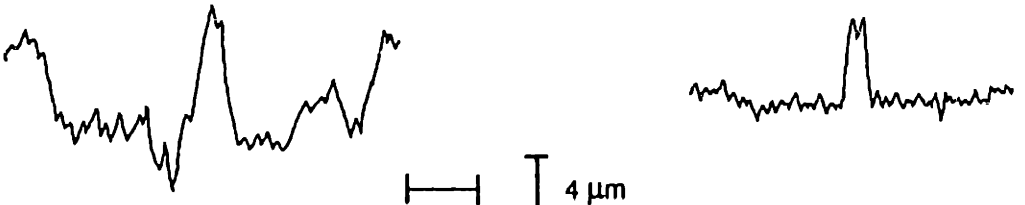

1. The ball surface

2. The plate surface

(c)

Fig. 2.12 Surface profiles of the specimens:
(a) before sliding
(b) after 197 sliding cycles
(c) after 473 sliding cycles

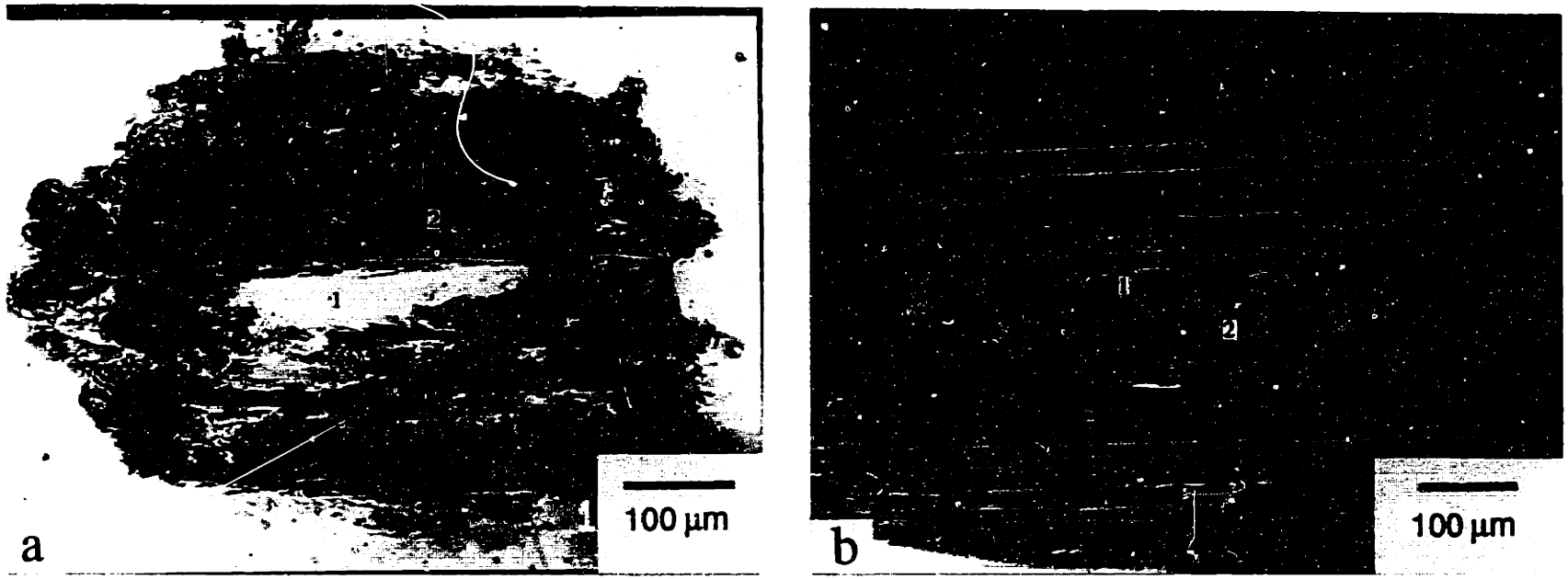

Fig. 2.13 Micrographs of worn surfaces after 473 sliding cycles:
(a) ball specimen and (b) plate specimen

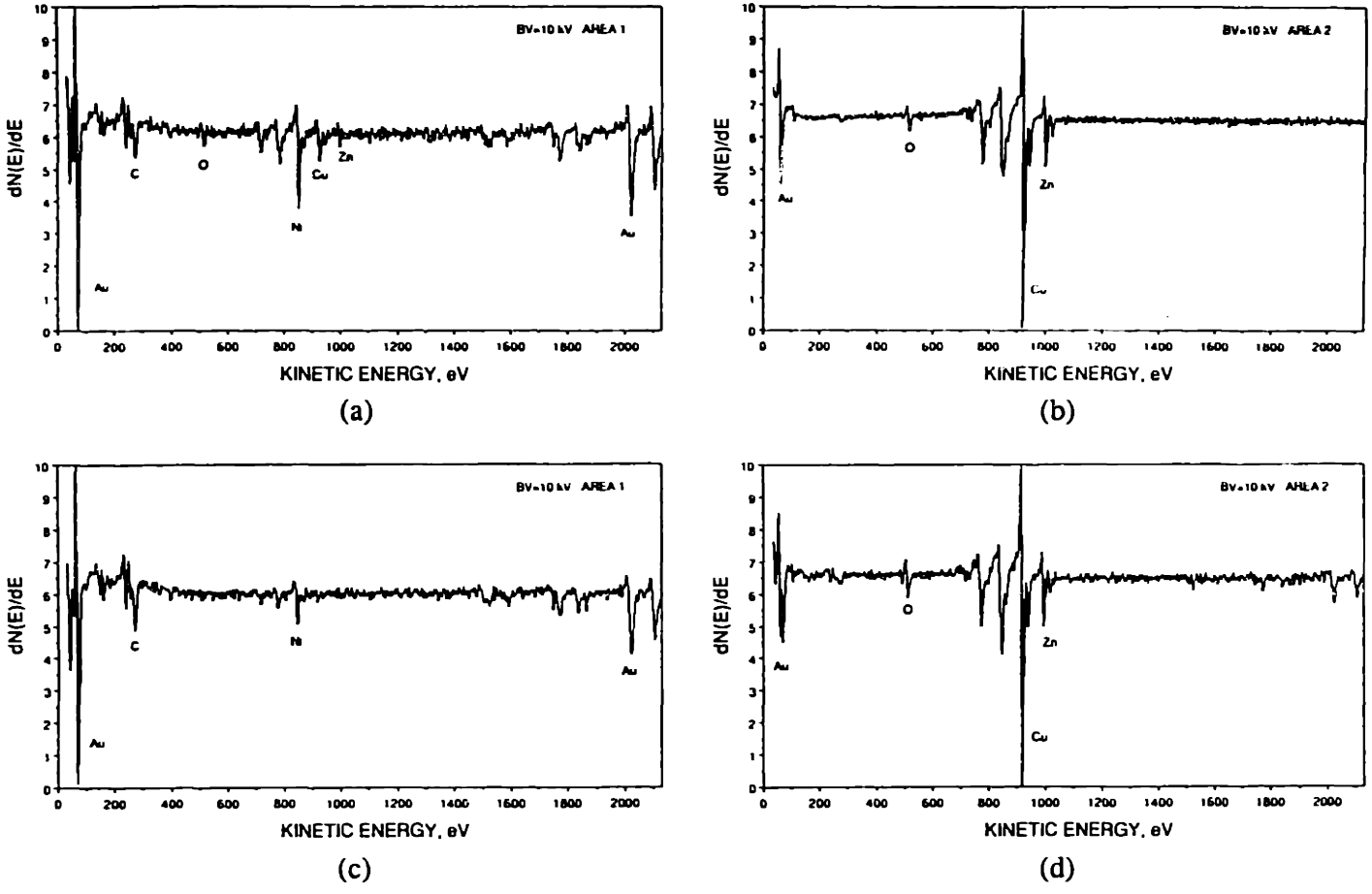

Fig. 2.14 Auger spectra at selected areas: (a) area 1 on the ball surface, (b) area 2 on the ball surface, (c) area 1 on the plate surface, and (d) area 2 on the plate surface.

and separation, wear particle formation, and so on. The frequency is usually below 1 MHz, or even smaller. The RMS value of an AE signal represents the effects of all events in the entire frequency range, and the detail of frequency response of AE is thus lost in the RMS plot. Therefore a detailed AE spectral analysis is presented in this section. The normalization procedure of AE spectra was already outlined in the experimental section.

Figure 2.15 shows the normalized AE spectra for different sliding cycles. No significant differences were found in the spectra in the frequency range 100 kHz to 1 MHz. Thus all spectra plotted here are only up to 100 kHz. These spectra correspond to the step-by-step sliding tests described in the previous section. All spectra were normalized with respect to the first spectrum of each sliding test. A linear scale was used in the spectral plots. Thus the amplitude of the reference spectrum (the first spectrum) was equal to one at all frequencies (Figure 15a).

The average AE spectrum for sliding cycles 42-47 is shown in Figure 2.15b (see Figures 2.6 and 2.7 for the micrographs and the AES spectra of the ball and the plate surfaces). The variations of the spectrum with respect to the reference spectrum were due to the prow formation or to the gold coating being pushed around. At the end of stage I (about 100 sliding cycles), the prow was rubbed off the ball surface (see Figure 2.8). Figure 2.15c shows the AE spectrum at this moment. Relative intensity variations in the AE spectrum are most likely due to the prow being rubbed off the ball surface. As sliding continued, the AE spectra were relatively "quiet" until the end of stage II. The micrographs, the AES spectra and the surface profiles clearly show that wear particles were delaminated from the nickel-brass interface of the ball specimen. Drastic changes in the AE spectrum at this moment, Figure 2.15d, confirm this view. In the stage III, the friction coefficient fluctuated, and the changes in the AE spectra were found to be irregular as seen in the RMS value plot in Figure 2.5b. Figure 2.15e shows the typical "quiet" spectrum and Figure 2.15f the typical "noisy" spectrum. It is believed that the "noisy" spectra correspond to the delamination events, and that the "quiet" spectrum are the responses before the delamination events.

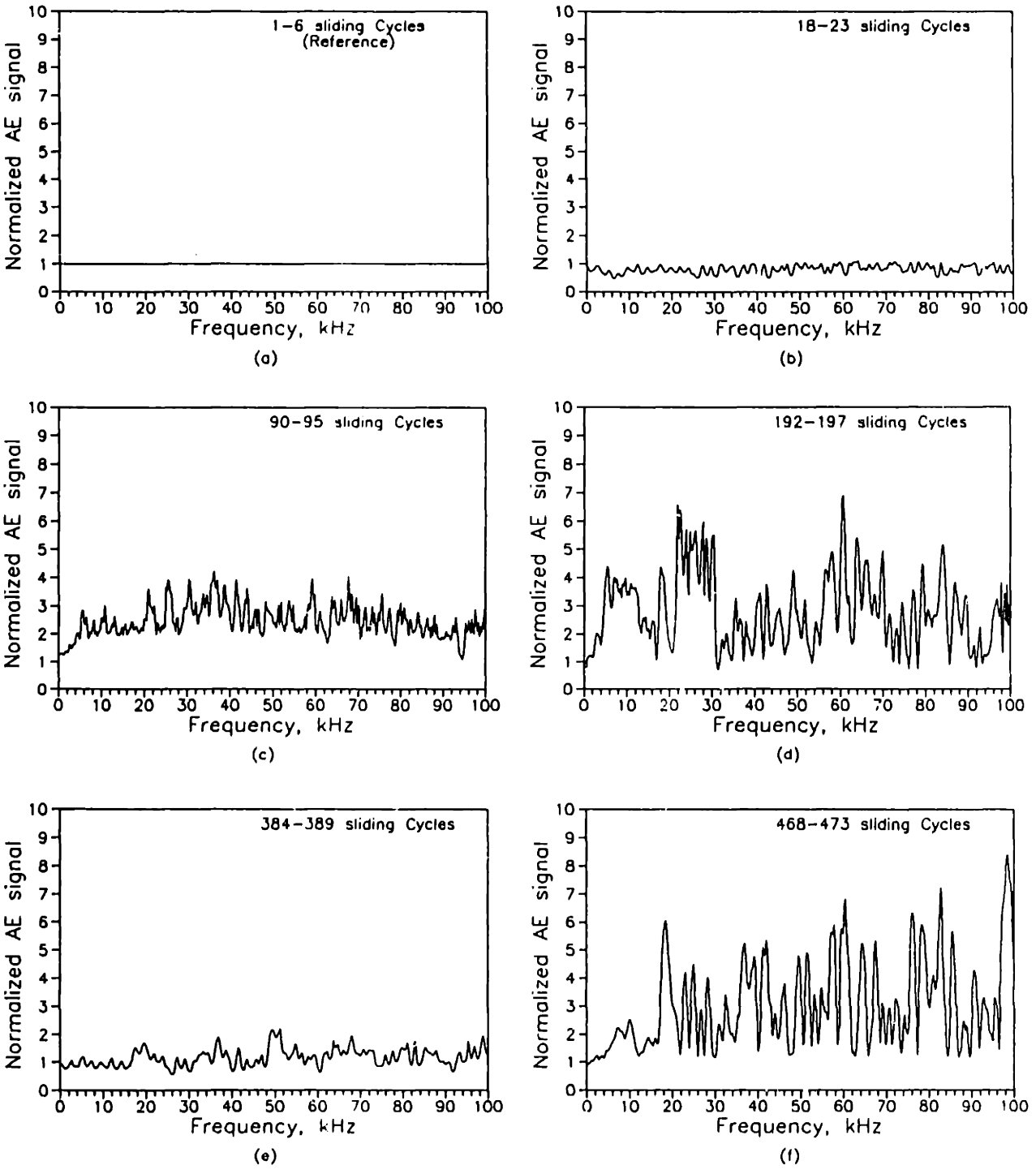

Fig. 2.15 The normalized AE spectra for different sliding cycles: (a) 1-6 cycles (reference spectrum), (b) 42-47 cycles, (c) 90-95 cycles, (d)192-197 cycles, (e) 384-389 cycles, and (f) 468-473 cycles

2.3.4 Wear coefficient

Table 2.2 lists the wear volumes and wear coefficients of the ball specimens at various sliding distances. The wear volumes were calculated based on the profiles of worn surfaces. The wear coefficient is calculated according to the Archard's equation V=kLx/p, where V is the wear volume, k the wear coefficient, L the normal load, x the sliding distance, and p the hardness of the worn materials. The Archard's equation was developed for the wear of homogeneous materials. For the multi-layer contact systems, the effective hardness may have to be used. In the present calculations, the hardness of the nickel was used.

2.3.5 Lubricated sliding

Effects of lubrication were also investigated. Two lubricants were used for study, a polyphenyl ether lubricant in Freon TA solvent and a 1% (by weight) mineral oil in 1,1,1 trichloroethane solution. Before the sliding test, the plate specimens were immersed in the lubricant for a few seconds, and then taken out for testing. Only the surfaces of the plate specimens were covered with lubricants.

Figure 2.16 shows the friction coefficient, the contact resistance and the RMS values of the AE signal versus sliding cycles when a polyphenyl ether lubricant in Freon TA solvent was used. The friction coefficient was low and remained low for a very long time. The contact resistance was also low throughout the test. The RMS value of the AE signal was almost constant throughout the sliding test. Figure 2.17 shows the micrographs of the ball and the plate surfaces after 500 sliding cycles when the polyphenyl ether lubricant in Freon TA solvent was used. The gold coating was pushed apart on the ball surface. AES spectral analysis on the ball surface did not show the presence of nickel. A visible wear track was found on the plate surface. AES spectra of the plate surface also did not show the presence of nickel. Some black spots were observed on the worn surface of the plate specimen. AES spectral analysis showed strong presence of nickel in the black spots.

It is apparent that lubrication considerably delays the sliding failure of electrical contacts. The topographies of the ball and the plate specimens indicate that even after 500 sliding cycles, the sliding system was only in stage I. Moreover, the

Table 2.2 Wear coefficient of the ball specimens at various sliding distances

Sliding Cycles	Sliding distance x, (m)	Wear volume V, (m^3)	Wear coefficient k
95	3.80	1.52×10^{-14}	1.02×10^{-5}
197	7.88	1.61×10^{-14}	5.21×10^{-6}
473	18.92	1.42×10^{-12}	1.91×10^{-4}

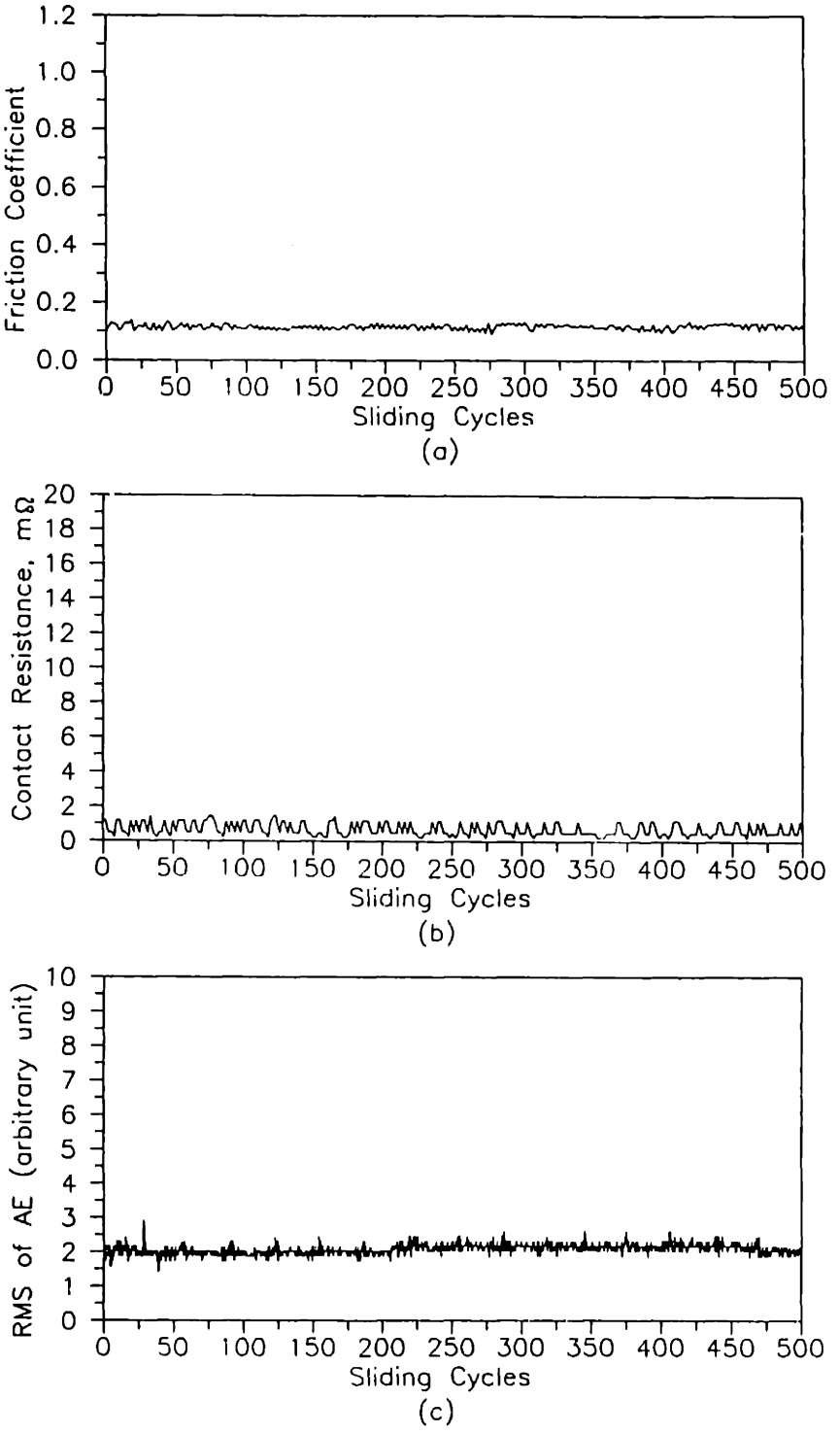

Fig. 2.16 (a) Friction coefficient, (b) contact resistance, and (c) RMS of AE signal versus sliding cycles with polyphenyl ether lubricant

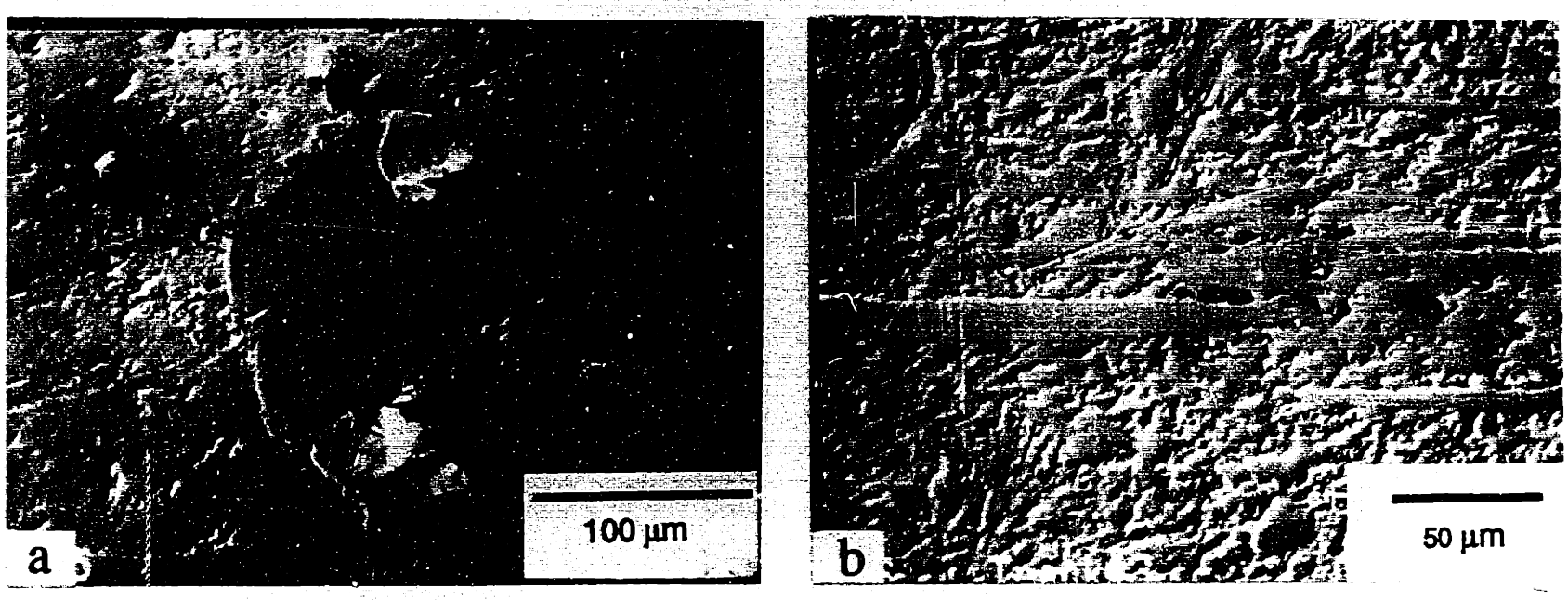

Fig. 2.17 Micrographs of test surfaces after 500 sliding cycles: (a) ball specimen and (b) plate specimen. Polyphenyl ether was used as a lubricant

friction coefficient was much lower than the initial friction coefficient of dry sliding tests.

2.4 Discussion

2.4.1 Contact stresses

Tribological phenomena such as prow formation and interfacial delamination are influenced by adhesion as well as mechanical stresses. Therefore a comprehensive knowledge of the sliding contact stress field of layered materials is important from both theoretical and practical points of view. Due to the size of this paper, however, only approximate analyses of the contact stresses will be presented.

The contact radius and stresses are functions of the coating thickness, Young's modulus, yield strength, and so on. The bounds for contact area can be obtained if the problem is simplified as an elastic sphere of radius R indenting an elastic half-space. From the Hertz solution, the contact area is circular, and has the radius

$$a = \left[\frac{3\, L\, R\, (1-\nu^2)}{2\, E} \right]^{1/3} \tag{2.1}$$

where L is the normal load, and E and ν are Young's modulus and Poisson's ratio of the materials of the sphere and the elastic half-space. For L=1 N and R=1.59 mm, the contact radius is 29.1 μm, 21.7 μm, and 25.5 μm for gold-on-gold, nickel-on-nickel, and brass-on-brass contacts, respectively. The contact radius of Au-Ni-Brass layered system should be in between 21.7 μm to 29.1 μm for a single elastic contact.

A more realistic approach is to treat the contact as an elastic contact surface layer on a rigid substrate. Figure 2.18 shows a schematic of a rigid sphere of radius R indenting a thin soft film of thickness t supported by a rigid substrate. The contact radius, a, is given from the geometrical relation

$$\begin{aligned} a &= \sqrt{(2hR - h^2)} \\ &\approx \sqrt{(2hR)} \end{aligned} \tag{2.2}$$

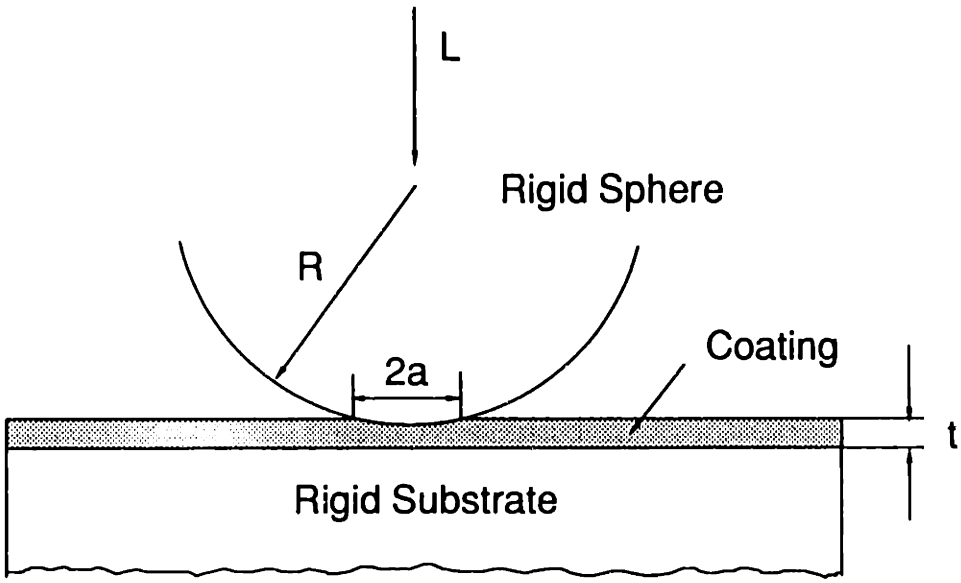

Fig. 2.18 Schematic of a rigid sphere indenting a thin soft film on a rigid substrate

where h is the penetration depth which is very small compared with the contact radius a. According to reference [9], h is given by

$$h = \left[\frac{L\,(1-\nu_f^2)\,t}{p\,E_f\,R}\right]^{1/2} \tag{2.3}$$

where L is the normal load, and E_f and ν_f are Young's modulus of elasticity and Poisson's ratio of the film. The through-thickness average stresses are given by

$$\sigma_z = \frac{-E_f\,a^2}{(1-\nu_f^2)\,2Rt}\left[1 - \frac{r^2}{a^2}\right] \tag{2.4}$$

$$\sigma_r = \frac{-\nu_f\,E_f\,a^2}{(1-\nu_f^2)\,4Rt}\left[1 - \frac{r^2}{2\,a^2}\right] \tag{2.5}$$

$$\sigma_\theta = \frac{-\nu_f\,E_f\,a^2}{(1-\nu_f^2)\,4Rt}\left[1 - \frac{3\,r^2}{2\,a^2}\right] \tag{2.6}$$

where σ_z, σ_r, and σ_θ are the axial, radial and circumferential stresses, and r the radial coordinate.

The maximum stresses occur along the z-axis, and are given by

$$\sigma_z = \frac{-E_f\,a^2}{(1-\nu_f^2)\,2Rt} \tag{2.7}$$

$$\sigma_r = \sigma_\theta = \frac{-\nu_f\,E_f\,a^2}{(1-\nu_f^2)\,4Rt} \tag{2.8}$$

Along the z axis, the Mises and Tresca equivalent stresses are identical and are given by

$$\sigma_{Mises} = \sigma_{Tresca} = |\sigma_z - \sigma_\theta| \tag{2.9}$$

For a normal load 1 N, film thickness 1.5 μm, the radius of sphere 1.58 mm, Young's modulus 79 GPa, and Poisson's ratio 0.35, the penetration depth, h, calculated from equation (2.3), is 0.058 μm. The contact radius, a, obtained from equa-

tion (2.2), is 13.5 μm. The axial stress, σ_z, and radial and circumferential stresses, σ_r, σ_θ, are –3,525 MPa, –616.8 MPa, –616.8 MPa, respectively. The yield strength of the gold film in compression is assumed to be one-third of its hardness (1,176 MPa), 392 MPa. The Mises equivalent stress is 2,908 MPa. Thus the gold film had deformed plastically as is evident from the micrographs. The ratio of penetration depth to the contact radius, h/a, is very small (0.004). Therefore the contact is essentially flat.

If the contact is assumed to be a single plastic contact, the bounds for the contact radius can be given by

$$L = A_r\, p = \pi\, a^2\, p$$

$$a = \sqrt{L/\pi p} \qquad (2.10)$$

where A_r is a real area of contact and p is the hardness of the material. For L=1 N, the contact radius for gold and for nickel, is 16.3 μm and 11.0 μm, respectively. Contact radius calculated from equation (2.2) is in between. Nevertheless, for a single contact under 1 N normal load, the contact radius is around 13 μm. For multiple contacts it will be less, but still much larger than the gold coating thickness.

2.4.2 Friction coefficient

It is well known that solid films on surfaces provide a lubricating effect due to the low shear strength of the soft surface film. This kind of solid lubrication is realized only when one of the sliding surface is coated with a soft surface film. For example, low friction (typically 0.1) was obtained when a very thin gold was deposited on one of the steel surfaces [10]. Several researchers have also developed theoretical expressions for sliding friction of thin film system [11-14]. However, when both sliding surfaces are electroplated with the same material, especially with gold as in this study, the strong adhesion effects may offset the "lubrication" effects. The initial friction coefficient in this study was about 0.3, which is much higher than typical friction coefficient values of solid film lubrication, though the coating thickness in this study is on the high side for thin film systems.

The friction coefficient data, the RMS of the AE signal, the AE spectral analysis suggest that the mechanisms of friction are quite different in the three stages of sliding. The friction coefficient is believed to consist of three components: adhesion, asperity deformation, and plowing. In stage I, since no plowing grooves were observed on either the ball or the plate surfaces, the friction mechanisms are adhesion and asperity deformation. According to the adhesion theory [15], the friction force is the product of the shear strength and the area of welded junctions between contacting asperities, and the friction coefficient is given by

$$\mu = \frac{s}{p} \tag{2.11}$$

where s is shear strength and p the hardness of the softer material. If this equation is used for thin film systems, s should be the shear strength of the surface film and p the effective hardness of the thin film system. The friction coefficient calculated from the equation (1) is 0.16 if the hardness of gold is used, and 0.09 if the hardness of nickel is used. These values are obviously much smaller than the initial friction coefficient observed in this study, which was about 0.3.

Rabinowicz [16] correlated the surface energy of contact materials with their frictional behavior. The friction coefficient is expressed as

$$\mu = \frac{s}{p}\left[\frac{1}{1 - 2W_{ab}\cot\alpha/ap}\right] \tag{2.12}$$

where W_{ab} is the work of adhesion between the surfaces of materials a and b, α is the roughness angle of contact surface or asperity slope, and a is an average junction radius. For materials in contact with themselves, W_{ab} is equal to 2γ, where γ is the surface energy of the material. Figure 2.12a shows the surface profiles of the ball and the plate specimens before sliding. The roughness angle of the ball surface is about 1.7 degrees. The roughness angle of the plate surface along the direction of sliding is about 1.5 degrees, and 0.9 degree in the direction transverse to sliding. For $W_{Au/Au} = 2\gamma_{Au} = 2.24 J/m^2$, α=1.5 degrees, and a=13 μm, the friction coefficient calculated from equation (12) is 0.162 if the hardness of gold is used, and 0.09 if the hardness of nickel is used. Thus these values are again much smaller than the initial friction coefficient of this study.

The approximate stress analysis of the previous section shows that the gold film is plastically deformed even under normal load. Assuming that the gold film is perfectly plastic, the friction coefficient due to asperity deformation can be expressed by using a slip-line field [17] as

$$\mu = \frac{A\sin\alpha + \cos(\cos^{-1}f - \alpha)}{A\cos\alpha + \sin(\cos^{-1}f - \alpha)} \qquad (2.13)$$

where

$$A = 1 + \frac{2}{\pi} + \cos^{-1}f - 2\alpha - 2\sin^{-1}\left[\frac{\sin\alpha}{\sqrt{(1-f)}}\right]$$

and α the asperity slope, and f the ratio of the shear strength of the interface to the shear strength of the softer material.Taking α = 1.5 degrees (0.026 radian), the friction coefficient obtained from equation (10) varies from 0.026 to 0.43 as f varies from 0 to 1. For the same materials in contact, f is close to 1. For f=0.9, the friction coefficient value calculated from equation (10) is 0.305 which is equal to the initial sliding friction coefficient in this study. Thus it seems that the initial friction is due to the deformation of well-adhered gold-gold contact spots.

It was found that friction coefficient increases steadily in stage I until the prow is rubbed off the ball surface.The gold film on the plate surface was subjected to plastic deformation. Antler [18] has studied extensively the prow formation in sliding contacts of gold electroplated materials. Prow formation occurs when the same noble metals are in sliding contact. A lump of metal is built up in front of the slider. The wear track is also enlarged due to prow formation. It has been observed by optical microscopy that after 10 sliding cycles, the width of the wear track on the plate surface was 40 μm, and 55 μm after 47 sliding cycles. At the end of stage I (about 100 sliding cycles), the width increased to 155 μm. When strong adhesion occurs at the regions of real contact between metal surfaces, the force to shear the junction so formed will be very close to the product of the area of the junction and the bulk shear strength of the metal [3]. Thus for a fixed normal load, the friction force increases with the junction size. The gradual increase in friction can therefore be explained in terms of junction growth.

In stages II and III, the friction behavior and surface topography are quite different from those in stage I. Plowing by hard asperities of nickel underplate and by wear particles delaminated from the ball specimen may contribute to overall high friction. Plowing friction has been investigated by many researchers [19-22]. The contribution of plowing to friction depends on the plowing angle of conical hard asperities or the ratio h/R of spherical asperities and wear particles. In stage II, the gold film on the ball surface is gradually worn out and some nickel underplate starts to emerge. No wear debris are delaminated from the ball surface in this stage. Plowing by the hard asperities of nickel underplate contributes to high but stable friction coefficients.

At the end of stage II, wear particles are delaminated from the ball surface. These wear particles are basically nickel, and they are relatively hard and sharp. Plowing by these hard wear particles results in increased friction and the initiation of stage III. In stage III, wear particles are continually delaminated from the nickel/brass interface of the ball specimen and the damage zone is enlarged. Consequently, plowing by these wear particles causes a steady wear of the brass substrate of the ball specimen and severe plastic deformation of the plate surface. These events result in large fluctuations in the friction coefficient and in the RMS values of the AE signal.

2.4.3 Contact resistance

The electrical resistance at the interface of two contacting surfaces consists of two components. One is the constriction resistance resulting from the convergence and divergence of current flow through the contact asperities. The other is the resistance due to any non-metallic film on the contact surfaces. Since no oxides are involved at the beginning of the sliding test and the contact surfaces are fairly clean, the contact resistance of a single contact according to Holm [23] is given by

$$R_c = \frac{\rho_1 + \rho_2}{4\,a} \tag{2.14}$$

where ρ_1 and ρ_2 are the resistivities of contact material 1 and material 2, respectively, and a is the contact radius.

For a single contact of radius 13 μm, the contact resistance calculated from equation (14) is 0.86 mΩ for gold/gold contact, 1.74 mΩ for gold/nickel contact and 1.92 mΩ for gold/brass contact. In this study, the contact resistance was low throughout the sliding tests even though the brass substrate of the ball specimen was completely exposed. The reason is that oxidation of the fresh brass substrate did not occur, or was not completed, in this kind of accelerated testing. In practice, however, exposure of the substrate can soon lead to severe oxidation and high contact resistance. Incidentally, this also shows that the contact resistance is not a good indication of sliding failure of electroplated contacts in the laboratory studies.

2.4.4 Mechanisms of Failure

Adhesion, delamination, and abrasion (or plowing) are the three basic mechanisms of sliding wear. In sliding contacts of electroplated gold systems, sliding failure becomes more complicated because both sliding surfaces are coated with thin films. High adhesion characteristic of gold could lead to some interesting tribological behavior. Recently, Antler [18] has reviewed the mechanisms of sliding wear of noble metallic contacts and has shown that adhesive wear is more important than abrasive wear and brittle fracture when noble metals such as gold, silver, palladium and their alloys are used. Prow formation in front of a spherical slider and wear particle transfer between sliding surfaces are claimed to be the main wear processes. In the multilayer thin film system, however, the contact radius is much larger than the film thickness and the prow formation is the dominant mechanism only in the early stage of sliding. As sliding continues, prow formation will cease and other mechanisms will initiate.

In repeat-pass sliding, cracks initiate at dislocation pile-ups, and especially around second-phase inclusions a short distance below the surface, as proposed by Suh [24]. Delamination occurs when the cracks propagate and emerge at the surface, resulting in thin sheets of wear particles. In the multilayer thin film systems, however, delamination could occur right at the interfaces between layers due to poor bonding. Indeed, recent experimental observations have shown that cracks could be readily initiated at interfaces due to thermal stresses when metal-ceramic

composite layers are quenched to low temperatures. Cracks were found to readily propagate along the interfaces [25-28].

Figure 2.19 schematically shows the mechanisms of failure in different stages. In stage I, prow forms in the front of a slider due to strong adhesion between the gold surfaces (Figure 2.19a). The wear of the gold plating is marginal in this stage. During sliding in stage II, cracks may initiate and propagate at the nickel-brass interface due to the large interfacial shear stress. These cracks propagate along the nickel-brass interface and finally emerge at the surface, resulting in thin plate-like wear particles (Figure 2.19b). These wear particles are broken into pieces and adhered to the plate surface. By this time, the electroplated system has technically failed because the exposure of substrate will soon lead to severe corrosion, resulting in unacceptable increases in contact resistance. Figure 2.19c shows that as sliding enters stage III, wear particles are continually delaminated from the nickel/brass interface of the ball specimen. The damage zone is enlarged, and a steady wear of the brass substrate takes place.

To quantitatively analyze this interfacial failure process, a rigorous stress and stain analysis under sliding contact is needed. Special attention should be paid to the shear stresses at interfaces between layers. A finite element analysis of sliding contacts of multilayer systems is under way to study this problem. In this paper, however, a simple surface energy-based analysis is given to obtain a qualitative understanding of the interfacial failure. Assuming that a wear particle is delaminated from the nickel-brass interface of the ball specimen, and then is adhered to the plate surface, the surface energy per unit area before delamination is given as

$$E_1 = \gamma_{Au} + \gamma_{Au} + \gamma_{Ni/Brass} \tag{2.15}$$

where γ_{Au} is the surface energy of gold, $\gamma_{Ni/Brass}$ is the interfacial energy between nickel and brass. The surface energy after delamination is given by

$$E_2 = \gamma_{Au/Au} + \gamma_{Ni} + \gamma_{Brass} \tag{2.16}$$

where $\gamma_{Au/Au}$ is the interfacial energy between gold. The energy change is given by

$$\Delta E = E_2 - E_1 = \gamma_{Au/Au} + \gamma_{Ni} + \gamma_{Brass} - 2\gamma_{Au} - \gamma_{Ni/Brass} \tag{2.17}$$

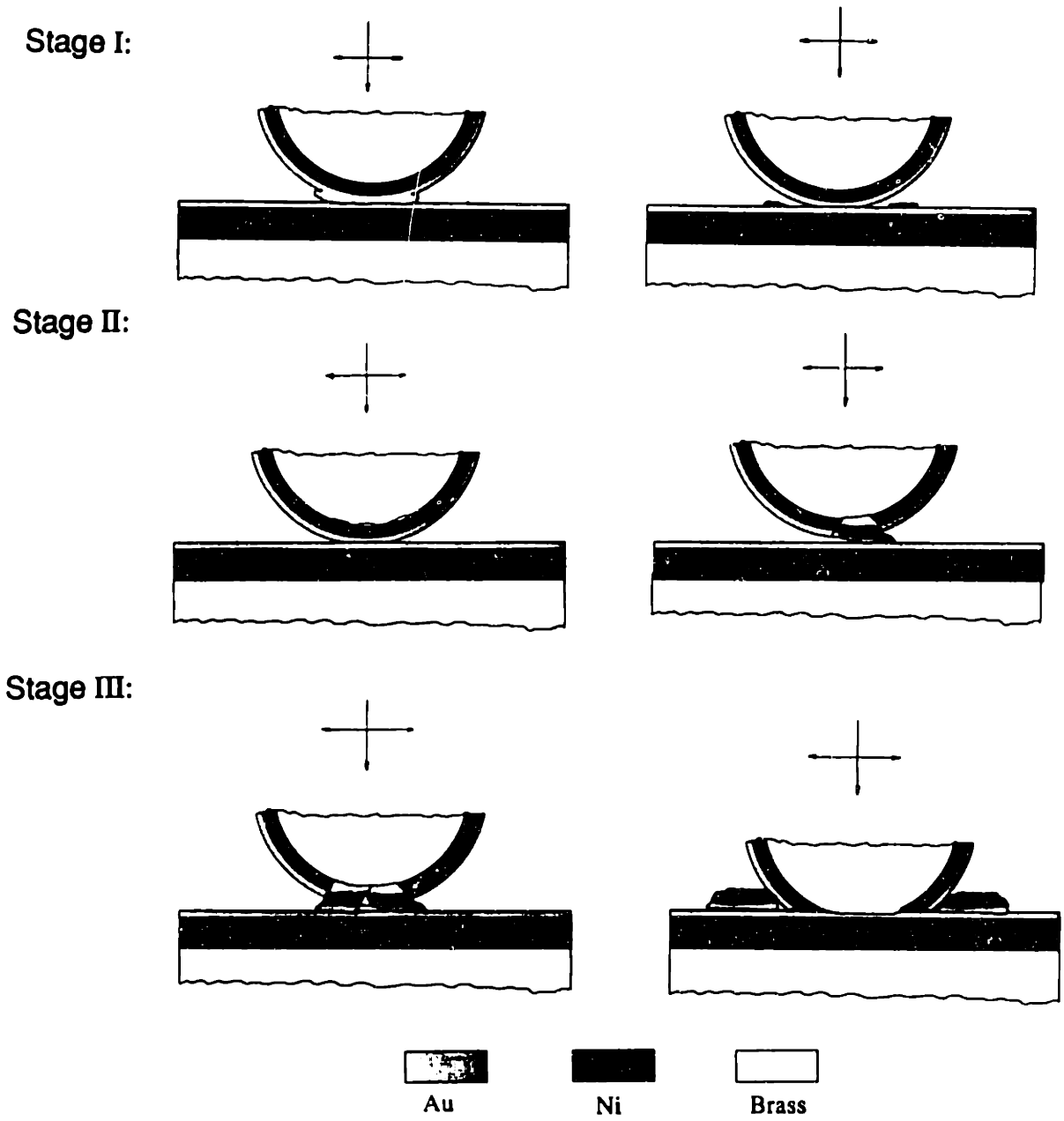

Fig. 2.19 Schematics of the mechanisms of failure in different stages.

The calculated results are listed in Table 2.3. The surface energy change due to delamination at nickel-brass interface is negative. Theoretically wear particles should delaminate from the nickel/brass interface without any external energy input. This is, of course, not true in reality. One of the reasons for this is that the binding energy between nickel and brass could be higher than the assumed interfacial energy. Another limitation of this model is that the magnitudes of surface energy are generally smaller than plastic deformation energy, thermal energy, and so on, and that the effects of surface energy may be washed out if the system is subjected to severe plastic deformation. Moreover, the energy criteria is only a necessary condition for interface debonding or interfacial delamination. Other interface failure criteria have to be established. All these can only be achieved when the sliding contact stresses and strains of the multilayer system are determined. Nevertheless, the energy-based analysis qualitatively indicates that the interfaces between layers are the most likely places for initiation of cracking.

It is clear now that interfacial failure of electroplated multilayer systems is a low-cycle fatigue process rather than steady-state wear or a one-time fracture event. Thus a low-cycle fatigue model should be developed to predict the sliding failure of electroplated multilayer contacts. Effects of multiple contacts, normal loads, and thicknesses of gold film and nickel underplate were not studied in this work. The pin holes, which exist in many electroplated systems, may also influence the interface failure. Finally, microstructures of the coating and residual stresses in the coating may be important in the failure of electroplated multilayer systems. All these factors need further investigation.

One obvious solution to the sliding failure is to use lubricants, which has been studied in this work. The great benefit of using lubricants is to reduce the friction coefficient down to such a low value that stage I is prolonged almost indefinitely, provided that the lubricant is always present. Another solution is to improve interface bonding between layers so that stage II is prolonged to avoid delamination. Interface strengthening by diffusion annealing has been tried to delay the sliding failure without using lubricants. The preliminary results are very encouraging.

Table 2.3 Surface Energy Analysis of Sliding Pairs *

γ_{Au}	γ_{Ni}	γ_{Brass}	$\gamma_{Au/Au}$**	$\gamma_{Ni/Brass}$ **	E_1	E_2	ΔE
1.12	1.70	0.99	0.00	0.67	2.91	2.69	-0.22

* Unit for all the parameter is J/m^2

** $\gamma_{a/b} = 0$ if materials a and b are identical

$\gamma_{a/b} = 0.25 (\gamma_a + \gamma_b)$ if materials a and b are compatible [16]

One of the implications of the present study is that low sliding friction is essential not only for low insertion and withdrawal forces, but also for low "wear" of the gold plating. More importantly, the shear stresses at interfaces and the delamination of surface coatings can be greatly reduced by low friction and strong interfacial bonding. Gold has high corrosion resistance, but it also has high adhesion characteristic which causes high friction if gold contacts itself. To circumvent these restrictions, incompatible noble metal pairs may be employed. Meta' pairs which are metallurgically incompatible show less friction and wear [29]. The noble metals which are incompatible with gold are: osmium, iridium, rhenium, ruthenium, and rhodium [30]. Adhesion and friction can be reduced if one of these is used as a coating on one of the contacts.

2.5 Conclusions

1. Three stages can be distinguished in the sliding behavior of electroplated gold contacts based on the friction coefficient and RMS value of acoustic emission.

(a) In stage I, the friction coefficient increases monotonically, and prows form on the ball surface and then are rubbed off the ball surface. AE spectrum gives strong indication of the rubbing-off process. Auger electron spectra on the ball and the plate surfaces show that the gold film on the substrates stays intact in this stage.

(b) In stage II, the friction coefficient is more or less a constant until wear particles are delaminated from the nickel-brass interface of the ball specimen. RMS value of the AE signal shows little fluctuation. Nickel underplate starts emerging on the surface of the ball specimen. Plowing by the hard asperities of nickel underplate results in high but stable friction coefficient.

(c) At the onset stage III, friction coefficient starts increasing again, and wear particles are delaminated from the ball surface periodically, resulting in high and fluctuating friction as well as severe wear. RMS values of AE signal are also high and fluctuate in this stage. Delamination occurs in one of the contact members, and severe plastic deformation takes place on the other.

2. High adhesion characteristic of gold is responsible for the prow formation and for progressive coating removal from the ball. High friction values seem to induce and promote the interfacial delamination process. Thus low adhesion and low friction are the essential requirements for the reliability of electroplated systems. Lubricated sliding with polyphenyl ether lubricant in Freon TA indeed confirms this view. Lubrication reduces the friction considerably and keeps the sliding system in the early stage of sliding.

3. Electrical contact resistance is not a good indicator of sliding failure of electroplated systems in laboratory tests.

4. Further work on rigorous stress analysis of multilayer sliding contacts and the criteria of interface failure is needed to fully understand and to prevent the interfacial delamination process which is a low-cycle fatigue process.

References

[1] Antler, M., "Wear of Electrodeposited Gold," *ASLE Trans.*, Vol. 11, 1968, pp 248-260.

[2] Cocks, M., "Interaction of Sliding Metal Surfaces," *J. Appl. Phys.*, Vol. 33, 1962, pp 2152-2101.

[3] Greenwood, J. A. and Tabor, D., "The Properties of Model Friction Junctions," *Conference on Lubrication and Wear*, London, Oct. 1-3, 1957, Inst. of Mechanical Engineers, paper 92, pp 314-317.

[4] Antler, M., "Tribological Properties of Gold for Electrical Contacts," *IEEE Trans. Parts, Hybrids, Packaging*, Vol. PHP-9, 1973, pp 4-14.

[5] Horn, G. L. and Merl, W. A., "Friction and Wear of Electroplated Hard Gold Deposits for Connectors," *IEEE Trans. Parts, Hybrids, Packaging*, Vol. PHP-10, 1974, pp 53-59.

[6] Liljestrand, L. G., Sjogren, L., Revay, L. and Asthner, B., "Wear Resistance of Electroplated Nickel-Hardened Gold," *IEEE Trans. Components Hybrids Manuf. Tech.*, Vol. 8 (1), 1985, pp 123-128.

[7] Antler, M. and Drozdowicz, M. H., "Wear of Gold Electrodeposites: Effect of Substrate and of Nickel Underplating," *Bell System Technical Journal*, Vol. 58, 1977, pp 323-349.

[8] Goodman, S. J. N. and Page, T. F., "The Contact Resistance and Wear Behavior of Separable Electrical Contact Materials," *Wear*, Vol. 131, 1989, pp 177-191.

[9] Conway, H. D., Lee, H. C. and Bayer, R. G., "The Impact Between a Rigid Sphere and a Thin Layer," *J. Applied Mechanics*, Vol. 37, 1970, pp 159-162.

[10] Takagi, R. and Liu, T., "The Lubrication of Steel by Electroplated Gold," *ASLE Trans.*, Vol. 10, 1967, pp 115-123.

[11] Rabinowicz, E., "Variation of Friction and Wear of Solid Lubricant Films With Film Thickness," *ASLE Trans.*, Vol. 10, 1967, pp 1-9.

[12] Finkin, E. F., "A Theory for the Friction of Sulfide and Other Thin Films," *Wear*, Vol. 18, 1971, pp 231-241.

[13] Heilmann, P. and Rigney, D. A., "An Energy-Based Model of friction and Its Application to Coated Systems," *Wear*, Vol. 72, 1981, pp 195-217.

[14] Kato, S., Yamaguchi, K., Marui, E. and Tachi, K., "Frictional Properties of a Surface Covered With a Soft Metal Film - Part II: Analysis of Friction Between a Single Protuberance and a Surface," *J. Lubrication Tech.*, Vol. 104, 1982, pp 39-45.

[15] Bowden, F. P. and Tabor, D., "Mechanism of Metallic Friction," *The Friction and Lubrication of Solids*, The Clarendon Press, Oxford, 1950, pp 90-121.

[16] Rabinowicz, E., *Friction and Wear of Materials*, John Wiley & Sons, Inc., New York, 1965, pp 10-66.

[17] Challen, J. M. and Oxley, P. L. B., "An Explanation of the Different Regimes of Friction and Wear Using Asperity Deformation Models," *Wear*, Vol. 53, 1979, pp 229-243.

[18] Antler, M., "Sliding Wear of Metallic Contacts," *IEEE Trans. Circuit, Hybrids and Manufacturing Technology*, Vol. CHMT-4, 1981, pp 15-29.

[19] Tzukizoe, T. and Sakamoto, T., "Friction in Scratching Without Metal Transfer," *Bull. JSME*, Vol. 18 (115), 1975, pp 65-72.

[20] Komvopoulos, K., Saka, N. and Suh, N. P., "Plowing Friction in Dry and Lubricated Metal Sliding," *Journal of Tribology*, Vol. 108, 1986, pp 301-313.

[21] Tian, H., Saka, N. and Suh, N. P., "Boundary Lubrication Studies on Undulated Titanium Surfaces," *STLE Tribology Trans.*, Vol. 32, 1989, pp 289-296.

[22] Saka, N., Tian, H. and Suh, N. P., "Boundary Lubrication of Undulated Metal Surfaces at Elevated Temperatures," *STLE Tribology Trans.*, Vol. 32, 1989, pp 389-395.

[23] Holm, R., *Electrical Contacts: Theory and Application*, Springer, New York, 4th edn., 1967, pp 9-16.

[24] Suh, N. P., "The Delamination Theory of Wear," *Wear*, Vol. 25, 1973, pp 111-124.

[25] Evans, A. G. and Hutchinson, J. W., "On the Mechanics of Delamination and Spalling in Compressed Films," *Int. J. Solids Structures*, Vol. 20, 1984, pp 455-466.

[26] Hu, M. S., Thouless, M. D. and Evans, A. G., "The Decohesion of Thin Films From Brittle Substrates," *Acta Metall.*, Vol. 36, 1988, pp 1301-1307.

[27] Cao, H. C., Thouless, M. D. and Evans, A. G., "Residual Stresses and Cracking in Brittle Solids Bonded With a Thin Ductile Layer," *Acta Metall.*, Vol. 36, 1988, pp 2037-2046.

[28] Bottega, W. J., "On Thin Film Delamination Growth in a Contracting Cylinder," *Int. J. Solids Structures*, Vol. 24, 1988, pp 13-26.

[29] Rabinowicz, E., "The Influence of Compatibility on Different Tribological Phenomena," *ASLE Trans.*, Vol. 14, 1971, pp 206-212.

[30] Barber, S. A. and Rabinowicz, E., "Material Selection for Noble Metal Slip Rings," *Proc. Holm Conference on Electrical Contacts*, Illinois Inst. of Technology, Chicago, IL, 1980, pp 33-40.

Chapter 3

Fretting Failure of Electroplated Gold Contacts

Summary

Fretting tests were carried out with a sphere-on-flat arrangement to investigate the failure mechanisms of electroplated gold contacts. Brass balls and plates electroplated with nickel and gold were used as contact specimens, and all fretting tests were conducted at amplitudes larger than the minimum amplitude necessary for gross slip. The friction force and the electrical contact resistance were continuously recorded during the fretting tests. Lubricated fretting tests were also conducted with mineral oil as a lubricant. Based on scanning electron microscopic and Auger electron spectroscopic observations, three failure stages could be distinguished. In stage I, the gold coating on both contact surfaces was pushed out along the fretting direction, and nickel appeared on the ball contact surface. In stage II, cracks were initiated and propagated due to the tensile stress at the edge of the contact and the shear stress at the layer interface, and eventually wear particles were removed from the nickel-brass interface. In stage III, thin plates of oxide-covered brass were detached from the ball contact surface due to fretting wear. Accumulation of oxidized wear particles at the contact spots resulted in sharp increase in the contact resistance. The friction coefficient was initially low but quickly reached a high steady-state value in the unlubricated tests. The high friction force was responsible for the interfacial failure of the nickel-brass interface. Electrical contact resistance measurement was found to be insensitive for detecting fretting failure of electroplated gold contacts in the accelerated laboratory tests.

3.1 Introduction

Fretting is the phenomenon that occurs when two contact surfaces undergo small oscillatory motion. There is not yet a generally accepted boundary between fretting and reciprocating sliding. Contacts sliding with slip amplitudes in the range 10-100 μm are usually assumed to be operating in the fretting mode [1]. Fretting damage in contacts of such common metals as steel, copper, and aluminum alloys was reported long ago [2-4], but fretting failure was not considered a serious problem of electrical connectors until 1974 when Bock and Whitley [5] first investigated the fretting corrosion of electrical connectors. Since then a good deal of effort has been devoted to investigating fretting failure of various contact metals; for example, aluminum, copper, gold, nickel, palladium, silver, and tin [6-11].

Recently Antler [12,13] has comprehensively reviewed the fretting failure of connector contact materials. Among these materials, gold has almost all the desirable properties for electrical contacts, namely high corrosion resistance, high electrical and thermal conductivities, high solderability, and so on. It is also easy to deposit gold on contact surfaces such as by electroplating and vacuum deposition. Thus electroplated gold has been widely used in low-voltage, low-current electrical connectors as well as in other electrical contacts.

Due to the high price of gold, thin gold coatings are commonly employed, typically in the range 0.25 - 2.5 μm. As the gold coating becomes thinner, however, reliability of contacts is sacrificed. Of the several contact failure modes, sliding and fretting failures are the most important. Sliding failure is caused by the frequent insertion and withdrawal of electrical connectors [14]; fretting failure is due to the oscillatory motion caused by mechanical vibration and differential thermal expansion of the contacts. In a previous study, we have investigated the sliding failure of electroplated gold contacts [15]. In this work, the mechanism of fretting failure is examined.

It is generally believed that gold-coated contacts are not prone to fretting corrosion because gold cannot form any oxides. However, as the gold coating is worn out and the base metal substrate is exposed, accumulation of insulating oxide wear debris at contact spots results in high contact resistance. Antler and

Drozdowicz [8] have studied the fretting behavior of electroplated gold in contact with solid gold. They found that thick gold deposits were more desirable than thin deposits to maintain low contact resistance, and that nickel underplating and lubrication were effective in preventing, or at least delaying, fretting failure. In practice, however, both contact surfaces are electroplated with thin gold films. Blanks [16] investigated vibration-induced wear in gold-plated edge connectors using spectral analysis of the contact voltage drop. He concluded that the most sensitive method of assessing plating degradation is by microscopic examination, and that contact resistance is an inadequate measure of contact damage and thus is potentially unreliable. Nevertheless, the nature of fretting damage of electroplated gold contacts is still not entirely clear, and the role of friction, an important aspect of fretting, is usually not explored in detail.

The objective of the present work therefore is to investigate the mechanisms of fretting failure of electroplated gold contacts. Friction and electrical contact resistance were measured in fretting tests of electroplated gold contacts with nickel underplating. Optical microscopy, scanning electron microscopy and Auger electron spectroscopy were used to determine the surface topographies and compositions of the damaged regions of the surface.

3.2 Experimental

3.2.1 Materials and Specimens

To simulate the possible oscillatory motion at the contact of electrical connectors, a sphere-on-flat geometry was chosen for the fretting tests. Brass balls, 3.175 mm in diameter, with 1.5 μm electroplated gold over 2.5 μm nickel underplate, and brass plates with 1.5 μm electroplated gold over 5 μm nickel underplate were used as contact specimens. The hardness of electroplated gold was measured using a Knoop microhardness tester under a penetration load of 0.1 N. The relevant bulk properties of the contact materials are listed in the Table 3.1.

Table 3.1 Properties of Experimental Materials

Material*	Electrical Resistivity ($\Omega m\ 10^{-8}$)	Yield Strength (MPa)	Penetration Hardness (MPa)
Au+1%Ni	2.24	298	953
Ni	6.84	815	2548
Brass(Cu-35%Zn)	7.80	405	1244

* The compositions are in wt%.
* The values of electrical resistivity come from *The Properties of Electrodeposited Metals and Alloys*, 2nd edition, ed. by William W. Safranek, American Electroplaters and Surface Finishes Society, 1986.

3.2.2 Apparatus and Instrumentation

Figure 3.1 is a block diagram of the instrumentation for the fretting tests. Figure 3.2 illustrates the fretting apparatus schematically. An electromagnetic shaker, which was driven by a function generator and a power amplifier, was used to provide the oscillatory motion. The frequency and the amplitude of the oscillatory motion were controlled by the function generator and the power amplifier. The frequency and the number of fretting cycles were counted by an electronic counter. The plate specimen was clamped onto a platform which was driven by the shaker, and the ball specimen was held in a stainless steel holder, which was connected to a rigid arm through a piezoelectric force transducer. The force transducer had a stiffness of 10^9 N/m and could measure both tensile and compressive dynamic forces. The friction force was measured by this transducer. A normal force of 1 N was applied by a dead weight directly over the ball holder after balancing the loading arm with a counterweight.

The fretting displacement was measured by a Linear Variable Differential Transformer (LVDT). The coil of the LVDT was attached to the vibrating platform and the core to the ball holder. The displacement waveform was monitored during the fretting tests by an oscilloscope and was found to be sinusoidal. The friction force signal was also monitored by the oscilloscope. Both friction force and displacement signals were sent to a microcomputer via RMS converters. One wire soldered to the plate specimen and the other screwed tightly to the ball specimen were connected to a Wheatstone bridge circuit to measure the contact resistance continuously during the fretting test. The contact voltage drop and the current through the contact spots were about 0.2 mV and 12 mA, respectively. Thus any heating effects at the contact spots were ignored.

3.2.3 Lubrication

Mineral oil was used in lubricated fretting tests. 1% mineral oil (by weight) was mixed with 1,1,1 trichloroethane solvent which acts as a lubricant carrier. The plate specimens were immersed in the lubricant solution for a few seconds, and then taken out for testing.

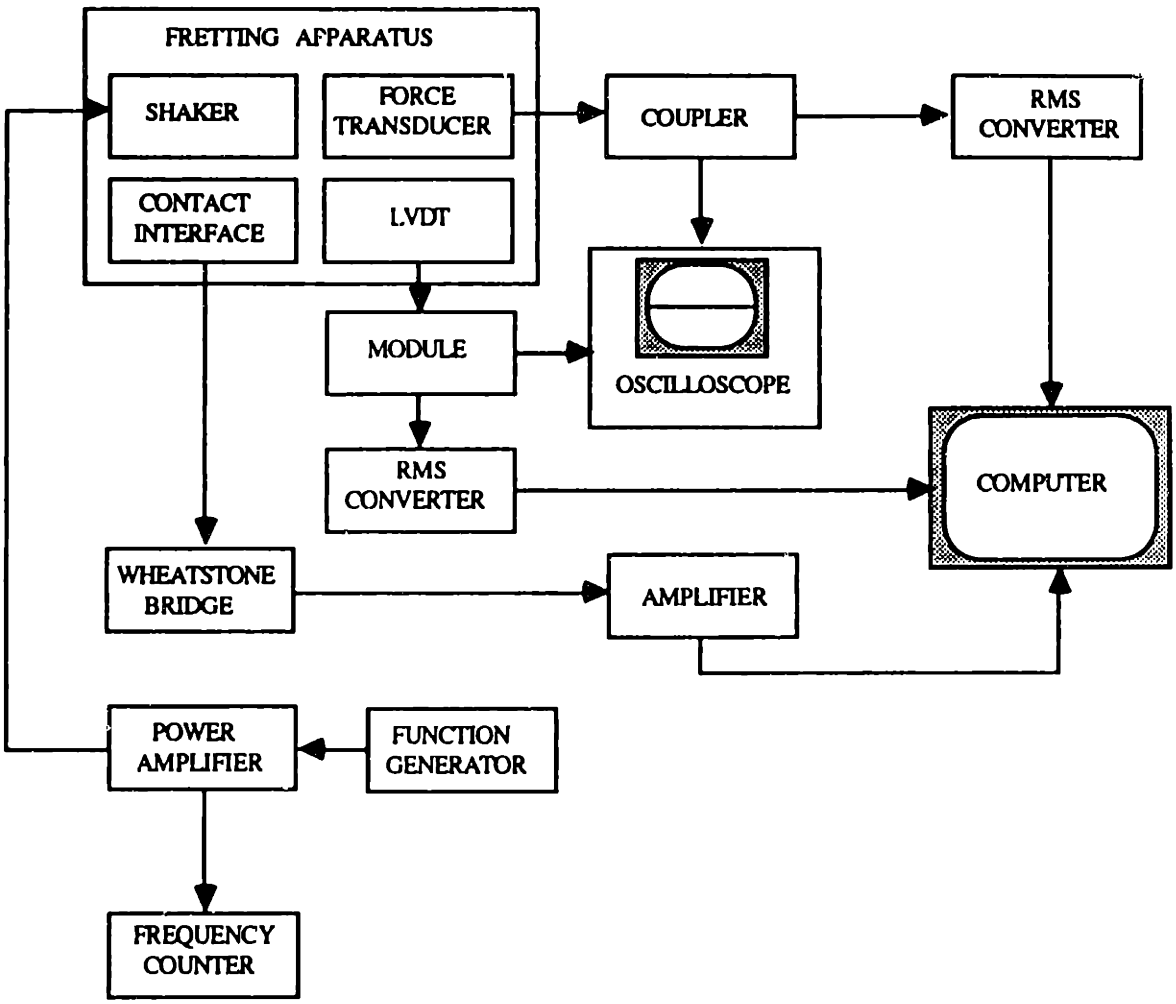

Fig. 3.1 Block diagram of the fretting setup

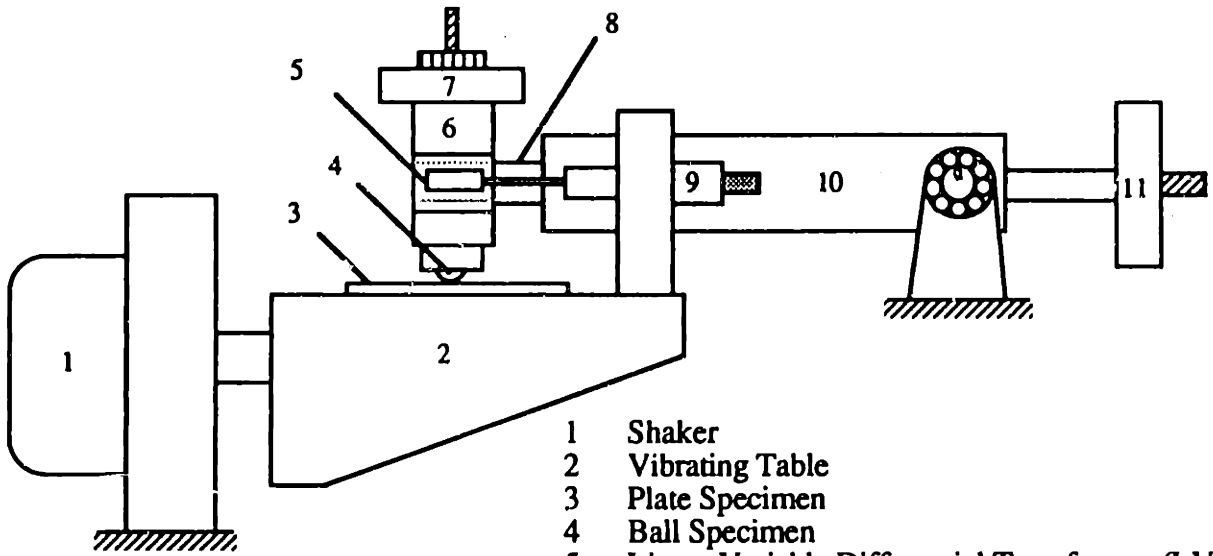

1 Shaker
2 Vibrating Table
3 Plate Specimen
4 Ball Specimen
5 Linear Variable Differential Transformer (LVDT)
6 Ball Holder
7 Dead Weight
8 Force Transducer
9 Micrometer
10 Rigid Arm
11 Counter Weight

Fig. 3.2 Schematic diagram of fretting test apparatus

3.2.4 Experimental Procedures

Experimental parameters for fretting tests include fretting amplitude, fretting frequency, normal load, number of cycles elapsed and the test environment. The amplitude of oscillatory motion that electrical connectors undergo in practice may vary from a few micrometers to a few hundred micrometers at various frequencies. In this study, however, all fretting tests were conducted at a frequency 80 Hz with amplitudes larger than the minimum amplitude necessary for gross slip. The minimum fretting amplitude for gross slip was to be determined by experiments. A normal load of 1 N, which is the industry standard for connectors, was used in this study. The total number of fretting cycles was up to 2 million cycles, which was sufficient to cause fretting failure. All tests were conducted in a laboratory environment, which however was not deliberately controlled. The temperature was about 20-25 ^{o}C, and the relative humidity was from 20 to 60%.

Before each test (except the lubricated tests), the ball and the plate specimens were cleaned with acetone in an ultrasonic cleaner for a few minutes and then cleaned with Freon TF solvent. After the fretting tests, both specimens were examined using an optical microscope and a scanning electron microscope (SEM). Optical microscopy was very useful because the exposure of the nickel underplate and the brass substrate could be easily identified by their color. Auger electron spectroscopy (AES) was also used to determine the composition of the damaged zone qualitatively. The surface profiles of the ball and the plate specimens were measured using a DEKTAK II pro-filometer. Profiles were taken along and perpendicular to the fretting direction.

3.3 Results

3.3.1 Fretting Amplitude

Figure 3.3a shows the typical displacement and the corresponding tangential force waveforms from the oscilloscope. The fretting amplitude, Δx, is defined as the distance between the extremes of the fretting displacement waveform. The displacement waveform was sinusoidal for all fretting amplitudes, but the tangential force waveform depended on the fretting amplitude. For a very small fretting

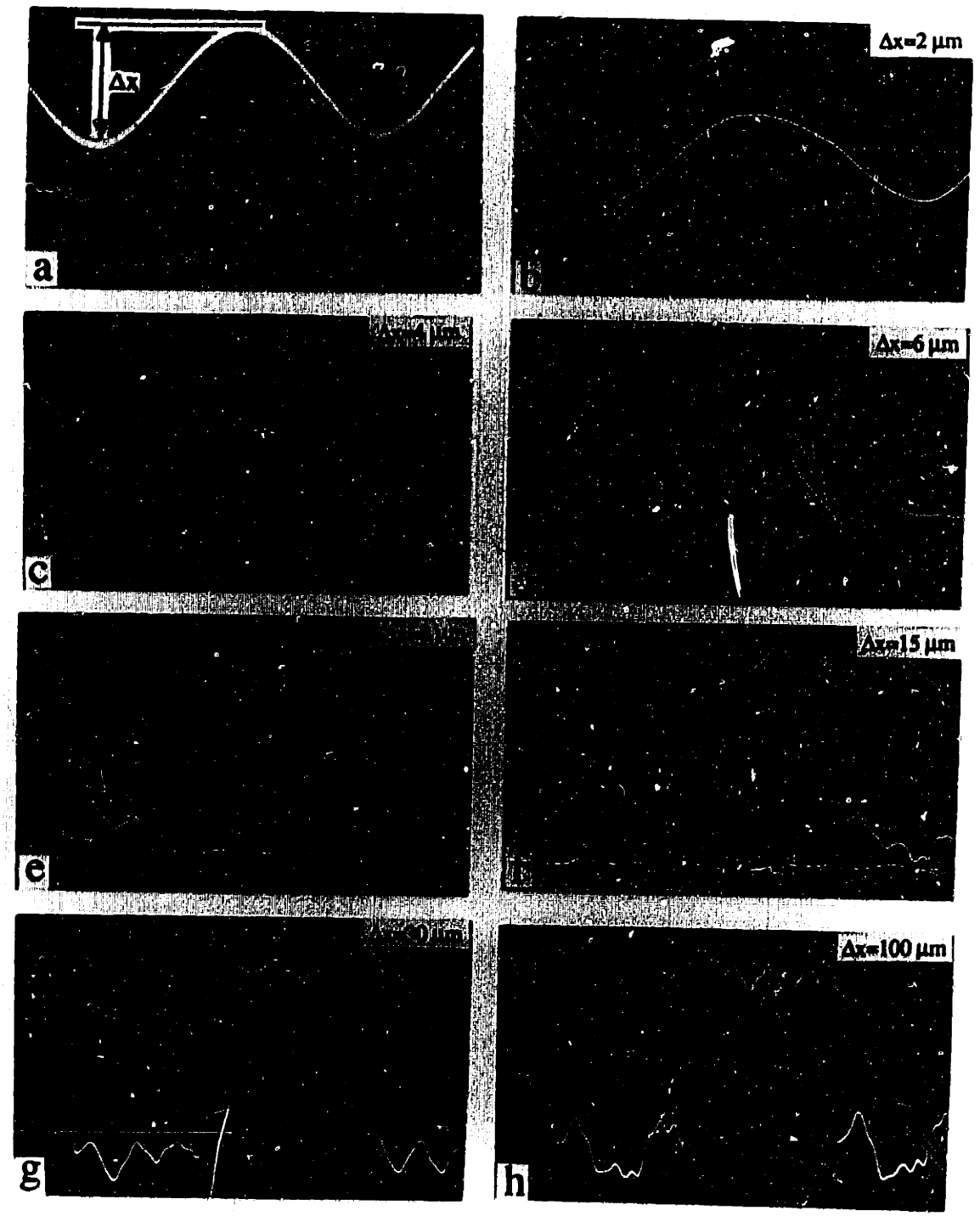

Fig. 3.3 Tangential force wave forms for different fretting amplitudes

amplitude (Δx=2 μm), the tangential force was also sinusoidal and was in phase with the displacement wave (Figure 3.3b). This indicates that the ball specimen was essentially moving in phase with the plate specimen and that no relative motion between the two contact surfaces took place. For Δx=4-8 μm, the friction force waveforms were distorted sinusoidal waves (Figures 3.3c-3e). Figures 3.3f-3i show that for Δx greater than 8 μm, the friction force waves were very much like square waves. Assuming that the fretting apparatus was a displacement generator which drove a spring in series with a Coulomb friction device, Goodman and Bowie [17] suggested that when the displacement was large enough to cause slip in the Coulomb device, the friction force wave would be a peak-clipped sinusoidal wave. Thus gross slip can be considered to have taken place when Δx is greater than 6 μm in this study. Accordingly all fretting tests were conducted with fretting amplitudes greater than 6 μm.

3.3.2 Friction Coefficient and Contact Resistance

The typical friction coefficient and contact resistance versus the number of fretting cycles are plotted in Figures 3.4a and 3.4b. The fretting amplitude was 30 μm. Assuming that the friction force waveform was a perfect square wave, the friction coefficients were calculated by dividing the RMS value of the calibrated friction force signal by the normal load. The friction coefficient was initially low, about 0.35. As fretting continued, it increased steadily up to 1.0 by about 2,000 fretting cycles, and stayed at this value thereafter. The contact resistance was below 5 mΩ up to 250,000 cycles. Then it started fluctuating to high values and eventually rose over 100 mΩ.

3.3.3 Lubricated fretting

Figures 3.4c and 3.4d show the friction coefficient and the contact resistance versus the number of fretting cycles when mineral oil was used as a lubricant. Again the fretting amplitude was 30 μm. The friction coefficient was low and remained low for a very long time (fretting tests were stopped at 2 million cycles). The contact resistance was also low throughout the test. It is apparent that lubrication considerably delays the fretting failure of electroplated gold contacts.

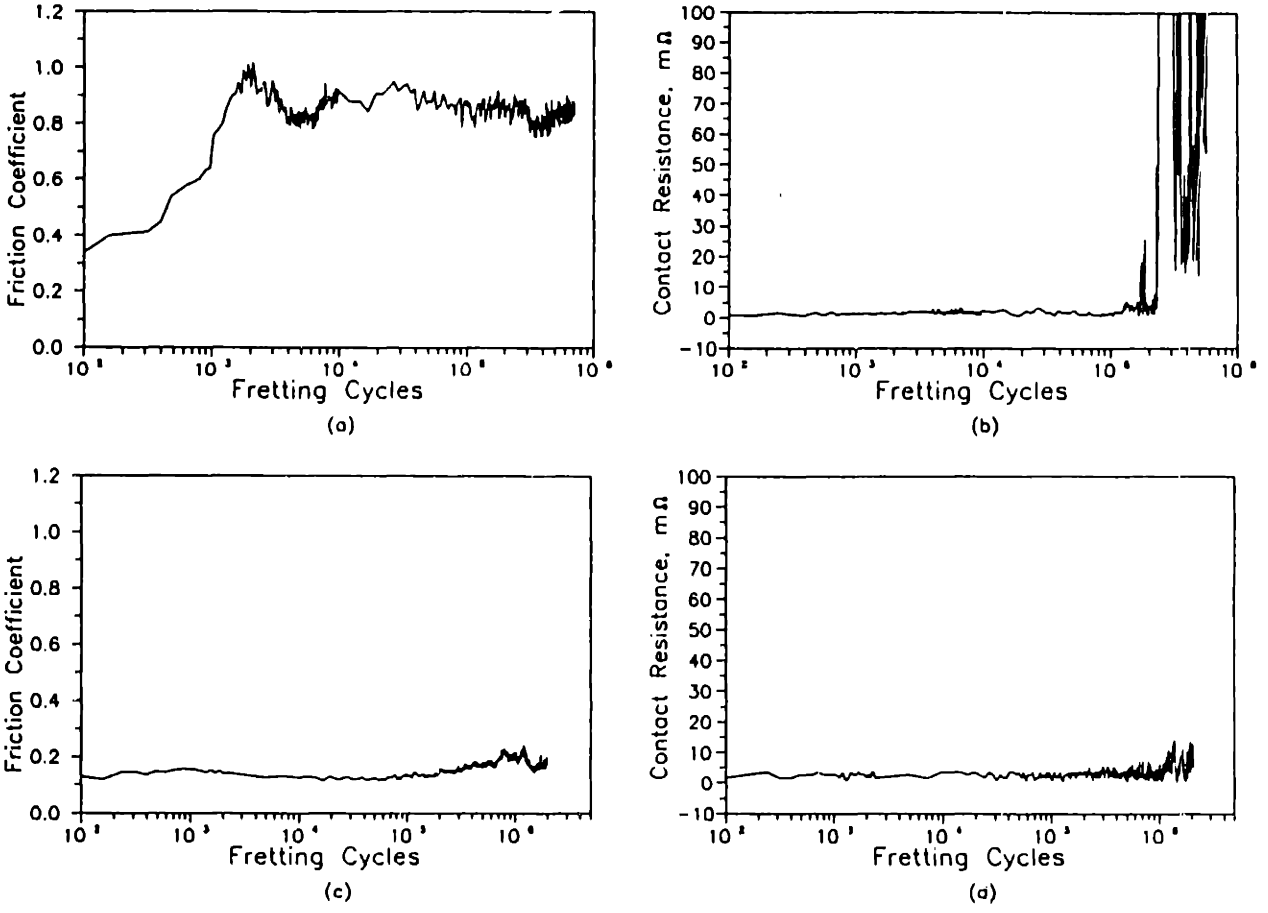

Fig. 3.4 (a) Friction coefficient, (b) contact resistance versus fretting cycles without lubricant; (c) Friction coefficient and (d) contact resistance versus fretting cycles with mineral oil as a lubricant

3.3.4 Effects of Fretting Amplitude

The effect of fretting amplitude on the fretting behavior has been reported in the literature [12,13]. It has been found that the larger the fretting amplitude, the more quickly did the contact resistance degrade. In the present study, the fretting amplitude was from 10 μm to 150 μm. Figures 3.5 and 3.6 show the friction coefficient and the contact resistance versus the number of cycles for different fretting amplitudes. In all tests, the friction coefficients quickly increased to high steady state (0.9-1.0) from the initial values (0.3-0.4), and remained high throughout the tests. The fretting amplitude had significant effect on the contact resistance. The contact resistance rose more readily for larger fretting amplitudes. A 25 mΩ contact resistance is chosen in the connector industry as a criterion of contact failure. Figure 3.7a shows the number of fretting cycles to obtain 25 mΩ contact resistance plotted against the fretting amplitude. The larger the fretting amplitude, the earlier did the contact resistance attain 25 mΩ. But the fretting distance per cycle was different for different fretting amplitudes. Fig. 3.7b shows the total fretting distance to obtain 25 mΩ contact resistance versus the fretting amplitude. Obviously, the total fretting distance to failure is not quite a constant.

3.3.5 Surface Topography and Auger Spectral Analysis

We have observed in a previous study that electrical contact resistance is not a good indicator of sliding failure of electroplated gold contacts in the accelerated laboratory tests [15]. Thus whether the contact resistance is a good or poor measure of fretting failure also needs to be determined. Accordingly, step-by-step fretting tests were conducted with 30 μm fretting amplitude. Five tests were conducted and each test was stopped at different number of cycles. (The number of fretting cycles to cause a noticeable increase in the contact resistance was not exactly the same in electron microscopy and Auger spectral analysis were then conducted on both the ball and the plate specimens, and the surface topographies and compositions were examined.

Figure 3.8 shows the SEM micrographs of the ball and the plate specimens after 2000 fretting cycles. In these micrographs the fretting direction was horizontal (as in all micrographs in the following). The friction coefficient had increased

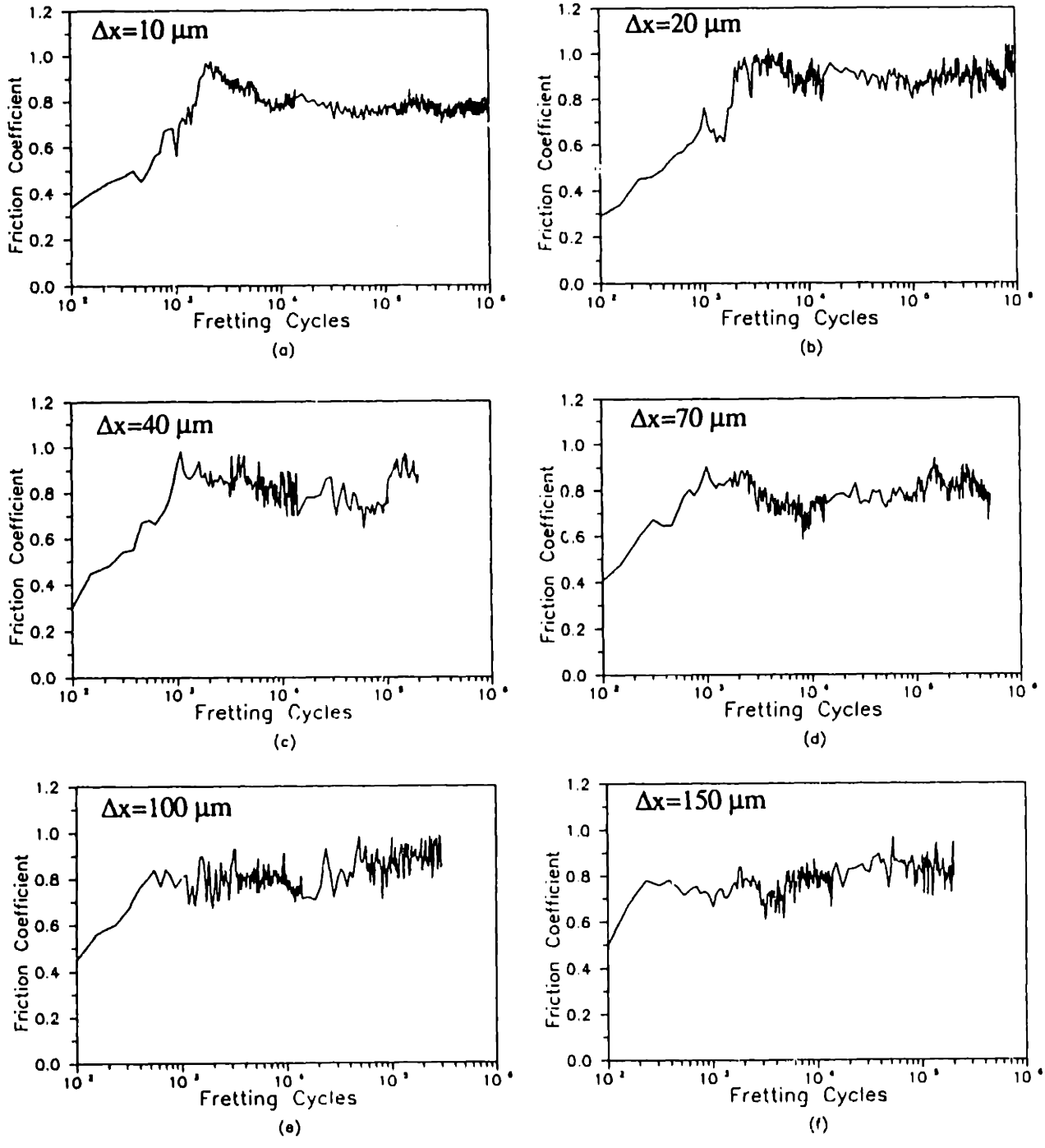

Fig. 3.5 Friction coefficient versus number of cycles for different fretting amplitudes: (a) Δx=10 μm, (b) Δx=20 μm, (c) Δx=40 μm, (d) Δx=70 μm, (e) Δx=100 μm, and (f) Δx=150 μm

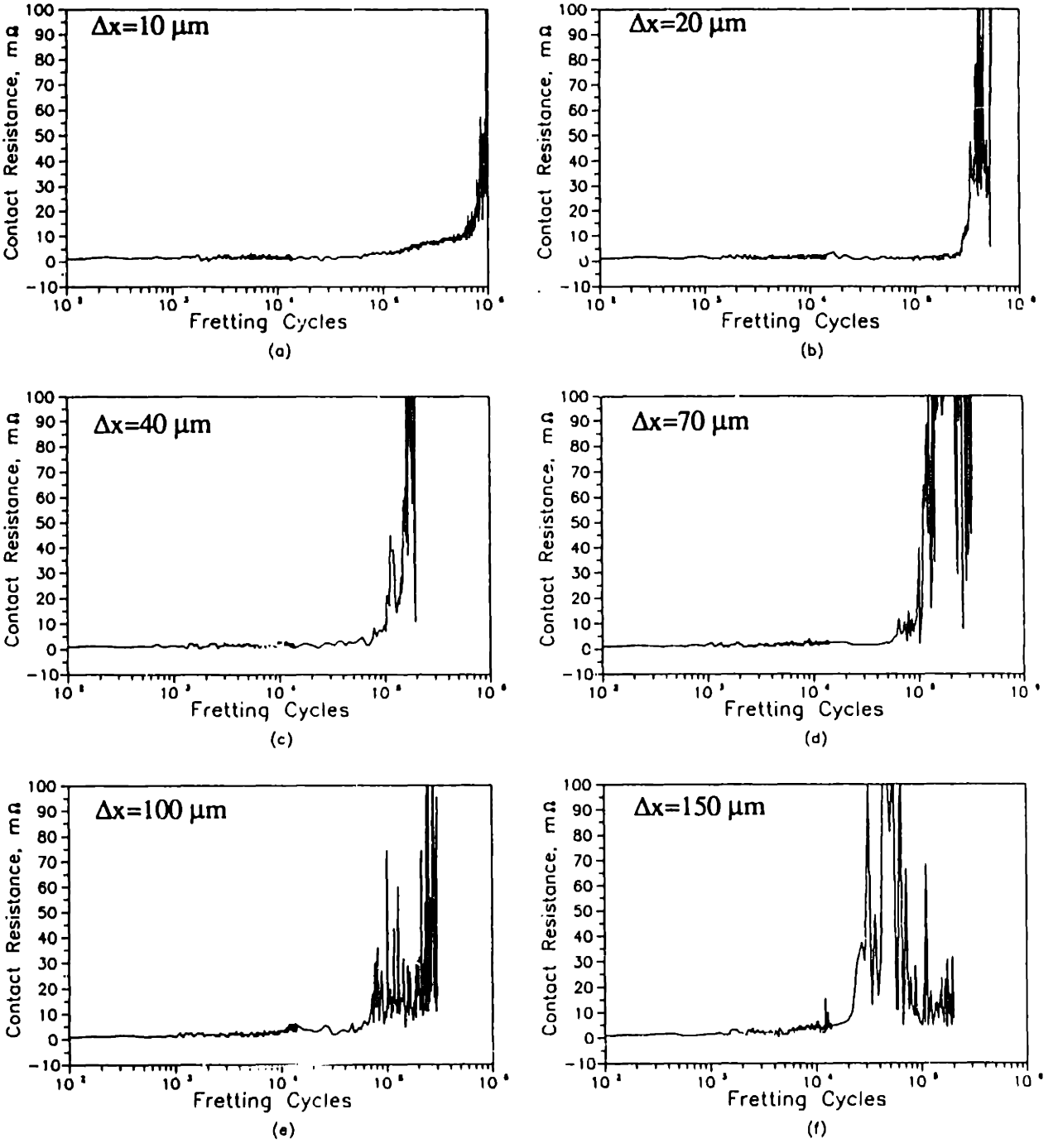

Fig. 3.6 Contact resistance versus number of cycles for different fretting amplitudes: (a) Δx=10 μm, (b) Δx=20 μm, (c) Δx=40 μm, (d) Δx=70 μm, (e) Δx=100 μm, and (f) Δx=150 μm

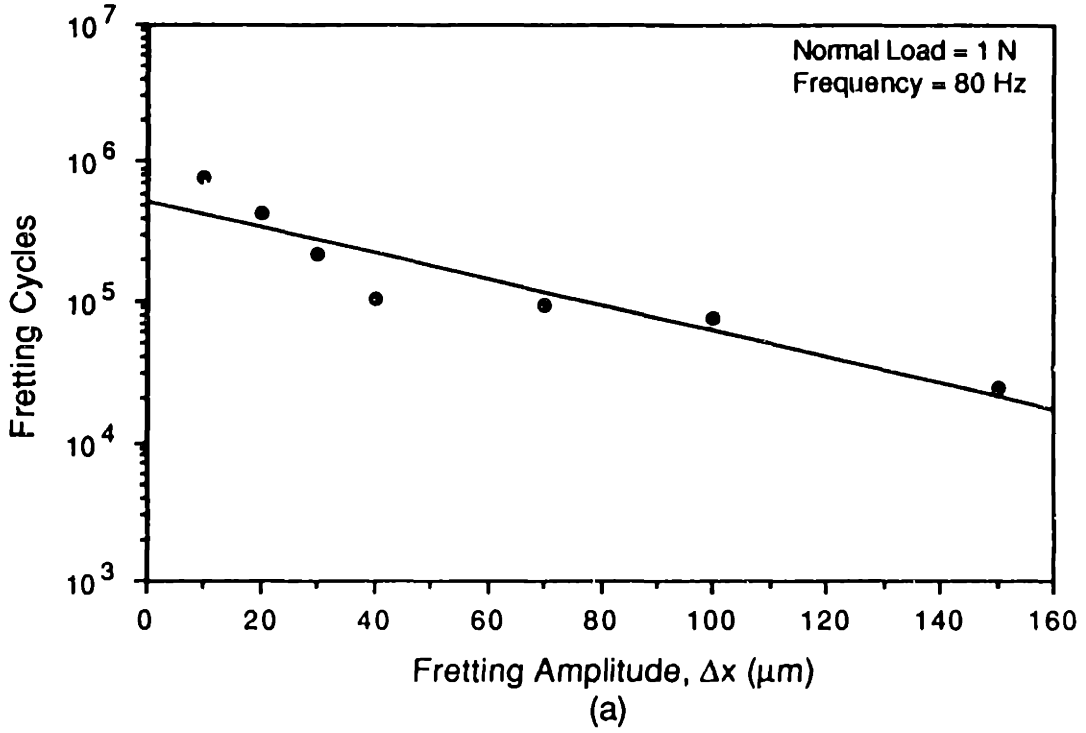

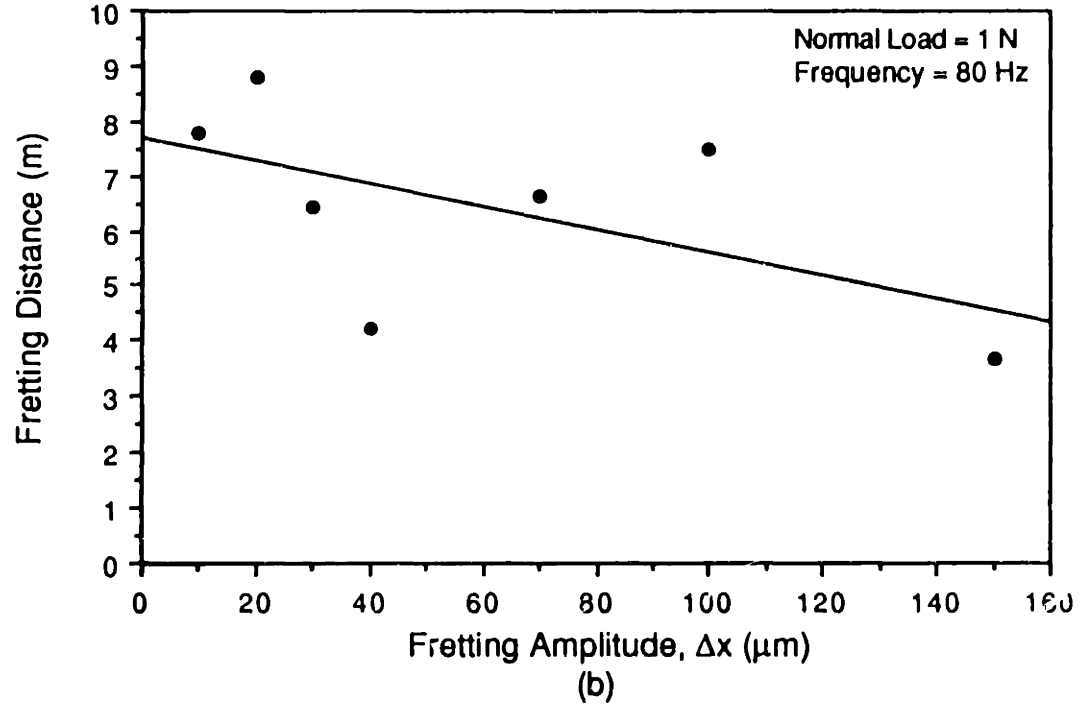

Fig. 3.7 (a) Number of fretting cycles and (b) total fretting distance versus fretting amplitude for the contacts to obtain 25 mΩ contact resistance

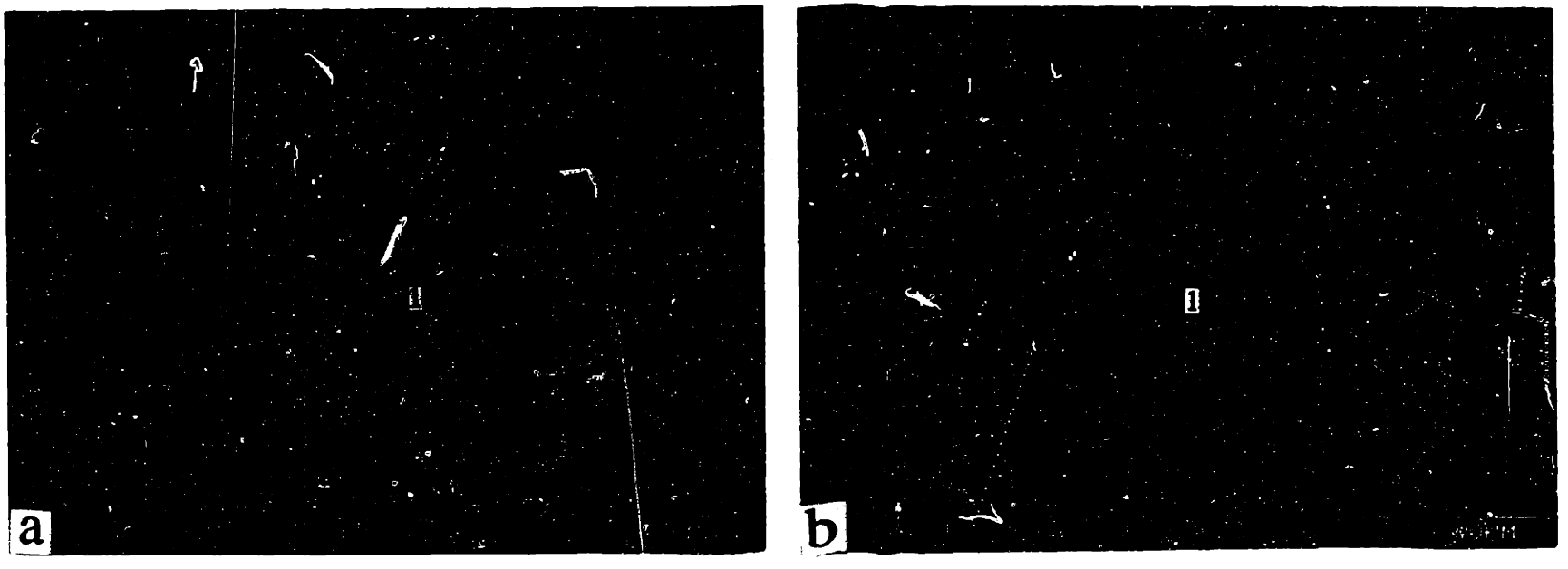

Fig. 3.8 Micrographs of specimens after 2,000 fretting cycles: (a) ball and (b) plate

readily from 0.35 to 0.9, while the contact resistance had been low, below 5 mΩ. A dark region at the contact center of the ball surface was observed. The contact surfaces were smooth, and no wear particles were observed. Auger electron spectroscopy (AES) survey was taken at both contact surfaces (Figure 3.9). Nickel was detected at the dark region and the rest of contact was gold. Figure 3.10 shows the SEM micrographs of the ball and the plate specimens after 65,000 fretting cycles. The dark region at the contact center of the ball surface became larger, and some "islands" were found all over the contact area. AES survey was taken in two areas on the ball surface, one in one of islands and the other in the dark region. The AES spectra of these two areas, Figures 3.11a and 3.11b, show that the islands are gold and the dark region is nickel. Figure 3.12a shows the surface profile of the ball specimen perpendicular to the fretting direction. The depth at the contact center was about 1.3 μm, which further confirms that the gold coating was removed at the center of the contact. On the surface of the plate specimen, the gold coating was pushed out from the contact center. The coating was torn apart in some areas. Figures 3.11c and 3.11d show that no trace of nickel was found on the plate surface and that the gold stayed on the plate surface. The surface profiles of the plate specimen, Figures 3.12b and 3.12c, clearly show that the gold coating was pushed out along the fretting direction. Thus after 65,000 fretting cycles, some of the gold coating on the ball specimen was worn out and nickel started to appear on the surface, while the gold coating on the plate specimen stayed on.

Figure 3.13 shows the micrographs of the ball and the plate specimens after 150,000 fretting cycles. A relatively large dark region is apparent at the center of the contact of the ball specimen. Some surface cracks are also apparent. It seems that a wear particle was removed from the central region. Figure 3.14a shows that the dark region is a mixture of nickel and oxygen, and that nickel, copper, zinc, and oxygen are detected in the area where the wear particle was removed (Figure 3.14b). The surface profile of the ball surface across the worn zone, (Figure 3.15a), shows that the depth of the wear zone from the zero-line of the surface was about 4.5 μm, which is roughly the sum of the thicknesses of the gold coating and the nickel underplate. This implies that a wear particle had been removed from the nickel/brass interface of the ball specimen. However, it is not clear whether the

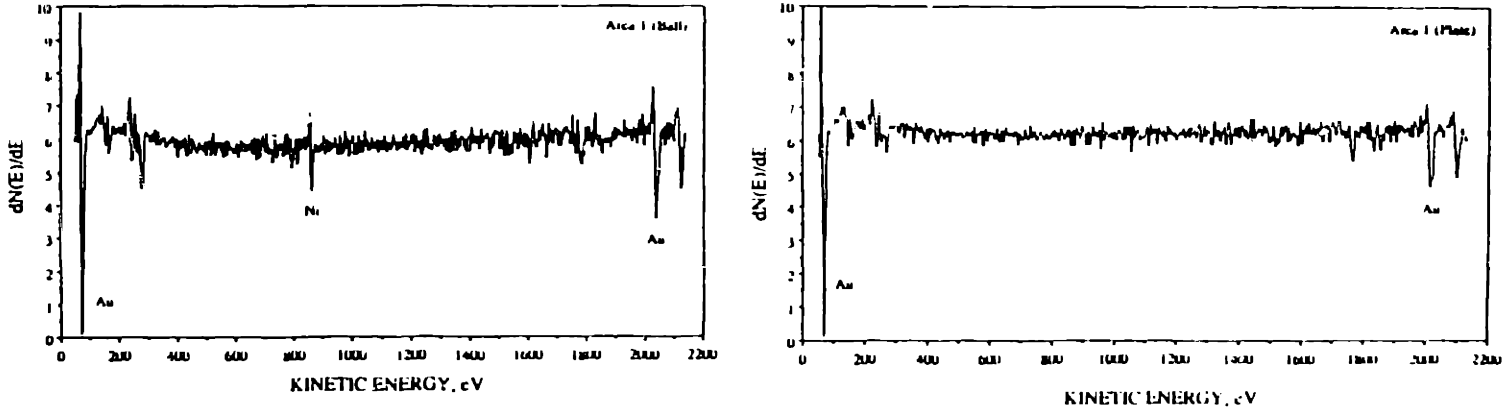

Fig. 3.9 AES spectral analysis for selected area:
(a) area 1 of the ball surface
(b) area 1 of the plate surface

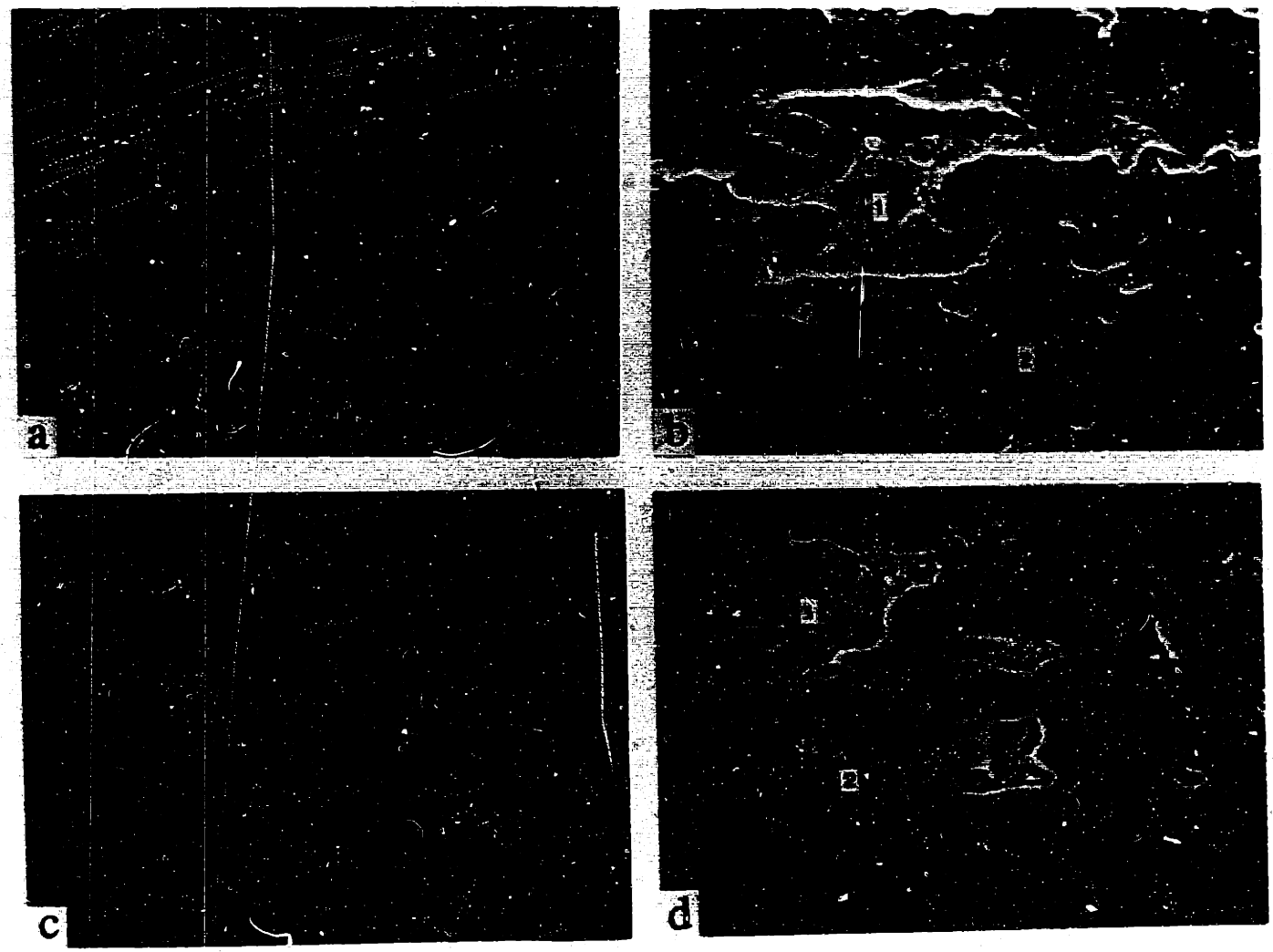

Fig. 3.10 Micrographs of specimens after 65,000 fretting cycles:
(a) & (b) ball, (c) & (d) plate

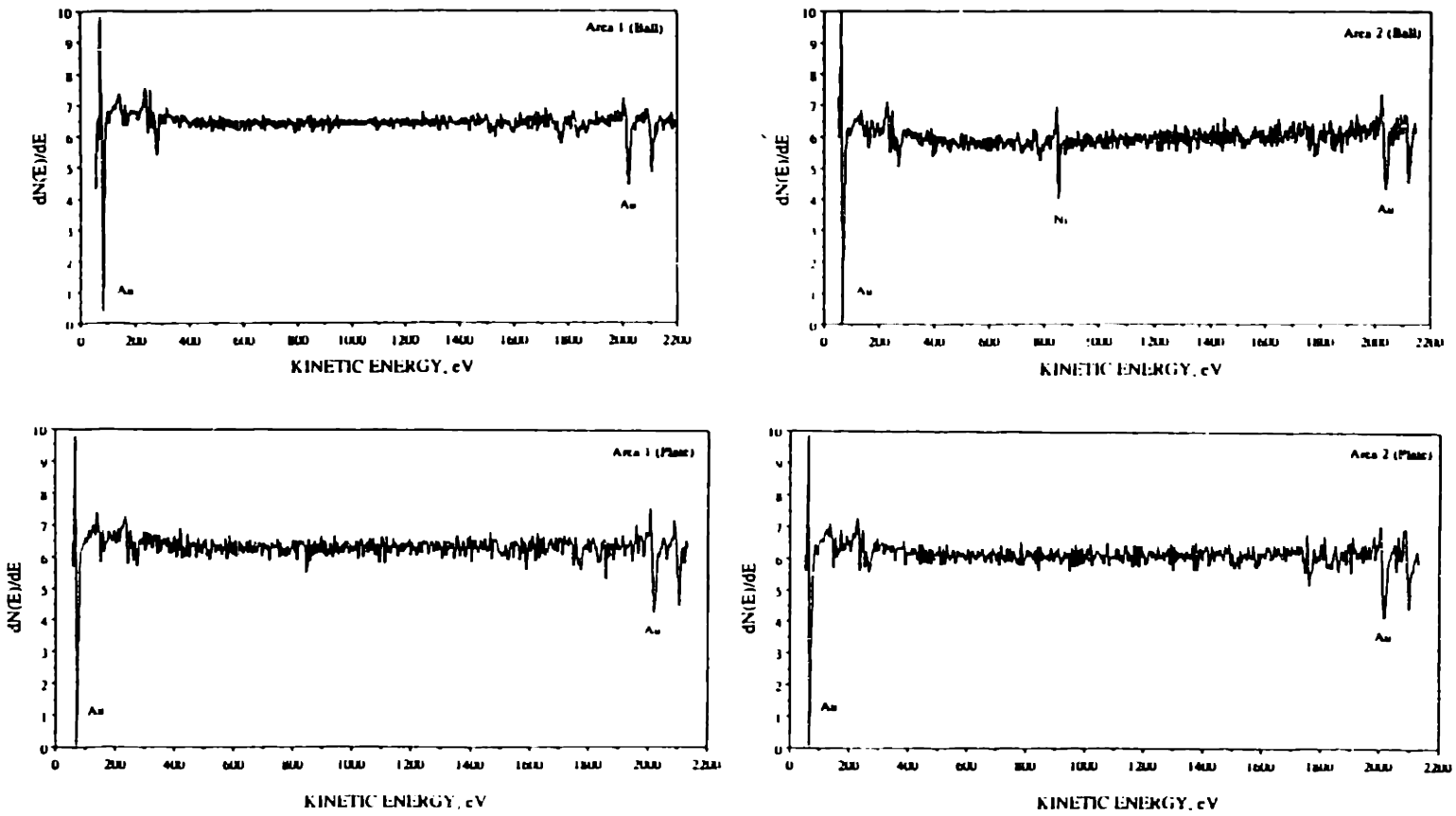

Fig. 3.11 AES spectral analysis for selected area:
(a) area 1 of the ball surface, (b) area 2 of the ball surface,
(c) area 1 of the plate surface, and (d) area 2 of the plate surface

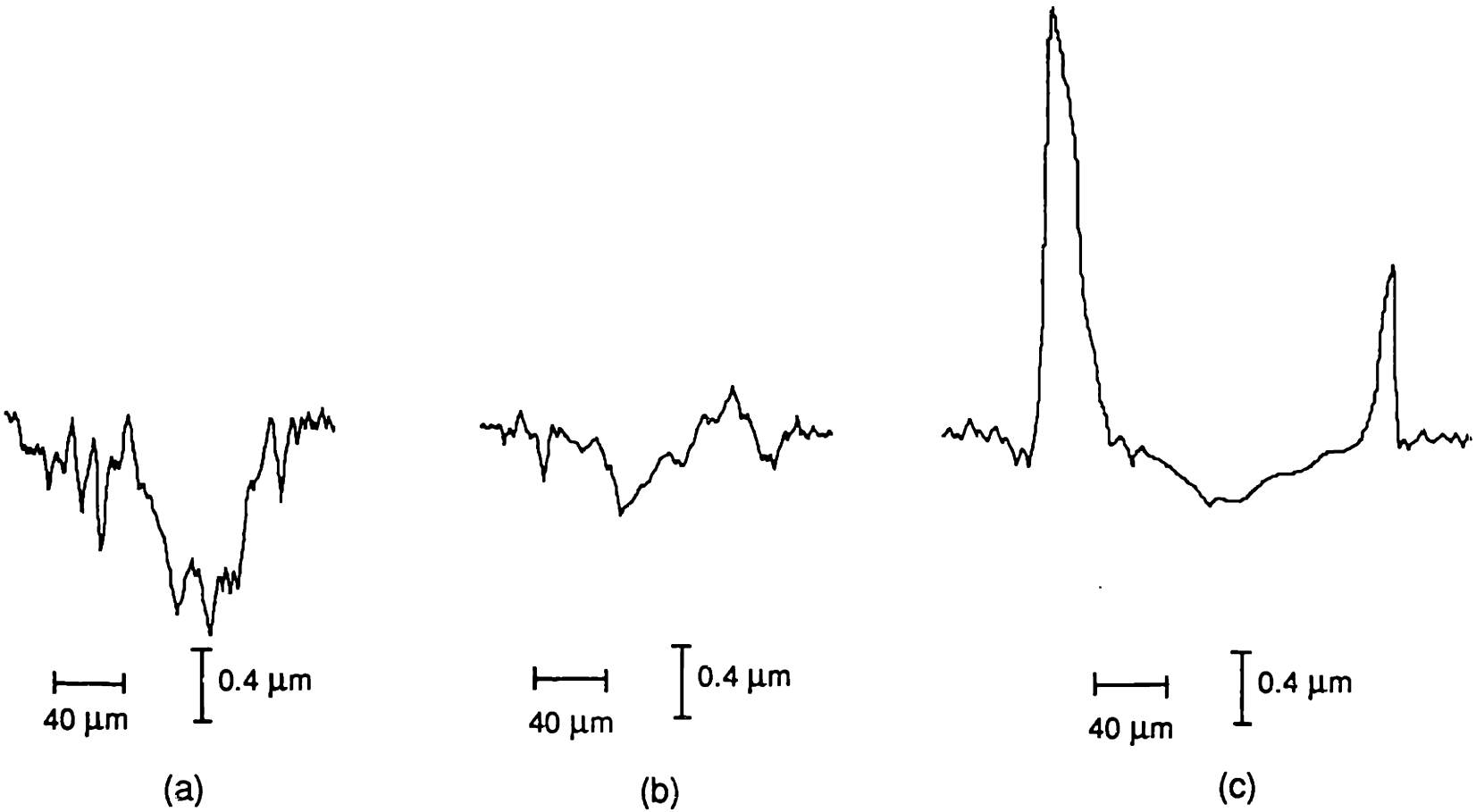

Fig. 3.12 Surface Profiles of the specimens after 65,000 fretting cycles:
(a) ball perpendicular to the fretting direction
(b) plate perpendicular to the fretting direction
(c) plate along the fretting direction

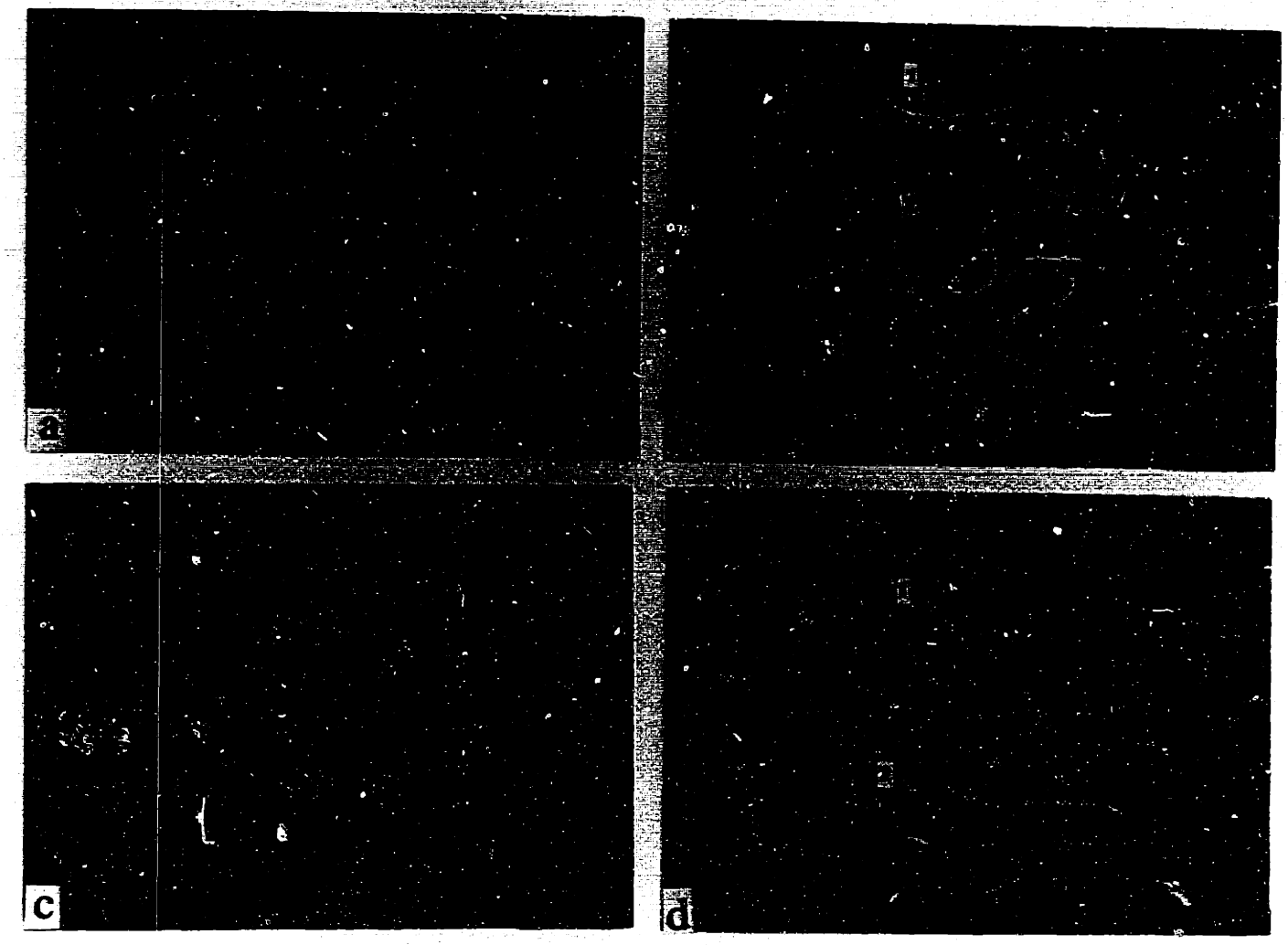

Fig. 3.13 Micrographs of specimens after 150,000 cycles:
(a) & (b) ball, (c) & (d) plate

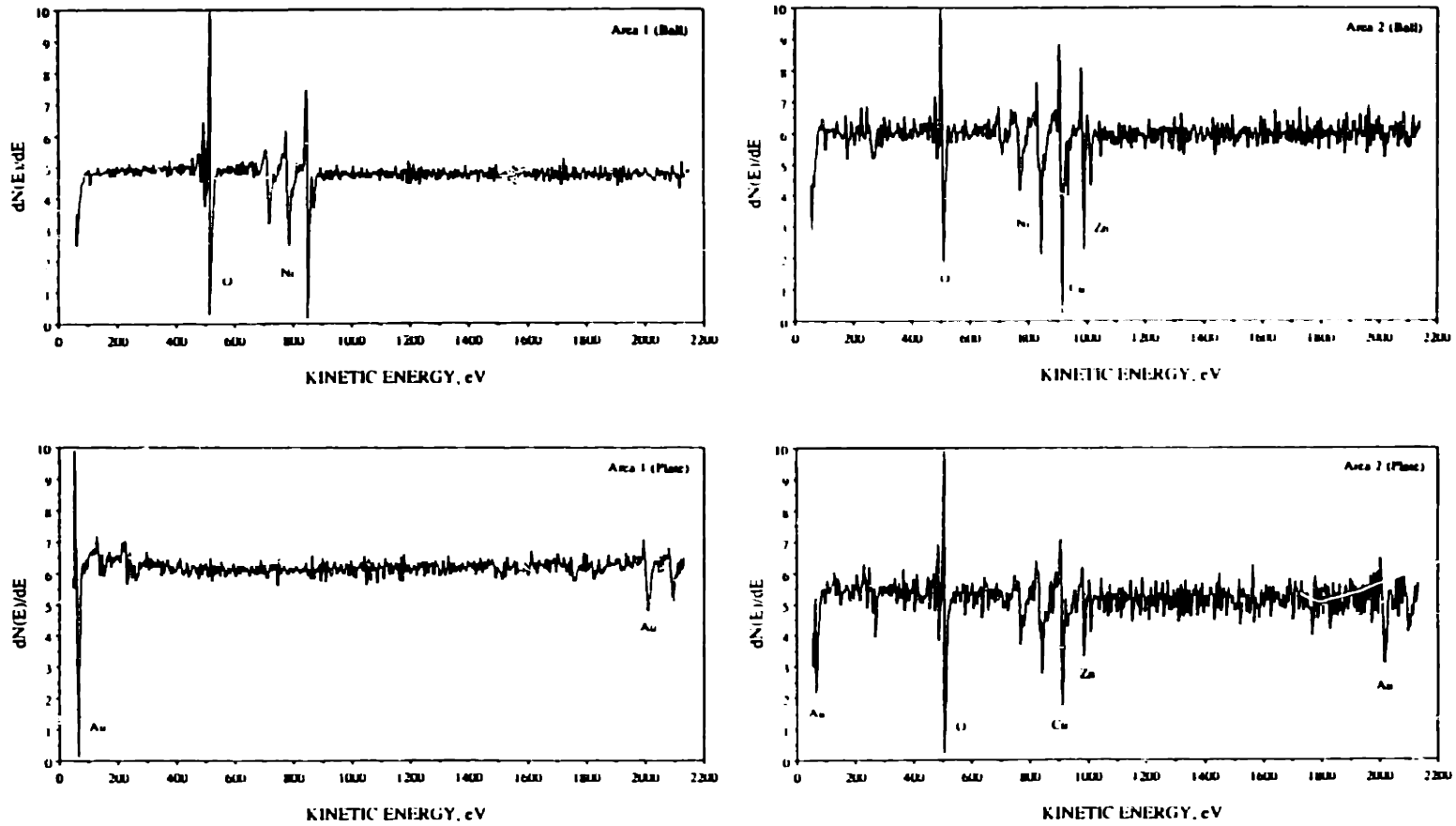

Fig. 3.14 AES spectral analysis for selected area:
(a) area 1 of the ball surface, (b) area 2 of the ball surface,
(c) area 1 of the plate surface, and (d) area 2 of the plate surface

surface cracks propagated down to the nickel/brass interface or interface cracks emerged to the surface. A dark region was also observed on the plate surface (Figure 3.13b), and the position of the dark region corresponded to the worn zone on the ball surface. The AES spectra, Figures 3.14c and 3.14d, show that the dark region is copper, zinc, and oxygen, and the rest of area is gold. But the profiles of the plated surface, Figures 3.15b and 3.15c, show that the depth of dark region was only about 2 μm. This implies that nickel started to be exposed on the plate surface, and that some part of the wear particle removed from the ball surface had been transferred to the plate surface. The friction coefficient was high at this stage, fluctuating at 0.9. However, the contact resistance was still below 5 mΩ.

As fretting continued, the friction coefficient stayed at a high value and the contact resistance was low until a noticeable increase in the contact resistance was detected from the contact resistance measurement after about 245,000 fretting cycles. Then the test was stopped and optical microscopy of the contact surfaces has shown the dark region extends to the whole contact area of the ball surface. Figure 3.16 shows the SEM micrographs of the ball and the plate surfaces at that moment. Cracks were observed at the center of the contact of the ball surface. AES spectrum of the ball surface, (Figure 3.17a), shows that the brass substrate (copper and zinc) was exposed. Figure 3.18a shows the surface profile of the ball specimen. The depth of the dark region indeed suggests that the brass substrate of the ball specimen was exposed and wear particles were removed even from the brass substrate. On the plate specimen, by contrast, only part of the contact was covered by the dark area in which the AES spectrum, Figure 3.17b, also shows copper, zinc and oxygen. The profiles of the plate specimen, Figures 3.18b and 3.18c, indicate that the dark region on the plate surface was copper and zinc oxides which were transferred from the ball surface. Oxidation of the whole contact area of the ball surface resulted in the increase in contact resistance.

Figure 3.19 shows the micrographs of the ball and the plate surfaces after 600,000 fretting cycles. Both surfaces were covered by dark oxides. The AES spectra show that both the contact surfaces comprise copper, zinc and oxygen. The profiles of the ball, Figure 3.20a, suggest that the brass substrate of the ball specimen was indeed exposed, but the profiles of the plate specimen, Figures 3.20b and

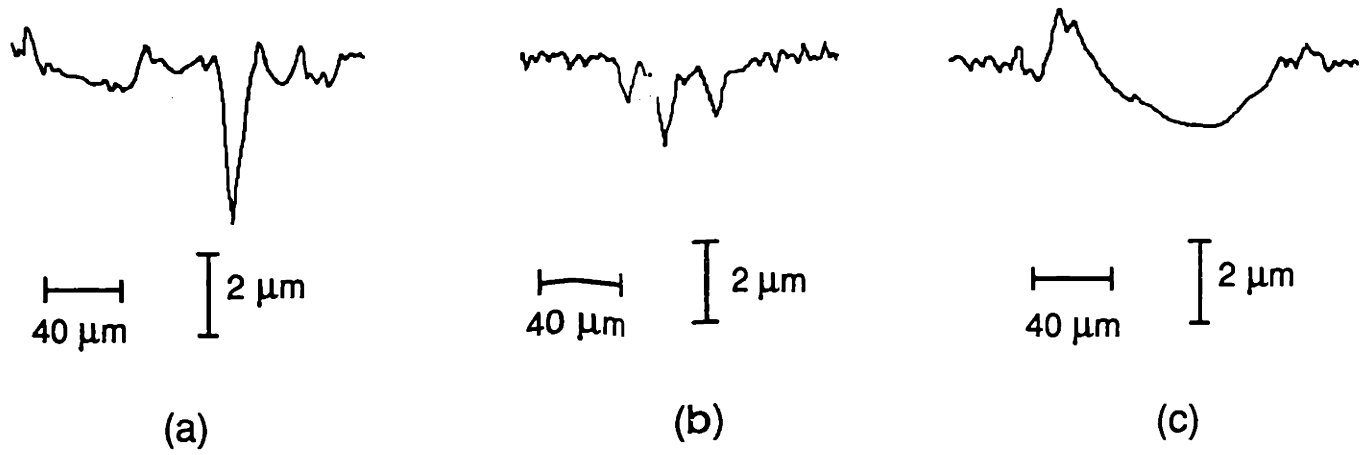

Fig. 3.15 Surface Profiles of the specimens after 150,000 fretting cycles:
(a) ball perpendicular to the fretting direction
(b) plate perpendicular to the fretting direction
(c) plate along the fretting direction

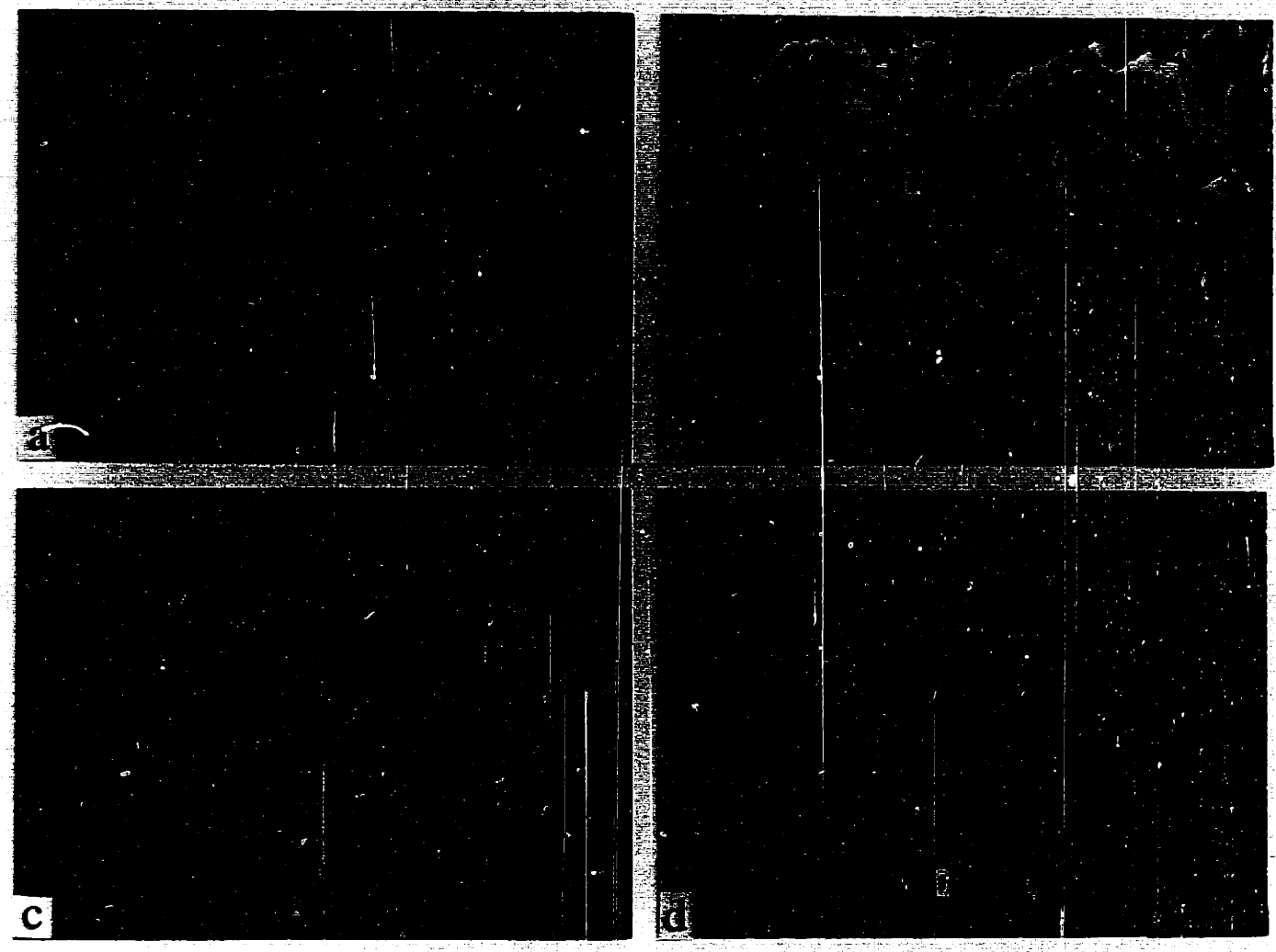

Fig. 3.16 Micrographs of specimens after 245,000 fretting cycles:
(a) & (b)ball, (c) & (d) plate

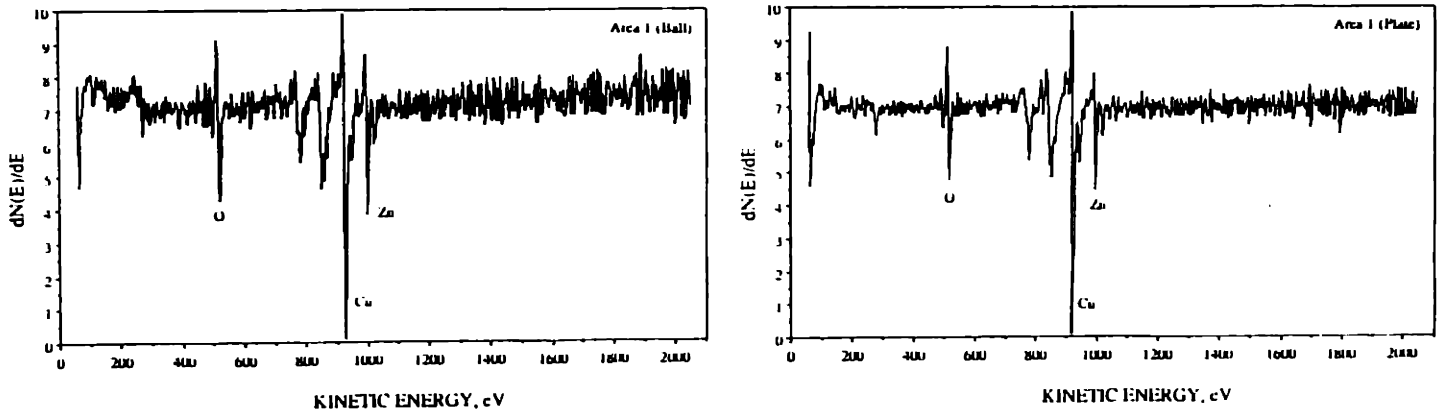

Fig. 3.17 AES spectral analysis for selected area:
(a) area 1 of the ball surface
(b) area 1 of the plate surface

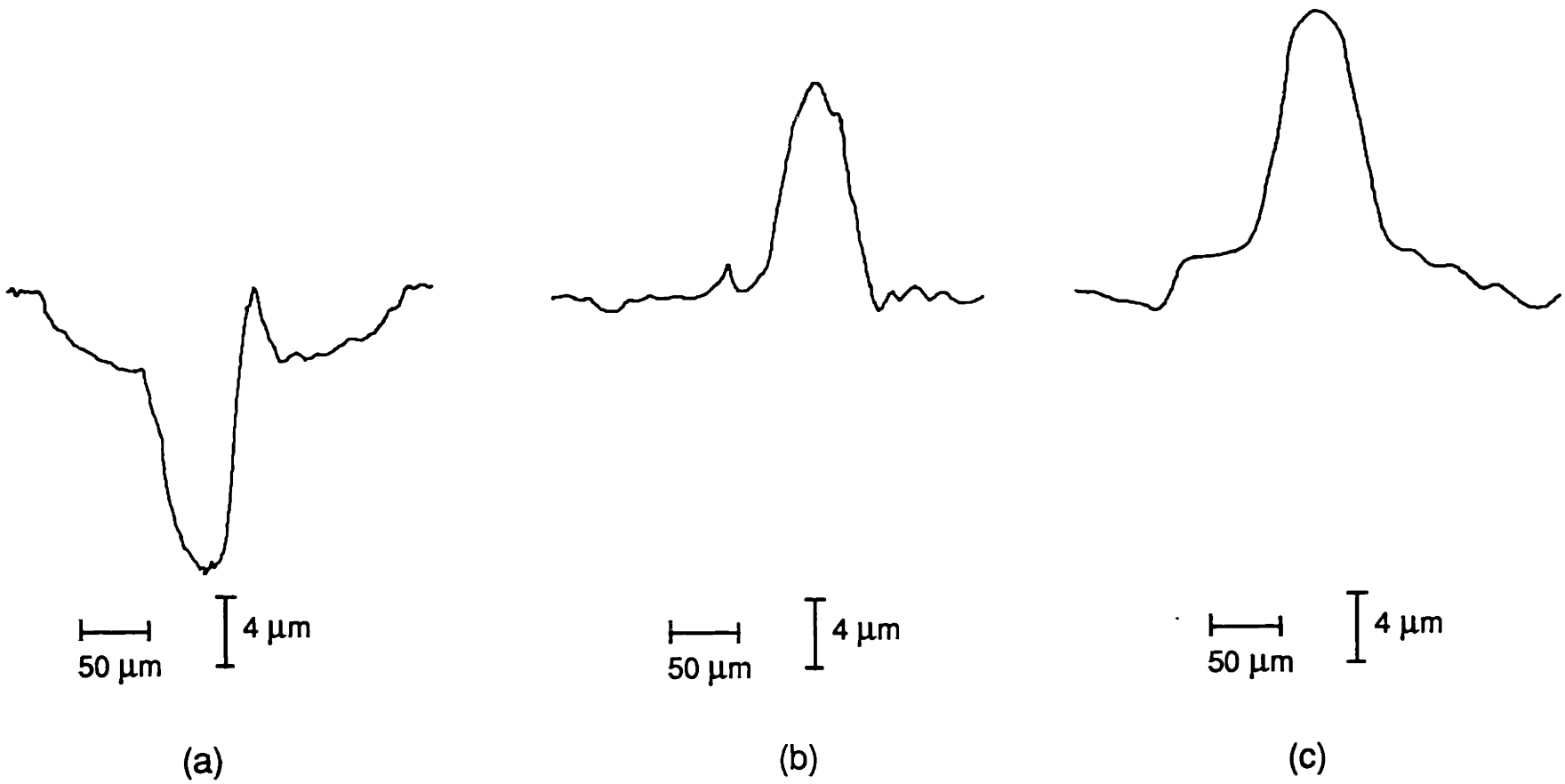

Fig. 3.18 Surface Profiles of the specimens after 245,000 fretting cycles:
(a) ball perpendicular to the fretting direction
(b) plate perpendicular to the fretting direction
(c) plate along the fretting direction

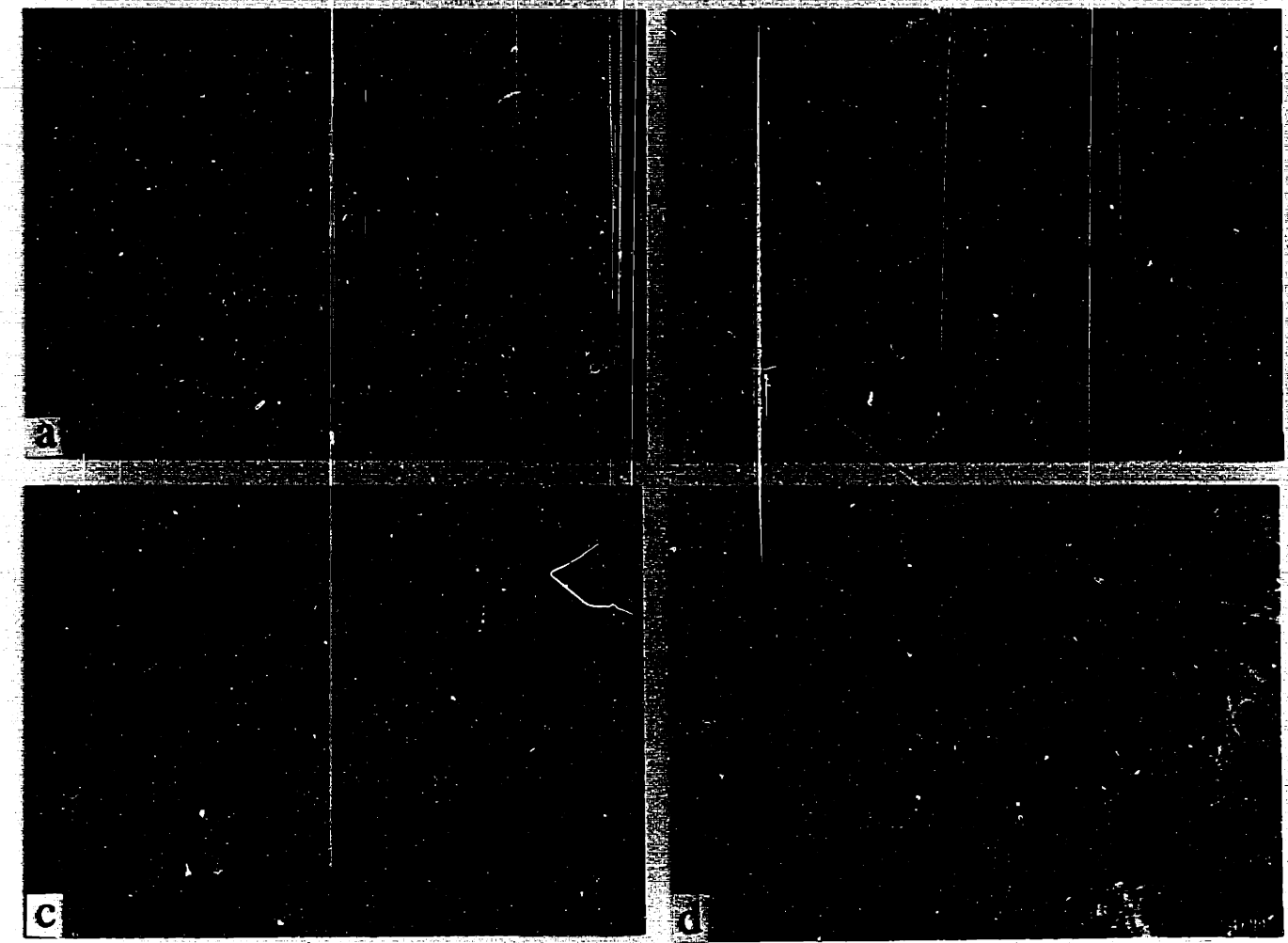

Fig. 3.19 Micrographs of specimens after 600,000 fretting cycles: (a) & (b)ball, (c) & (d) plate

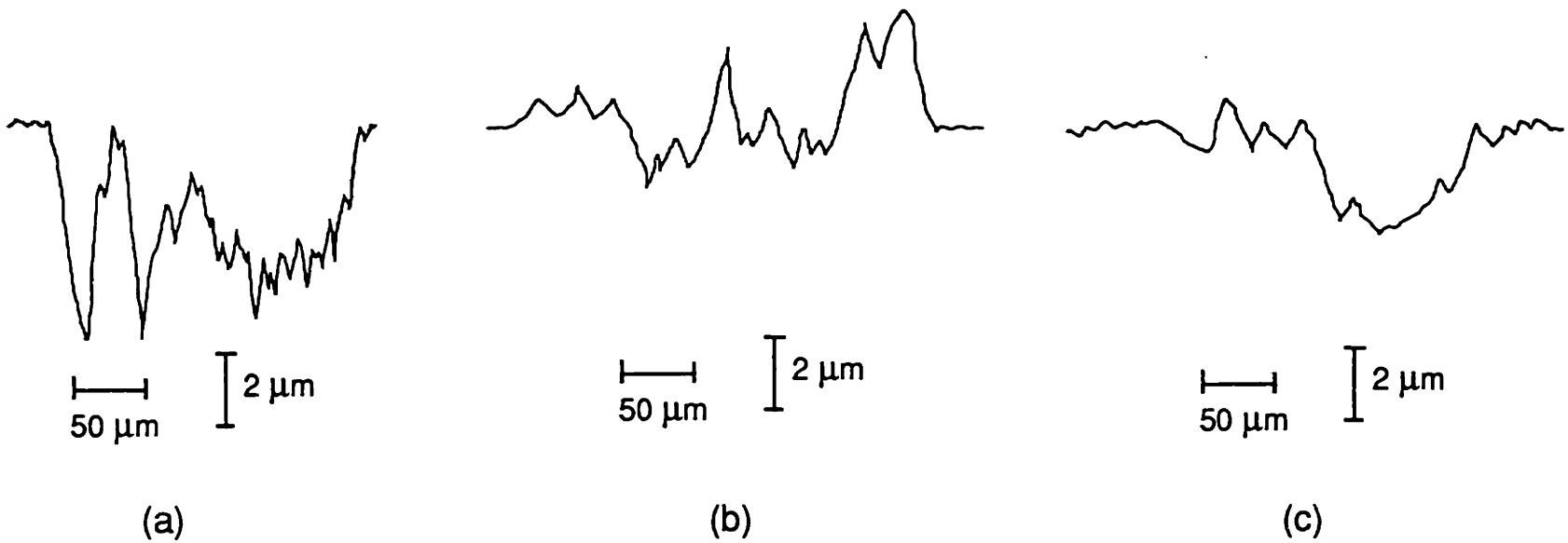

Fig. 3.20 Surface Profiles of the specimens after 600,000 fretting cycles:
(a) ball perpendicular to the fretting direction
(b) plate perpendicular to the fretting direction
(c) plate along the fretting direction

3.20c, show that the depth of the damaged region was about 2 μm. This implies that only the gold coating on the plate surface was removed, and that the copper and zinc detected from the plate surface were due to wear particle transfer from the the ball specimen. The friction coefficient was high and the contact resistance was over 100 mΩ (beyond the range of the data acquisition system).

Figures 3.21a and 3.21b are the micrographs of the ball and the plate surfaces in the lubricated fretting test. After two million fretting cycles, the gold coating of the ball specimen was worn away, while the gold coating on the plate surface was extruded along the fretting direction. AES spectral analysis shows that the dark area on the ball contact is nickel. No cracks were observed on either contact surface. Thus lubrication has considerably delayed the fatigue damage of nickel-brass interface, but the accumulation of plastic deformation and the extrusion of the gold coating led to the appearance of the nickel underplate of the ball specimen.

3.4 Discussion

3.4.1 The Minimum Fretting Amplitude for Gross Slip

The experimental data suggest that there is a minimum fretting amplitude for gross slip (see Fig. 3.3). The theoretical aspect of this problem was studied long ago by several researchers [18-20, 17]. For simplicity, consider two elastic bodies that are in contact under a normal force L and a tangential force T (Figure 3.22), where T is smaller than the product of static friction coefficient between the contact surfaces, μ, and the normal load, L. Assuming no slip between the contacting surfaces, Mindlin [18] found that the shear stress is singular at the boundary of the contact region. Thus he concluded that slip must occur at the boundary of the contact region in reality. By assuming that the shear stress cannot exceed the product of the static friction coefficient and the normal stress at any point within the contact, he found that relative slip between the two bodies starts at the contact boundary and spreads from the outer contact radius, a, to an inner radius, c. The relation between the radii is given by

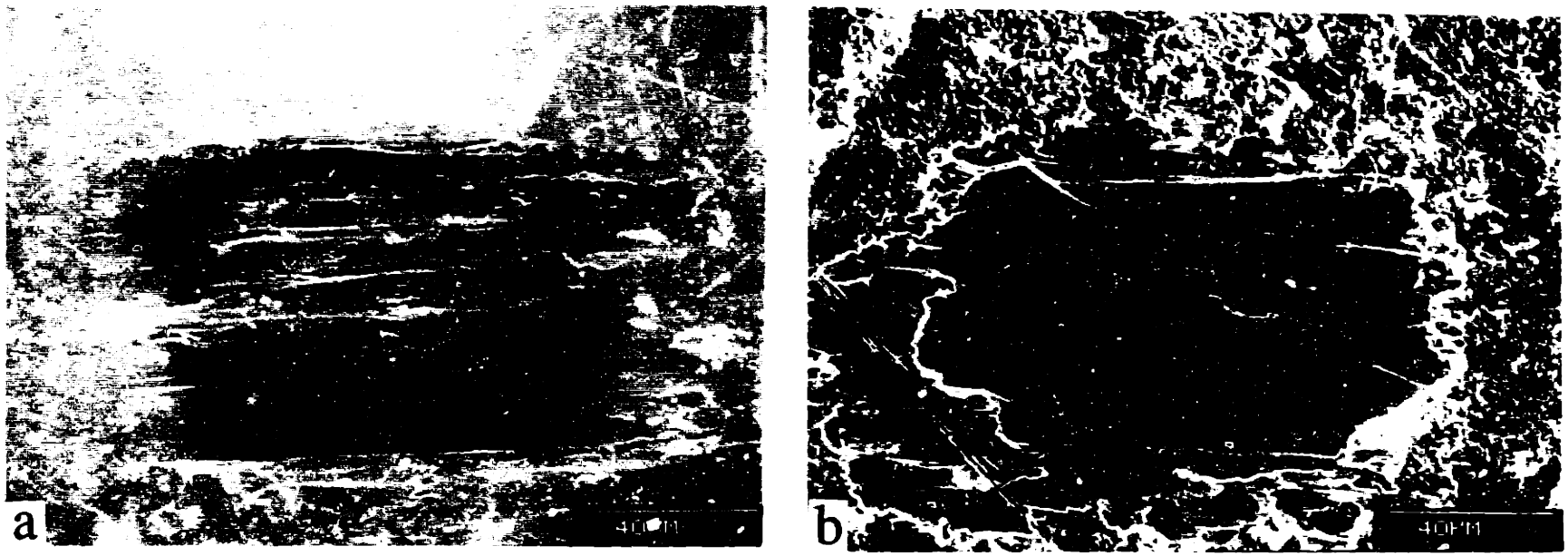

Fig. 3.21 Micrographs of the specimens after 2 million fretting cycles with mineral oil as a lubricant: (a) ball and (b) plate

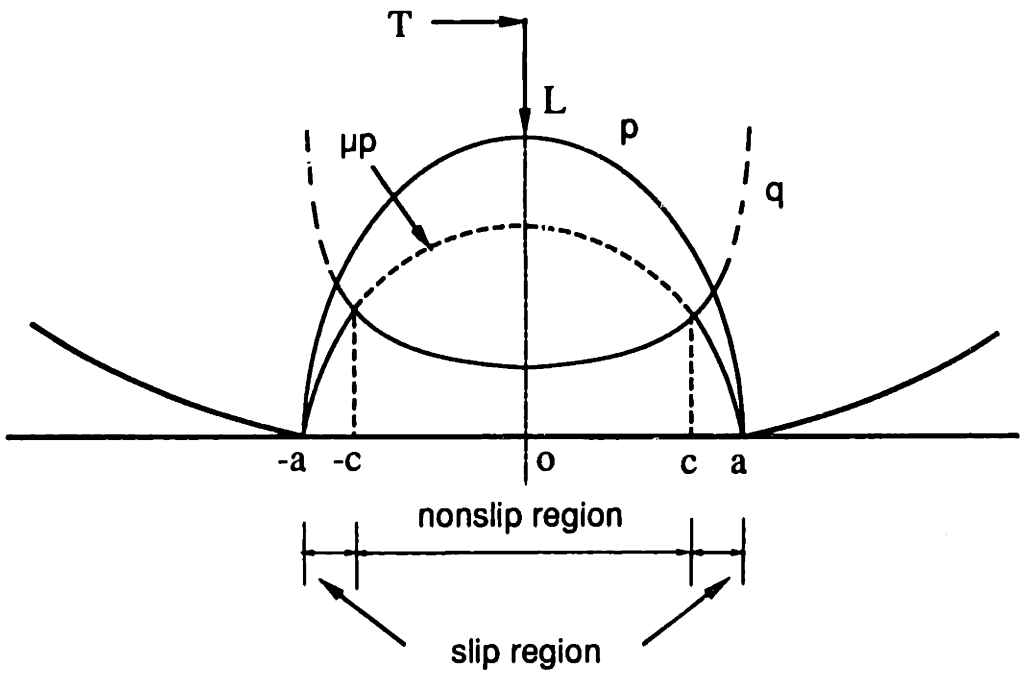

Fig. 3.22 The normal stress distribution, p, tangential stress distribution, q, and the frictional stress distribution, μp, of the elastic contact under normal load L and tangential load T

$$\frac{c}{a} = \left[1 - \frac{T}{\mu L}\right]^{1/3} \tag{3.1}$$

The tangential displacement of one body relative to the other, δ, is given by

$$\delta = \frac{3(2-\nu)(1+\nu)}{8 E a} \mu L \left[1 - \left(1 - \frac{T}{\mu L}\right)^{2/3}\right] \tag{3.2}$$

where E is the Young's modulus and ν the Poisson's ratio. When the tangential force T is equal to μL, gross slip occurs over the entire contact area, and the minimum fretting amplitude for gross slip is given by

$$\delta^* = \frac{3(2-\nu)(1+\nu)}{8 E a} \mu L \tag{3.3}$$

For L=1 N, a=13 μm [15], and μ=0.6, the minimum fretting amplitude is 0.48 μm if the Young's modulus and the Poisson's ratio of gold are used, and 0.19 μm if the Young's modulus and the Poisson's ratio of nickel are used. The observed value, however, was much higher, namely avout 6 μm.

The difference may be explained as follows. It is apparent from equation (3.2) that the critical value of tangential force necessary for gross slip depends only on the normal load and the friction coefficient between contacting surfaces. From equation (3.3), the tangential force is the product of the stiffness of the system and the imposed displacement. To obtain gross slip in the displacement-controlled fretting tests, such as in the present study, the imposed displacement (fretting amplitude) has to be such that the product of the stiffness and the imposed displacement is equal to the critical value of tangential force. Now if the elastic analysis is assumed to be approximately valid for the elastic-plastic frictional contacts, the "effective stiffness" of contact system in the elastic-plastic regime, which is much smaller than that in the elastic regime, should be used to estimate the minimum fretting amplitude for gross slip. Thus to obtain gross slip, a larger imposed displacement is needed for compliant contact systems. Assume that the "effective modulus" in the plastic regime is 10% of the Young's modulus. For L=1 N, a=13 μm, μ=0.6, and ν=0.5, the minimum fretting amplitude calculated from equation (3) is 4.87 μm if the modulus of gold is used. This value is close to the observed value (6 μm). Another view of this problem is that the minimum fretting magnitude for gross

sliding is simply the maximum total deformation of the contacting asperities before the junctions are torn apart. Thus the minimum fretting magnitude depends on the normal force and the characteristics of adhered junctions.

3.4.2 Mechanisms of Fretting Failure

Fretting failures may be classified as fretting wear, fretting corrosion, and fretting fatigue. Fretting wear is characterized by loss of material at the contact spots such as the formation of craters in the fretted area. For example, Feng and Rightmire [21] stated that fretting damage begins with adhesive wear and that abrasion by loose wear particles causes eventual failure of fretting members. Stowers and Rabinowicz [22] evaluated fretting wear using the Archard's wear equation. They concluded that material loss due to fretting resembles that produced by adhesive wear in unidirectional sliding. Fretting corrosion is the damage by the formation of a surface oxide layer or by the accumulation of oxidized wear particles at the contact spots. Uhlig [23] suggests that the mechanism of fretting corrosion usually has the dual chemical and mechanical nature. Fretting fatigue is any fatigue damage caused by fretting. If the contact pressure and the friction coefficient are sufficiently high, the local cyclic stresses could initiate fatigue cracks. The cracks could propagate resulting in delamination wear [24-26].

In electroplated gold contacts, all three modes indeed play important roles in fretting failure. Since gold does not form any oxides, there may only be fretting wear in the early stages of fretting damage. As the gold coating wears out, and the substrate base materials are exposed, severe corrosion may ensue. Moreover, high cyclic normal and shear stresses due contact pressure and friction may induce and promote interface failure between the coatings and the substrates.

Based on the observations in this study, the fretting failure of electroplated gold contacts can be divided into three stages. In stage I, the gold coating on both contact surfaces is pushed out along the fretting direction. Then accumulation of surface plastic deformation due to the fretting motion tears the gold coating apart, resulting in island-like gold patches on the ball surface. As a result, nickel appears on the surface within the contact region. The damages by fretting motion in this

stage are plastic deformation of the gold coating and the appearance of nickel due to gold coating being pushed away. No corrosion is involved and thus the contact resistance is low.

In stage II, cracks may initiate on the contact surface or at the nickel/brass interface. Since one of the contact surface is nickel underplate, tensile stresses on the edge of the contact region due to high contact pressure and high friction force could initiate surface cracks. Also the high friction causes high shear stresses at the nickel/brass interface, and cracks may also be initiated at the nickel/brass interface. As fretting continues, these cracks propagate and wear particles are removed from the nickel/brass interface.

In stage III, the brass substrate is exposed to the atmosphere, and oxidation of brass takes place. Thin plates of oxide-covered wear particles are detached from the contact surface, and are transferred to the other side of the surface. These oxidized wear particles accumulate in the contact region due to the small relative displacement between the contact surfaces, and contact resistance starts to increase. When one of the surfaces is completely covered by oxidized layers of the brass substrate, the contact resistance becomes infinitely large.

3.4.3 The Effect of Friction Coefficient on Fretting Failure

One important aspect of interactions at contacting spots is the friction behavior. In this study, the initial friction coefficient is low, about 0.35, which is more or less the same as that observed in the sliding tests [15]. As fretting continues, the friction coefficient quickly increases to a high value (0.9-1.0) and maintains at this high value throughout the tests. Since no wear particle was observed in the period (see Figure 3.8), the increase in friction is possibly due to growth of gold-gold junctions [27]. After that, the nickel underplate is exposed and oxidized wear particles are removed from one of the contact surfaces. Since the displacement amplitude is small, wear particles cannot be readily removed from the contact spots and thus plowing by the wear particles contributes to the high friction.

It can be seen from the experimental observations that high friction causes severe plastic deformation and induces the fatigue failure of the contacts. Wear

particles are generated due to the accumulation of plastic strain and the interface failure. Plowing by the wear particles which accumulate at the contact surfaces in turn produces high friction, resulting in accelerated damage to the contacts. To quantitatively analyze the effect of friction on the fatigue failure of the multilayer contacts, a rigorous stress and strain analysis under fretting contacts is needed. A finite element analysis of this problem is under way to tackle this problem.

The effects of friction on the stress distribution can be qualitatively seen from the elastic analyses under normal and tangential loadings. Hamilton [28] derived explicit equations for the contact stresses of two homogeneous materials under normal and tangential loadings. It was shown that the effect of friction is to add a compressive stress to the leading edge of the contact and to augment the tensile stress at the trailing edge. Thus high friction may induce the initiation and and promote the propagation of surface cracks of brittle materials due to high tensile stresses on the surface. It was also shown that yielding is initiated in the subsurface region if the friction coefficient $\mu < 0.3$ and on the surface if $\mu \geq 0.3$. Recently O'Sullivan and King [29] have studied the stress field of a layered elastic half-space under normal and tangential surface tractions. They found that the maximum Mises equivalent stress occurs on the surface if the friction coefficient is 0.5, no matter whether a soft or a hard layer is bonded onto the substrate. The interfacial shear stress becomes larger with increasing friction coefficient. All these analyses suggest that the high friction is the main cause for severe plastic deformation of coatings and interfacial failure of layered systems, and that low friction should result in no plasticity on the contact surface or even elastic sliding. However, a contact is in the elastic-plastic regime whenever a friction force exists. The reason is that the friction force is simply taken as a tangential force acting on one of the contact bodies in traditional stress analysis of elastic and elastic-plastic sliding contacts. Lubricated fretting tests conducted in this study have shown that the low friction indeed delays the crack initiation and the interface failure. Although the friction coefficient is less than 0.2, the micrographs of both contact surfaces show plastic deformation of the gold coating. Thus the plastic deformation of the gold coating is inevitable even for very low friction, but the magnitude of plastic strain and the extent of plastically deformed region may be reduced by decreasing friction.

3.4.4 Contact Resistance and Failure Criterion

Low contact resistance is an essential requirement of electrical connectors. Thus the contact resistance has naturally been used as a criterion of fretting failure. The electrical resistance of a contact consists of two parts: the bulk resistance and the resistance of the contact itself. The bulk resistance is relatively small compared with the contact resistance, and it remains constant through the life time of an electrical connector. The contact resistance, R_c, in turn is the sum of two components. One is the constriction resistance, R_{cn}, resulting from the convergence and the divergence of current flow. The other is the resistance due to any non-conducting film on the contact surfaces, R_f. The contact resistance of a single asperity contact is given by [30]

$$R_c = R_{cn} + R_f$$

$$= \frac{\rho_1 + \rho_2}{4a} + \frac{\rho_f t}{p a^2} \qquad (3.4)$$

where a is the contact radius, t the thickness of the surface film; ρ_1, ρ_2, and ρ_f are the resistivities of contact material 1, material 2, and the surface film, respectively. For multiple contacts, Greenwood [31] has shown that the contact resistance is lower than that of a single contact of the same total area.

For clean metal-to-metal contacts, the contact resistance is just the constriction resistance. When the contact spot is completely covered by a surface film, however, the second term in equation (3.4), R_f, will dominate if the film resistivity is high and the film thickness is large. For a single contact of radius 13 μm [15], the constriction resistances of various contacting pairs are calculated from equation (3.4) and are listed in Table 3.2. If the contact comprises many small contacts, the contact resistance will be somewhat smaller.

The contact resistance in all fretting tests exhibited a general trend. That is, the contact resistance remained low and stable for the most part of the failure life. Once the contact resistance started increasing, though, it quickly rose to high values. At the early stage of fretting, both contacting surfaces were gold. Since gold does

Table 3.2 Constriction resistance for different contact pairs*

	Au	Ni	Brass
Au	0.86	1.75	1.93
Ni	--	2.63	2.81
Brass	--	--	3.00

* Radius of single contact a = 13 μm.
Unit of contact resistance: mΩ

not react with the atmosphere to form any oxides or tarnish films on the surface, the contact resistance was just the low constriction resistance of gold-to-gold contact. As fretting continued, the extrusion of gold coating and interface failure resulted in the exposure of nickel underplate or even brass substrate. In the accelerated laboratory tests, however, the oxidation of nickel or brass may not have been fast enough to separate the contact surfaces and gold-to-gold contact still existed at the contact spot. It is also possible that the oxidation rate may not have caught up with the breaking rate of oxides due to fretting motion, and fresh nickel and brass contacts occurred at the contact spot. Table 3.3 shows that the constriction resistances of various metal-to-metal contacts are low. Thus even if the nickel underplate and the brass substrate are exposed, the contact resistance will still be low as long as the oxides are broken up in time or the oxidation rate is not appreciable.

In practice, however, any exposure of the nickel underplate and the brass substrate will sooner or later lead to oxidation. Since the fretting motion may not be continuous, the oxides will not be broken up in time and the oxidation layer can easily build up at the contact spot. Because the resistivity of oxide layer is very high, the total contact resistance will be high and unacceptable. Thus if nickel or brass is exposed even in part of the contact area, the potential for failure is there and the reliability will be obviously uncertain. In terms of reliability of electrical connectors, then, exposure of the nickel underplate or the brass substrate marks the contact failure. It is apparent from the present study that the contact resistance does not give a sensitive indication of nickel and brass exposure and thus is not a good indicator of fretting failure in the laboratory tests. The contact resistance criterion based on the results of laboratory experiments, therefore, is a poor criterion for the design of electrical connector.

3.5 Conclusions

1. Based on the surface topographies and Auger spectral analysis of the present investigation, fretting failure of electroplated gold contacts can be divided into three stages:

(a) In stage I, the gold coating on both contact surfaces is pushed out in the direction of fretting. Then accumulation of plastic deformation due to the fretting motion tears the gold coating apart, resulting in island-like gold patches in the contact. Nickel starts to appear on the surface at the contact center due to the extrusion of the gold coating.

(b) In stage II, tensile stresses at the edge of the contact region and high shear stresses at the nickel/brass interface, due to the high friction on the surface, result in the initiation of surface and interface cracks. As fretting continues, these cracks propagate and wear particles are removed from the nickel/brass interface.

(c) In stage III, the brass substrate is exposed to the atmosphere, and oxidation of the brass substrate takes place. Thin plates of oxide-covered wear debris are detached from the surface due to the fretting wear process. These wear particles accumulate at the contact interface due to the small relative motion between the contact surfaces, and contact resistance starts to increase.

2. The friction coefficient is independent of the fretting amplitude.

3. The larger the fretting amplitude, the smaller is the number of cycles to obtain 25 mΩ contact resistance.

4. The electrical contact resistance is low as long as metal-to-metal contact exists at the contact spot. In the accelerated laboratory tests, the nickel underplate and the brass substrate are exposed long before any increase in contact resistance is noticeable.

5. Low friction coefficient and low contact resistance were observed in the lubricated fretting tests up to 2 million cycles. Low friction delays the crack initiation and the failure of the nickel-brass interface, but the gold coating was still pushed out possibly due to lack of continuous supply of the lubricant.

References

[1] Waterhouse, R. B., "Fretting wear," *Wear*, Vol. 100, 1984, pp. 107-118.

[2] Tomlinson, G. A., "The rusting of steel surfaces in contact," *Proc. R. Soc. London*, Ser. Vol. A 115, 1927, pp. 472-483.

[2] Tomlinson, G. A., Thorpe, P. L. and Gough, H. J., "An investigation of the fretting corrosion of closely fitting surfaces," *Proc. Inst. Mech. Engr.*, Vol. 141, 1939, pp. 223-237.

[3] Feng, I.-M. and Uhlig, H. H., "Fretting corrosion of mild steel in air and nitrogen," *J. of Appl. Mech.*, Vol. 21, 1954, pp. 395-400.

[4] Bethune, B. and Waterhouse, R. B., "Electrochemical studies of fretting corrosion," *Wear*, Vol. 12, 1968, pp. 27-34.

[5] Bock, E. M. and Whitley, J. H., "Fretting corrosion in electric contacts," *Proc. Holm Seminar on Electrical Contacts*, Chicago, Illinois Inst. Tech., 1974, pp. 128-138.

[6] Kongsjorden, H., Kulsetas, J. and Sletbak, J., "Degradation of electrical contacts caused by oscillatory micromotion between the contact members," *Proc. 9th Int. Conf. Electrical Contact Phenomena*, Chicago: Illinois Inst. Tech., 1978, pp. 87-92.

[7] Gyurina, D. and Smith, E. F., "A laboratory study of the electrical properties of copper alloys in electric contact applications," *Proc. Holm Conf. Electrical Contacts*, Chicago: Illinois Inst. Tech., 1980, pp. 85-93.

[8] Antler, M. and Drozdowicz, M. H., "Fretting corrosion of gold-plated connector contacts," *Wear*, Vol. 74, 1981-1982, pp. 27-50.

[9] Antler, M. and Sproles, E. S., "Effect of fretting on the contact resistance of palladium," *IEEE Trans. Components Hybrids Manuf. Tech.*, Vol. 5, 1982, pp. 158-166.

[10] Braunovic, M., McIntyre, N. S., Chauvin, W. J. and Aitchison, I., "Surface analysis of fretting damage in electrical contacts of aluminum with different contact materials," *IEEE Trans. Components Hybrids Manuf. Tech.*, Vol. 7, 1984, pp. 96-106.

[11] Neijzen, J. H. M. and Glashorster, J. H. A., "Fretting corrosion of tin-coated electrical contacts," *IEEE Trans. Components Hybrids Manuf. Tech.*, Vol. 10, 1987, pp. 68-74.

[12] Antler, M., "Electrical effects of fretting connector contact materials: a review," *Wear*, Vol. 106, 1985, pp. 5-33.

[13] Antler, M., "Survey of contact fretting in electrical connectors," *IEEE Trans. Components Hybrids Manuf. Tech.*, Vol. 8 (1), 1985, pp. 87-104.

[14] Antler, M., "Wear of electrodeposited gold," *ASLE Trans.*, Vol. 11, 1968, pp. 248-260.

[15] Tian, H., Saka, N. and Rabinowicz, E., "Friction and failure of electroplated sliding contacts," submitted to *Wear*, 1989.

[16] Blanks, H. S., "Detection and accelerated testing of vibration-induced contact wear," *IEEE Trans. Components Hybrids Manuf. Tech.*, Vol. 7 (1), 1984, pp. 3-10.

[17] Goodman, L. E. and Bowie, G. E., "Experiments on damping at contacts of a sphere with flat plates," *Experimental Mechanics*, Vol. 1, 1961, pp. 48-54.

[18] Mindlin, R. D., "Compliance of elastic bodies in contact," *J. of Appl. Mech.*, Vol. 16, 1949, pp. 259-268.

[19] Mindlin, R. D., Mason, W. D., Osmer, T. F. and Deresiewicz, K., "Effects of an oscillatory force on the contact surfaces of elastic spheres," *Proc., First U.S. Nat. Congr.*, Appl. Mech. Group, 1951, pp. 203-208.

[20] Johnson, K. L., "Surface interaction between elastically loaded bodies under tangential forces," *Proceedings of the Royal Society of London*, Series A, Vol. 230, 1955, pp. 531-548.

[21] Feng, I.-M. and Rightmire, B. G., "The mechanism of fretting," *Lubr. Engr.*, Vol. 9, 1953, pp. 134-136, 158-161.

[22] Stowers, I. F. and Rabinowicz, E., "The mechanism of fretting wear," *J. Lubr. Tech.*, Vol. 95, 1973, pp. 65-70.

[23] Uhlig, H. H., "Mechanism of fretting corrosion," *J. Appl. Mech.*, Vol. 21, 1954, pp. 401-407.

[24] Waterhouse, R. B. and Taylor, D. E., "Fretting debris and the delamination theory of wear," *Wear*, Vol. 29, 1974, pp. 337-344.

[25] Waterhouse, R. B., "The role of adhesion and delamination in the fretting wear of metallic materials," *Wear*, Vol. 45, 1977, pp. 355-364.

[26] Sproles, E. S. Jr., Gaul, D. J. and Duquette, D. J., "A new interpretation of the mechanism of fretting and fretting corrosion damage," in N. P. Suh and N. Saka, (eds) *Fundamentals of Tribology*, The MIT Press, Cambridge, MA,, 1978, pp. 585-596.

[27] Greenwood, J. A. and Tabor, D., "The properties of model friction junctions," *Conference on Lubrication and Wear*, London, Oct. 1-3, 1957, Inst. of Mechanical Engineers, paper 92, 314-317.

[28] Hamilton, G. M., "Explicit equations for the stresses beneath a sliding spherical contact," *Proc. Instn Mech. Engrs.*, Engr. Sci. Div., Vol. 197C, 1983, pp. 53-59.

[29] O'Sullivan, T. C., and King, R. B., "Sliding contact stress field due to a spherical indenter on a layered elastic half-space," *J. of Tribology*, Vol. 110, 1988, pp. 235-240.

[30] Holm, R., *Electrical Contacts*, Springer, New York, 4th edn., 1967, pp. 9-16.

[31] Greenwood, J. A., "Constriction resistance and the real area of contact," *Br. J. Appl. Phys.*, Vol. 17, 1966, pp. 1621-1623.

Chapter 4

Finite Elment Analysis of An Elastic-Plastic Two-Layer Half-Space: Normal Contact

Summary

The contact problem of a rigid cylinder indenting an elastic-plastic two-layer half-space, in particular the Au/Ni/Copper structure used in electrical contacts, is analyzed using the finite element method. The contact pressure, subsurface stresses and strains, interfacial stresses and strains are obtained for various thicknesses of the interlayer. Under elastic loading, the contact pressure distributions are bounded by parabolic and Hertzian elliptic distributions. As the normal load increases, plastic deformation initiates in the substrate for a thin interlayer. For a thick interlayer, plastic deformation initiates at the interface between the top layer and the interlayer. In the elastic-plastic regime, the contact pressure distribution becomes flatter and the peak pressure moves slightly away from the contact center as the plastic zone breaks out to the contact surface. In the light of the finite element results, the mechanisms of crack initiation at interfaces and the interfacial delamination process are qualitatively addressed.

Nomenclature

a	=	half contact width
a_o	=	half width of Hertzian contact
C_1, C_2	=	constants
E	=	Young's modulus
E_p	=	plastic modulus
h_1	=	thickness of top layer
h_2	=	thickness of interlayer
L	=	normal force per unit length
p	=	pressure
p_o	=	center pressure of Hertzian contact
p^*	=	center pressure
$\bar{p}$	=	normalized Hertzian pressure($=p/p_o$)
$\bar{p}^*$	=	normalized pressure ($=p/p^*$)
R	=	radius of cylindrical indenter
u, v	=	components of displacement
x, y, z	=	cartesian coordinates
α	=	coefficient of linear workhardening
δ	=	penetration depth of the indenter
$\varepsilon_{xx}, \varepsilon_{yy}, \varepsilon_{xy}$	=	components of strain
ν, ν_1, ν_2	=	Poisson's ratios
σ_{Mises}	=	Mises equivalent stress
$\sigma_{xx}, \sigma_{yy}, \sigma_{zz}, \tau_{xy}$	=	components of stress
σ_Y	=	yield strength in simple tension
τ_Y	=	shear yield strength

4.1 Introduction

Layered metallic, ceramic, and polymeric surfaces are of widespread use in modern mechanical, electronic, magnetic, and optical devices. In electrical connectors in particular, multi-layer metallic surfaces are often used to satisfy multiple functional requirements, such as high electrical conductivity, wettability and solderability, corrosion resistance, and wear resistance [1]. For example, an electroplated thin gold coating on copper, or a copper-alloy substrtate, with a nickel interlayer is the typical structure for low-voltage, low-current electrical contacts. In designing these multi-layer contact systems, it is important to have a comprehensive knowledge of the contact stress and strain fields of the layered materials. A detailed knowledge of the magnitude and the distribution of interfacial stresses is also necessary for assessing the mechanical reliability and in the analysis of contact failures of the multi-layer systems.

The contact mechanics of layered materials has been studied for over four decades. Burmister [2] was one of the first to develop the elasticity theory for solving the stress field of a single layer on a half-space under an axisymmetic normal loading. Hannah [3] used an integral equation approach to formulate the line contact problem for a thin elastic layer on a rigid substrate. Analyses of the contact problem of thin and thick elastic layers were also conducted by Aleksandrov [4-6], Miller [7], Meijers [8], and Alblas and Kuipers [9]. Due to the mathematical difficulties in obtaining explicit closed-form expressions for the contact stresses of layered systems, approximate methods were used by several researchers to obtain numerical solutions [10-13]. The contact pressure distribution of layered systems was found to deviate from the Hertzian solution of homogeneous media, depending on the layer thickness and the ratio of elastic moduli of layers. The boundary constraints at the interfaces between layers were also reported to affect the contact pressure distribution. The role of several interface constraints (e.g., zero friction, frictional slip, and perfect bonding between layers and substrates) has also been studied [14-16].

Two kinds of layered contact systems are of special interest: (a) soft or compliant coatings on hard or stiff substrates; (b) hard or stiff coatings on soft or compliant substrates. Conway et al. [17] studied the impact between a rigid sphere

and a thin compliant layer supported on a rigid substrate, and the average stresses through the layer thickness were obtained. Kennedy and Ling [18] studied the elastic-plastic indentation of a single-layer medium using the finite element method. They found that the layer thickness, stiffness of the substrate, and the interface constraints have considerable influences on the contact size, the pressure distribution and the size of plastic zones. Matthewson [19, 20] calculated the elastic stress fields of an indented compliant layer bonded to a rigid substrate for various indenter geometries, and two extreme cases (perfect and zero adhesion between the layer and the substrate) were compared. He concluded that the thickness of the protective layer should be more than 20% of the contact radius and that an incompressible layer material (Poisson's ratio > 0.4) is preferable. Tangena and Hurkx [21] obtained the stress field of an indented thin gold layer on a nickel substrate using the finite element analysis. It was shown that the thinner gold coating is preferable in avoiding yielding of the coating under their given load. Recently Ihara et al. [22] considered the indentation of a thin elastic layer on a rigid substrate using the finite element analysis. They found that the Hertzian solution for a semi-infinite elastic solid holds good if the indentation depth is small compared with the layer thickness.

For a thin stiff layer on a compliant substrate, however, the pressure distribution was found to deviate from the Hertzian distribution considerably [11-13]. Zwaag and Field [23] investigated the axisymmetric indentation of a thin stiff coating on a elastic substrate using the finite element approach. They found that the stresses in the substrate were reduced with stiffer and thicker coatings, but the reduction was accompanied by an increase in the maximum tensile stresses in the coating itself. Komvopoulos [24] considered a rigid cylinder indenting a stiff layer on an elastic substrate, and he found that the plastic deformation in the substrate could be avoided by increasing the ratio of the layer thickness to the half-width of the contact. In an extension of the above work to an elastic-plastic loading, the size and location of plastic zones were found to depend strongly on the layer thickness [25].

Although considerable work has been done on the contact problem of layered systems, most analyses have been conducted for the indentation of a single-layer half-space, the layer being either softer or harder than the substrate. For the multi-

layer contact systems, such as the Au/Ni/Copper structure of the electrical contacts, these analyses are not usually applicable for predicting the stress and the strain fields because both soft and hard layers are involved now. Thus more complex stress fields are expected for the multi-layer systems. Tangena and Wijnhoven [26] conducted a finite element analysis of Au/Ni/Copper multi-layer contacts under axisymmetric loading. The Mises equivalent stress averaged over the contact area and the thickness of the gold coating was correlated with the wear data in the literature. However, the stress and the strain fields, which are important in the analysis of contact failure, were not presented. More importantly, the effect of the interlayer thickness on the stresses and strains at the two interfaces were not addressed.

The objective of the present study, therefore, is to examine the contact stresses and strains due to a rigid cylinder indenting a two-layer half-space in the elastic-plastic (work hardening) regime, in particular for the electric contacts. A plane strain finite element mesh was set up to conduct the stress analysis. The effects of the interlayer thickness on the contact width, pressure distribution, location of initial yielding, and interfacial stresses and strains are examined. The mechanisms of crack initiation at the interfaces and interfacial delamination are also qualitatively addressed.

4.2 Statement of Problem

Consider a rigid cylinder of radius R indenting a two-layer half-space under a normal force per unit length, L. Figure 4.1 illustrates the coordinate system and the dimensions of the two-layer half-space. The thicknesses of the top layer (layer 1) and the interlayer (layer 2) are h_1 and h_2, respectively. The boundary conditions are as follows:

On the contact surface,

$$v(x, 0) \equiv \delta - \frac{x^2}{2R} \qquad |x| \le a \qquad (4.1a)$$

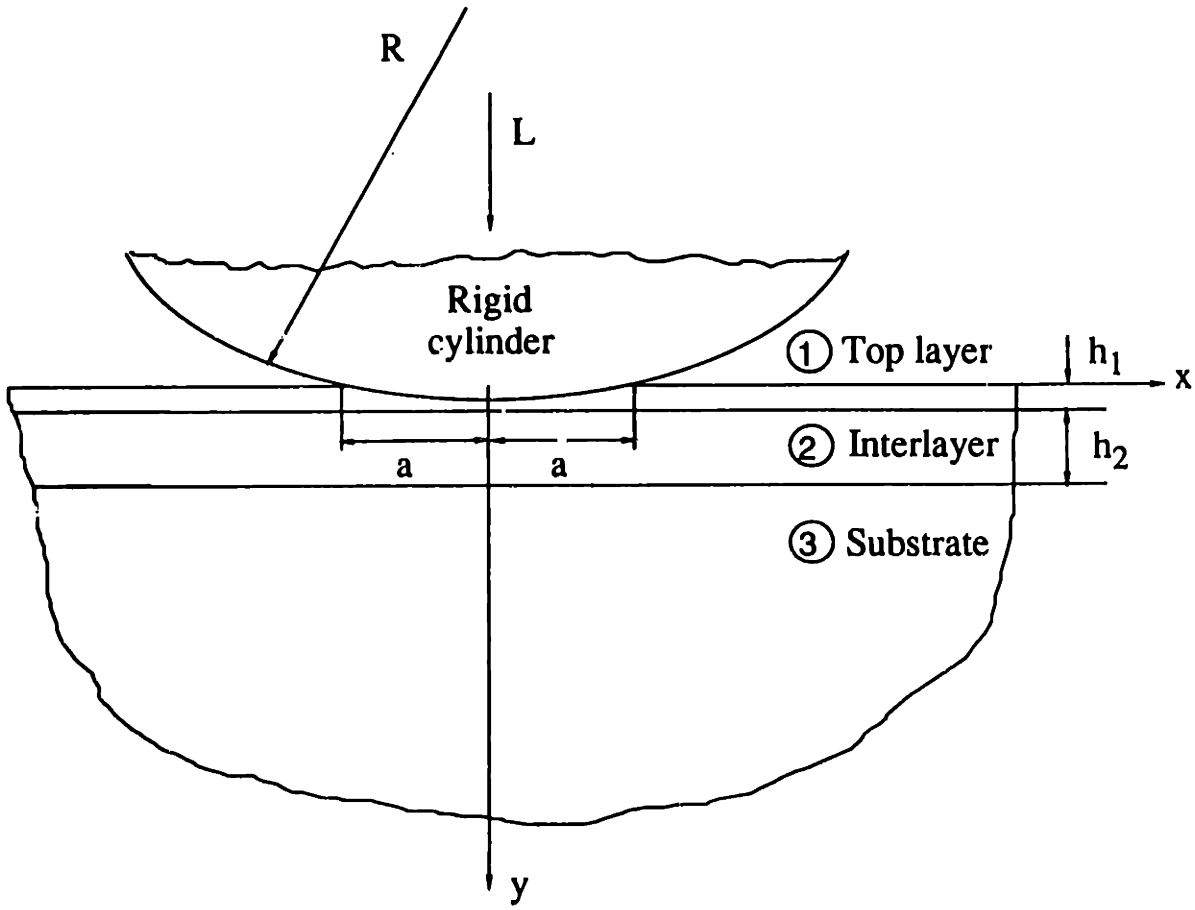

Fig. 4.1 Schematic of a rigid cylinder indenting a two-layer half-space

$$\sigma_{yy}(x, 0) = 0 \qquad |x| > a \qquad (4.1b)$$

$$\tau_{xy}(x, 0) = 0 \qquad -\infty < x < \infty \qquad (4.1c)$$

where a is the half-width of the contact and δ the penetration depth of the indenter. The penetration depth, δ, was assumed to be smaller than the radius of the indenter, R, or the half-width of the contact, a. Perfect bonding is assumed at the interfaces between layers, i.e., displacements across the interfaces are continuous:

$$u^{(1)}(x, h_1) = u^{(2)}(x, h_1) \qquad (4.2a)$$

$$v^{(1)}(x, h_1) = v^{(2)}(x, h_1) \qquad (4.2b)$$

$$u^{(2)}(x, h_1+h_2) = u^{(3)}(x, h_1+h_2) \qquad (4.3a)$$

$$v^{(2)}(x, h_1+h_2) = v^{(3)}(x, h_1+h_2) \qquad (4.3b)$$

$$u = v = 0 \qquad \text{as } x, y \rightarrow \infty \qquad (4.4)$$

where the superscripts 1-3 stand for the top layer, the interlayer, and the substrate, respectively.

The primary emphasis of this study is on the normal contact of multi-layer systems employed in electrical contacts. That is, the top layer is gold which is hardened with 0.5% nickel, the interlayer is nickel, and the substrate is copper or a copper alloy. All materials are assumed to possess a bilinear elastic-plastic behavior (Figure 4.2). The relevant elastic and plastic properties of the layers and the substrate are listed in Table 4.1. These values fall in the typical range of electrical contact materials. Table 4.2 lists the load and geometrical parameters used in the finite element analysis. Indentation under three normal loads, 5, 10 and 20 N/mm, has been chosen for analysis. Since the thickness of the top layer (gold) is more or less fixed in the specifications of electrical contacts, only the thickness of the inter-layer (nickel) is varied in the present study.

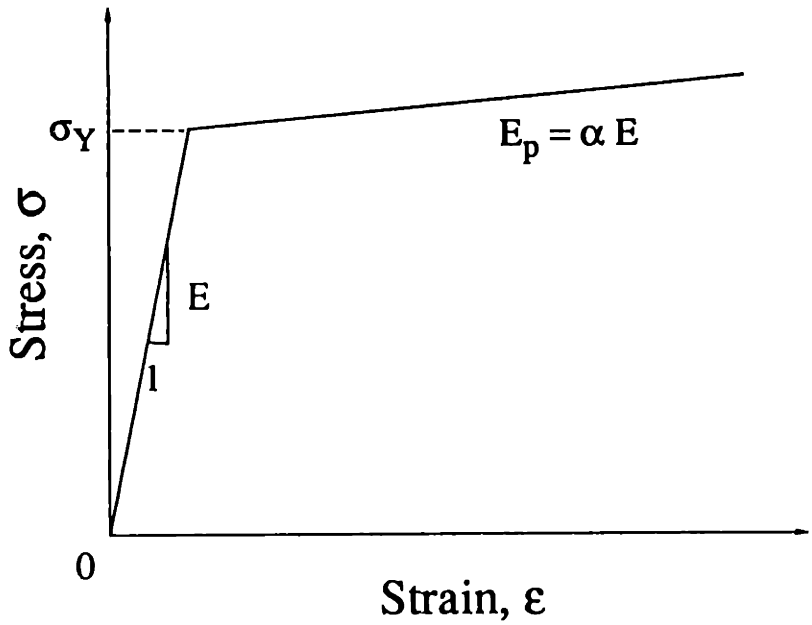

Fig. 4.2 Bilinear elastic-plastic behavior of contact materials

Table 4.1 Mechanical properties of contact materials

Material	E (GPa)	ν	σ_Y (MPa)	α
Top Layer (Au+0.5%Ni)	79	0.32	298	0.1
Interlayer (Ni)	205	0.32	811	0.1
Substrate (Brass: Cu-35%Zn)	125	0.32	405	0.1

Table 4.2 Load and geometrical parameters used in stress analysis

Radius of indenter, R	0.75	mm
Normal load, L	5, 10, 20	N/mm
Thickness of top layer, h_1	1.25	μm
Thickness of interlayer, h_2	0, 1.25 - 20	μm

4.3 The Finite Element Model

To conduct the finite element analysis of indentation of a cylindrical indenter on a two-layer half-space, the semi-infinite dimensions of the half-space are modelled by the two finite lengths along x and y axis, respectively. The dimensions of both the indenter and the indented surface in z-axis are assumed to be infinite, i.e., the indentation is in plain strain. Thus the indentation of the half-space becomes an indentation of a finite block whose dimensions are much larger than the expected contact width. The displacements at the boom plane of the block are far away from the contact and are assumed to be zero. Further more, the indentation now is equivalent to fixing the indenter and moving the bottom plane of the block upward uniformly by a distance equal to the indentation depth.

Figure 4.3a shows the finite element model and the boundary conditions. Because of the loading symmetry, only half of the two-layer half-space was considered. Points in the mid plane (OC) was restricted to move only along the y-direction due to the symmetry. The rigid indenter was fixed at the top. The vertical displacements of points in the bottom plane were assumed to be uniform, but the horizontal displacements at the bottom plane (CB) were not restricted except that of point C. The indentation was applied by a concentrated load at point C of the bottom plane CB. Unlike the displacement-controlled indentation, the load-controlled indentation plus the constraints of uniform vertical displacement at the bottom plane makes it possible to analyze the contact problem at a prescribed normal load. The magnitude of uniform displacements of points in the bottom plane is thus equal to the penetration depth of the indenter, δ.

Figure 4.3b is the whole finite element mesh, and Figure 4.3c the details of the mesh near the contact. The whole mesh is an arrangement of 330 quadrilateral, eight-node, isoparametric elements, and the total number of nodes is 1088. The hori-zontal and vertical dimensions of the mesh are 100 μm and 200 μm, respectively, but being large enough to allow the stresses and the displacements to be insignificant at the boundaries. The mesh was refined in the region below the contact. The horizontal and vertical spacings of nodes on and below the contact surfaces are 0.5 μm and 0.3125 μm, respectively. The two-layer half-space was modelled by assigning different elastic and plastic properties to the elements of top

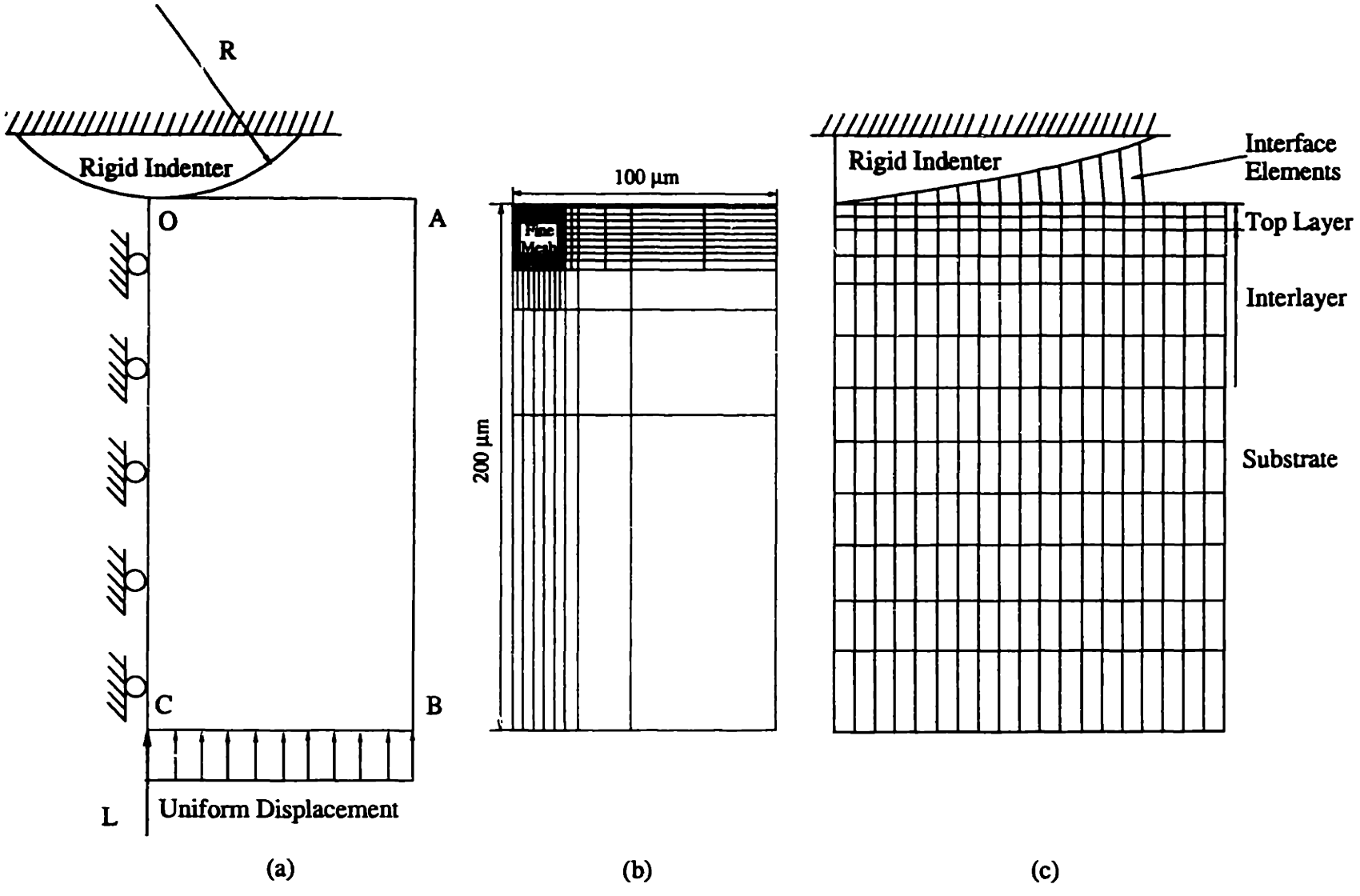

Fig. 4.3 (a) The finite element model and the boundary conditions, (b) the finite element mesh, and (c) the detail of the fine mesh

rows of the mesh. The first two rows were assigned to be the top layer. The rows immediately below the top layer were assigned to the interlayer. The number of rows assigned for the interlayer depends on the layer thickness prescribed. The interfaces between the layers were assumed to be perfectly bonded, i.e., the displacements at the interfaces were continuous (Eqs. 2 and 3). These interface constraints were satisfied by using common nodes at the interfaces, and the common nodes belong to the elements on both sides of the interface. The normal contact between the rigid cylinder and the layered half-space was modelled by 15 three-node interface elements (Figure 4.3c). The initial nodal gaps between the rigid cylinder and the surface of the layered half-space are prescribed by the circumference of the rigid cylinder. The ABAQUS finite element program [27] detects the gap changes and indicates the gap closure in the y-direction. Whenever the closure distance becomes zero at any node, contact is assumed and an external reaction force is exerted on that node; otherwise no force is transferred. The parameter associated with the interface elements, the "friction coefficient", was assumed to be zero.

To obtain a converged solution in a reasonable period of time, the force tolerance was set to 10^{-2} of nodal force at the point O. The maximum number of allowed increments was 20, and the maximum number of allowed iterations in each increment was 6. The magnitude of the initial load increment was 2% of the total load. The maximum magnitude allowed in one increment was 25% of the total load. The ABAQUS program automatically changes the magnitude of the load increment based on converging rate of the solution in the previous increments. The nodal stresses and strains were obtained by extrapolating the values at the integration points, and the integration scheme for the 8-node quadrilateral elements was 3 x 3. The updated total Lagrangian method in the ABAQUS Code was used for both the elastic and the elastic-plastic analyses. This method allows the stiffness matrix used for the current iteration to be constructed based on the previous mesh configuration. The computations were performed on a MicroVax II computer, and the typical CPU time for one run was 60-80 minutes.

To verify whether the boundary conditions and the finite element mesh in Figure 4.3 is a fair representation of a semi-infinite solid, first the indentation of a homogeneous elastic half-space was analyzed. The two layers and the substrate were

assigned the same Young's modulus and Poisson's ratio. The results were compared with the analytical solutions, and the difference between the two solutions was found to be negligible. Thus the present finite element model and mesh are assumed to be an acceptable representation of an elastic half-space.

4.4 Results and Discussion

The results presented here are for a rigid cylinder of radius R (0.75 mm) which is much larger than the expected half contact width, a. The normal loads were 5, 10, and 20 N/mm. The calculated stresses are presented both in the absolute values and in the normalized forms. In the elastic stress analysis of homogeneous media, the stresses are usually normalized by the maximum Hertzian pressure of the contact [28]. In the elastic-plastic regime, however, normalization by such properties as the yield strength or hardness may be more appropriate. Because the stress fields of the multi-layer contact systems cannot be scaled as in the case of elastic homogeneous media, it is not possible to plot the stresses and the strains of multi-layer media in a meaningful normalized form. In the present study, therefore, the stresses are normalized with respect to several quantities such as the center pressure p^*, and the yield strengths of the top layer, $\sigma_{Y,top}$, the interlayer, $\sigma_{Y,int}$, and the substrate, $\sigma_{Y,sub}$, depending on the appropriateness. The positive values indicate tensile stresses and strains, and the negative values compressive stresses and strains.

4.4.1 Contact pressure distribution

In the contact stress analysis, obtaining an accurate pressure distribution is the necessary first step in determining the subsurface stresses and strains. It is well known that when a homogeneous elastic half-space is indented by an elastic or rigid cylinder, an elliptic pressure distribution (Hertzian distribution) is produced. The contact pressure distribution, $\bar{p}$, and the half-width of the contact, a_o, in that case are given by [28]

$$\bar{p}_o = \frac{p}{p_o} = \left[1 - \frac{x^2}{a^2}\right]^{1/2} \tag{4.5a}$$

$$p_o = \frac{2L}{\pi a_o} \tag{4.5b}$$

$$a_o = \left[\frac{4 L R (1-\nu^2)}{\pi E}\right]^{1/2} \tag{4.5c}$$

where L is the normal force per unit length, R the radius of indenter, E the Young's modulus, and ν the Poisson's ratio. When a single-layer half-space is indented by a rigid cylinder, Gupta and Walowit [13] have shown that the contact pressure distribution is quite non-Hertzian for a stiff layer. For a compliant layer, however, the contact pressure distribution falls between parabolic and elliptic distributions; Gupta and Walowit suggested that the pressure distribution, $\bar{p}$, be written as a weighted sum of the elliptic and the parabolic distributions:

$$\bar{p} = \frac{p}{p^*} = C_1 \left[1 - \frac{x^2}{a^2}\right]^{1/2} + C_2 \left[1 - \frac{x^2}{a^2}\right] \tag{4.6}$$

where C_1 and C_2 are constants to be determined, a is half-width of the contact, and p^* the center pressure. In the present case of an elastic-plastic two-layer half-space indented by a rigid cylinder, since both compliant and the stiff layers are involved, the contact pressure distribution is expected to be more complex.

To investigate the role of the interlayer on the contact pressure distribution, a normal load of 5 N/mm was applied so that plastic deformation does not take place in the two-layer half-space. Figure 4.4 shows the pressure distributions of the indented two-layer half-space for various interlayer thicknesses. The pressure was normalized by the center pressure, p^*, and the distance from the contact center by the half contact width, a. The solid line is the elliptic distribution (Hertzian distribution) and the dashed line the parabolic distribution. All the calculated contact pressure data points of the indented two-layer half-space fall between the two distributions. This indicates that the interlayer thickness has only minor effect on the shape of the contact pressure distribution. This also implies that Eq. (6) is a good approximation for the contact pressure distribution of an indented multi-layer medium, provided that the top layer is more compliant than the interlayer and the substrate.

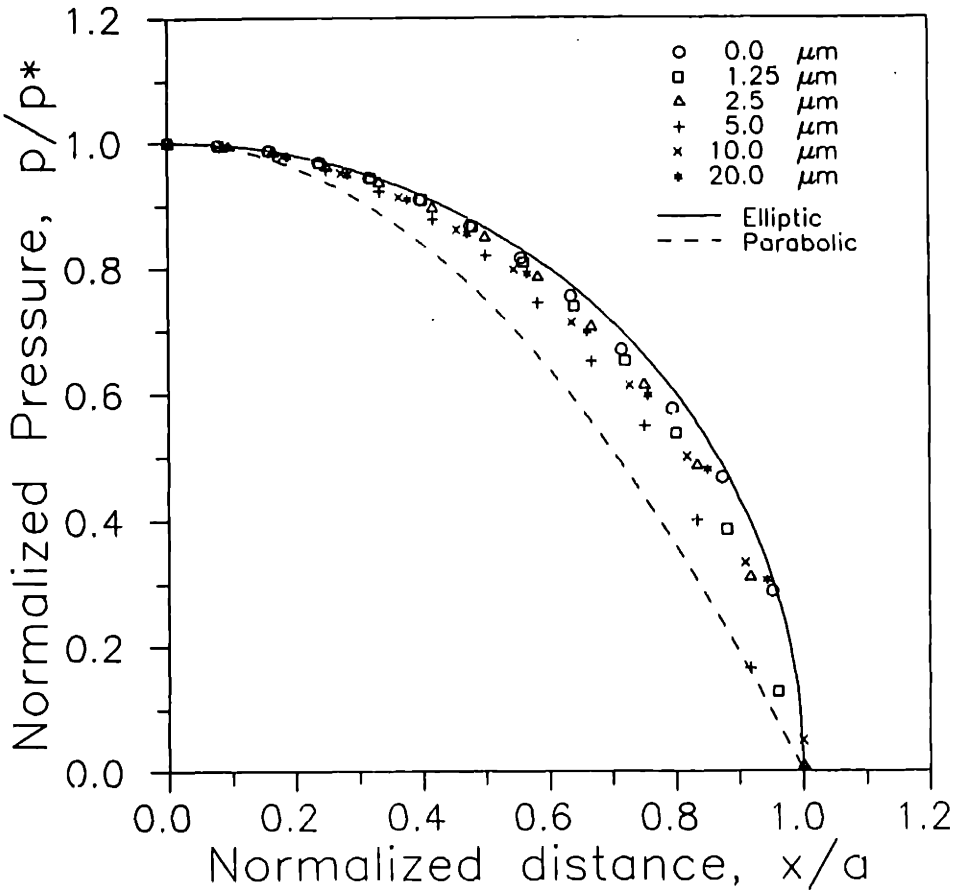

Fig. 4.4 **Normalized elastic contact pressure distributions for various interlayer thicknesses**

As the normal load increases, plastic deformation occurs. In the indentation of homogeneous media, plastic flow leads to a flattened pressure distribution, and the peak pressure moves slightly away from the contact center at higher loads [29]. In the case of a single-stiff-layer half-space also, a similar trend was observed [18]. Figures 4.5a-5f are the contact pressures of the two-layer half-space with various interlayer thicknesses under the three normal loads, 5, 10, and 20 N/mm. The 10 N/mm normal load is large enough to cause plastic deformation for the whole range of the interlayer thickness investigated. Due to the use of interface elements in modelling the contact interface, the increase in the contact width was discontinuous with each loading increment. The contact width could not be precisely determined from the finite element results. Thus the contact width was obtained by elliptically extrapolating the pressure values at the two most outside nodes in contact to the abscissa. When the normal load increases from the elastic loading (5 N/mm) to an elastic-plastic loading (10 N/mm), the center pressure increases and the contact width decreases. Figures 4.5a-5f also show that thicker interlayer produces higher center pressure p* and smaller half-width of the contact when the normal load is 5 and 10 N/mm. When the normal load is 20 N/mm, however, the trend is a little different. The pressure distribution becomes, as expected, flatter at 20 N/mm. As the interlayer thickness, h_2, increases from 0 to 2.5 μm, the center pressure, p*, remains essentially the same and the pressure distributions become more flatter (Figures 4.5a-5c). At h_2=5 μm, the peak pressure moves slightly away from the contact center (Figure 4.5d). At h_2=10, 20 μm, however, the center pressures become much greater and the pressure distributions seem to be back to the shape of the elastic distribution (Figures 4.5e and 5f).

In order to clearly identify to what extent do the contact pressure distributions of the elastic-plastic multi-layer media deviate from the Hertzian elliptic distribution, all the pressure data in Figures 4.5a-5f are replotted in normalized forms in Figures 4.6a-6f. The pressure, p, is normalized by the center pressure, p*, and the distance from the contact center, x, by the corresponding half-width of the contact, a. The dashed curves are the Hertzian elliptic distributions. Under elastic loading (5 N/mm), the pressure distributions are below the elliptic for all interlayer thicknesses (also see Figure 4.4). At 10 N/mm normal load, the pressure distribu-

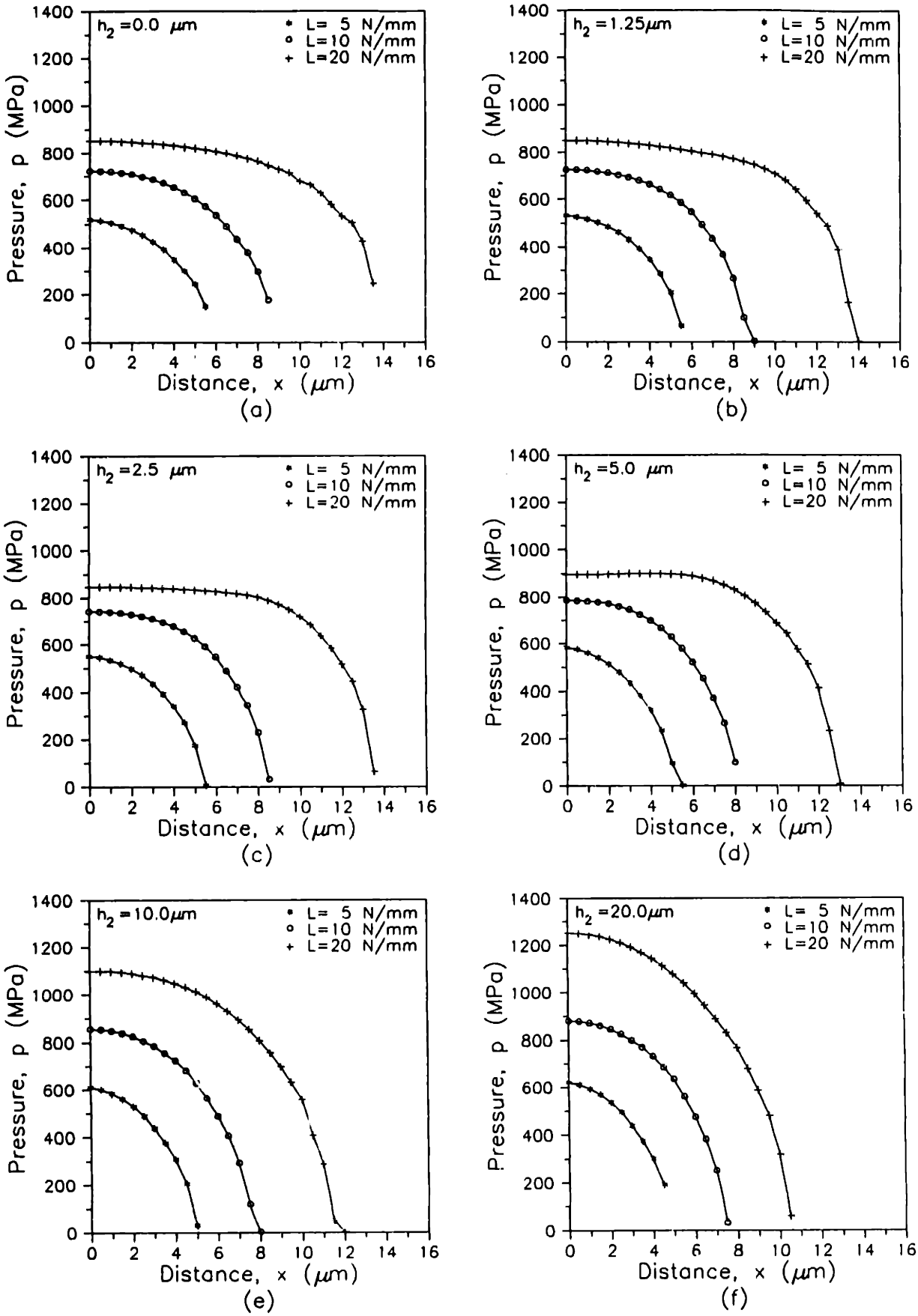

Fig. 4.5 Contact pressure distributions for various interlayer thicknesses under elastic and elastic-plastic loadings

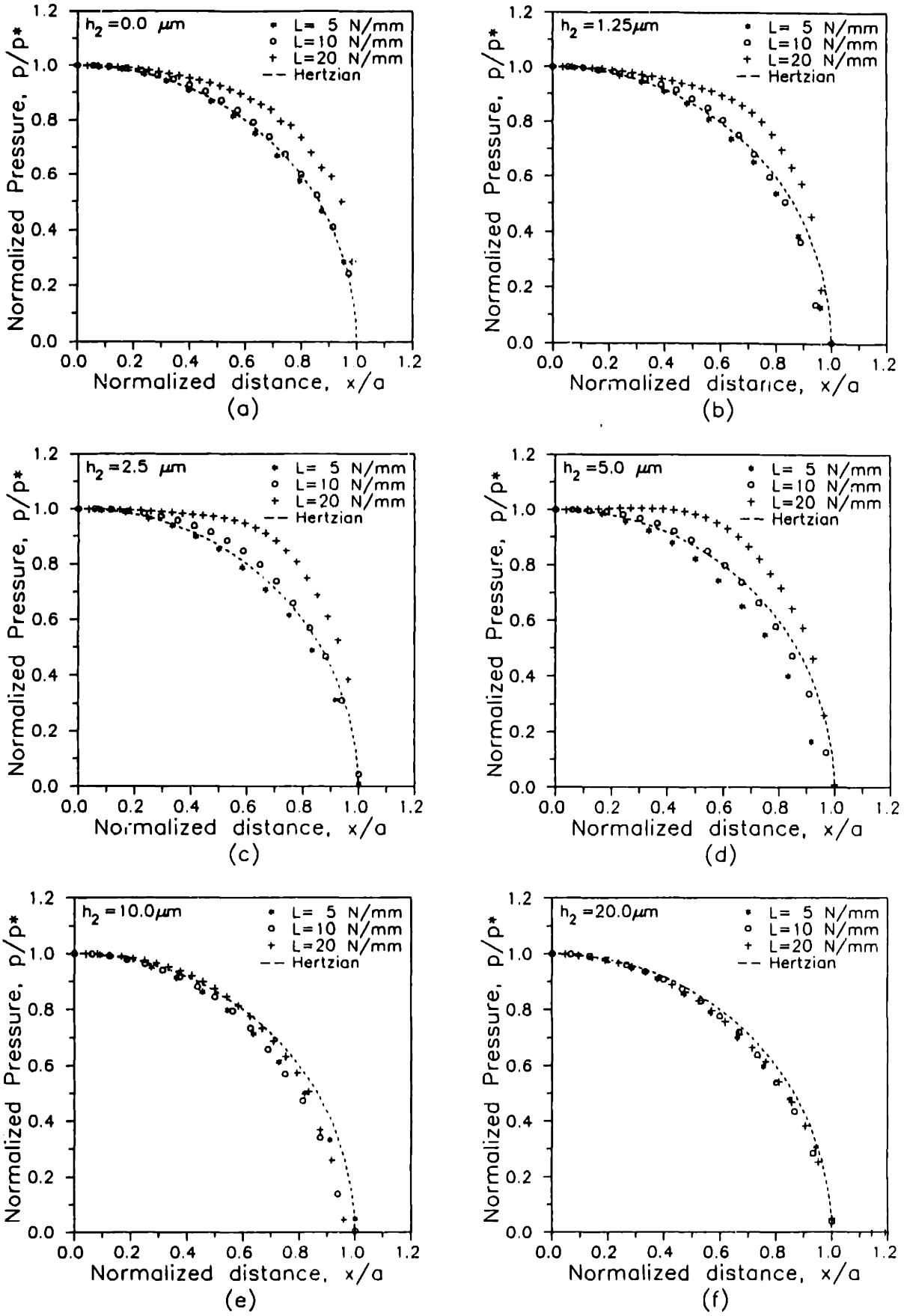

Fig. 4.6 Normalized contact pressure distributions for various interlayer thicknesses under elastic and elastic-plastic loadings

tions are also very close to the elliptic distributions, though slightly above the ellipse when $h_2 \leq 5$ μm and below when $h_2>5$μm. At 20 N/mm normal load, however, the pressure distributions considerably deviate from the elliptic distribution when $h_2 \leq 5$ μm. When $h_2>5$ μm, the pressure distributions under all three normal loads are surprisingly very close to but below the elliptic distribution (Figures 4.6e and 4.6f).

It is apparent thus that under an elastic loading, the contact pressure distributions of the indented multi-layer media with a compliant top layer are bounded by the parabolic and elliptic distributions. The interlayer thickness has insignificant effect on the shape of the pressure distributions, but the thicker interlayer produces a greater center pressure and a smaller contact width. For the elastic-plastic loadings, the contact pressure distribution tends to be flatter compared with the elliptic distribution. The interlayer thickness seems to have a dual effect on the pressure distribution. The pressure distribution becomes flatter as h_2 increases from 0 to 5 μm. For $h_2>5$ μm, however, the pressure distribution more or less falls in the Hertzian elliptic distribution. Thus the contact pressure distribution is influenced by plastic deformation which in turn is affected by the interlayer thickness.

4.4.2 Initiation of yielding

The onset of plastic deformation often induces other types of contact failure. Thus it is important to locate where and when yielding initiates. It is well known from the Hertzian analysis that yielding initiates in the subsurface region of a homogeneous elastic half-space, at roughly y=0.70a below the contact center. In the case of an indented multi-layer medium, however, the location of initial yielding needs to be determined. Yielding occurs when the Mises equivalent stress, σ_{Mises}, is equal to the yield strength in simple tension, σ_Y. In plane strain, σ_{Mises}, is given by

$$\sigma_{Mises} = \frac{1}{\sqrt{2}}\left[(\sigma_{xx} - \sigma_{yy})^2 + (\sigma_{yy} - \sigma_{zz})^2 + (\sigma_{zz} - \sigma_{xx})^2 + 6\tau_{xy}^2\right]^{1/2} \qquad (4.7)$$

Figures 4.7a-7f are the contours of the Mises equivalent stress and the equivalent total plastic strain for various interlayer thicknesses under the 10 N/mm normal load. The total plastic strain is the accumulated plastic strain from each loading increment. Only the stress and plastic strain contours in the region near the

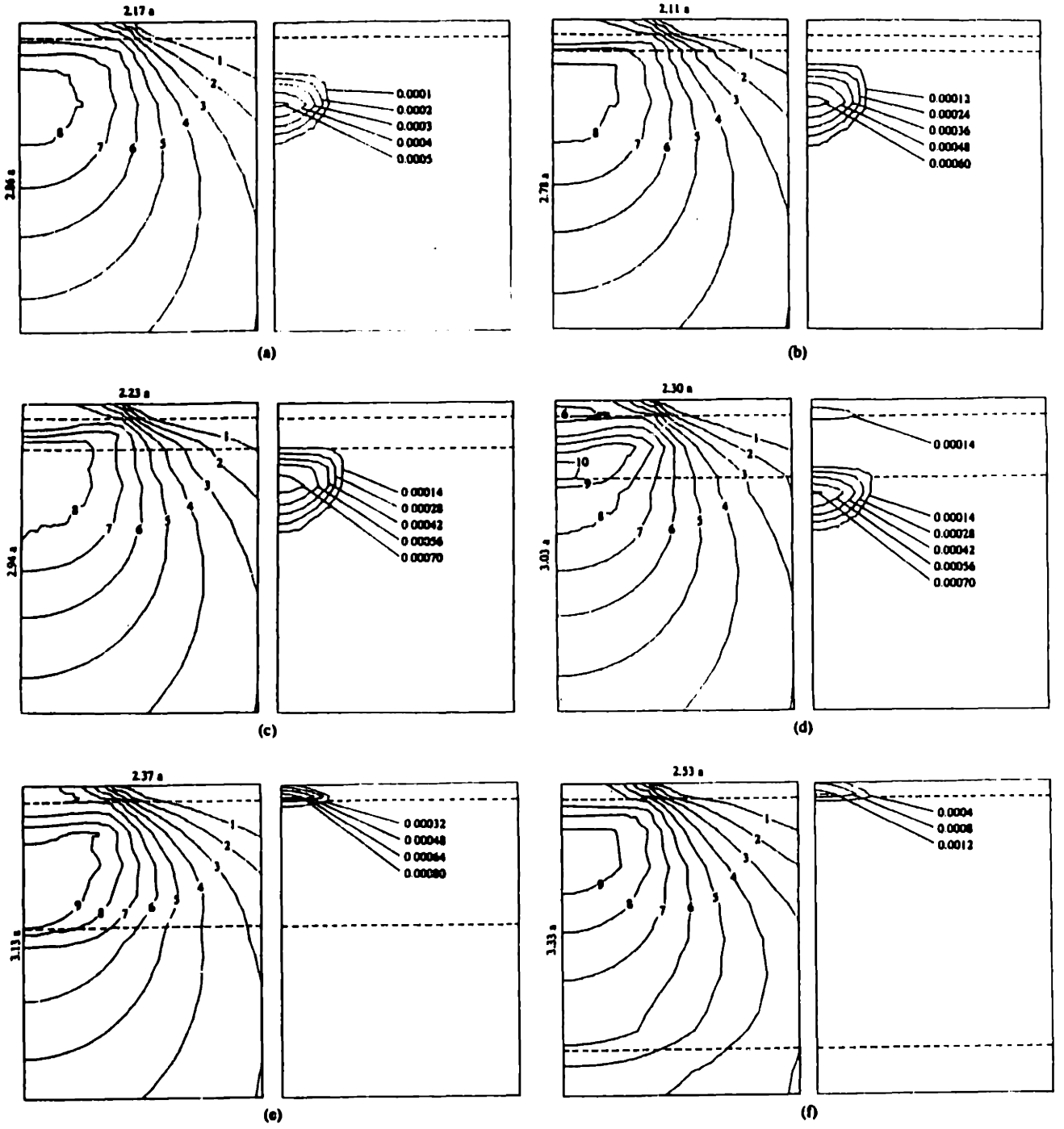

Fig. 4.7 Mises equivalent stress and equivalent total plastic strain contours: (a) h_2=0 μm, (b) h_2=1.25 μm, (c) h_2=2.5 μm, (d) h_2=5 μm, (e) h_2=10 μm, and (f) h_2=20 μm. Mises stress contour numbers: 1--50 Mpa, 2--100 MPa, 3--150 MPa, 4--200 MPa, 5--250 MPa, 6--300 MPa, 7--350 MPa, 8--400 MPa, 9--450 MPa, 10--500 MPa. Load=10 N/mm.

contact center are plotted for clarity. The horizontal dashed lines in the plots represent the approximate locations of the interfaces between layers. For a soft thin layer bonded to the substrate without the interlayer (Figure 4.7a, h_1=1.25 μm, h_2=0), yielding initiates in the substrate at roughly the same location predicted by the elastic analysis for a homogeneous half-space. The plastic zone is fully contained by material which still remains elastic so that the equivalent total plastic strain (0.05%) is of the same order of magnitude as the surrounding elastic strains.

As a thin and hard layer is introduced between the top layer and the substrate (Figure 4.7b, h_1=1.25 μm, h_2=1.25 μm), the plastic deformation still initiates in the substrate, at roughly the same location as before. The plastic zone size is slightly larger, and the equivalent total plastic strain is also slightly greater. As the interlayer thickness is increased to 2.5 μm, yielding initiates still in the substrate and the plastic zone expands in all directions (Figure 4.7c). The growth of the plastic zone, however, is blocked by the hard interlayer, and thus only one side of the interlayer-substrate interface is in plastic regime. The maximum equivalent plastic strain is larger compared with the previous cases in Figures 4.7a and 4.7b. So far it is apparent that the location of initial yielding is independent of the interlayer thickness, but the growth of plastic zone and the extent of plastic deformation are slightly greater as the interlayer thickness increases.

Further increase in the interlayer thickness, however, shows a different trend. When h_2=5 μm, two plastic zones are initiated, one in the top layer and another in the substrate (Figure 4.7d). The location of initial yielding in the substrate is slightly farther from the contact center, but closer to the interlayer-substrate interface. The other plastic zone begins at the interface between the top layer and the interlayer, and expands toward the contact surface. However, the plastic zone has not broken out to the contact surface and the contact is in the "contained" mode of plastic indentation [29]. The interlayer which separates the two plastic zones is still stressed in the elastic regime. (Figure 4.7d shows that the equivalent total plastic strain contours have expanded into the interlayer, but a careful check on each element showed no plastic deformation in the interlayer. These plastic strain contours were directly called from the ABAQUS program, and the reason why the equivalent total plastic strain contours penetrate the interlayer is

possibly due to the extrapolation scheme used in contour calculations.) As the interlayer thickness increases further to 10 μm, yielding initiates only at the top layer-interlayer interface (interface 1-2), and no plastic deformation takes place in the substrate (Figure 4.7e). The plastic zone does not expand downwards, but expands to the contact surface. The contact becomes an "uncontained" plastic indentation. The size of the plastic zone is relatively small, but the equivalent total plastic strains are relatively large. It should be noted that the Mises equivalent stress on the substrate side at the interlayer-substrate interface is still very close to the yield strength of the substrate. When the interlayer thickness is increased to 20 μm, the plastic zone initiates at the top layer-interlayer interface and the total equivalent plastic strain becomes greater due to the uncontained surface (Figure 4.7f). The Mises equivalent stress at the interlayer-substrate interface, however, is reduced considerably.

Table 4.3 lists the indentation depth, contact half-width, and the deformation mode under different normal loads. As expected, deeper indentation is obtained with the higher normal load. The indentation depth decreases with the interlayer thickness due to increase in the stiffness of the multi-layer media. At 20 N/mm normal load, the plastic deformation in the top layer has expanded to the contact surface for all values of interlayer thicknesses. Plastic zone initiates at the interlayer-substrate interface for all interlayer thicknesses except for h_2=20 μm. The interlayer has a relatively higher yield strength, but plastic zone has even expanded to the interlayer near the interlayer-substrate interface when the interlayer thickness is in the middle range (h_2=5 μm and 10 μm). Only when the interlayer is sufficiently thick (h_2=20 μm), plastic deformation occurs only in the top layer while both the interlayer and the substrate are in the elastic regime.

It is apparent from the above results that the interlayer thickness has different effects on the location where yielding initiates. Yielding initiates in the substrate when the interlayer thickness is small, and in the top layer when the interlayer thickness is large. Generally it is undesirable for one of the materials at the interfaces to be in the plastic regime, especially at the interlayer-substrate interface. Under cyclic loading, plastic deformation can accumulate to cause the interface failure or interfacial delamination if the interfacial bonding is not strong enough.

Table 4.3: Deformation mode of the two-layer half-space under different loads

Normal Load (N/mm)	Interlayer Thickness (h_2, μm)	Half-Width of the Contact (a, μm)	Indentation Depth (δ, μm)	Mode of Deformation* Top layer	Interlayer	Substrate
5	0.00	5.75	0.1081	E	---	E
	1.25	5.6	0.1069	E	E	E
	2.50	5.5	0.1058	E	E	E
	5.00	5.5	0.1034	E	E	E
	10.00	5.0	0.0992	E	E	E
	20.00	4.75	0.0933	E	E	E
10	0.00	8.75	0.1992	E	---	E-P
	1.25	9.0	0.1977	E	E	E-P
	2.50	8.5	0.1963	E	E	E-P
	5.00	8.25	0.1932	E-P	E	E-P
	10.00	8.0	0.1857	E-P	E	E
	20.00	7.5	0.1747	E-P	E	E
20	0.00	13.75	0.3830	E-P	---	E-P
	1.25	14.0	0.3812	E-P	E	E-P
	2.50	13.5	0.3794	E-P	E	E-P
	5.00	13.0	0.3740	E-P	E-P**	E-P
	10.00	12.0	0.3562	E-P	E-P**	E-P
	20.00	10.5	0.3266	E-P	E	E

* E = Elastic deformation; E-P = Elastic-Plastic deformation.

** The plastic deformation of the interlayer takes place near the interlayer-substrate interface.

Therefore if the thickness of top layer is fixed, the interlayer thickness must be so chosen that plastic deformation does not reach the interlayer-substrate interface under the designated normal load. However, for the thicker interlayer, the plastic zone initiates at the top layer-interlayer interface and expands toward the contact surface. Failure may then occur at the interface between the top layer and the interlayer.

4.4.3 Stresses along the loading axis

The subsurface stresses along the loading axis (y-direction) are presented in Figures 4.8a-8f for various interlayer thicknesses. In plane strain, the shear stresses τ_{xz} and τ_{yz} are zero everywhere, and τ_{xy} is zero along the loading axis due to the loading symmetry. Thus the stresses σ_{xx}, σ_{yy}, and σ_{zz} are principal stresses along the loading axis. The vertical distance below the contact, y, is normalized by the half-width of the contact, a, and the stresses by the center contact pressure, p*. The Mises equivalent stress, σ_{Mises}, is also plotted along the loading axis. The Mises equivalent stress is normalized in each region by the local yield strength, i.e., the yield strength of the corresponding material. Since the maximum Mises equivalent stress is on the loading axis, the initiation of yielding can also be examined from the plots of the Mises equivalent stress along the loading axis: whenever $\sigma_{Mises}/\sigma_Y \geq 1$, yielding initiates.

The elastic analysis of a homogeneous elastic half-space indented by a rigid cylinder shows that σ_{xx} is equal to σ_{yy} on the contact surface (y=0) [28]. Figures 4.8a-8f show, however, that for the indentation of a layered half-space, the magnitude of the stress σ_{xx} on the contact surface (y=0) is smaller than the normal stress σ_{yy}. As y/a increases, all the subsurface stresses decrease as they should. The normal stress σ_{yy} is compressive all along the loading axis for any interlayer thickness, and is continuous across the top layer-interlayer and interlayer-substrate interfaces. σ_{xx} and σ_{zz}, however, are discontinuous across the interfaces because of different elastic moduli and the displacement continuity constraint at the interfaces. Thus all these discontinuities in Figures 4.8a-8f mark the location of the interfaces between layers. The magnitude of stress jumps first increases with the interlayer

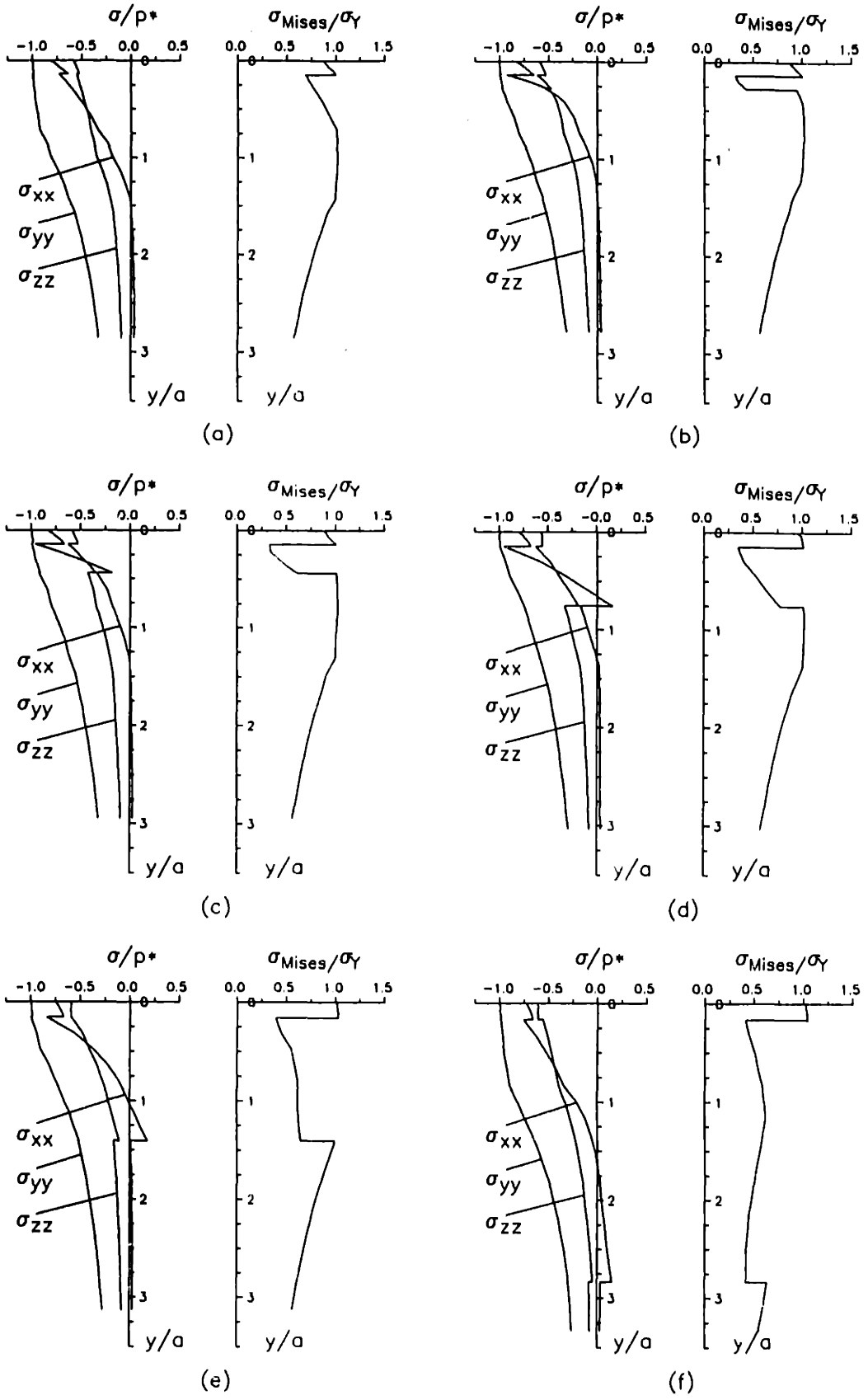

Fig. 4.8 Stresses along the loading axis: (a) h_2=0 μm, (b) h_2=1.25 μm, (c) h_2=2.5 μm, (d) h_2=5 μm, (e) h_2=10 μm, and (f) h_2=20 μm. Load=10 N/mm.

thickness and then decreases. When h_2=5 μm, the stress jumps reach their maxi--mums at both interfaces (Figure 4.8d).

Tensile stresses are the most undesirable stresses since they may promote crack nucleation and crack propagation. Since the normal stress σ_{yy} is compressive all along the loading axis, it is unlikely that the tensile interfacial cracks initiate or propagate along the interfaces. If a large tensile σ_{xx} exists at the interfaces, however, it may promote the growth of interface cracks into the layers. Figures 4.8d-8f show that tensile σ_{xx} stress indeed exists in the interlayer near the inter-layer-substrate interface when the interlayer thickness is larger than 5 μm. However, these tensile stresses are relatively small, about 20% of the center pressure. Whether this much tensile stress has any effect on the interfacial failure needs further investigation.

4.4.4 Interfacial stresses

The magnitude and the distribution of subsurface stresses along the interfaces are of great importance in multi-layer systems. For the layers to remain bonded to the substrates, adhesion between the layers should be strong enough to resist the tensile or shear stresses. The effect of the interlayer thickness on the interfacial stresses are presented for only three interlayer thicknesses (h_2=1.25, 5, and 20 μm) under the normal load 10 N/mm. Figures 4.9a-9c show the interfacial stresses along the top layer-interlayer interface, and Figures 4.9d-9f along the interlayer-substrate interface. The normal interfacial stresses are normalized by the yield strength of the top layer for the stresses at the top layer-interlayer interface, and by the yield strength of the substrate for the stresses at the interlayer-substrate interface. The shear stresses are normalized by the shear yield strength, τ_Y, ($\tau_Y=\sigma_Y/\sqrt{3}$). Because σ_{xx} is discontinuous across the interfaces, two sets of σ_{xx} curves appear in Figures 4.9a and 4.9d. The solid lines are for the stresses in the top layer and the substrate, where as the dashed lines are for the stresses in the interlayer.

Figure 4.9a shows that σ_{xx} is maximum (compressive) below the contact center (x=0), and becomes smaller along the interface, and is tensile at about x/a>1.5. The magnitude of σ_{xx} in the top layer is smaller than that in the interlayer. And σ_{xx} increases with the interlayer thickness. The magnitude of σ_{yy} also

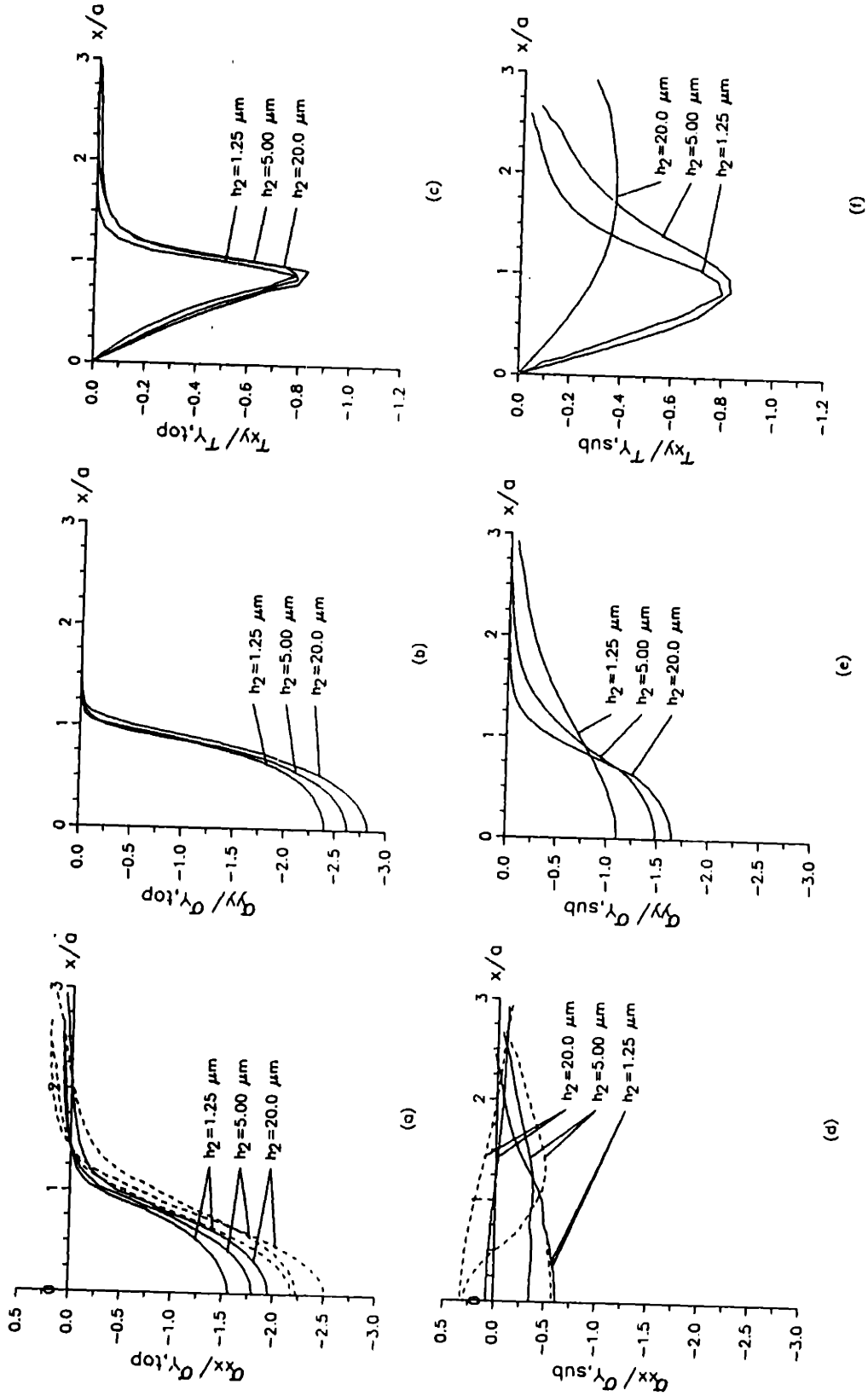

Fig. 4.9 Normalized stresses σ_{xx}, σ_{yy}, and τ_{xy} along the top layer-interlayer (a-c), and along the interlayer-substrate interface (d-f). Load=10 N/mm, h_2=1.25, 5, and 20 μm.

increases with the interlayer thickness and is compressive all along the interface (Figure 4.9b). The interfacial shear stress, τ_{xy}, is zero directly below the contact center, and is maximum at a distance from the center plane (around x/a=1). τ_{xy} increases only slightly with the interlayer thickness (Figure 4.9c).

At the interlayer-substrate interface (Figure 4.9d-9f), σ_{xx} is compressive along the interface when the interlayer thickness is 1.25 μm. For a thick interlayer (h_2=5 μm), σ_{xx} in the interlayer is tensile near x/a=0, while σ_{xx} in the substrate remains compressive. For a very thick interlayer (h_2=20 μm), σ_{xx} is tensile in the interlayer and in the substrate . Figure 4.9e shows normal stress, σ_{yy}, along the interface. It becomes smaller as the interlayer thickness increases because the thicker interlayer pushes the interface away from the contact. The magnitude and the position of the maximum interfacial shear stress, τ_{xy}, depend strongly on the interlayer thickness (Figure 4.9f). As the interlayer thickness increases from 1.25 μm to 5 μm, the magnitude of shear stress increases. When the interlayer thickness is 20 μm, however, τ_{xy} is reduced considerably and the maximum shear stress is also located roughly at x/a >1.

4.4.5 Interfacial strains

In the traditional analyses of contact problems, the focus has been usually on the stress field, and the strain field has not received much attention. In the contact mechanics of layered media, however, the strain field, especially the interfacial strains, is important in determining the initiation and propagation of interface cracks. Moreover, unlike the dimensionless stresses, strain being a dimensionless number requires no normalization by arbitrarily chosen parameters. Figures 4.10a-10f are the interfacial strains for three interlayer thicknesses at 10 N/mm normal load. The strains at the interface of the top layer and the interlayer are presented in Figures 4.10a-10c, and the strains at the interlayer-substrate interface in Figures 4.10d-10f. The x-component of strain, ε_{xx}, is continuous across the interfaces, while the normal strain, ε_{yy}, and the shear strain, ε_{xy}, are discontinuous across the interfaces. Thus two interfacial strain curves are plotted for ε_{yy} and ε_{xy}. The solid lines represent the interfacial strains in the top layer or in the substrate. The dashed lines are for the interfacial strains in the interlayer.

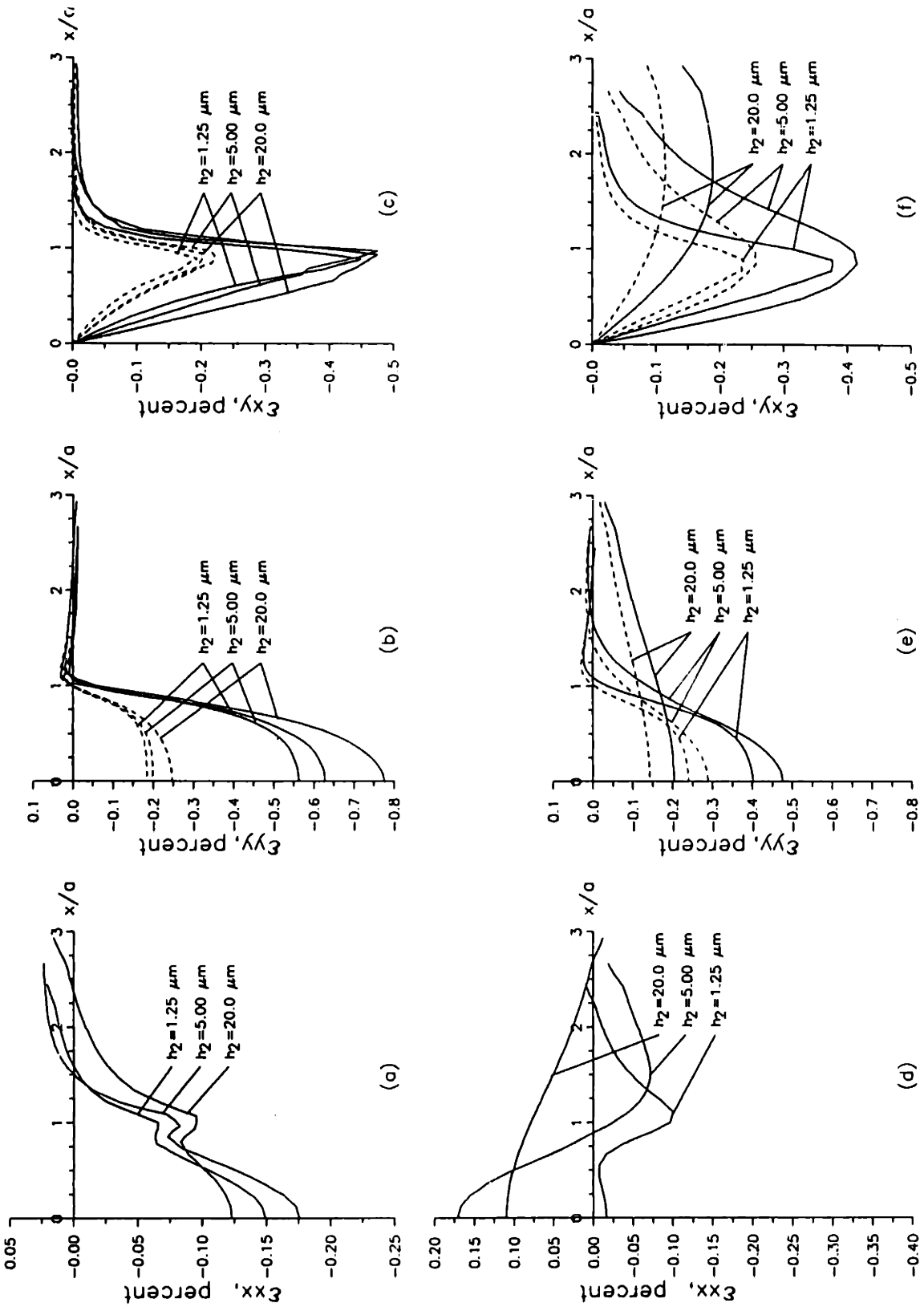

Fig. 4.10 Strains ε_{xx}, ε_{yy}, and ε_{xy} along the top layer-interlayer (a-c), and along the interlayer-substrate interface (d-f). Load=10 N/mm, h_2=1.25, 5, and 20 μm.

Along the top layer-interlayer interface, ε_{xx} is mostly compressive and becomes tensile as x/a increases (Figure 4.10a). The magnitude of ε_{xx} increases with the interlayer thickness. Figure 4.10b shows that the normal strain ε_{yy} is also compressive along the interface except near x/a=1. The magnitude of ε_{yy} experienced by the top layer is much larger than that of the interlayer. The magnitude of ε_{yy} increases with the interlayer thickness. It should be noted that small tensile ε_{yy} strains are found just outside x/a=1 for both the top layer and the interlayer, though the normal stress σ_{yy} is compressive all along the interface (Figure 4.9b). The interfacial shear strain, ε_{xy}, is zero at x/a=0 and reaches its maximum value at about x/a=1 (Figure 4.10c), which corresponds the location of the maximum shear stress in Figure 4.9c. The magnitude of ε_{xy} in the top layer is also much greater than that in the interlayer. It seems that the interlayer thickness has little effect on the location and magnitude of the maximum interfacial shear strains.

However, the interlayer thickness has significant effect on strains at the interlayer-substrate interface. When the interlayer is thin (h_2=1.25 μm), ε_{xx} is small and compressive along the interface (Figure 4.10d); the normal strain ε_{yy} is compressive and becomes tensile at x/a>1 (Figure 4.10e); and the shear strain ε_{xy} reaches its maximum near x/a=1 (Figure 4.10f). For h_2=5 μm, however, larger tensile ε_{xx} is found at x/a=0, and ε_{xx} remains tensile until x/a≈1. The magnitudes of the normal and shear strains, ε_{yy} and ε_{xy}, are also greater than those when h_2=1.25 μm. But for a very thick interlayer (h_2=20μm), the interface is far away from the contact spot, and the magnitudes of all interfacial strains are reduced considerably.

4.4.6 Implications for interfacial fracture

In the present finite element analysis, the interfacial bonding was assumed to be infinitely strong, which is unlikely in reality. When sufficient stresses and strains are developed at interfaces, localized microfracture or initiation of cracks will eventually take place. The criteria for initiation of interfacial cracks have been developed over a few decades. Such criteria include the energy criterion, the local strain criterion, and the local stress criterion. Gurland and Plateau [30] proposed that cracks form when the strain energy released upon decohesion becomes comparable with the surface energy of newly formed crack surfaces. McClintock [31]

suggested a critical local strain criterion, which states that a critical shear strain has to be reached before the initiation of a crack. Merwin and Johnson [32] analyzed the strain filed of an elastic-perfectly plastic half-space in rolling contact, and they found that the plastic shear strain is accumulated with repeated passages of the load. Jahanmir and Suh [33] related the accumulation of plastic shear strain to the void nucleation in sliding contacts. In the layered media also, an interface crack may initiate if the plastic shear strain at the interface is beyond a critical value. Argon and Safoglu [34] proposed that cracks initiate when the interfacial tensile stress reaches the interface bond strength. In the compression-dominated contact problems, however, the local tensile stress criterion seems unsuitable. The local shear strain or stress criterion, however, is more relevant. If the bond strength of interfaces is less than the shear stress needed to maintain displacement compatibility along the interface, debonding or microcracking will occur.

All these criteria for interfacial cracking suggest that material compatibility should be considered in designing the multi-layer systems, and that the interfacial tensile stresses are undesirable. Moreover, the interfacial shear stresses and strains should be kept as small as possible. From the foregoing analysis and results it may be concluded that the intermediate thickness of the interlayer (h_2=5 μm) is undesirable, because plastic deformation initiates at both interfaces and the interfacial shear stress and strain are also greater than those of other interlayer thicknesses.

The stress and the strain fields of indented multi-layer media, unfortunately, cannot be generalized in a concise and elegant form as in the Hertzian elastic contact of homogeneous media. Thus the results obtained here may not be strictly valid for other combinations of multi-layer contact systems. Additionally, in the multi-layer contact systems, especially the electroplated layers, residual stresses, porosity, pin holes, and other microstructural defects may exist in the layers or at the interfaces. These factors obviously affect contact stresses and initiation of cracks. Also, the defects or weakly bonded areas at the interfaces can be treated as pre-existing interface cracks. These aspects as well as the role of friction in the multi-layer contacts need to be explored.

4.5 Conclusions

A finite element analysis of a rigid cylinder indenting an elastic-plastic two-layer half-space was conducted. The following conclusions can be drawn from the analysis.

(a) For elastic loading, the contact pressure distributions of indented multi-layer media with a soft top layer and a hard interlayer are bounded by parabolic and elliptic distributions. The pressure distribution is flatter and the peak pressure moves slightly away from the contact center under high elastic-plastic loadings. Higher center pressure and smaller contact width are obtained with thicker interlayers.

(b) The location of initial yielding strongly depends on the interlayer thickness. Plastic deformation initiates in the substrate when a thin, hard interlayer is used. As the interlayer thickness increases, both the top layer and the substrate are subjected to plastic deformation. For very thick interlayer, however, only the top layer deforms plastically.

(c) Stress discontinuities occur at the interfaces since perfect bonding between layers is assumed. The maximum stress jumps are obtained for an intermediate thickness of the interlayer.

(d) Interfacial stresses and strains at the top layer-interlayer interface are not greatly affected by the interlayer thickness. At the interlayer-substrate interface, however, the highest shear stress and strains are produced when the interlayer thickness is of intermediate value.

References

[1] *Principles of Electronic Packaging*, Ed. by D. P. Seraphim, R. Lasky, and C-Y, Li, McGraw-Hill, Inc., New York, 1989.

[2] Burmister, D. M., "The General Theory of Stresses and Displacements in Layered Systems. I, II, III," *J. of Appl. Phys.*, Vol. 16, 1945, pp. 89-94, 126-127, 296-303.

[3] Hannah, M., "Contact Stress and Deformation in a Thin Elastic Layer," *Quart. J. Mech. and Appl. Math.*, Vol. 4, 1951, pp. 94-105.

[4] Aleksandrov, V. M., "On the Approximate Solution of a Certain Type of Integral Equation," *Prikl. Math. Mekh.*, Vol. 26, 1962, pp. 1410-1424 (in English translation).

[5] Aleksandrov, V. M., "On the Solution of Certain Problems of the Theory of Elasticity," *Ibid.*, Vol. 27, 1963, pp. 1490-1494 (in English translation).

[6] Aleksandrov, V. M., "Asymptotic Solution of the Contact Problem for a Thin Layer," *Ibid.*, Vol.33, 1969, pp. 61-73 (in English translation).

[7] Miller, R. D. W., "Some Effects of Compressibility on the Indentation of a Thin Elastic Layer by a Smooth Rigid Cylinder," *Appl. Sci. Res.*, Vol 16, 1966, pp. 405-424.

[8] Meijers, P., "The Contact Problem of Rigid Cylinder on an Elastic Layer," *Appl. Sci. Res.*, Vol. 18, 1968, pp. 353-383.

[9] Alblas, J. B. and Kuipers, M., "On the Two Dimensional Problem of a Cylindrical Stamp Pressed onto a Thin Elastic Layer," *Acta Mechanica*, Vol. 9, 1970, pp. 292-311.

[10] Chen, W. T., "Computation of Stresses and Displacements in a Layered Elastic Medium," *Int. J. of Eng. Science*, Vol. 9, 1971, pp. 775-799.

[11] Chen, W. T. and Engel , P., "Impact and Contact Stress Analysis in Multilayered Media," *Int. J. of Solids Structures*, Vol. 8, 1972, pp. 1257-1281.

[12] Gupta, P. K., Walowit, J. A., and Finkin, E. F., "Stress Distributions in Plane Strain Layered Elastic Solids Subjected to Arbitrary Boundary Loading," *Trans. ASME, J. of Lubrication Technology*, Vol. 95, 1973, pp. 427-433.

[13] Gupta, P. K. and Walowit, J. A., "Contact Stresses Between an Elastic Cylinder and a Layered Elastic Solid," *Trans. ASME, J. of Lubrication Technology*, Vol. 96, 1974, pp. 250-257.

[14] Pao, Y. C., Wu, T.-S., and Chiu, Y. P., "Bounds on the Maximum Contact Stress of an Indented Elastic Layer," *J. of Applied Mechanics*, Vol. 38, 1971, pp. 608-614.

[15] Ratwani, M. and Erdogan, F., "On the Plane Contact Problem for a Frictionless Elastic Layer," *Int. J. Solids Structures*, Vol. 9, 1973, pp. 921-936.

[16] Schmueser, D., Comninou, M., and Dundurs, J., "Frictional Slip Between Layer and Substrate," *J. Engin. Mech. Div., ASCE*, Vol. 107, 1981, pp. 1103-1118.

[17] Conway, H. D., Lee, H. C. and Bayer, R. G., "The Impact Between a Rigid Sphere and a Thin Layer," *J. Appl. Mech.*, Vol. 37, 1970, pp. 159-162.

[18] Kennedy, F. E. and Ling, F. F., "Elasto-Plastic Indentation of a Layered Medium," *J. Eng. Mat. Tech.*, Vol. 96, 1974, pp. 97-103.

[19] Matthewson, M. J., "Axi-symmetric Contact on Thin Compliant Coatings," *J. Mech. Phys. Solid*, Vol. 29, 1981, pp. 89-113.

[20] Matthewson, M. J., "The Effect of a Thin Compliant Protective Coating on Hertzian Contact Stresses," *J. Phys. D. Appl. Phys.*, Vol. 15, 1982, pp. 237-249.

[21] Tangena, A. G. and Hurkx, G. A. M., "Calculations of Mechanical Stresses in Electrical Contact Situations," *IEEE Trans. on Components, Hybrids, and Manufacturing Technology*, Vol. CHMT-8 (1), 1985, pp. 13-20.

[22] Ihara, T., Shaw, M. C. and Bhushan, B., "A Finite Element Analysis of Contact Stress and Strain in an Elastic Film on a Rigid Substrate-Part I: Zero Friction, Part II: With Friction," *J. of Tribology, ASME Trans.*, Vol. 108, 1986, pp. 527-533, pp. 534-539.

[23] Van Der Zwaag, S. and Field, J. E., "The Effect of Thin Hard Coatings on the Hertzian Stress Field," *Phil. Mag.*, Vol. 46, 1982, pp. 133-150.

[24] Komvopoulos, K., "Finite Element Analysis of a Layered Elastic Solid in Normal Contact With a Rigid Surface," *J. Tribology, ASME Trans.*, Vol. 110, 1988, pp. 477-485.

[25] Komvopoulos, K., "Elastic-Plastic Finite Element Analysis of Indented Layered Media," *J. of Tribology, ASME Trans.*, Vol. 111, 1989, pp. 430-439.

[26] Tangena, A. G. and Wijnhoven, P. J. M., "The Correlation Between Mechanical Stresses and Wear in a Layered System," *Wear*, Vol. 121, 1988, pp. 27-35.

[27] *ABAQUS User's Manual*, Version 4.5.171 (a), Hibbitt, Karlsson and Sorenson, Inc., Providence, RI, 1985.

[28] Johnson, K. L., *Contact Mechanics*, Cambridge University Press, Cambridge, UK, 1985, pp. 84-106.

[29] Johnson, K. L., *Ibid*, 1985, pp. 171-184.

[30] Gurland, J. and Plateau, J., "The Mechanism of Ductile Rupture of Metals Containing Inclusions," *Trans. ASME*, Vol. 56, 1963, pp. 442-454.

[31] McClintock, F. A., "On the Mechanics of Fracture from Inclusions," *Ductility*, ASM. Metals Park, Ohio, 1968, pp. 225-275.

[32] Merwin, J. E. and Johnson, K. L., "An Analysis of Plastic Deformation in Rolling Contact," *Proc. Instn. Mech. Engrs.*, Vol. 177, 1963, pp. 676-690.

[33] Jahanmir, S. and Suh, N. P., "Mechanics of Subsurface Void Nucleation in Delamination Wear," *Wear*, Vol. 44, 1977, pp. 17-38.

[34] Argon, A. S. and Safoglu, R., "Cavity Formation from Inclusions in Ductile Fracture," *Metallurgical Trans. A*, Vol. 6A, 1975, pp. 825-837.

Chapter 5

Finite Elment Analysis of An Elastic-Plastic Two-Layer Half-Space: Sliding Contact

Summary

A plane strain finite element stress and strain analysis of the sliding contact of two-layer elastic-plastic half-space for various friction coefficients was conducted. First the contact pressure of the two-layer half-space under normal indentation was determined. Then the normal and tangential loadings were applied proportionally and incrementally on the surface. Surface deformation, location of initial yielding, stresses and strains along the interfaces between layers and between layer and substrate are found strongly depend on the friction coefficient. When the friction coefficient is small (< 0.3), yielding initiates in the subsurface region near the leading edge of the contact, provided that the normal load is large enough. When the friction coefficient is large (> 0.3), yielding initiates on the surface at the trailing edge of the contact. The surface strains, especially the shear strains, are large due to the uncontained deformation. The magnitude of shear stresses and strains along both interfaces are significantly large for high friction. Based on the analysis, the implications for interface failures are qualitatively addressed.

Nomenclature

a	=	half contact width
E	=	Young's modulus
E_p	=	plastic modulus
F	=	tangential force
h_1	=	thickness of top layer
h_2	=	thickness of interlayer
L	=	normal force per unit length
N	=	normal force
p	=	pressure
q	=	tangential traction
R	=	radius of cylindrical indenter
T	=	tangential force per unit length
u, v	=	components of displacement
α	=	coefficient of linear work-hardening
β	=	angle of oblique loading
δ	=	penetration depth
$\varepsilon_{xx}, \varepsilon_{yy}, \varepsilon_{xy}$	=	components of strain
μ	=	friction coefficient
ν	=	Poisson's ratio
σ_{Mises}	=	Mises equivalent stress
$\sigma_{xx}, \sigma_{yy}, \sigma_{zz}, \tau_{xy}$	=	components of stress
σ_Y	=	yield strength
τ_Y	=	shear yield strength

5.1 Introduction

Thin films are widely used in modern mechanical, electronic, magnetic, and optical devices. In electrical connectors, in particular, thin composite layers of gold, nickel, and copper or copper alloys are widely used to meet multi-functional requirements [1]. A minimum normal force is also required to maintain low electrical contact resistance and low noise; but the high friction forces generated by high friction coefficients during frequent insertion and withdrawal cause contact failures. To better understand the mechanisms of the contact failures of thin film systems, it is necessary to have a comprehensive knowledge of the sliding contact stress and strain fields of the thin film systems.

The contact stress analyses of homogeneous media have been made for many decades. Johnson [2] has recently reviewed the mechanics of non-conforming contacts. The two-dimensional quasi-static frictional or sliding contact of a homogeneous elastic half-space was investigated by M'Ewan [3], Poritsky [4], and Smith and Liu [5]. It has been found that the effect of tangential force is to bring the point of maximum shear stress closer to the surface. Johnson and Jefferis [6] used both the Mises and Tresca yield criteria to determine the location of initial yield in a sliding contact. They found that yielding initiates in the subsurface region when the friction coefficient, μ, is small ($\mu < 0.25$ for Tresca criterion and $\mu < 0.3$ for Mises criterion), and on the contact surface when the friction coefficient is larger than 0.25 for Tresca and 0.3 for Mises criteria. The sliding contact of a spherical indenter on an elastic half-space was studied by Hamilton and Goodman [7], and elaborated later by Hamilton [8]. Bryant and Keer [9] have extended the work of Hamilton and Goodman [7] for the general case of an elliptical contact with a stick zone within the contact region. The contact with elliptically distributed traction was also analyzed by Sackfield and Hills [10,11]. Recently Sackfield and Hills [12] studied the sliding contacts under three special pressure distributions over a circle. It was found that the flatter the pressure distribution the more resistant the contact is to yielding. Since it is difficult to obtain analytical solutions of sliding contacts of elastic-plastic media, the finite element method has been recently used extensively in the stress analysis of the sliding contact in the elastic-plastic regime. For example, Nagaraj [13] showed that the relative tangential displacements at sliding contact

interfaces has only a slightly influence on the contact pressure distribution, but has significant effects on the extent of plastic deformation. Tangena and Hurkx [14] used the finite element method to analyze the sliding contact of a rigid cylinder on an elastic-plastic half space. A hump, which resembles the prow in sliding contacts, was predicted at the leading edge of the cylinder when the friction coefficient is high (μ=1).

All these analyses, as remarked earlier, are for sliding contacts of homogeneous half-spaces. The analysis of sliding contacts of a layered medium has been performed only recently. Ihara et al. [15] conducted the finite element analysis of the contact stresses and strains in an elastic film on a rigid substrate under normal and tangential loading. King and O'Sullivan [16] investigated the sliding line contact of a single-layer elastic half-space. They established integral equations based on displacement constraints at the contact interface and at the layer-substrate interface which was assumed to be perfectly bonded, and solved the equations numerically using a least-square iterative method. Komvopoulos et al. [17] studied the sliding contact of a rigid cylinder contacting a stiff-layer elastic half-space using the finite element analysis. They showed that the Mises equivalent stress in the substrate is greatly reduced if a thicker layer is used. Recently O'Sullivan and King [17] extended their own analysis to three-dimensional sliding spherical contact of a layered medium.

The above analysis of the sliding contact of layered systems are elastic solutions for a single layer half-space, the layer being either compliant or stiff than the substrate. For the multi-layer contact systems, such as the Au/Ni/Copper structure of the electrical contacts, these analyses are not quite applicable in predicting the stress and the strain fields because both compliant (or soft) and stiff (or hard) layers are involved. Moreover, the stress and the strain fields of multi-layer contact systems in the elastic-plastic regime are expected to be more complex, and are unlikely solved analytically. Therefore the objective of this paper is to analyze the sliding contact of multi-layer systems used in electrical contacts using the finite element method. In a previous paper by the present authors [18], only normal loading of the multi-layer system was considered. In the present study, the stress and strain fields of sliding contact of a two-layer half-space in the elastic-plastic

(work hardening) regime are determined by the finite element analysis. A plane strain finite element mesh was set up to conduct the analysis. The effects of the friction coefficient on the stresses and strains at various locations is examined, and the mechanisms of interface cracking and interfacial delamination are qualitatively addressed.

5.2 Statement of the Problem

In the normal contact, friction at the contact interface of two non-conforming bodies affects the stress field only if the elastic constants of the two materials are different [19]. Under combined normal and tangential loading, the friction at the contact interface has different effects on the stress field, depending on whether the contact is static or sliding. In a static contact, Mindlin [20] showed that, under a constant normal load, N, even the smallest tangential force, F, will result in some slip at the contact edge. The annular slip zone spreads into the contact region as F increases until $F=\mu N$ when gross slip occurs. Due to the "irreversibility" implied by the frictional contact, the final contact stress field depends on not only the final values of normal and tangential forces, but also the history of loading. If the normal and tangential loads are applied simultaneously and proportionally, i.e., the oblique loading, the slip zone does not exist when the angle of the oblique loading β ($\beta=\tan^{-1}(F/N)$) is less than the angle of friction ($\tan^{-1}\mu$) [21,22].

In sliding contacts, it is usually assumed that (1) the contact pressure distribution is independent of the tangential loading; and (2) that Amonton's Law of sliding friction holds both macroscopically and microscopically, i.e.,

$$F = \mu N \tag{5.1}$$

and

$$q(x) = \mu p(x) \tag{5.2}$$

where $q(x)$ and $p(x)$ are the tangential and normal surface traction distributions within the contact region.

In the elastic analysis of homogeneous half-spaces, the normal pressure is usually specified by the Hertzian pressure and the tangential traction by Eq. (5.2)

on the contact surface [4-7, 23, 9]. However, in the case of layered media [25] or when plastic deformation is involved [26], the contact pressure distribution deviates from the Hertzian distribution. In a finite element analysis of normal indentation of two-layer elastic-plastic half-space by the present authors [18], it was shown that the contact pressure no longer obeys the Hertzian pressure distribution and that the deviation from the Hertzian distribution depends on the layer thickness and the extent of plastic deformation. In the sliding contact, the tangential loading has insignificant effect on the contact width and the contact pressure distribution, especially if $\mu<1$ [27]. Thus for the analysis of sliding contacts of layered elastic-plastic media, a two-step procedure can be used. First the contact pressure distribution under normal indentation is determined, and then apply the normal and tangential loading which is specified by Eq. (5.2). Since the final contact stress field depends on the history of loading, only the simultaneous and proportional loading scheme of normal and tangential forces is considered in the present analysis.

Consider a rigid cylinder of radius R indenting a two-layer half-space under a normal force per unit length, L, and a tangential force per unit length, T. Fig. 5.1 illustrates the coordinate system and the dimensions of the layers. The contact edge (x=a) is defined as the leading edge, and x=-a as the trailing edge of the contact. The thicknesses of the top layer (layer 1) and the interlayer (layer 2) are h_1 and h_2, respectively. Perfect bonding is assumed at the interfaces between layers, i.e., displacements across the interfaces are continuous:

$$u^{(1)}(x, h_1) = u^{(2)}(x, h_1) \tag{5.3a}$$

$$v^{(1)}(x, h_1) = v^{(2)}(x, h_1) \tag{5.3b}$$

$$u^{(2)}(x, h_1+h_2) = u^{(3)}(x, h_1+h_2) \tag{5.4a}$$

$$v^{(2)}(x, h_1+h_2) = v^{(3)}(x, h_1+h_2) \tag{5.4b}$$

$$u = v = 0 \qquad \text{as } x, y \to \infty \tag{5.5}$$

where the superscripts 1-3 stand for the top layer, the interlayer, and the substrate, respectively. A two-step procedure is followed to obtain the stress and strain fields. First the contact pressure of frictionless indentation of the two-layer half-space is

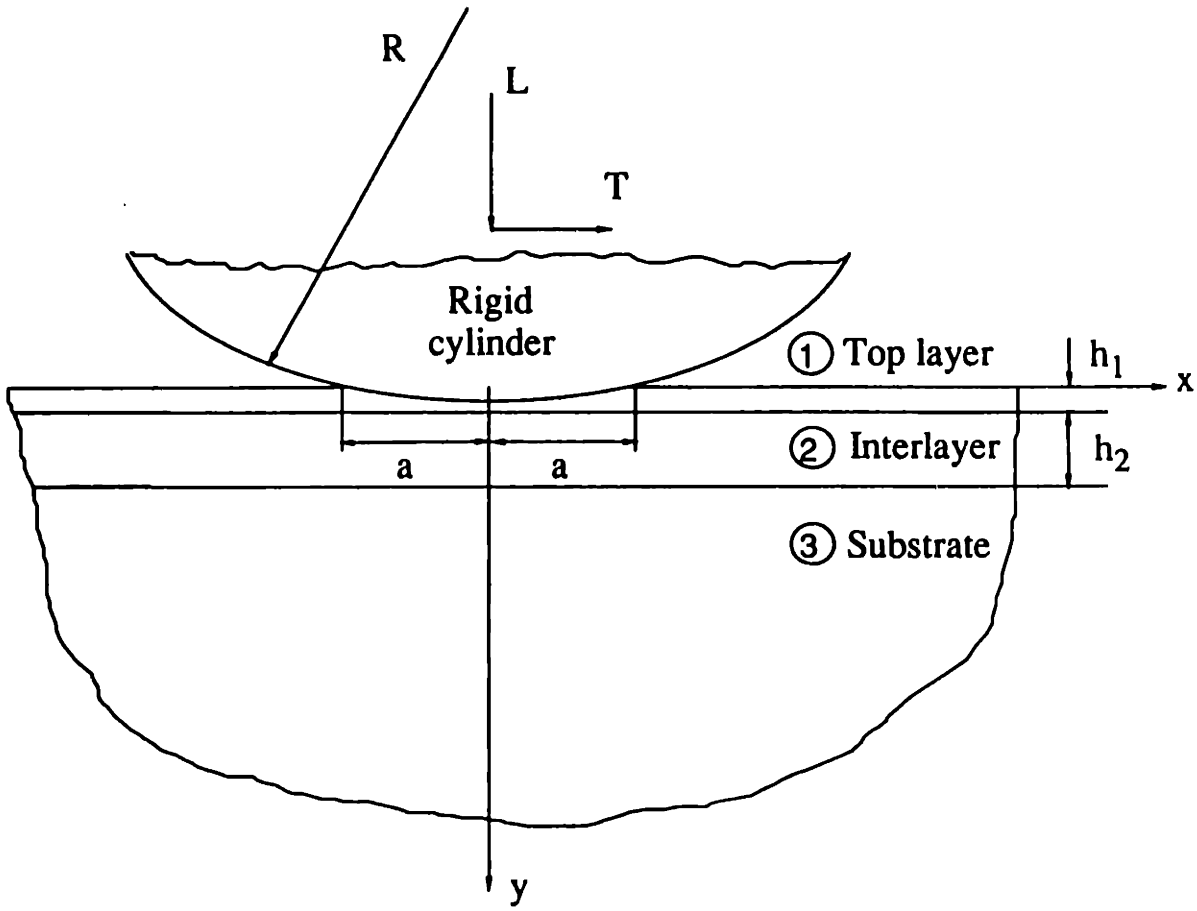

Fig. 5.1 Schematic of sliding contact of a rigid cylinder on a two-layer half-space

determined. The boundary conditions for the first step are as follows:

On the contact surface,

$$v(x, 0) \equiv \delta - \frac{x^2}{2R} \qquad |x| \le a \qquad (5.6a)$$

$$\sigma_{yy}(x, 0) = 0 \qquad |x| > a \qquad (5.6b)$$

$$\tau_{xy}(x, 0) = 0 \qquad -\infty < x < \infty \qquad (5.6c)$$

The penetration depth, δ, is assumed to be smaller than the radius of the indenter, R, or the half contact width, a. After the contact pressure, p(x), is obtained from the first step, the normal and tangential loadings are applied proportionally. The boundary conditions for the second step are as follows:

$$\sigma_{yy}(x, 0) = -p(x) \qquad |x| \le a \qquad (5.7a)$$

$$\tau_{xy}(x, 0) = \mu p(x) \qquad |x| \le a \qquad (5.7b)$$

$$\sigma_{yy}(x, 0) = 0 \qquad |x| > a \qquad (5.7c)$$

$$\tau_{xy}(x, 0) = 0 \qquad |x| > a \qquad (5.7d)$$

The primary emphasis of this study is on the sliding contact of multi-layer systems employed in electrical contacts. That is, the top layer is gold which is hardened with 0.5% nickel, the interlayer is nickel, and the substrate is copper or a copper alloy. All materials are assumed to possess a bilinear elastic-plastic behavior (Figure 5.2). The relevant elastic and plastic properties of the layers and the substrate are listed in Table 5.1. These values fall in the typical range of electrical contact materials. Table 5.2 lists the geometric and loading parameters used in the finite element analysis. The normal loads, 5 N/mm and 10 N/mm, have been chosen for analysis with the friction coefficient varying from 0 to 0.5.

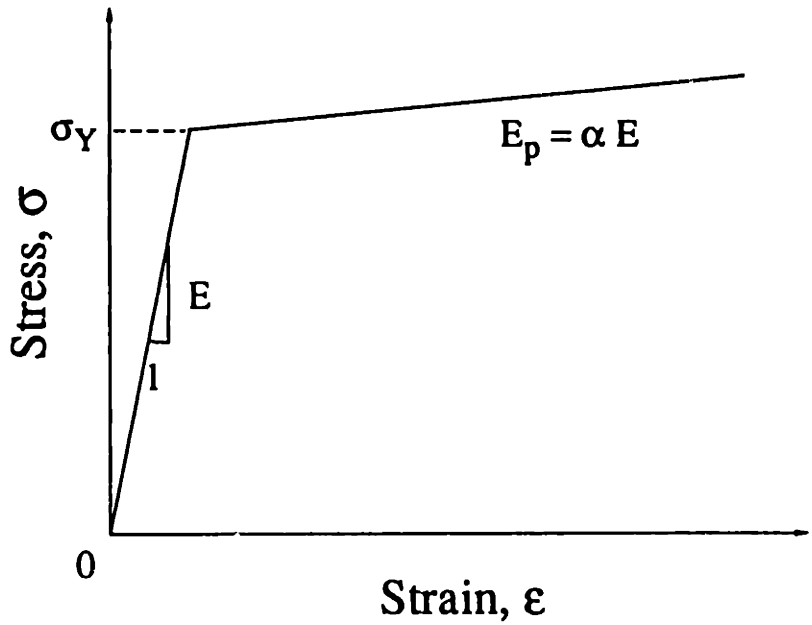

Fig. 5.2 Bilinear elastic-plastic behavior of contact materials

Table 5.1 Mechanical properties of contact materials

Material	E (GPa)	ν	σ_Y (MPa)	α
Top Layer (Au+0.5%Ni)	79	0.32	298	0.1
Interlayer (Ni)	205	0.32	811	0.1
Substrate (Brass: Cu-35%Zn)	125	0.32	405	0.1

Table 5.2 Load and geometrical parameters used in stress analysis

Radius of indenter, R	0.75	mm
Normal load, L	5, 10	N/mm
Thickness of top layer, h_1	1.25	μm
Thickness of interlayer, h_2	2.5	μm

5.3 The Finite Element Model

The contact pressure distribution and contact width of two-layer half-space under normal indentation have been obtained in a previous work [18]. The results are directly used for the present analysis. Since the combined normal and tangential loading is no longer symmetric, the whole layered half-space has to be modelled. Figure 5.3a shows the finite element mesh and the boundary conditions. Figure 5.3b the details of the mesh near the contact. It was assumed that the bottom plane CD is far away from the contact center, and that the vertical displacements are equal to zero according to the Saint-Venant's principle. The horizontal displacements at the bottom plane (CD) were not restricted except that of point C which stays put. The normal and tangential loads were applied on the top plane AB within the contact region. The horizontal and vertical dimensions of the mesh are 200 μm x 200 μm, both being large enough to allow the stresses to be insignificant at the boundaries. The whole mesh is an arrangement of 630 quadrilateral, eight-node, isoparametric elements, and the total number of nodes is 2023. The mesh was refined in the region below the contact. The horizontal and vertical spacing of nodes on and below the contact surfaces are 0.5 μm and 0.3125 μm, respectively. The two-layer half-space was modelled by assigning different elastic and plastic properties to the elements of top rows of the mesh. The first two rows were assigned to the top layer, and the next two rows immediately below the top layer were assigned to the interlayer. The interfaces between the layers were assumed to be perfectly bonded, i.e., the displacements at the interfaces were continuous (Eqs. 3-5). These interface constraints were satisfied by using common nodes at the interfaces, and the common nodes belong to the elements on both sides of the interface.

The multi-purpose finite element program ABAQUS was used to conduct the analysis. The normal and tangential loads were applied node-by-node with a consistent loading scheme within the contact region, and they were in the same executing step of the ABAQUS code so that the incremental and proportional loading was able to be undertaken. The parameter settings of executing programs were detailed in the previous work [18]. The computations were performed on a MicroVAX II computer, and the typical CPU time for one run was about 90 minutes.

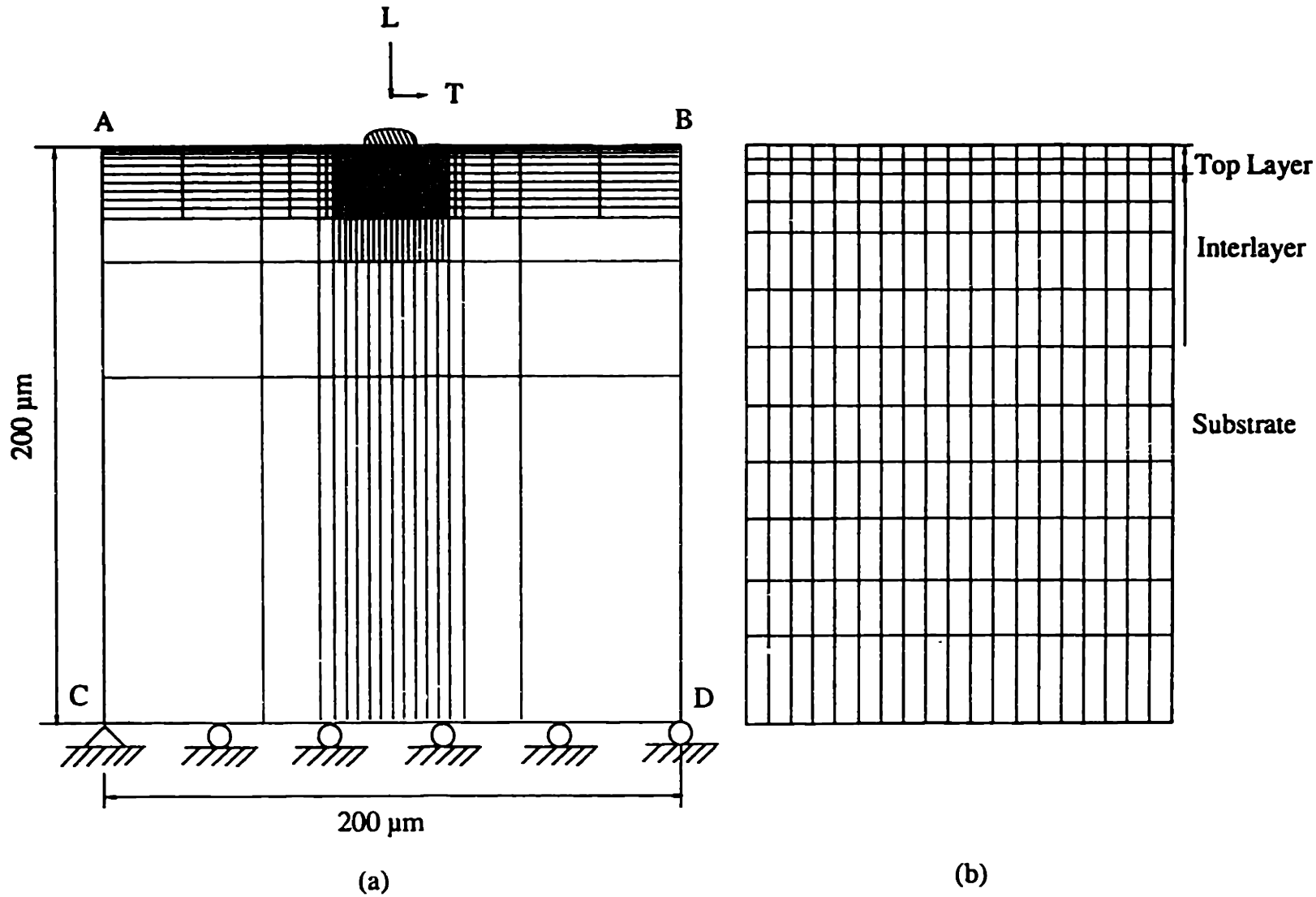

Fig. 5.3 (a) The finite element mesh and the boundary conditions, and (b) the detail of the fine mesh

5.4 Results and Discussion

The results presented here are for a rigid cylinder of radius R (0.75 mm) which is much larger than the expected half contact width, a. The normal loads were 5, and 10 N/mm. It was shown in reference [18] that the 5 N/mm normal load is an elastic loading, while 10 N/mm normal load is an elastic-plastic loading. The ratio of the tangential force to the normal force, i.e., the friction coefficient, was from 0 to 0.5. (The finite element of analysis for a larger friction coefficient (μ=1.0) was tried, but no converged solution was obtained in the allowed number of increments. The strain increment was larger than fifty times the yield strain due to relatively small work-hardening of the contact materials considered in the present study. Thus it is unlikely to obtain converged solutions in reasonably short period of time.) The thicknesses of the top layer and the interlayer were chosen as 1.25 μm and 2.5 μm. The Poison's ratios for both the layers and the substrate were assumed to be 0.32. The calculated stresses are normalized by the yield strengths of the top layer, $\sigma_{Y,top}$, or $\tau_{Y,top}$, and of the substrate, $\sigma_{Y,sub}$, or $\tau_{Y,sub}$, depending on the appropriateness. The positive values indicate tensile stresses and strains, and the negative values compressive stresses and strains.

5.4.1 Surface deformation and penetration depth

To qualitatively illustrate the effect of friction on deformation flow in the layers and the substrate, especially in the top layer, the deformed meshes are shown in Figure 5.4 for 5 N/mm normal load at various friction coefficients. The displacements in the deformed mesh are magnified 20 times for clarity. The top two rows of elements are the top layer, the next two rows are the interlayer, and the rest of the elements are the substrate. For normal indentation (μ=0), displacements of the layers and the substrate are, as expected, symmetric about the y-axis. When the friction coefficient is greater than zero, however, the symmetry is lost and the materials deform largely along the direction of the tangential force. In the finite element analysis of an elastic-plastic half-space by Tangena and Hurkx [14], a hump was found at the leading edge of the sliding contact as the friction coefficient increases. In the present case, a two-layer half-space, the displacements in the top layer are clearly much larger than those of the interlayer and the substrate, but no hump is found at the leading edge of the contact. Fig 5 shows the deformed meshes

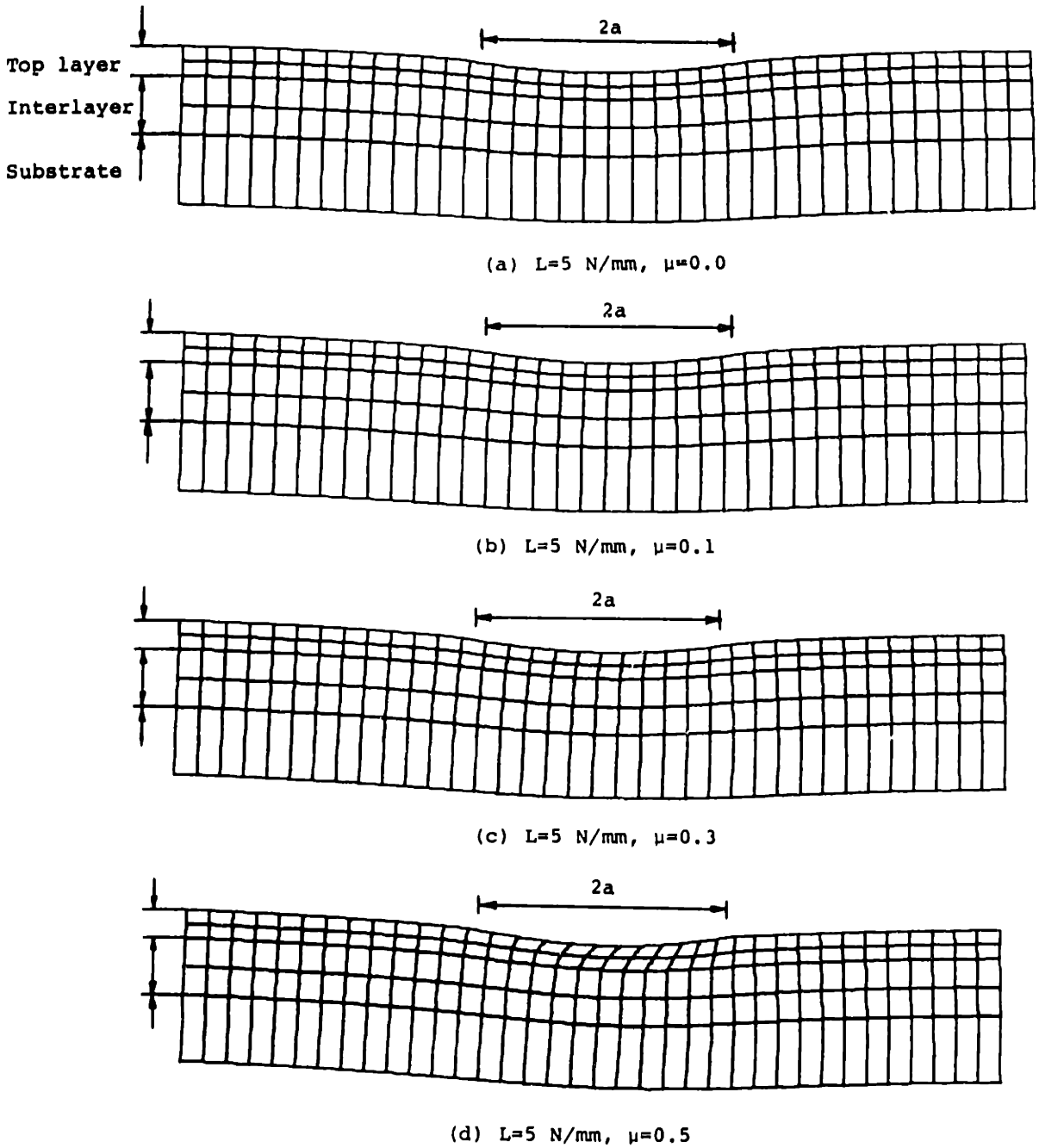

Fig. 5.4 Deformed meshes under 5 N/mm normal load at various friction coefficients. Magnification factor=20

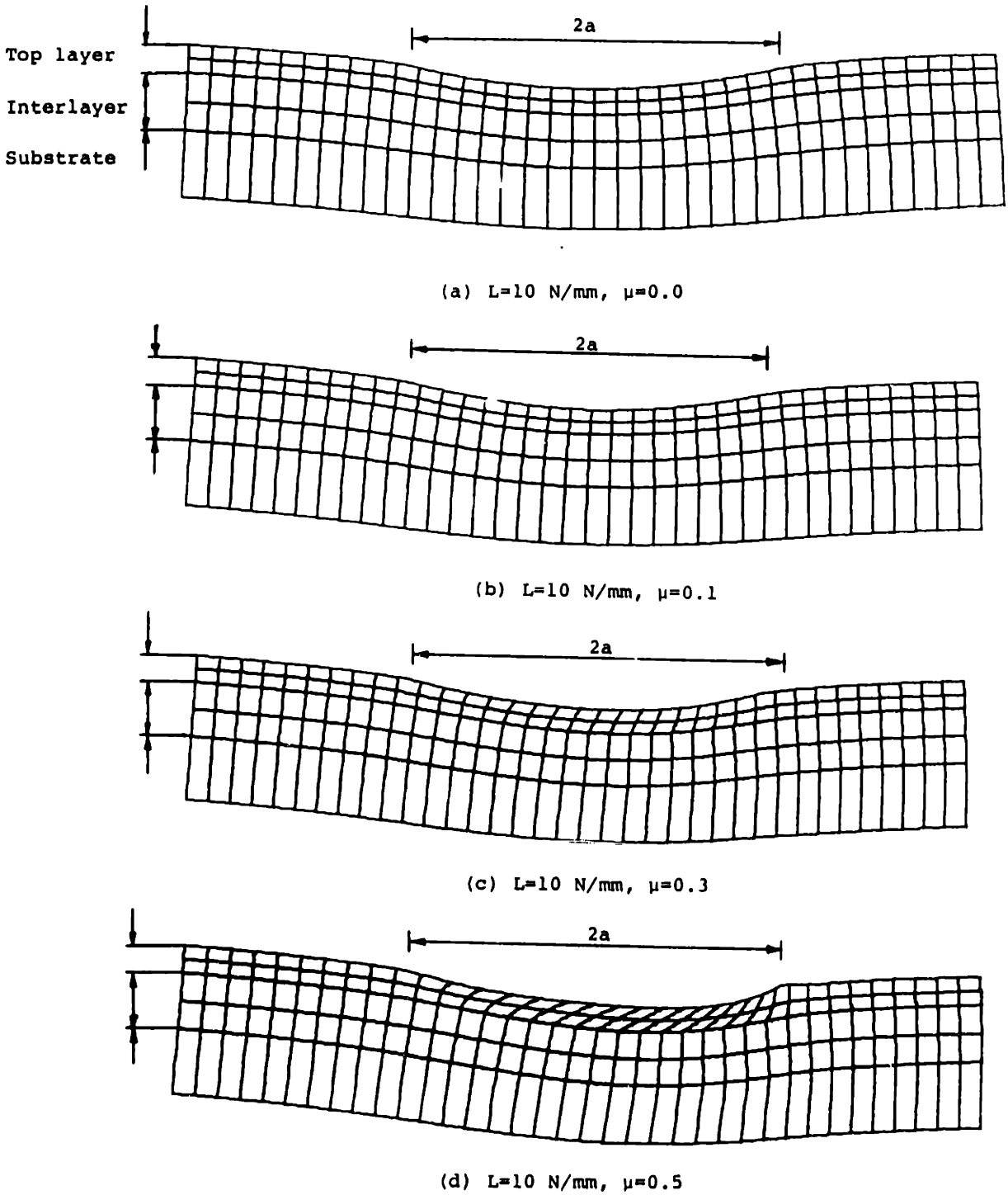

Fig. 5.5 Deformed meshes under 10 N/mm normal load at various friction coefficients. Magnification factor=20

for 10 N/mm normal load at various friction coefficients. As expected, the contact width and the displacements are greater than in the case of 5 N/mm normal load. As the friction coefficient increases, the meshes of the top layer are deformed along the sliding direction. For the friction coefficient of 0.5, a small hump is observed at the leading edge of the contact.

Table 5.3 lists the penetration depth of the two-layer half-space under combined normal and tangential loadings. The penetration depth increases with the normal load as well as the friction coefficient. Thus the tangential force contributes not only to the horizontal displacement, but also to the vertical indentation. The same observation was reported by Johnson [28] for a homogeneous elastic half-space under normal and tangential loadings. The penetration depth δ, however, is still small compared with the thickness of the top layer, h_1. The ratio δ/h_1 in Table 5.3 shows that the penetration depth is about 10% of thickness of the top layer under 5N/mm normal load, less than 20% under 10 N/mm normal load, for the whole range of friction coefficients considered here.

To illustrate the effect of the friction coefficient on the surface deformation, the strains on the contact surface are plotted in Figure 5.6. The horizontal strain, ε_{xx}, under 5 N/mm and 10 N/mm normal load with various friction coefficients are plotted in Figs 6a and 6b, respectively. As the friction coefficient increases, the material at the trailing side of the contact ($x/a<0$) is stretched horizontally ($\varepsilon_{xx}>0$), and the material at the leading side ($x/a>0$) is squeezed ($\varepsilon_{xx}<0$). In the vertical direction, however, the trailing side is compressed further as the friction coefficient increases. At $\mu=0.5$, the tensile strain ε_{yy} is generated at the leading side of the contact about $x/a>0.5$ (Figures 5.6c and 5.6d). The surface shear strains are plotted in Figures 5.6e and 5.6f. For $\mu=0$, the contact surface is free of shear traction. Thus the shear strain is zero everywhere on the surface. When $\mu>0$, the surface shear strain is generated within the contact region ($|x/a|\leq 1$). The direction of the shear strain is along the sliding direction, and its magnitude increases significantly with the friction coefficient. At $\mu=0.5$, the maximum shear strain on the surface is about 1.5% for 5N/mm normal load, and 8.5% for 10 N/mm normal load.

Table 5.3 Contact width and penetration depth of two-layer half-space under combined normal and tangential loading

Normal Load L, (N/mm)	Friction Coefficient	Half-width of Contact, a, (μm)	Penetration Depth δ, (μm)	$\frac{\delta}{h_1}$
5	0.0	5.5	0.106	0.0848
	0.1	5.5	0.107	0.0856
	0.3	5.5	0.109	0.0872
	0.5	5.5	0.113	0.0904
10	0.0	8.5	0.197	0.1576
	0.1	8.5	0.199	0.1592
	0.3	8.5	0.207	0.1656
	0.5	8.5	0.216	0.1728

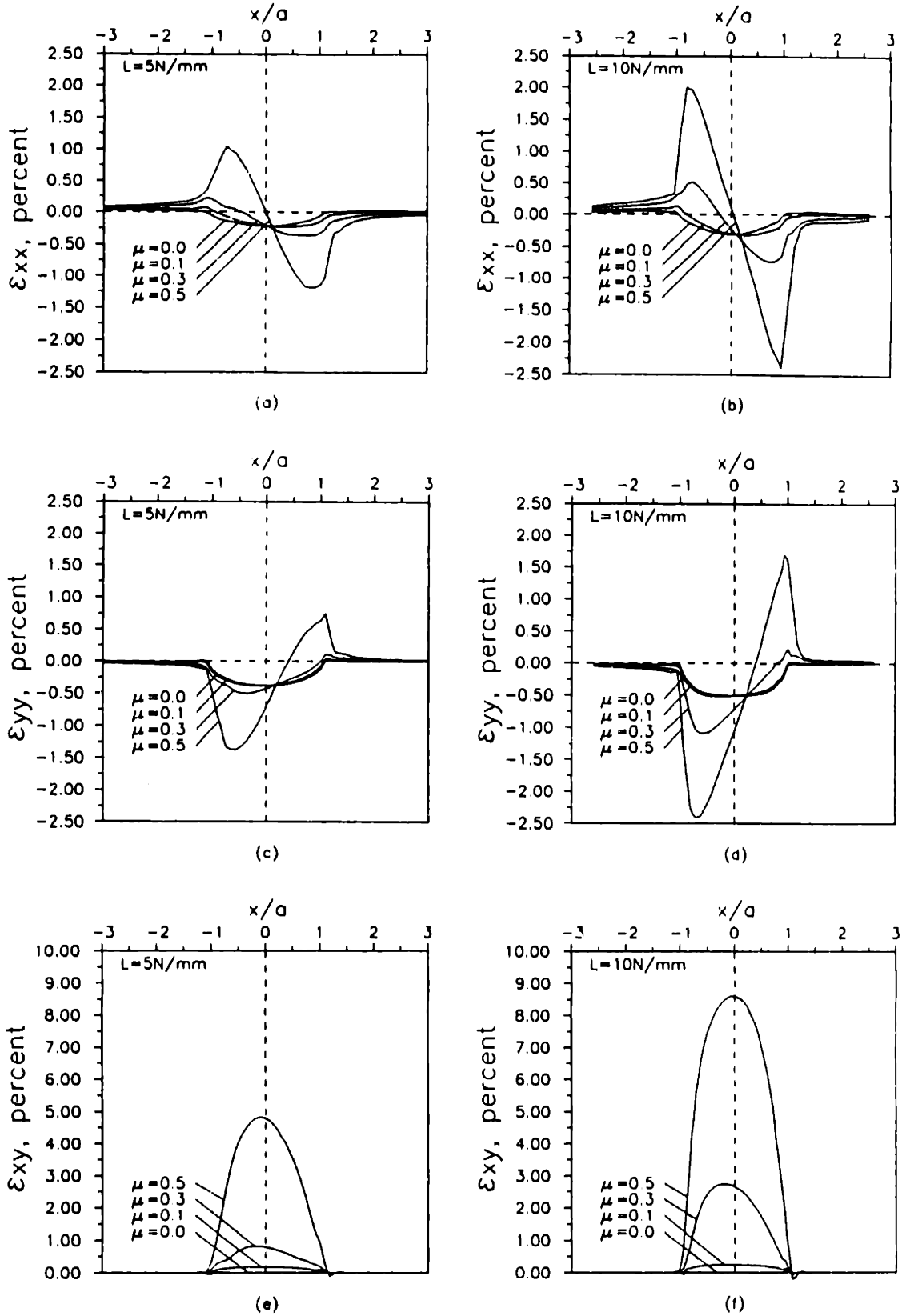

Fig. 5.6 Surface strains: (a) ε_{xx}, L=5N/mm, (b) ε_{xx}, L=10N/mm, (c) ε_{yy}, L=5N/mm, (d) ε_{yy}, L=10N/mm, (e) ε_{xy}, L=5N/mm, and (f) ε_{xy}, L=10N/mm

5.5.2 *Location of initial yielding*

Yielding occurs when the Mises equivalent stress, σ_{Mises}, is equal to the yield strength in simple tension, σ_Y. In plane strain, σ_{Mises} is given by

$$\sigma_{Mises} = \frac{1}{\sqrt{2}}\left[(\sigma_{xx} - \sigma_{yy})^2 + (\sigma_{yy} - \sigma_{zz})^2 + (\sigma_{zz} - \sigma_{xx})^2 + 6\tau_{xy}^2\right]^{1/2} \qquad (5.8)$$

In the normal contact, i.e., without friction, of a homogeneous elastic half-space, yielding initiates in the subsurface region at roughly y=0.70a below the contact center. Under combined normal and tangential loadings, the maximum Mises equivalent stress or maximum shear stress is brought closer to the surface, or even to the surface when the friction coefficient is large (about 0.25 for Tresca yielding criterion, and 0.3 for Mises criterion) [3-6]. King and O'Sullivan [15] show that this conclusion is also true when a stiff or compliant layer bonded on an elastic half-space is under normal and tangential loading. For sliding contact of a two-layer half-space comprising materials of different yield strength, however, the location of the maximum Mises equivalent stress is not necessarily the location of the initial yielding.

Figure 5.7 shows the Mises equivalent stress and the equivalent total plastic strain contours under the 5 N/mm normal load for various friction coefficients. Only the stress and plastic strain contours in the region near the contact are plotted for clarity. The horizontal dashed lines in the plots represent the approximate locations of the interfaces between layers. For normal indentation (Figure 5.7a, μ=0), the top layer, the interlayer and the substrate are all in the elastic regime. For μ=0.1 (Fig.7b), the Mises stress contours are only slightly different from those of normal indentation. The maximum Mises equivalent stress moves slightly closer to the surface. But no plastic deformation occurs either in the layers or in the substrate. At μ=0.3 (Figure 5.7c), however, the Mises equivalent stress in the top layer has reached the yield strength, and plastic deformation initiated on the surface near the trailing edge of the contact. But the maximum Mises stress occurs inside the interlayer. No plastic deformation occurs in the interlayer because of high yield strength of the interlayer. Figure 5.7d shows that at μ=0.5, the Mises stress

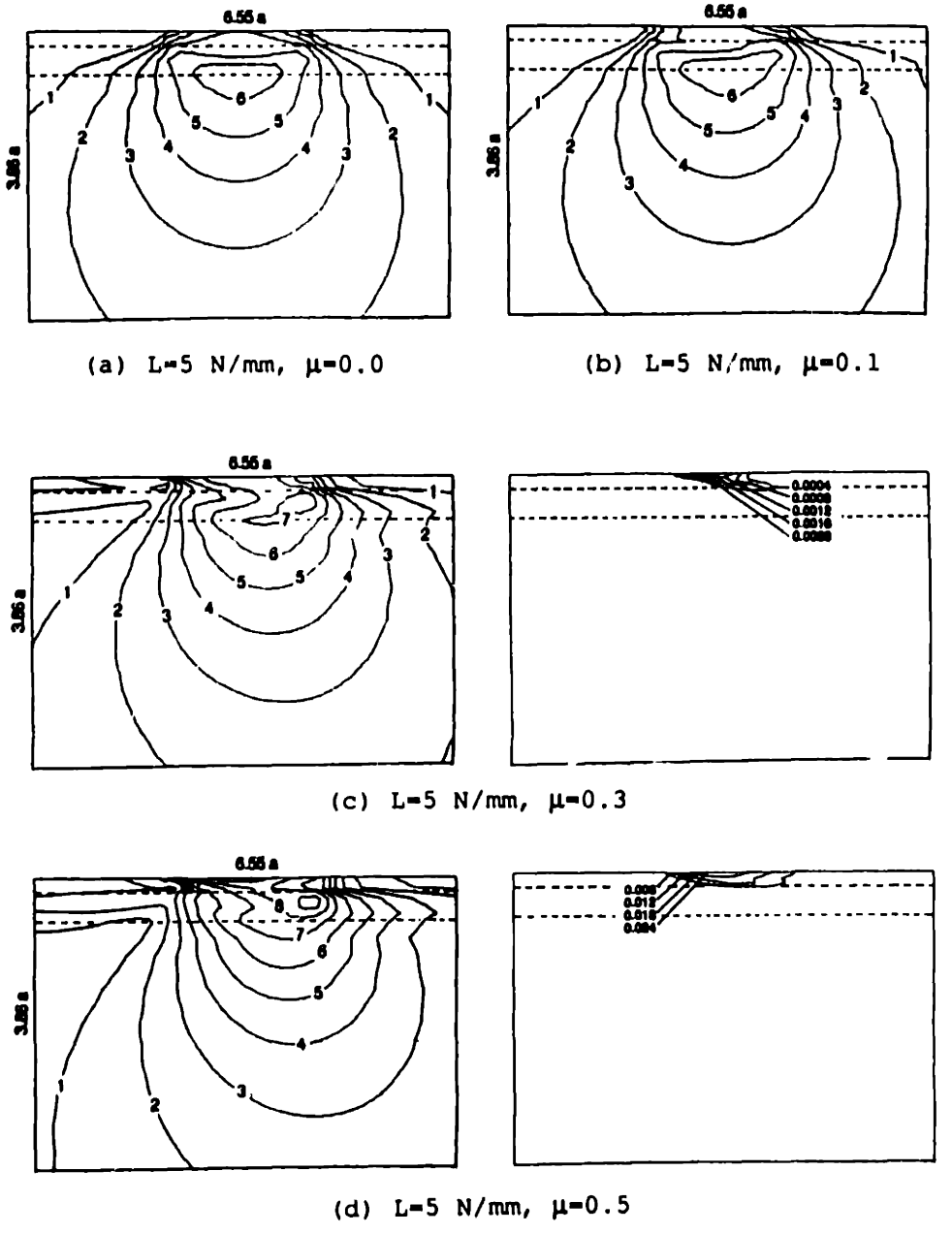

Fig. 5.7 Mises equivalent stress and equivalent total plastic strain contours for 5 N/mm normal load. The value of Mises stress contour numbers: 1--50 MPa, 2--100 MPa, 3--150 MPa, 4--200 MPa, 5--250 MPa, 6--300 MPa, 7--350 MPa, 8--400 MPa, 9--450 MPa, 10--500 MPa, 11--550 MPa

contours are further distorted toward the leading side, i.e., in the direction of the tangential force. The top surface is subject to more severe plastic deformation, while the interlayer and the substrate are in the elastic regime.

The layers and the substrate are in the elastic regime under normal indentation at 5 N/mm load. When an oblique load is applied, the top layer is in plastic regime only if the ratio of the tangential load to the normal load is larger than a critical value, about 0.3 for the present case. The plastic deformation initiates on the surface near the trailing edge of sliding contact, which is a little different from the case of a homogeneous half-space. Yielding initiates on the surface near the leading edge of the contact for two-dimensional sliding contacts of homogeneous media [3-6], and at the trailing edge for spherical sliding contacts [8,9]. In cylindrical sliding contact of a single-layer half-space ($\mu \geq 0.3$), the maximum Mises stress is on the surface near the leading edge if the layer is stiff, and near the trailing edge if the layer is compliant [15]. Thus for a two-layer half-space with a soft top layer, the yielding is initiated near the trailing edge at $\mu \geq 0.3$. Moreover, in the elastic analysis of the homogeneous half-space and the single-layer half-space, the maximum Mises stress is always on the surface when $\mu \geq 0.3$. For the two-layer elastic-plastic half-space of the present case, however, the maximum Mises stress is always inside the interlayer due to the high elastic modulus and high yield strength of the interlayer.

To see the effect of the tangential force more extensively, a normal load of 10 N/mm, which can cause plastic deformation of the two-layer half-space in normal indentation [18], was applied along with various friction forces. Figure 5.8 shows the Mises equivalent stress and equivalent total plastic strain contours. For normal indentation ($\mu=0$), yielding initiates in the substrate. The plastic zone is fully contained by material which still remains elastic so that the equivalent total plastic strain (0.07%) is of the same order of magnitude as the surrounding elastic strains. As a small tangential force is applied on the surface (Figure 5.8b, $\mu=0.1$), the Mises stress in the top layer has reached its yield strength and yielding takes place in the top layer at the top layer-interlayer interface. Notice that the location of initial yielding in the top layer is in the subsurface at the right side of the contact, i.e., the region near the leading edge of the contact. Another plastic zone is

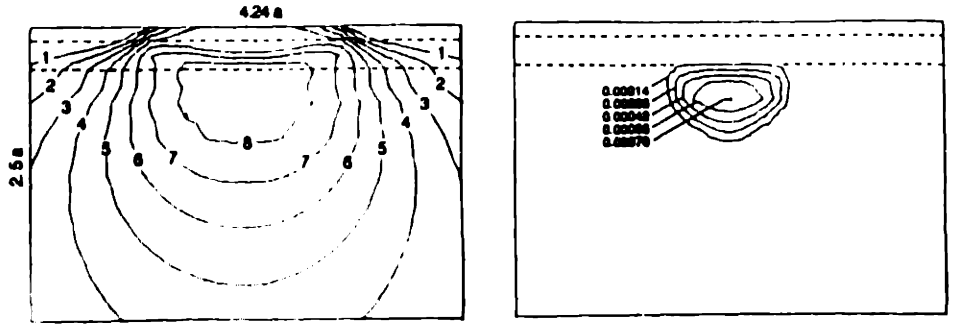

(a) L=10 N/mm, μ=0.0

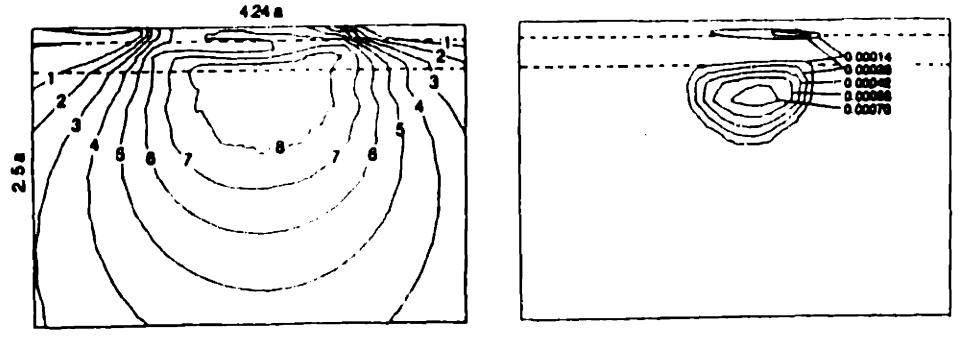

(b) L=10 N/mm, μ=0.1

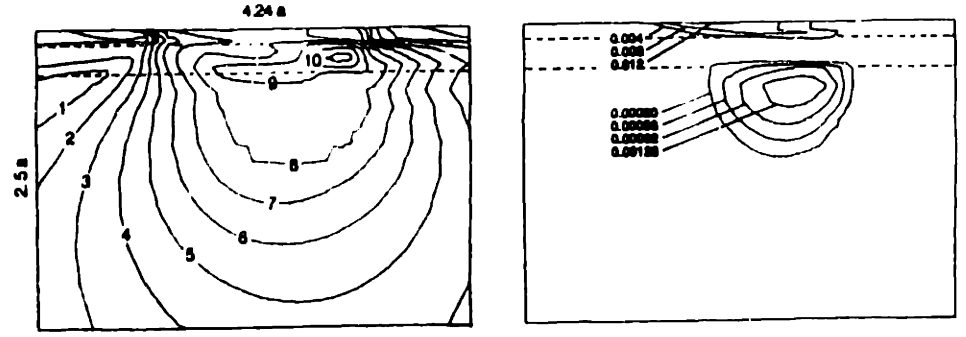

(c) L=10 N/mm, μ=0.3

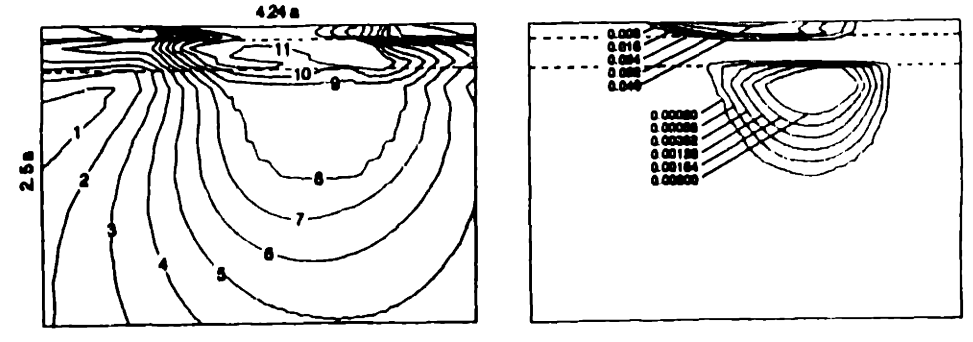

(d) L=10 N/mm, μ=0.5

Fig. 5.8 Mises equivalent stress and equivalent total plastic strain contours for 10 N/mm normal load. The value of Mises stress contour numbers: 1--50 MPa, 2--100 MPa, 3--150 MPa, 4--200 MPa, 5--250 MPa, 6--300 MPa, 7--350 MPa, 8--400 MPa, 9--450 MPa, 10--500 MPa, 11--550 MPa

in the substrate. Its location moves slightly toward top-right and the growth of the plastic zone is blocked by the hard interlayer. For μ=0.3 (Figure 5.8c), the Mises equivalent stress on the surface reaches the yield strength of the top layer first, and thus yielding initiates on the surface near the trailing edge of the contact. Plastic strain on the surface is larger (about 1.2%) due to uncontained deformation mode. The location of initial yielding in the substrate moves further right. The extent of the plastic deformation in the plastic zone of the substrate is greater than in the case of μ=0.1. Figure 5.8d shows that yielding takes place in both the top layer and the substrate when μ=0.5. The plastic zones and the extent of the plastic deformation are greater than in the previous case (μ=0.3). Although the Mises equivalent stress is high in the interlayer, still no plastic deformation has taken place in the interlayer due to high yield strength of the interlayer.

It is apparent from above analysis that the tangential force is the primary cause of the uncontained plastic deformation of the top layer. For small normal load (5N/mm), no plastic deformation takes place in the top layer when μ=0.1 (Fig.5b). For a larger normal load (10N/mm), plastic deformation does take place in the top layer when μ=0.1 (Figure 5.6b). When $\mu \geq 0.3$, yielding initiates on the surface (and in the substrate also if the normal load is larger). For the sliding contact of a two-layer half-space of the present case, surface yielding initiates near the trailing edge, which is different from the case of a homogeneous half-space. Whenever the yielding initiates in the subsurface, however, it occurs at the region near the leading edge of the contact.

5.4.3 Interfacial stresses

The magnitude and the distribution of subsurface stresses along the interfaces are of great interest in assessing mechanical reliability of the multi-layer systems. Figures 5.9a and 5.9b show the normal stress σ_{yy} along the top layer-interlayer interface, and Figures 5.9c and 5.9d along the interlayer-substrate interface. σ_{yy} is normalized by the yield strength of the top layer for the stress at the top layer-interlayer interface, and by the yield strength of the substrate for the stress at the interlayer-substrate interface. σ_{yy} is compressive along both interfaces for the range of friction coefficients considered in the present study except for the case of

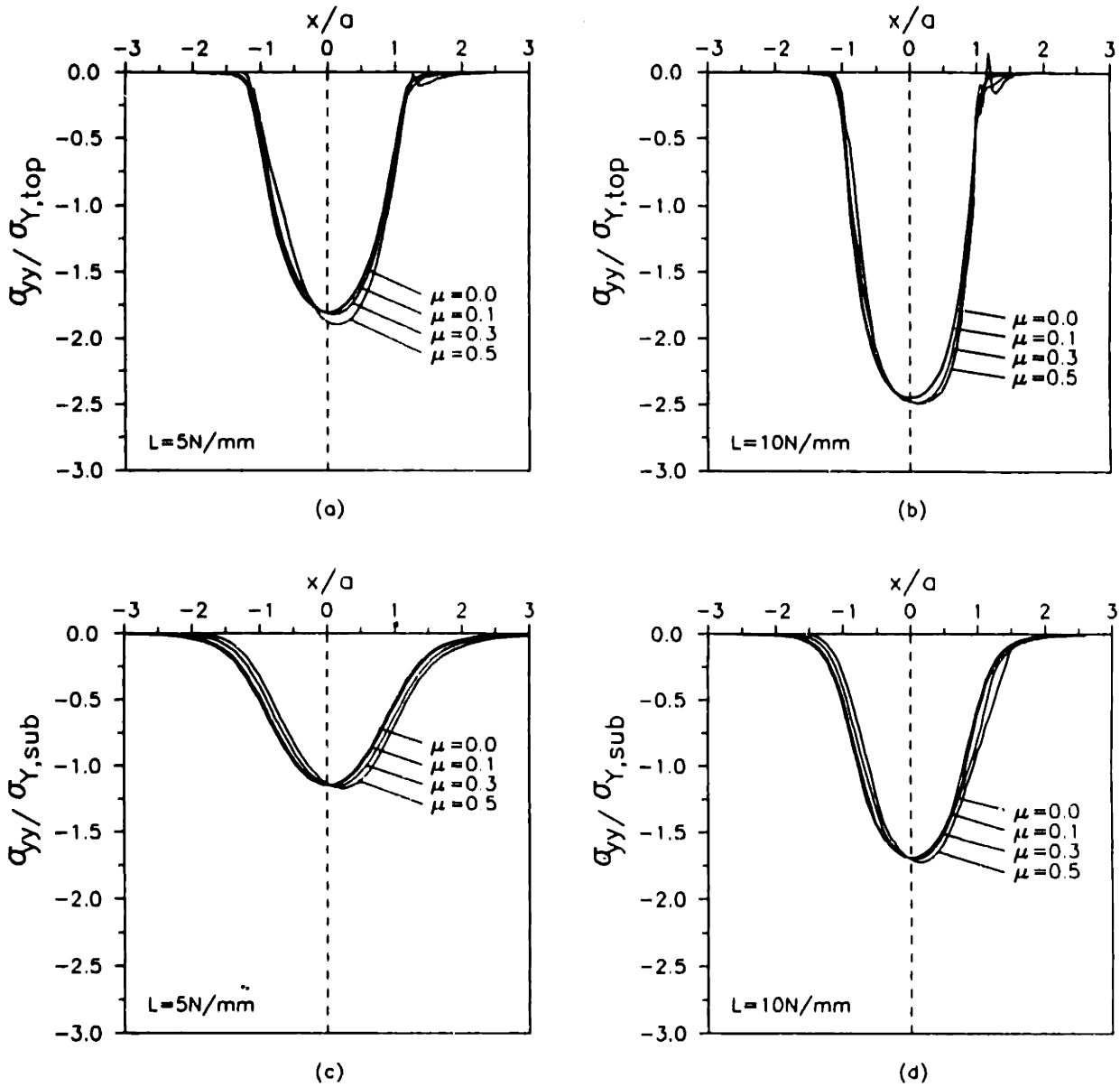

Fig. 5.9 Normalized σ_{yy} for various friction coefficients: (a) & (b) along the top layer-interlayer interface, (c) & (d) along the interlayer-substrate interface

10N/mm normal load with μ=0.5, when a small tensile stress is generated at x/a>1. Thus the friction coefficient has insignificant effect on the normal stress along the interfaces. The distributions move slightly to the right for μ>0.

Figure 5.10 shows the σ_{xx} stress along the top layer-interlayer interface for various friction coefficients. Because σ_{xx} is discontinuous across the interfaces, two sets of σ_{xx} curves appear in Figures 5.10a-10d. The solid lines are for the stresses in the top layer, σ_{xx}^{top}, whereas the dashed lines are for the stresses in the interlayer, σ_{xx}^{int}. σ_{xx}^{int} is greater than σ_{xx}^{top} along the interface. The friction coefficient has significant effect on the magnitude and the distribution of σ_{xx}. When μ>0, tensile σ_{xx} stress, both in the top layer and in the interlayer, is found at the trailing side of the contact, and the magnitudes of the tensile stress increase with the friction coefficient. The location of the maximum compressive stress σ_{xx} is shifted to the leading side (x/a>0), and the magnitude of the compressive stress also increases with the friction coefficient.

At the interlayer-substrate interface, again two sets of σ_{xx} curves appear in Figures 5.11a-11d. The solid lines are for the stresses in the substrate, σ_{xx}^{sub}, whereas the dashed lines are for the stresses in the interlayer, σ_{xx}^{int}. For normal indentation (μ=0), σ_{xx} is mostly compressive. The magnitude of σ_{xx}^{sub} is greater than that of σ_{xx}^{int} at $|x/a|<1$, and smaller at $|x/a|>1$. For an oblique loading (μ>0), the maximum compressive σ_{xx} occurs at about x/a=1, and the magnitude of σ_{xx} increases with the friction coefficient. σ_{xx} at the left side of the contact, i.e., x/a<0, is tensile, and the magnitude of the tensile stress also increases with the friction coefficient.

For a compression-dominated stress field such as the present one, shear stresses along the interfaces are particularly important. Figure 5.12 shows shear stress, τ_{xy}, along the top layer-interlayer interface (Figures 5.12a and 5.12b) and along the interlayer-substrate interface (Figures 5.12c and 5.12d). The shear stresses are normalized by the local shear yield strength, $\tau_{Y,top}$ or $\tau_{Y,sub}$, ($\tau_Y=\sigma_Y/\sqrt{3}$). At the top layer-interlayer interface, the magnitude of τ_{xy} increases considerably with the friction coefficient at the leading side (x/a>0), and decreases with the friction coefficient at the trailing side of the contact (x/a<0). The same trend is found at the interlayer-substrate interface, but the changes in the magni-

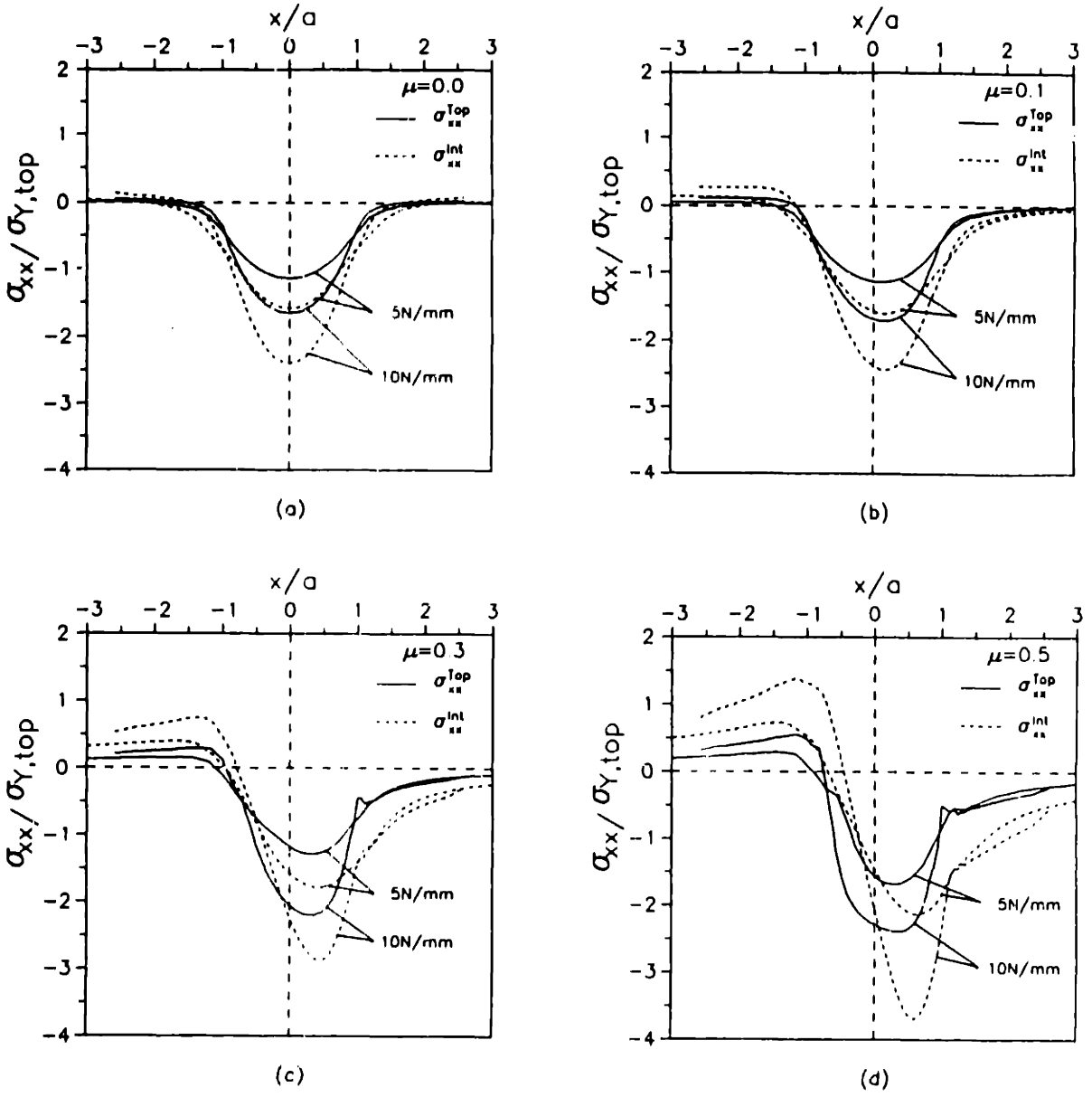

Fig. 5.10 Normalized σ_{xx} along the top layer-interlayer interface for various friction coefficients

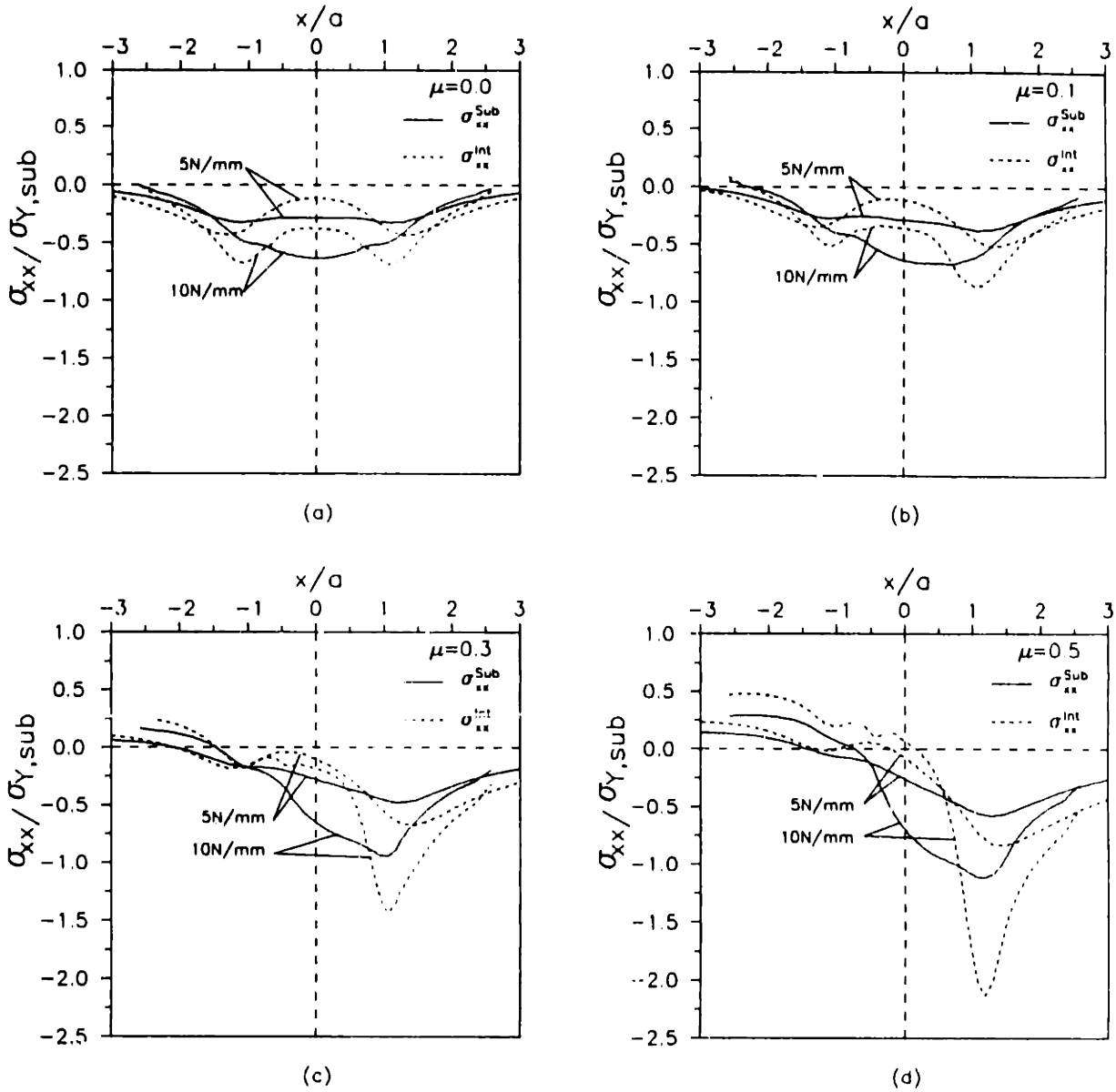

Fig. 5.11 Normalized σ_{xx} along the interlayer-substrate interface for various friction coefficients

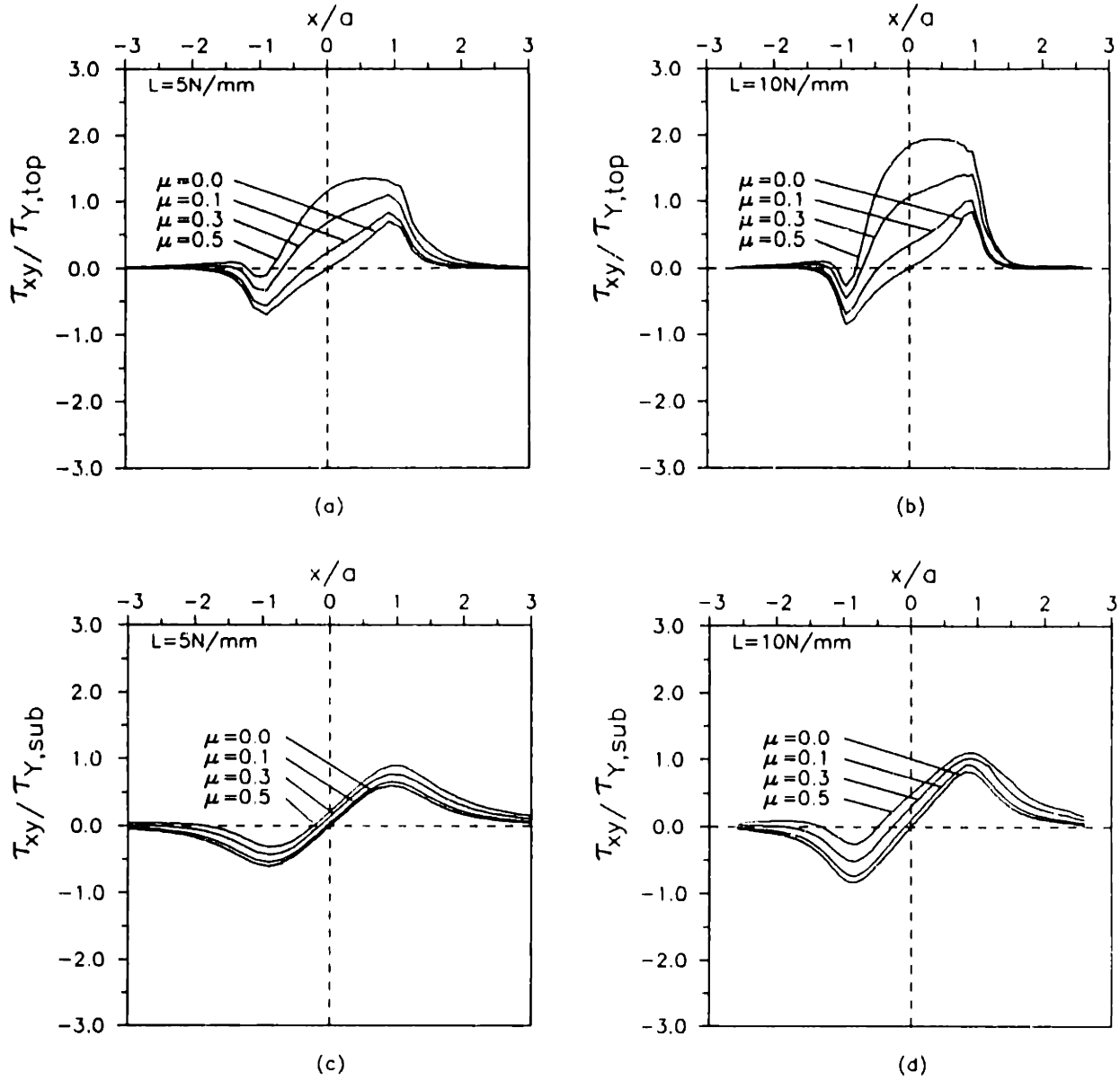

Fig. 5.12 Normalized τ_{xy} for various friction coefficients: (a) & (b) along the top layer-interlayer interface, (c) & (d) along the interlayer-substrate interface

tudes are much smaller than at the top layer-interlayer interface. Thus as the friction coefficient increases, the interfacial shear stresses at both interfaces become greater.

5.4.4 Interfacial strains

As discussed in a previous paper [18], the strain field, especially the interfacial strains, is important in determining the initiation and propagation of interface cracks in the contact mechanics of layered media. Strain plots are especially important when the contact is in the elastic-plastic regime. Also, strain being a dimensionless number requires no normalization by arbitrarily chosen parameters. Thus in the present study, attention is also focused on the interfacial strains. Figures 5.13a-13d are the normal strains, ε_{yy}, along the top layer-interlayer interface for various friction coefficients. Figures 5.14a-14d are the normal strains, ε_{yy}, along the interlayer-substrate interface for various friction coefficients. Because of constraints of displacement continuity at the interface, two sets of strain curves are plotted. The solid lines represent the interfacial strains in the top layer, and the dashed lines for the strains in the interlayer. For μ=0, ε_{yy} is mostly compressive, though very small tensile strain is found at $|x/a|>1$. The magnitude of ε_{yy} in the top layer is much larger than that in the interlayer. For oblique loading, the magnitude of the tensile strain at $x/a>1$ increases slightly with the friction coefficient, and the magnitudes of compressive strain at $|x/a|<1$ also increases. Thus the friction coefficient has only marginal effect on the interfacial normal strains.

The x-component of strain, ε_{xx}, is continuous across the interfaces. Figures 5.15a and 5.15b are for the strains at the top layer-interlayer interface, and Figs.15c and 15d for the interlayer-substrate interface. For normal indentation (μ=0), the ε_{xx} strain is mostly compressive along both interfaces. As expected, the 10 N/mm normal load causes larger magnitude of strains at interfaces than the 5 N/mm normal load. At the top layer-interlayer interface, ε_{xx} on the left side of the contact ($x/a<0$) is tensile due to the tangential force, and the magnitude of the tensile strain increases with the friction coefficient. The magnitude of the compressive strain on the right side of the contact ($x/a>0$) also increases with the friction coefficient. Thus the tangential loading causes larger tensile ε_{xx} strain on the

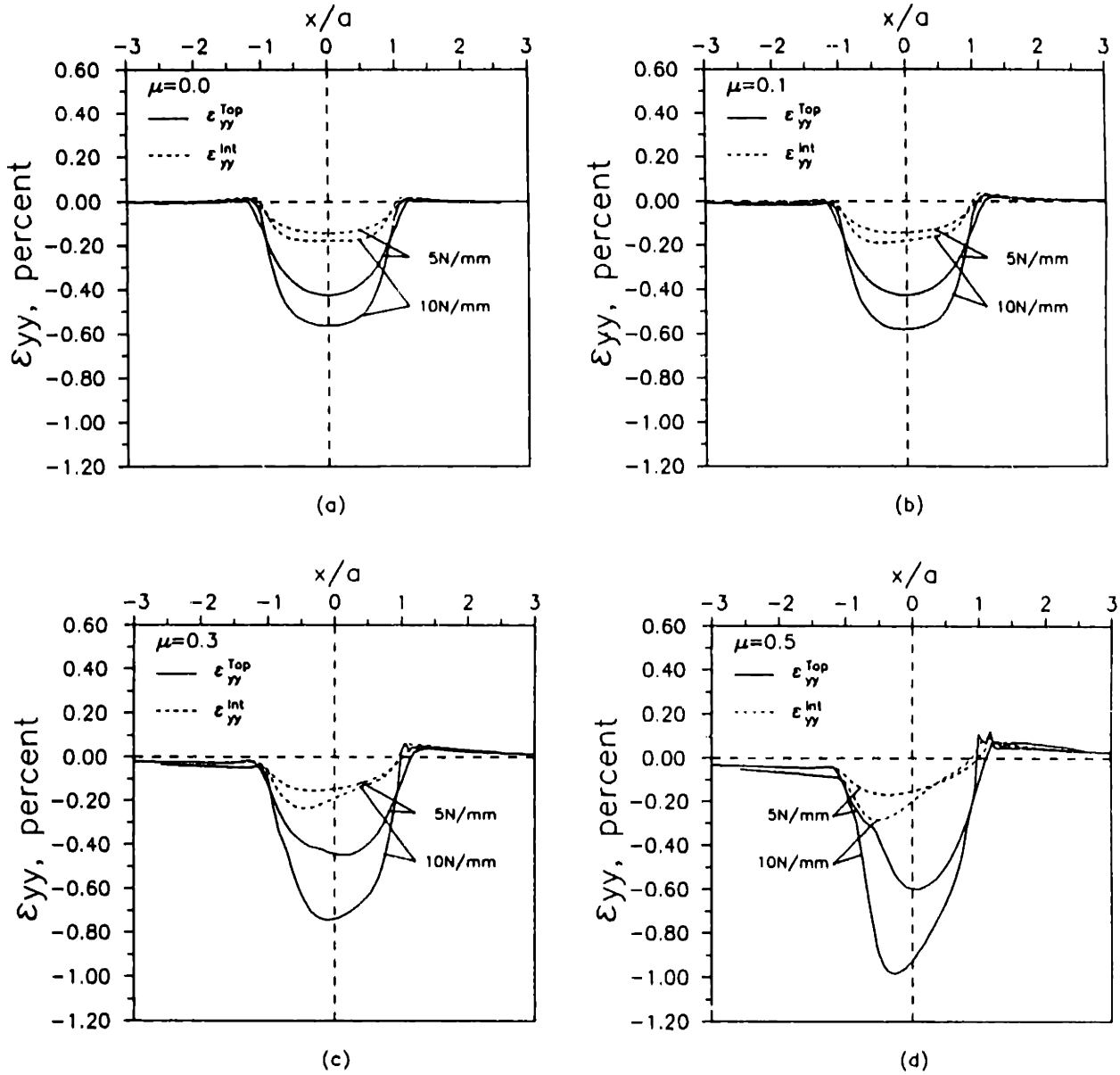

Fig. 5.13 ε_{yy} along the top layer-interlayer interface for various friction coefficients

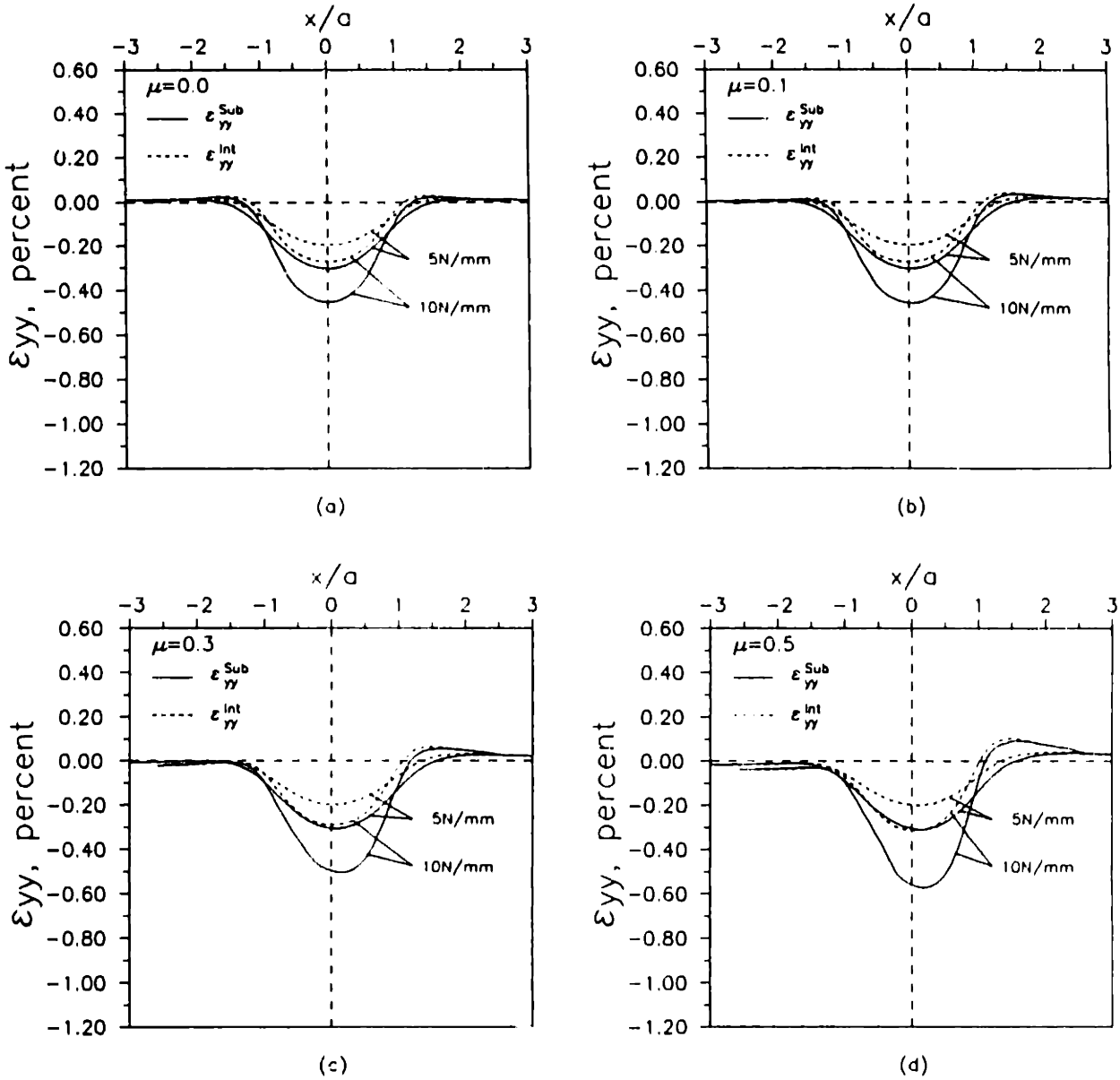

Fig. 5.14 ε_{yy} along the interlayer-substrate interface for various friction coefficients

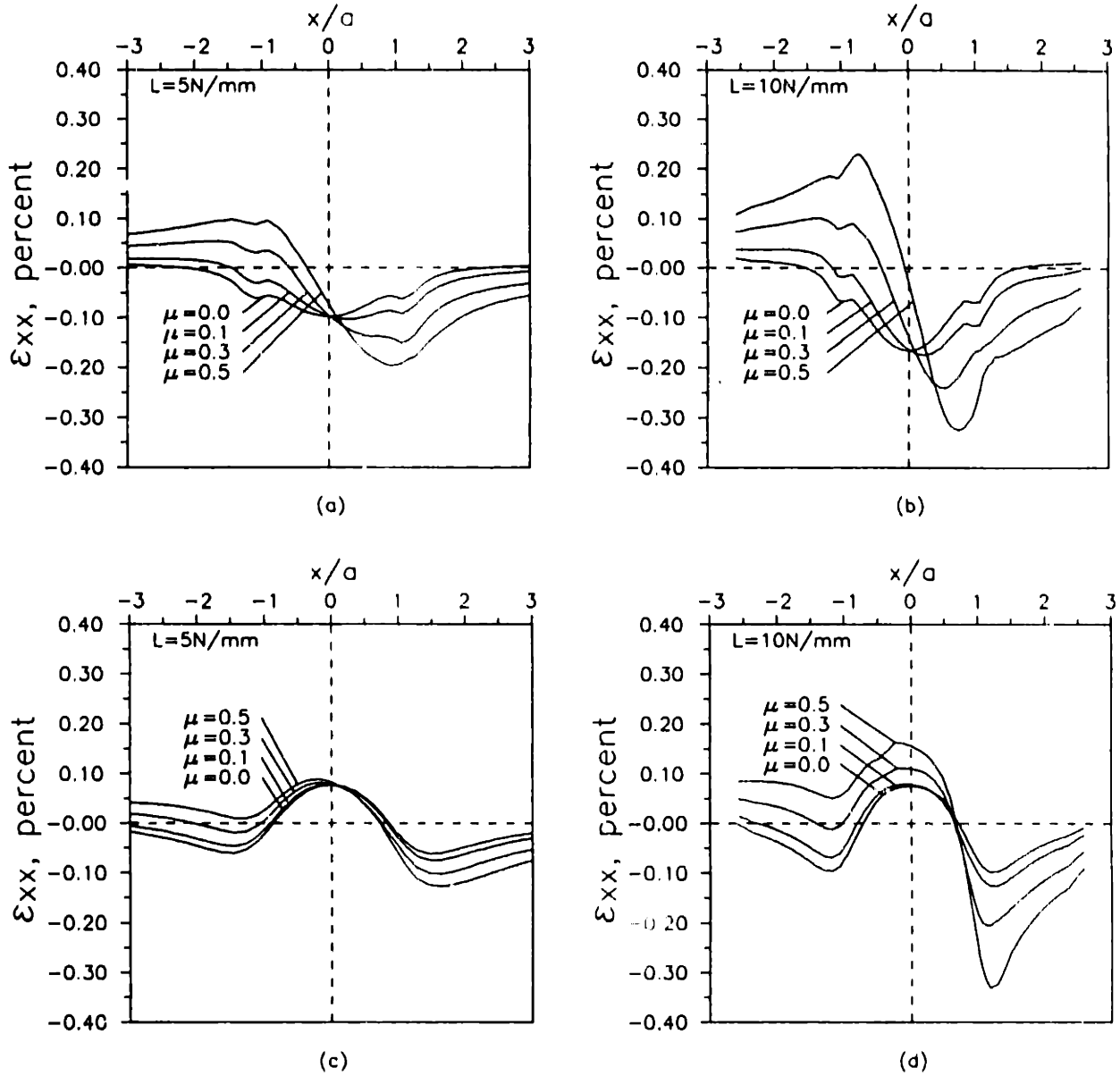

Fig. 5.15 Interfacial ε_{xx} for various friction coefficients: (a) & (b) along the top layer-interlayer interface, (c) & (d) along the interlayer-substrate interface

trailing side and larger compressive ε_{xx} strain at the leading side of the contact. The same effects are also observed at the interlayer-substrate interface (Figures 5.15c and 5.15d).

The shear strain along the interfaces are plotted in Figures 5.16a-16d for the top layer-interlayer interface, and in Figures 5.17a-17d for the interlayer-substrate interface. Again, two sets of shear strain curves appear in the plots because of the constraints of displacement continuity at the interfaces. The solid lines represent the interfacial strains in the top layer or in the substrate, whereas the dashed lines for the strains in the interlayer. For μ=0, the shear strains on the trailing side ($x/a<0$) are in opposite direction to the shear strain on the leading side of the contact. The maximum interfacial shear strain occurs at about $|x/a|=1$ along both interfaces. The shear strains in the interlayer are smaller than those in the top layer or in the substrate. For $\mu>0$, the shear strains tend to be in the direction of sliding. As the friction coefficient increases, the interfacial shear strains in the top layer along the top layer-interlayer interface increase significantly, while the magnitude of interfacial shear strains in the interlayer only increases slightly. Along the interlayer-substrate interface, the magnitudes of the shear strain in the substrate also increase considerably with the friction coefficient, while the shear strains in the interlayer are not greatly affected. At μ=0.5, the interfacial shear strains are almost all along the sliding direction. The maximum magnitude of the interfacial shear strain in the top layer is about 7%, and 1.5% in the substrate. Thus friction has significant impact on the magnitude and distribution of shear strains along both interfaces.

5.4.5 Implications for interfacial cracking

It is evident that the tangential force, or the friction coefficient has a significant effect on the location of yielding, surface deformation, interfacial stresses and strains, etc., especially the shear stresses and strains along the interfaces. In the present study, the interfaces are assumed to be infinitely strong. In reality, the interface can sustain only certain level of stress or strain. As discussed before [18], three criteria have been developed for the initiation of interfacial cracks: energy criterion, the local strain criterion, and the local stress criterion. Among the three, the local shear strain criterion seems to be relevant to the compression-dominated

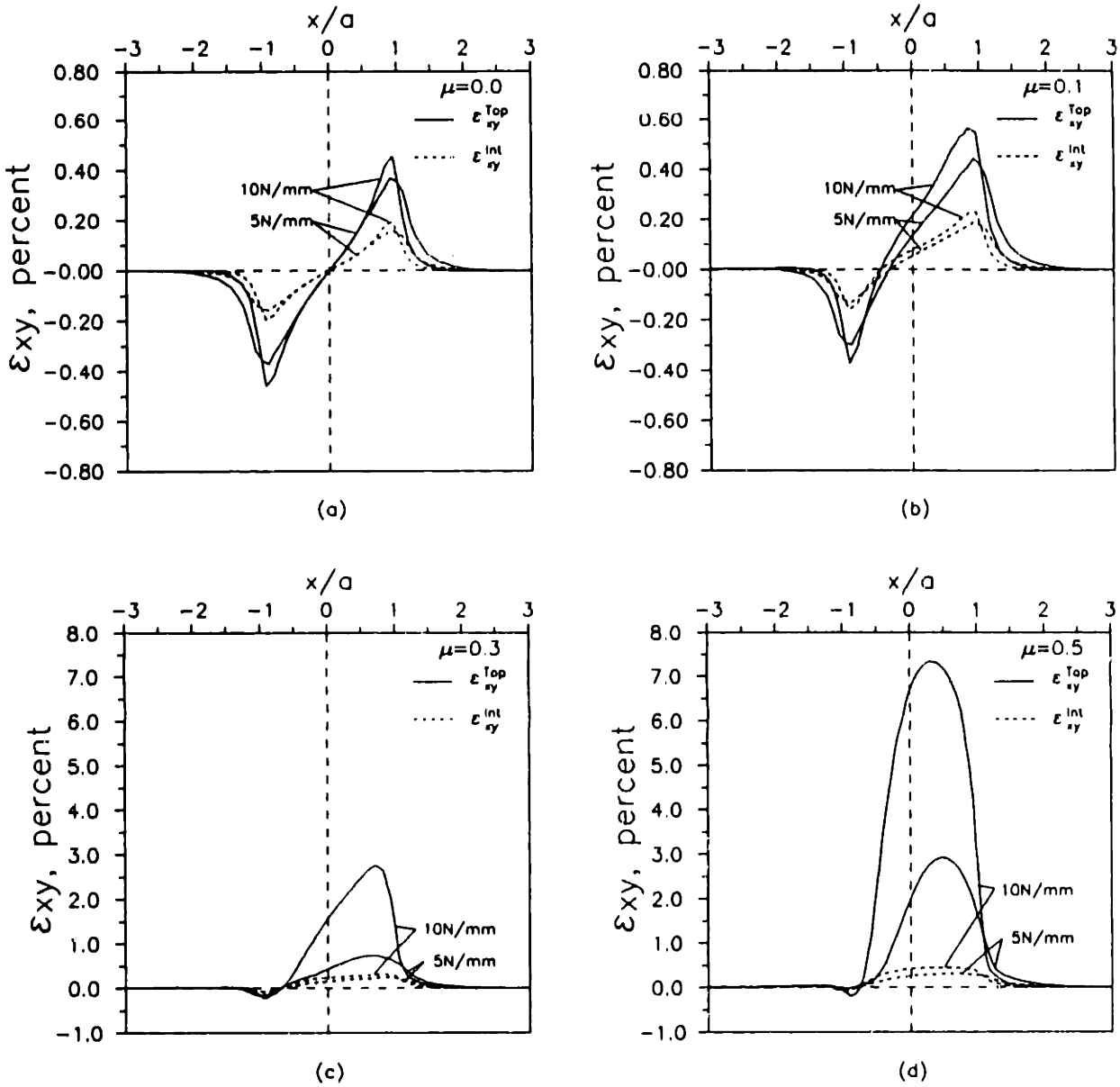

Fig. 5.16 ε_{xy} along the top layer-interlayer interface for various friction coefficients

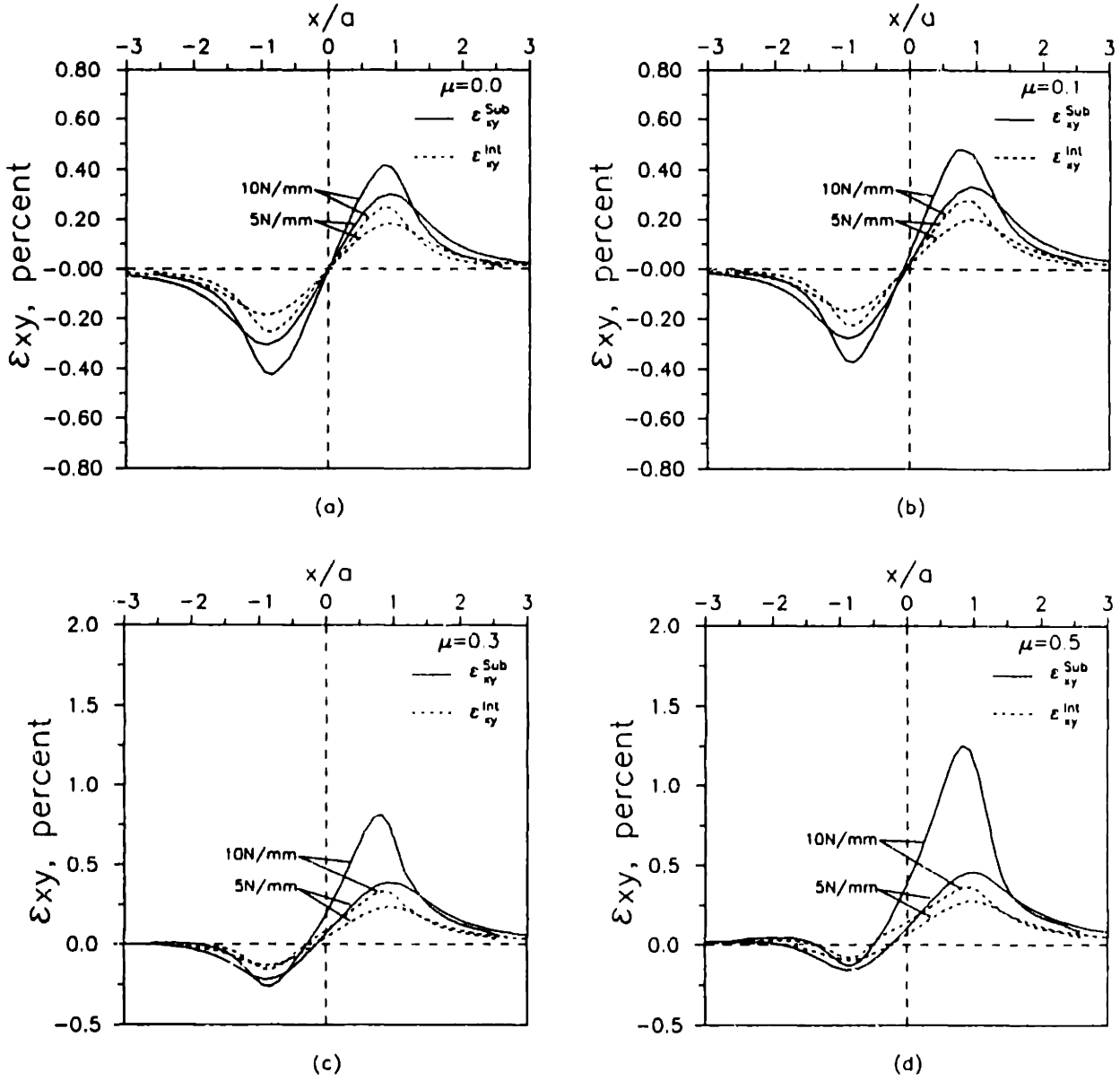

Fig. 5.17 ε_{xy} along the interlayer-substrate interface for various friction coefficients

contact problems. When the interfacial shear strain exceeds a critical value, it is likely that debonding or microcracking occurs.

Thus the interfacial stresses and strains should be minimized as much as possible. It is apparent from the FEM analysis that when the friction coefficient is less than 0.3, the interfacial shear stresses and strains are not much different from the case of normal indentation. But they become significantly larger when the friction coefficient is larger than 0.3, and then the interfacial failure is likely. Thus the sliding friction of a multi-layer contact system should be kept below 0.3. One obvious solution is to use lubricants. When lubricants are not preferable, one should consider the compatibility of sliding contact materials [29, 30]. Low sliding friction can be obtained with incompatible sliding pairs.

The contact stress and strain fields of multi-layer media, unfortunately, cannot be generalized in a concise and elegant form as in the case of homogeneous elastic media [5, 8]. Thus the results obtained here may not be strictly valid for other combinations of multi-layer contact systems. In addition, the analysis presented here is actually for oblique loading on a two-layer half-space. The friction force is modelled by a tangential force acting on the surface. Whether the sliding friction between the contact interfaces can be precisely represented by the surface tractions needs closer examination. Nevertheless, the effect of friction on subsurface stresses and strains are well represented by this study. Moreover, the present study considers only one-time loading. In practice, the contact failure usually takes place after more than one sliding cycle. Merwin and Johnson [31] showed that the plastic shear strain accumulates under repeated loading. Thus the history of loading and accumulation of plastic shear strain are also important in assessing the sliding life of the multi-layer contact systems.

5.5 Conclusions

A finite element analysis of the sliding contact of a two-layer elastic-plastic half-space was conducted. The following conclusions can be drawn from the analysis.

(a) Surface deformation and profile are strongly affected by the friction coefficient. The surface material is deformed along the sliding direction. A small hump is observed at the leading edge of the contact when the friction coefficient is large.

(b) The location of initial yielding strongly depends on the friction coefficient as well as the normal load. Yielding initiates in the substrate for a small friction coefficient if the normal load is large enough. When $\mu \geq 0.3$, yielding initiates on the surface (and in the substrate as well if the normal load is larger). Whenever yielding initiates on the surface, it always occurs near the trailing edge of the contact. Whenever the yielding initiates in the subsurface, however, it occurs at the leading region of the contact. The tangential force is the primary cause of the uncontained plastic deformation of the top layer.

(c) Normal stresses and strains along the interfaces are not greatly affected by friction. The horizontal and shear stresses and strains along the interfaces are strongly influenced by the friction coefficient. For frictional loading, σ_{xx} in the trailing region of the contact is tensile, and is compressive in the leading region of the contact. The magnitudes of shear stress and strain along both interface increases significantly with the friction coefficient.

References

[1] *Principles of Electronic Packaging*, ed. by D. P. Seraphim, R. Lasky, and C-Y. Li, McGraw-Hill, Inc., New York, 1989.

[2] Johnson, K. L., "One Hundred Years of Hertz Contact," *Proc. Institution of Mechanical Engineers*, Vol. 196, 1982, pp. 363-378.

[3] M'Ewan, E., "Stresses in Elastic Cylinders in Contact Along a Genratrix," *Phil. Mag.*, Vol. 40, 1949, pp. 454-459.

[4] Poritsky, H., "Stresses and Deflections of Cylindrical Bodies," *J. Appl. Mech.*, Vol. 17, 1950, pp. 191-201.

[5] Smith, J. L. and Liu, C. K., "Stresses Due to Tangential and Normal Loads on an Elastic Solid with Application to Some Contact Stress Problems," *J. Appl. Mech.*, Vol. 20, 1953, pp. 157-166.

[6] Johnson, K. L. and Jefferis, J. A., "Plastic Flow and Residual Stresses in Rolling and Sliding Contact," *Proc. Institution of Mechanical Engineers Symposium on Rolling Contact Fatigue*, London, 1963, pp. 54-77.

[7] Hamilton, G. M. and Goodman, L. E., "The Stress Field Created by a Circular Sliding Contact," *J. Appl. Mech.*, Vol. 33, 1966, pp. 371-376.

[8] Hamilton, G.M., "Explicit Equations for the Stresses Beneath a Sliding Spherical Contact," *Proc. Institution of Mechanical Engineers* , Vol. 197C, 1983, pp. 53-59.

[9] Bryant, M. D. and Keer, L. M., "Rough Contact Between Elastically and Geometrically Identical Curved Bodies," *J. Appl. Mech.*, Vol. 49, 1982, pp. 345-352.

[10] Sackfield, A. and Hills, D. A., "Some Useful Results in the Classical Hertz Contact Problem," *J. Strain Analysis*, Vol. 18, 1983, pp. 101-105.

[11] Sackfield, A. and Hills, D. A., "Some Useful Results in the Tangentially Loaded Hertzian Contact Problem," *ibid*, 1983, pp. 107-110.

[12] Sackfield, A. and Hills, D. A., "Sliding of a General Axisymmetric Point Contact," *J. of Tribology, Trans. ASME*, Vol. 110, 1988, pp. 492-498.

[13] Nagaraj, H. S., "Elastoplastic Contact of Bodies With Friction Under Normal and Tangential Loading," *J. of Tribology, Trans. ASME*, Vol. 106, 1984, pp. 519-526.

[14] Tangena, A. G. and Hurkx, G. A. M., "Calculations of Mechanical Stresses in Electrical Contact Situations," *IEEE Trans. on Components, Hybrids, and Manufacturing Technology*, Vol. CHMT-8 (1), 1985, pp. 13-20.

[15] Ihara, T., Shaw, M. C. and Bhushan, B., "A Finite Element Analysis of Contact Stress and Strain in an Elastic Film on a Rigid Substrate -- Part II: With Friction," *J. Tribology, Trans. ASME,* Vol. 108, 1986, pp. 534-539.

[16] King, R. B. and O'Sullivan, T. C., "Sliding Contact Stresses in a Two-Dimensional Layered Elastic Half-Space," *Int. J. of Solids Structures,* Vol. 23, 1987, pp. 581-597.

[17] Komvopoulos, K., Saka, N., and Suh, N. P., "The Role of Hard Layers in Lubricated and Dry Sliding," *J. of Tribology, Trans. ASME,* Vol. 109, 1987, pp. 223-231.

[18] O'Sullivan, T. C. and King, R. B., "Sliding Contact Stress Field Due to a Spherical Indenter on a Layered Elastic Half-Space," *J. of Tribology, Trans. ASME,* Vol. 110, 1988, pp. 235-240.

[19] Tian, H. and Saka, N., "Finite Element Analysis of A Two-Layer Elastic-Plastic Half-Space: Normal Contact," Submitted to *J. Tribology, Trans. ASME* , 1989.

[20] Johnson, K. L., *Contact Mechanics,* Cambridge University Press, Cambridge, U.K., 1985, pp. 119-124.

[21] Mindlin, R. D., "Compliance of Elastic Bodies in Contact," *J. Appl. Mech., ASME Trans.*, Vol. 16, 1949, pp. 259-268.

[22] Mindlin, R. D. and Deresiewicz, H., "Elastic Spheres in Contact Under Varying oblique Forces," *J. Applied Mechanics, ASME Trans.*, Vol. 20, 1953, pp. 327-344.

[23] Deresiewicz, H., "Oblique Contact of Nonspherical Elastic Bodies," *J. Applied Mechanics, ASME Trans.*, Vol. 24, 1957, pp. 623-624.

[24] Jahanmir, S. and Suh, N. P., "Mechanics of Subsurface Void Nucleation in Delamination Wear," *Wear,* Vol. 44, 1977, pp. 17-38.

[25] Gupta, P. K., Walowit, J. A., and Finkin, E. F., "Stress Distributions in Plane Strain Layered Elastic Solids Subjected to Arbitrary Boundary Loading," *J. of Lubrication Technology, Trans. ASME,* Vol. 95, 1973, pp. 427-433.

[26] Johnson, K. L., *Contact Mechanics,* Cambridge University Press, Cambridge, U.K., 1985, pp. 171-184.

[27] Johnson, K. L., *Ibid,* 1985, pp. 202-210.

[28] Johnson, K. L., "Aspects of Friction," *Proc. 7th Leeds-Lyon Symposium on Tribology,* University of Leeds, England, 1980, pp. 3-12.

[29] Rabinowicz, E., "The Influence of Compatibility on Different Tribological Phenomena," *ASLE Trans.* Vol. 14, 1971, pp. 206-212.

[30] Barber, S. A. and Rabinowicz, E., "Material Selection for Noble Metal Slip Rings," *Proc. Holm Conference on Electrical Contacts,* Illinois Inst. of Technology, Chicago, IL, 1980, pp. 33-40.

[31] Merwin, J. E. and Johnson, K. L., "An Analysis of Plastic Deformation in Rolling Contact," *Proc. Instn. Mech. Engrs.,* Vol. 177, 1963, pp. 676-690.

Chapter 6

Finite Element Analysis of Interface Cracking in Sliding Contacts

Summary

A plane strain finite element model for the growth of an interface crack in an elastic-plastic two-layer half-space in a sliding contact is presented. The elastic theories of interface cracking are briefly reviewed, and the limitations of elastic solutions to the present problem are discussed based on the finite element calculations. The elastic-plastic analysis has shown that the size of plastic zone around the crack tips is comparable to the crack length and the coating thickness. Plastic deformation at crack tips expands primarily in two directions as predicted by a slip-line field for a closed interface crack. The crack sliding displacements (CSD) for various loading positions are calculated. Both the surface friction and the crack face friction have significant effects on the plastic zone size and the values of CSD. The surface friction tends to increase the plastic zone size and enhance the relative displacement of the crack faces in the direction of the friction force. The crack face friction, by contrast, considerably reduces the plastic zone size and the values of CSD.

Nomenclature

a	=	half contact width
c	=	half crack length
E	=	Young's modulus
E_p	=	plastic modulus
$\bar{E}$	=	plane strain elastic modulus
f	=	friction coefficient
f_c	=	friction coefficient between crack faces
f_{ij}^k	=	dimensionless angular function
G	=	strain energy release rate
G_c	=	critical strain energy release rate (toughness)
g_{ij}^k	=	dimensionless angular function
h_1	=	thickness of top layer
h_2	=	thickness of interlayer
J	=	J - integral
k	=	shear yield strength
$\mathbf{K}$	=	complex stress intensity factor
K_{II}^c	=	strength of singularity at closed crack tip
L	=	characteristic length
N	=	normal force per unit length
p, p_c	=	pressure
R	=	dimensionless angular function
$r, \theta,$	=	cylindrical coordinates
r_p	=	plastic zone size of traction-free crack tip
r_p^c	=	plastic zone size of closed crack tip
T	=	tangential force per unit length
u_i	=	components of displacement
$x, y,$	=	cartesian coordinates
$\Delta u_x, \Delta u_y,$	=	components of relative crack face displacement
α, β	=	Dundurs' parameters of bimaterials
δ	=	contact length in the contact zone behind closed crack tip

ε	=	oscillatory index of bimaterials
$\gamma_{r\theta}$	=	shear strain
φ	=	angle
μ, μ_1, μ_2	=	shear moduli
ν, ν_1, ν_2	=	Poisson's ratios
$\sigma_{rr}, \sigma_{\theta\theta}, \tau_{r\theta}$	=	components of stress in cylindrical coordinates
$\sigma_{xx}, \sigma_{yy}, \tau_{xy}$	=	components of stress in cartesian coordinates
σ_{ys}	=	yield strength in simple tension
ψ	=	phase angle of $KL^{i\varepsilon}$
ζ	=	phase angle

1. Introduction

Multi-layer systems, which consist of two or more different materials, have been commonplace in electrical packaging, optical devices, megnetic recording, and electrical connectors. And the evaluation and enhancement of the mechanical reliability of these multi-layer systems have become the immediate concern of both applied mechanicians and materials scientists. Naturally, the attention is focused on the strength and fracture behavior of the interfaces. It has been reported from a number of experimental observations that the decohesion or delamination process occur at various bimaterial interfaces due to thermal stresses [1-4] and mechanical loading [5-7]. Therefore a basic understanding of the mechanics of interface cracking is necessary to assure better design of the multi-layer systems.

The present study focuses on a tribological problem, interface cracking in sliding contacts. To our knowledge, the interface cracking or the delamination of multi-layer systems in sliding contacts has not been studied yet. Subsurface cracking in homogeneous materials, however, has been extensively analyzed since the delamination theory of wear was advanced by Suh [8]. For example, Jahanmir and Suh [9] showed that subsurface cracks nucleate most likely due to void coalescence. Fleming and Suh [10,11] used the concepts of Linear Elastic Fracture Mechanics (LEFM) to analyze the subsurface crack growth. They showed that the propagation, not the nucleation, of subsurface cracks is the main part of the delamination process in materials with second phase particles [12]. LEFM was also used by Rosenfield [13], Hills and Ashelby [14,15], Keer et al. [16], and others [17-21] to study subsurface cracking. One of the major conclusions of the LEFM analyses is that the mode II stress intensity factor is the driving force for subsurface cracking. Because the subsurface crack is in a compressive stress field in a sliding contact, it propagates most likely in shear, parallel to the contact surface to a certain length [22], and breaks through the surface under certain loading and geometric conditions.

The LEFM approach, however, has serious limitations when the plastic zone surrounding the crack tip is large, i.e., when the assumption of small-scale yielding is not satisfied. Rosenfield [23,24] applied a dislocation model developed by Bilby, Cottrell and Swinden [25] to model the large plastic deformation at the crack tip.

The relative sliding displacement between the crack face, referred to as crack sliding displacement (CSD), was considered as a control parameter of the crack propagation rate. The experimental observations have shown that the CSD is indeed a fair indicator of the fatigue crack growth under mode II loading conditions [26]. This view was also adopted by Sin and Suh [27] in their elastic-plastic finite element analysis of subsurface cracking in sliding contact, and by Bastias et al. [28] in their elastic modelling of subsurface cracking in rolling contact.

While the extensive experimental and theoretical studies have greatly contributed to the understanding of subsurface cracking in homogeneous materials, subsurface cracking along interfaces in multi-layer media is expected to be far more complex. But the techniques used in the analysis of homogeneous materials can be readily adopted to the analysis of interface cracking. Recently Kim et al. [29] have analyzed the interface cracking of a single layer bonded to an elastic substrate under a moving concentrated load. They concluded that the crack growth is governed by the mode II stress intensity factor but is retarded by the presence of crack face friction. Their elastic solutions are valid for the fracture of hard coatings along the interface. For the ductile multi-layer contact systems, however, plastic deformation around the crack tip cannot be ignored.

In the present study, the interface cracking of the multi-layer contact systems primarily used in electrical connectors is considered. First the elastic theory of fracture mechanics of bimaterials is briefly reviewed and the limitations of elastic solutions are discussed on the basis of the finite element analysis. Then an elastic-plastic finite element analysis is carried out to study the interface cracking in sliding contacts, i.e., under normal and tangential loading. The effects of friction (both on the surface and between crack faces) are also investigated. Finally the implications to the fatigue life of sliding and fretting multi-layer systems are discussed.

2. Elasticity Theory of Interface Fracture

Fracture mechanics of interface cracking deals with the growth of a planar or curved crack along the interface of a bimaterial structure. The bimaterial is a "composite" of two homogeneous materials, isotropic or anisotropic, with continu-

ity of traction and displacements across the interfaces. In the present study only the zero-thickness mathematical interfaces is considered.

In general, the elastic stress field in a bimaterial depends on three dimensionless parameters, ν_1, ν_2, and μ_1/μ_2, where ν's are the Poisson's ratios and μ's the shear moduli. Subscripts 1 and 2 refer to the two materials. For traction prescribed boundary value problems, Dundurs [30] showed that the stresses in the bimaterial depend on only two dimensionless parameters, α and β, which are referred to as the Dundurs' bimaterial parameters:

$$\alpha = \frac{(1-\nu_2)/\mu_2 - (1-\nu_1)/\mu_1}{(1-\nu_2)/\mu_2 + (1-\nu_1)/\mu_1}, \qquad \beta = \frac{1}{2}\frac{(1-2\nu_2)/\mu_2 - (1-2\nu_1)/\mu_1}{(1-\nu_2)/\mu_2 + (1-\nu_1)/\mu_1} \tag{6.1}$$

α can also be expressed as:

$$\alpha = \frac{\bar{\bar{E}}_1 - \bar{\bar{E}}_2}{\bar{\bar{E}}_1 + \bar{\bar{E}}_2}, \qquad \bar{\bar{E}} = \frac{E}{1-\nu^2} = \frac{2\mu}{1-\nu} \tag{6.2}$$

where E is the Young's modulus. Equation (6.2) shows that α measures the relative stiffness of the two materials. Another useful parameter, ε, called oscillatory index, is related to β as:

$$\varepsilon = \frac{1}{2\pi} \ln \frac{1-\beta}{1+\beta} \tag{6.3}$$

The three parameters α, β and ε, are defined according to the configuration in Fig. 6.1. Their signs change when materials 1 and 2 switch, and their values vanish when the two materials have identical elastic constants. Based on the data of various material combinations, Suga et al. [31] showed that $|\alpha| \leq 1$, $|\beta| \leq 0.25$, implying that $|\varepsilon| \leq 0.0813$. For example, $\alpha = \pm 1$, $\beta = \pm 0.25$, and $\varepsilon = \pm 0.0813$ (for $\nu = 1/3$) if one of the materials is rigid.

Two kinds of modelings of interfacial crack tips have been developed over the past four decades. The first model assumes that the crack faces are traction-free,

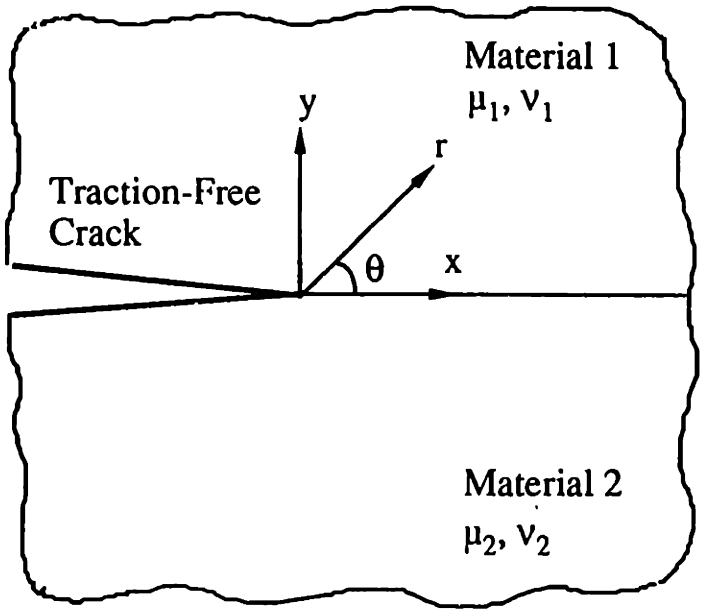

(a)

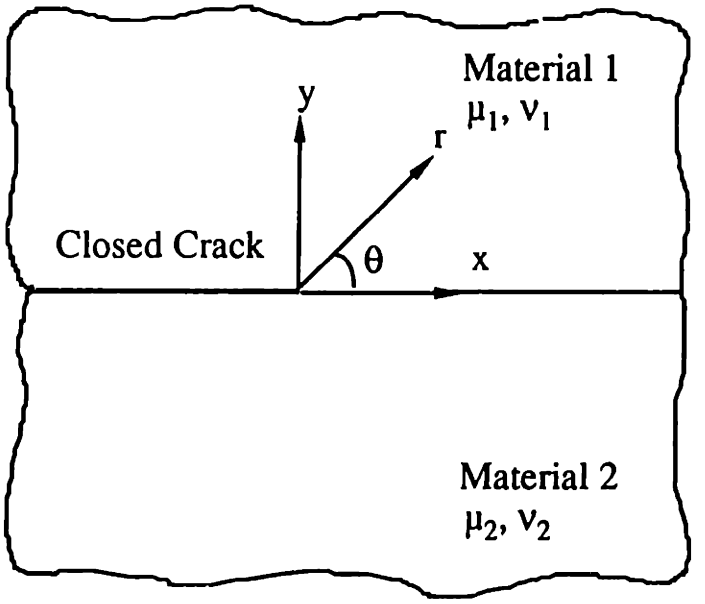

(b)

Fig. 6.1 Schematic models of interface cracks: (a) Traction-free crack tip and (b) closed crack tip model

known as traction-free crack tip model. The other model, known as the closed crack tip model, assumes that the crack faces immediately behind the crack tip are in contact. The contact zone is assumed to be frictionless. Thus in the second model the crack faces within the contact zone can transmit the normal compressive stresses but are free to slide relative to each other.

Rice [32] and Hutchinson [33] have recently reviewed the elasticity theories of interface fracture mechanics and generalized a universal singular crack tip field for a traction-free planar interface crack. Williams [34] was the first to obtain the asymptotic solutions for a traction free crack tip of an interface crack between two dissimilar elastic isotropic materials. The elastic solutions to various loadings and geometries concerning the interface cracks were also obtained by England [35], Erdogan [36], Sih and Rice [37], Rice and Sih [38], and recently by Park and Earmme [39], Hutchinson et al. [40], Shih and Asaro [41,42], and Suo and Hutchinson [43]. The general results presented here are based on the solutions obtained by Rice [32]. Consider a semi-infinite traction-free crack lying along the interface between two homogeneous isotropic half space, with material 1 above and material 2 below (Fig. 6.1a). A cartesian coordinate system (x, y, z) and a cylindrical coordinate system (r, θ, z) are set up at the crack tip. The asymptotic stresses and displacements in material 1 can be expressed as [32]

$$\sigma_{ij} = \frac{1}{\sqrt{2\pi r}}\left[\mathrm{Re}\left(\mathbf{K}r^{i\varepsilon}\right) f_{ij}^{(1)}(\theta, \varepsilon) + \mathrm{Im}\left(\mathbf{K}r^{i\varepsilon}\right) f_{ij}^{(2)}(\theta, \varepsilon)\right] \tag{6.4}$$

$$u_i = \frac{1}{2\mu_1}\sqrt{\frac{r}{2\pi}}\left[\mathrm{Re}\left(\mathbf{K}r^{i\varepsilon}\right) g_{ij}^{(1)}(\theta, \varepsilon, \nu_1) + \mathrm{Im}\left(\mathbf{K}r^{i\varepsilon}\right) g_{ij}^{(2)}(\theta, \varepsilon, \nu_1)\right] \tag{6.5}$$

where **K** is the complex stress intensity factor, and is defined as [40]

$$\mathbf{K} = \lim_{r\to 0} \sqrt{2\pi r}\,\frac{\left[\sigma_{yy}(r, \theta=0) + i\sigma_{xy}(r, \theta=0)\right]}{r^{i\varepsilon}} \tag{6.6}$$

The dimensionless angular functions $f_{ij}^{k}(\theta, \varepsilon)$ and $g_{ij}^{k}(\theta, \varepsilon, \nu)$ can be obtained from the complex potentials in reference [32].

The stresses ahead of the crack tip (θ=0) reduce to a simple equation:

$$\sigma_{yy} + i\sigma_{xy} = \frac{1}{\sqrt{2\pi r}} \mathbf{K} r^{i\varepsilon} \tag{6.7}$$

The displacement jumps across the interface behind the crack tip ($\theta=\pm\pi$) are

$$\Delta u_y + i\Delta u_x = \frac{4}{\sqrt{2\pi}} \frac{(1/\bar{E}_1 + 1/\bar{E}_2)}{(1+2i\varepsilon)\cosh(\pi\varepsilon)} \mathbf{K} \sqrt{r}\, r^{i\varepsilon} \tag{6.8}$$

and the strain energy release rate per unit length of interface crack growth is

$$G = J = \frac{(1/\bar{E}_1 + 1/\bar{E}_2)}{2\cosh^2(\pi\varepsilon)} \mathbf{K}\bar{\mathbf{K}} \tag{6.9}$$

where J is the conservation integral [44] and $\bar{\mathbf{K}}$ the complex conjugate of **K**.

In real materials, however, these asymptotic stress fields are disturbed by the inelastic behavior of the crack tip and by the finite geometry. Zywicz and Parks [45] considered an interface crack between two elastic half-spaces and provided an estimate of the plastic zone size r_p around the traction free interface crack tip as

$$r_p(\theta) = \frac{\mathbf{K}\bar{\mathbf{K}}}{\sigma_{ys}^2 \pi \cosh^2(\pi\varepsilon)} R[\theta, \varepsilon, \zeta(\theta)] \tag{6.10}$$

where

$$\zeta(\theta) = \angle\mathbf{K} + \varepsilon \ln r_p(\theta) \tag{6.11}$$

If $r_p \ll L$, where L is a characteristic length (usually the crack length), then the small-scale yielding (SSY) assumption is satisfied and the asymptotic **K**-fields are valid in an annulus larger than the plastic zone but smaller than the external geometry. Rice [32] was the first to assemble the concepts of interface fracture mechanics based on Irwin's K-annulus notion and Williams' interface crack tip field. The critical strain energy release rate of the interface (toughness), G_c, is not a single value as in the fracture mechanics of homogeneous materials; rather, it is a function of the angle ψ, where ψ is the phase angle of the quantity $\mathbf{K}L^{i\varepsilon}$. G_c has to be measured experimentally for all mode combinations. Once The G_c-ψ curve is obtained for a particular interface, then the stress intensity factor **K**, the energy

release rate G, and the phase angle ψ need to be determined for prescribed geometries and loadings. The energy release rate G for a specific ψ is compared with $G_c(\psi)$ to examine whether the interface crack grows or stays put.

A characteristic feature of the traction-free crack tip field is that the overlapping of crack faces behind the crack tip is predicted by the asymptotic solutions, which implies that a contact zone must exist behind the crack tip. For a large range of the phase angle ψ, the contact zone is small enough so that the K-annulus still exist around the crack tip. In most tribological problems, however, a large contact zone exists between crack faces. Thus the traction free model is no longer applicable, and the effect of the contact zone must be explicitly considered.

Comninou [46-48] incorporated a frictionless contact zone at the interface crack tip into the crack-tip model (Fig. 6.1b). In the contact zone, the crack faces are subjected to compressive normal traction but are free to slide over each other. As $r\to 0$, the dominant stress and displacement fields in the material 1 (above) are given by

$$\sigma_{rr} = \frac{-K_{II}^c}{4\sqrt{2r}}\left[5(1-\beta)\sin\frac{\theta}{2} - (3+\beta)\sin\frac{3\theta}{2}\right] \tag{6.12a}$$

$$\sigma_{r\theta} = \frac{K_{II}^c}{4\sqrt{2r}}\left[(1-\beta)\cos\frac{\theta}{2} + (3+\beta)\cos\frac{3\theta}{2}\right] \tag{6.12b}$$

$$\sigma_{\theta\theta} = \frac{-K_{II}^c}{4\sqrt{2r}}\left[3(1-\beta)\sin\frac{\theta}{2} + (3+\beta)\sin\frac{3\theta}{2}\right] \tag{6.12c}$$

$$u_r = \frac{-K_{II}^c\sqrt{2r}}{4\mu_1}\left[(2\kappa_1-1)(1-\beta)\sin\frac{\theta}{2} - (3+\beta)\sin\frac{3\theta}{2}\right] \tag{6.13a}$$

$$u_\theta = \frac{-K_{II}^c\sqrt{2r}}{4\mu_1}\left[(2\kappa_1+1)(1-\beta)\cos\frac{\theta}{2} - (3+\beta)\cos\frac{3\theta}{2}\right] \tag{6.13b}$$

where $\kappa_1=3-4\nu$ for plane strain, $\kappa_1=(3-\nu)/(1+\nu)$ for plane stress, and K_{II}^c is the strength of singularity which is defined as

$$K_{II}^c = \lim_{r\to 0}\left[\sqrt{2r}\,\sigma_{xy}(r,\theta=0)\right] \tag{6.14}$$

K_{II}^c is the common mode II stress intensity factor when $\beta=0$. The stresses and displacements in material 2 can also be obtained from the above equations by changing the sign of β, and by changing μ and κ accordingly. The strain energy release rate, G, is related to K_{II}^c as follows

$$G = J = \frac{K_{II}^{c\,2}\,\pi\,(1/\bar{E}_1 + 1/\bar{E}_2)}{2\cosh^2(\pi\varepsilon)} \tag{6.15}$$

Comninou's closed crack tip model predicts square-root singularity of shear stress $\sigma_{r\theta}$. Zywicz and Parks [49] calculated the Mises equivalent stress based on this asymptotic stress field and suggested that the characteristic length scale of plastic zone at the closed crack tip can be well represented by

$$r_p^c = \frac{3}{2}\left[\frac{K_{II}^c}{\sigma_{ys}}\right]^2 \tag{6.16}$$

The relationship between **K** of traction-free crack tip model and K_{II}^c of closed crack tip model was also obtained by Zywicz and Parks [49] for the case of small-scale contact (SSC), i.e., when the length of the contact zone, δ, is small compared with other characteristic lengths.

$$K_{II}^c = \pm\sqrt{\frac{1}{\pi}\mathbf{K}\bar{\mathbf{K}}} \tag{6.17}$$

where the sign of K_{II}^c is so chosen as to assure the compressive normal traction in the contact zone, i.e., $K_{II}^c < 0$ if $\beta < 0$; $K_{II}^c > 0$ if $\beta > 0$.

The application of **K**-field and K_{II}^c-field depends on the two conditions: small-scale contact (SSC) and small-scale yielding (SSY) [50]. When the SSC is in the SSY, i.e, the contact length δ is smaller than the characteristic size of a plastic zone ($\delta << r_p << L$), the **K**-field can be used to accurately represent the elastic behavior of crack tip region. On the other hand, when the SSY is in the SSC, i.e., $r_p << \delta << L$, the K_{II}^c-field would well describe the crack tip elastic behavior. When r_p is of the same order of δ, however, it is not clear which model provides better description of crack tip behavior. At any rate, for most tribological problems, the contact length is much larger than the plastic zone size. Thus the K_{II}^c-field can be used provided that the SSY conditions are satisfied.

The elastic solutions are now available for Griffith's type interface cracks and for some interface cracks with finite but simple geometries. For a multi-layer half-space in a sliding contact, is is difficult (if it is not impossible) to obtain the analytical solutions. Thus the finite element method must be used to obtain the elastic and elastic-plastic solutions of interface cracking.

3. Finite Element Model

3.1 Statement of the problem

Now, consider a two-layer half-space under normal and tangential forces per unit length, N and T. Fig. 6.2 illustrates the coordinate system and the dimensions of the layers. The thicknesses of the top layer and the interlayer are h_1 and h_2, respectively. In electrical connectors, the top layer is gold, and the interlayer is nickel, and the substrate is brass or other copper-based alloys. From experimental observations [6,7], the interface failure was found to occur primarily at the nickel-brass interface, i.e., the interface between interlayer and substrate. Thus the pre-existing crack of length 2c is placed at the interlayer-substrate interface. The tangential surface traction is in the positive x direction. The distance from the loading centerline to the crack centerline is denoted by x_L. The negative values of x_L indicate that the loading centerline is on the left-hand side of crack centerline, and the positive values on the right side.

The elastic and plastic properties of the layers are listed in Table 6.1. In the elastic-plastic finite element analysis, the interlayer was assumed to be infinitely stiff, and the top layer and the substrate were assumed to follow a bilinear elastic-plastic behavior. The plastic modulus, E_p, was assumed to be a fraction of elastic modulus. The tractions and the displacements were assumed continuous in the bonded part of the interface. The crack faces were assumed to transfer the normal compressive traction as well as slide relative to each other. The crack faces were assumed to be frictional, with a friction coefficient f_c.

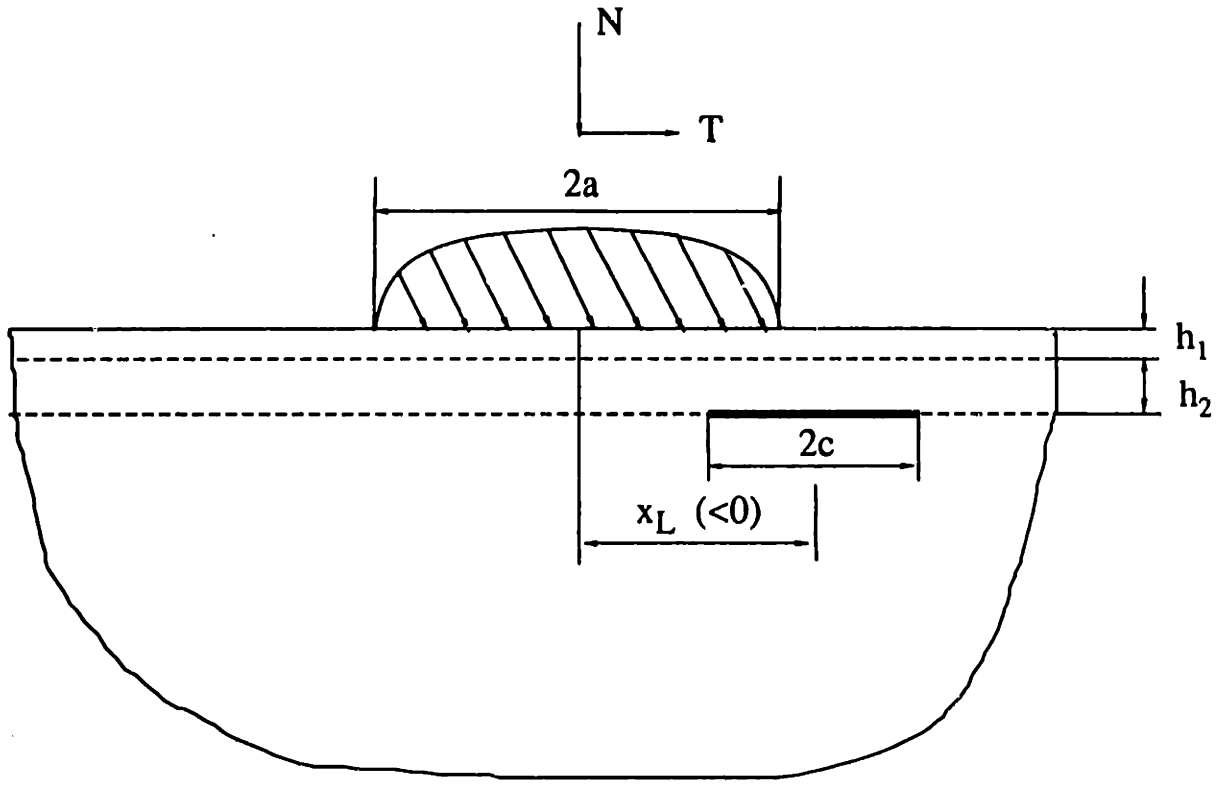

Fig. 6.2 Schematic of geometry of an interface crack

Table 6.1 Mechanical properties of layered materials

Material	E (GPa)	ν	σ_{ys} (MPa)	E_p(GPa)
Top Layer (Au+0.5%Ni)	79	0.32	298	7.90
Interlayer (Ni)	205	0.32	811	-
Substrate (Brass: Cu-35%Zn)	125	0.32	405	1.25

3.2 Finite element mesh and procedures

The finite element mesh used for the stress analysis of sliding contact without an interface crack in the previous work [51] was used, with a specially refined mesh near the region below the contact for modelling the interface crack. The global dimensions of the mesh and boundary conditions were the same as those in [51]. The whole mesh is an arrangement of 1200 quadrilateral, eight-node, isoparametric elements, and the total number of nodes is 4423. The two-layer half-space was modelled by assigning different elastic and plastic properties to the elements of top rows of the mesh. Fig. 6.3 shows the fine mesh for the region of interface crack. The mesh for the regions around the crack tips consists of a series of circles, logarithmically spaced toward the crack tip. Fig. 6.4 shows the configurations at the crack tip. All crack tip elements are collapsed into triangles at the tip. All the nodes at the crack tip have the same initial coordinates and were constraned for the elastic analsysis. For the elastic-plastic analysis, however, no constraints were imposed on the nodes at the crack tips. The uncracked part of the interfaces between the interlayer and substrate were assumed to be perfectly bonded, i.e., the displacements at the interfaces were continuous ahead of the crack tips. The crack faces were modelled by 24 three-node interface elements, which prevent the interpenetration of the crack faces but allow relative motions between them. The initial nodal spacings between the crack faces were zero. The parameter associated with the interface elements, the "friction coefficient", was assumed to represent the true friction coefficient between the crack faces, f_c.

Two more assumptions were made in modelling the sliding contact. It was assumed that the pressure distribution in the contact region on the surface is not influenced by the presence of the interface crack. Further, tangential force or friction force was assumed not to affect the normal pressure distribution. Accordingly, the pressure distribution of the sliding contact was obtained by using the previous finite element mesh in reference [52] based on the current geometrical parameters and elastic-plastic properties. Then the calculated normal pressure plus the tangential traction (which is equal to the friction coefficient times the pressure) was used in the analysis of interface cracking.

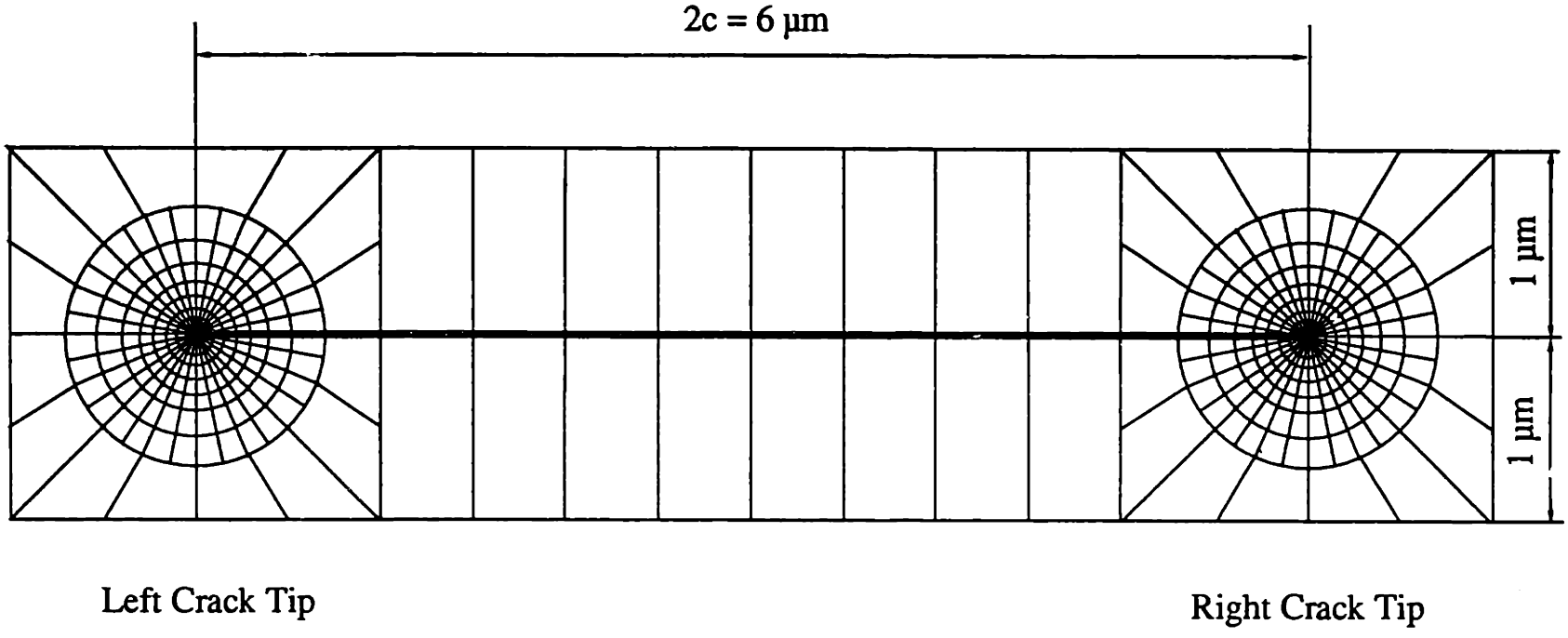

Fig. 6.3 Finite element mesh for an interface crack

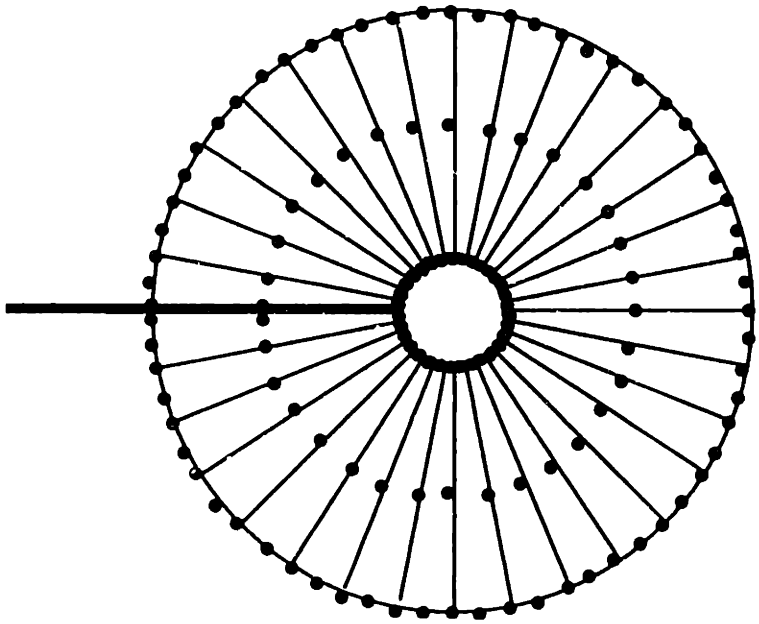

Fig. 6.4 Assembly of finite element mesh around the crack tip

Two different meshes, different only in element type, were employed for elastic and elastic-plastic analyses. For the elastic analysis, all the elements were 8-node isoparametric elements with full 3 x 3 Gaussian integrations. For the elastic-plastic analysis, the elements around crack tips are 8-node isoparametric linear pressure hybrid elements with 2 x 2 reduced Gaussian integration scheme. Since large plastic zones are expected at the crack tips, modelling the crack tip with these hybrid elements seems more appropriate due to the incompresibility of these hybrid elements. The multi-purpose finite element code ABAQUS was used to conduct the analysis. The computations were performed on a MicroVax II computer, and the CPU time for one run was 15 to 28 hours. Six different loading positions were studied with various friction coefficients. The loading scheme is shown in Fig. 6.5. The geometric and loading parameters are listed in Table 6.2.

4. Results and Discussion

4.1 Applicability of the elasticity theory of interface cracking

For the case the layers and the substrate are elastic and the crack faces are frictionless ($f_c=0$), Fig. 6.6 shows the variation of the strength of singularity at the closed crack tip, K_{II}^c, versus the normalized distance from the crack centerline to the loading centerline, x_L/a, where a is the half contact width. The surface friction coefficient (the ratio of tangential force to the normal force), f, was set at 0, 0.25, 0.5 and 1.0. The values of K_{II}^c were obtained from the relationship between K_{II}^c and the J-integral (Eqn. 6.15), and the values of the J-integral were obtained from the ABAQUS output. Fig. 6.6a shows that values of K_{II}^c at the left crack tip as the surface load moves from left to right. When the left crack tip is directly under the contact edge ($x_L/a=-1.5$), K_{II}^c has the greatest value. As the load moves toward the right crack tip, the value of K_{II}^c vanishes. The friction coefficient, f, has a strong effect on the magnitude of K_{II}^c. Larger friction coefficient resulted in larger magnitude of K_{II}^c when $x_L<0$. However, the opposite was true when $x_L>0$, i.e., when the surface load was moving away from the crack.

Fig. 6.6b shows the results for the right crack tip. The behavior is slightly different from that of the left crack tip. The value of K_{II}^c increases as the surface

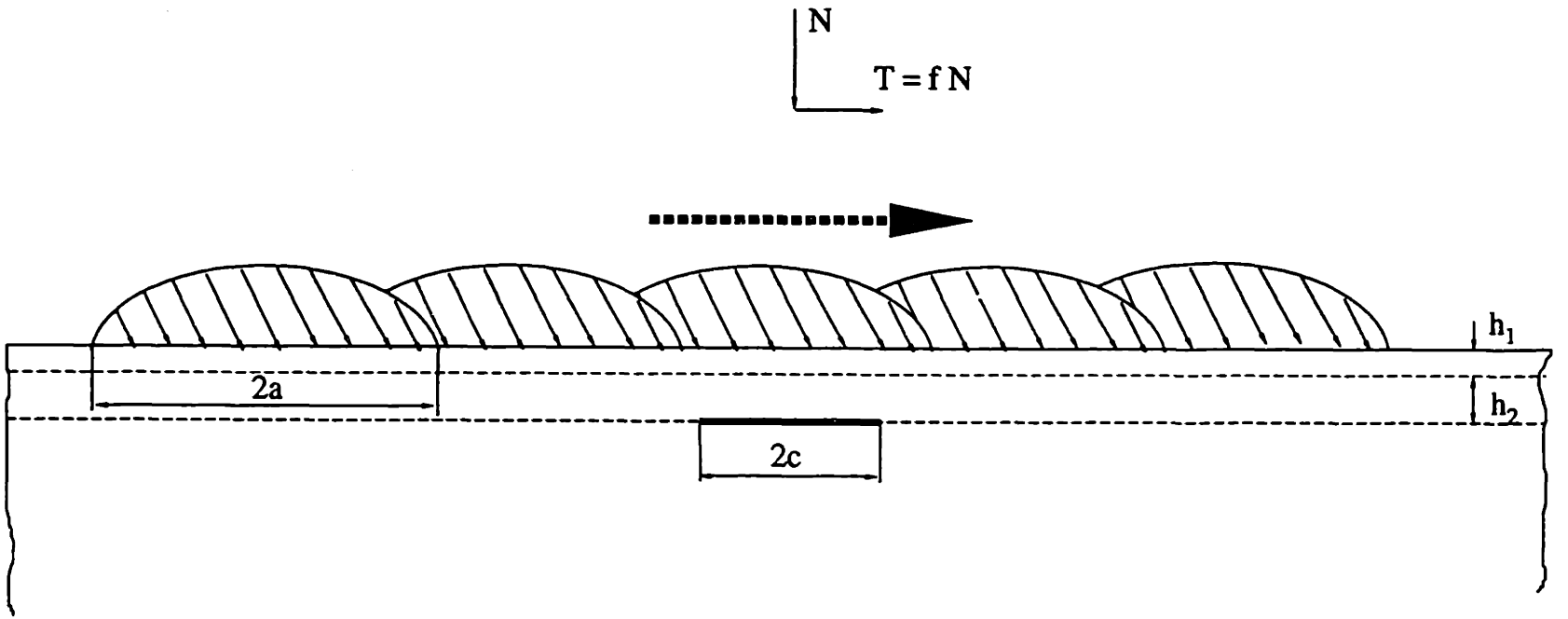

Fig. 6.5 Schematic of loading sequence in the FEM analysis

Table 6.2 Geometrical and loading parameters

Thickness of top layer, h_1	1.25	μm
Thickness of interlayer, h_2	2.50	μm
Crack length, 2c	6	μm
Half contact width, a	6	μm
Loading position, x_L/a	-2.17 ~ 2.17	
Normal load, N	5	N/mm
Surface friction coefficient, f	0, 0.25, 0.5, 1.0	
Friction coefficient between crack faces, f_c	0, 0.25, 0.5	

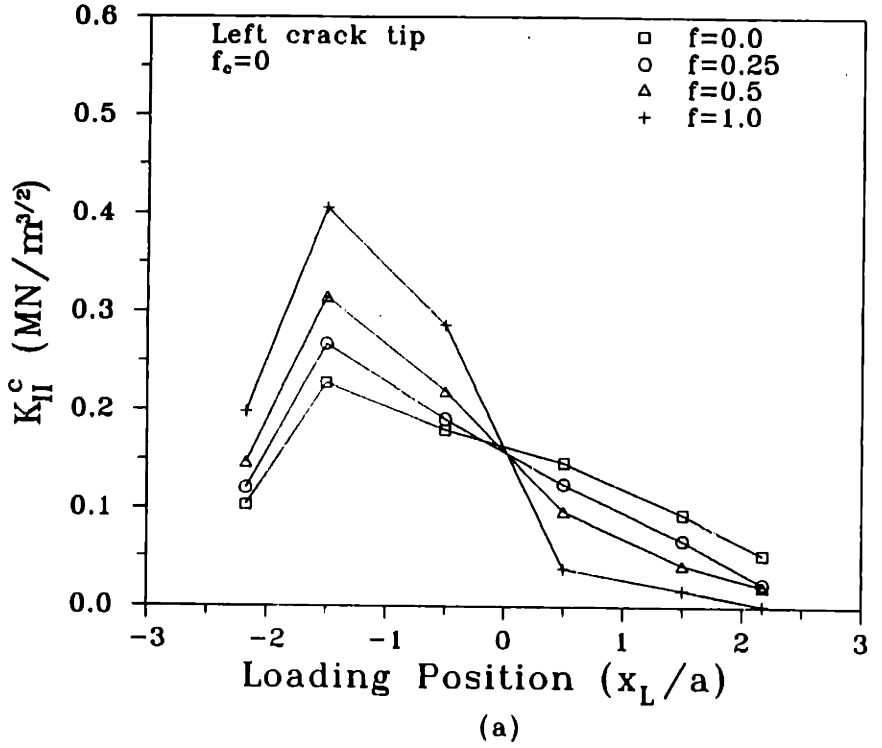

Fig. 6.6 The strength of singularity of a closed crack tip versus the loading positions for various surface friction coefficients: (a) left crack tip and (b) right crack tip

load moves toward the crack ($x_L<0$), and it also increases with the friction coefficient. As the load moves away from the crack ($x_L>0$), the value of K_{II}^c decreases with the friction coefficient.

Small-scale yielding is the basis for using the elasticity theory of interface cracking. Figs. 6.7a and 6.7b show the characteristic plastic zone size, r_p^c, at the left and right crack tips versus the various loading positions. The values of r_p^c were calculated from Eqn. (6.16). Clearly, the variations of the plastic zone with the loading position and the friction coefficient have the same trend as the values of K_{II}^c. The plastic zone size is up to as large as 25 percent of the crack length for a larger friction coefficient at a certain loading position. Even for normal contact ($f=0$), the plastic zone size was up to 8 percent of the crack length as the load moves over the interface crack. Since the coating thicknesses, h_1 and h_2, are of the same order of magnitude as the crack length in the present study, the plastic zone size is also comparable with the coating thickness. Thus it is obvious that the elastic analysis of the interface cracking is not suitable for the present problem because the plastic zones around the crack tips are too large to be ignored.

In the inelastic fracture mechanics of homogeneous materials, the J-integral approach has been widely used, i.e., when the small-scale yielding is not strictly satisfied. Unfortunately, even this approach to the present problem is questionable. The main reason is that the crack faces in most tribology problems are not traction free, i.e., they are frictional crack faces. Thus the J-integral is path-dependent for frictional interface cracks, and the applicability of the J-integral is limited because the J-integral must be path-independent. Accordingly the elastic-plastic finite element analysis of interface cracking was conducted, and the crack sliding displacement (CSD) was considered as the control parameter.

4.2 Plastic zones and stress states at the crack tips

Fig. 6.8 shows the plastic zones around the left and right crack tips for various surface friction coefficients. The crack faces were assumed frictionless, and the loading position was at $x_L/a=-0.5$. The boundaries of the dark areas around the crack tips are the equivalent plastic strain contours at a plastic strain of 0.02 percent. The upper region (interlayer) is in the elastic regime, while the bottom region

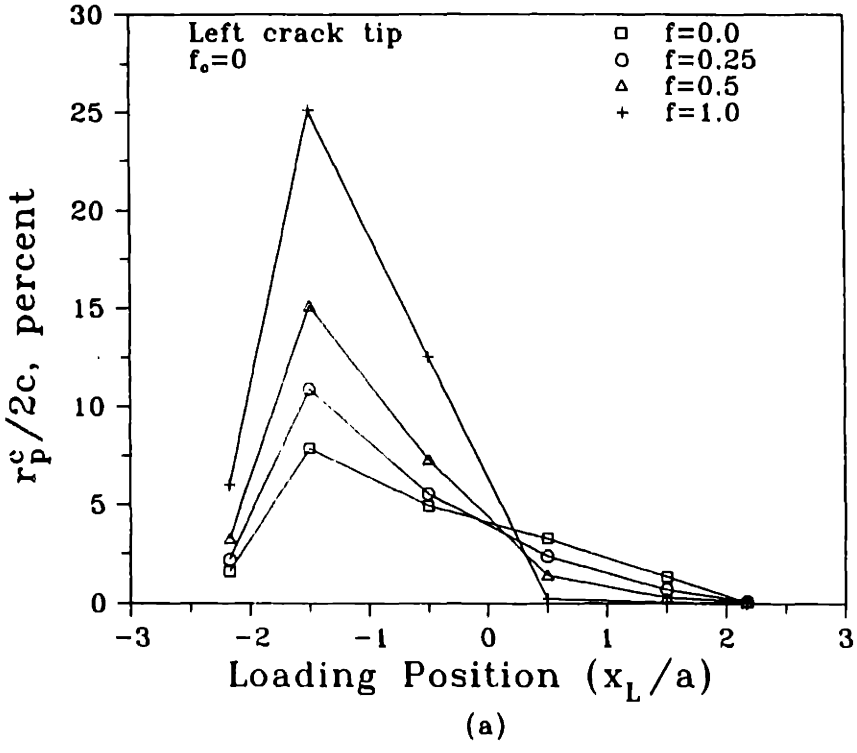

Fig. 6.7 The normalized plastic zone size versus the loading positions for various surface friction coefficients:
(a) left crack tip and (b) right crack tip

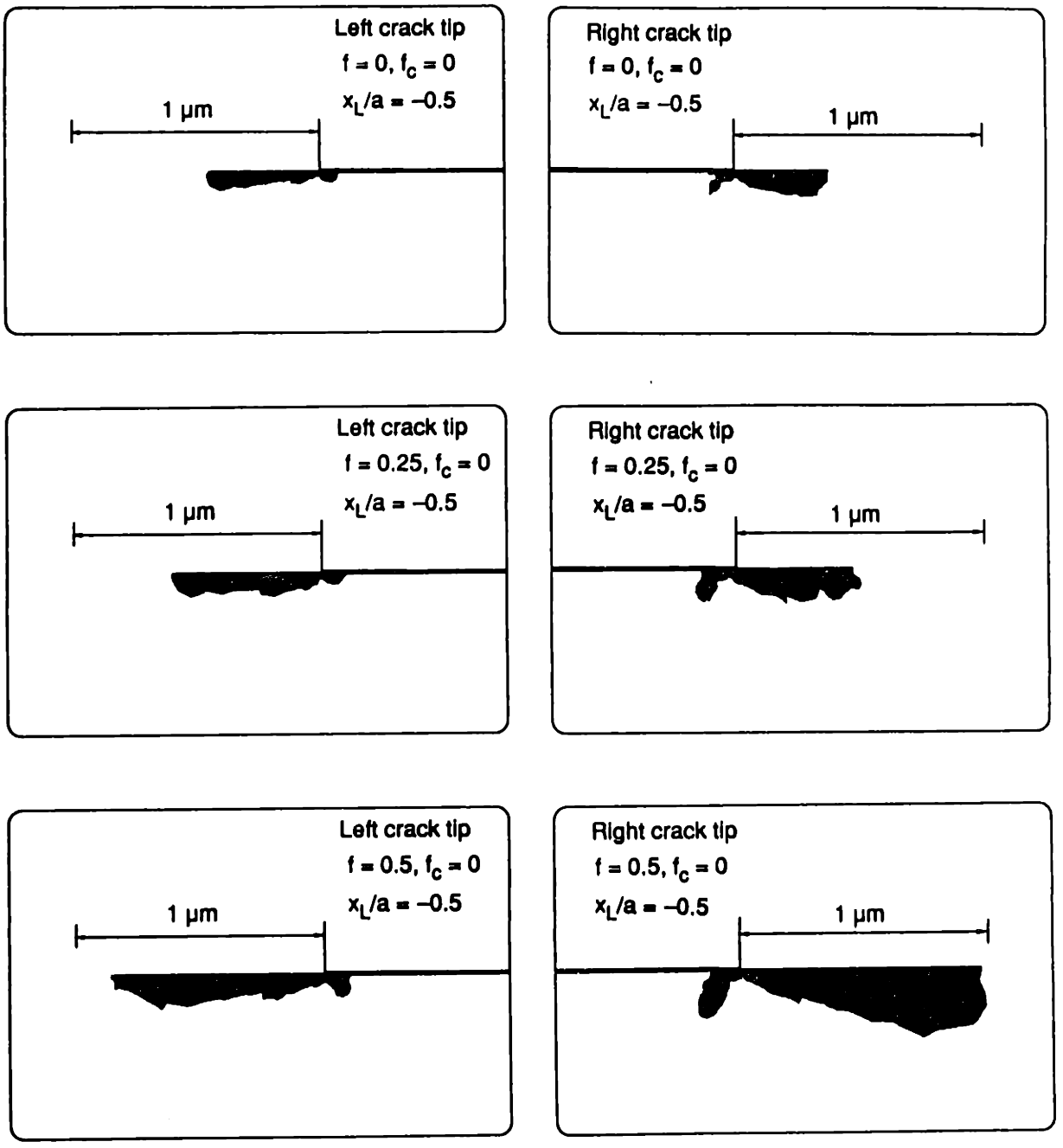

Fig. 6.8 Plastic zones around the crack tips for various surface friction coefficients

(substrate) is in the plastic regime around the crack tips. The plastic zones extend considerably in two directions. One is in the front of the crack tips (θ =180 degrees for the left crack tip, and θ=360 degree for the right crack tip). The other is in the directions $\theta \approx 315$ degree for the left crack tip and $\theta \approx 235$ degree for the right crack tip. However, the extent of plastic deformation in front of each crack tip is much larger than that in the other direction. The surface friction coefficient, f, has significant effects on the size of the plastic zones. The larger the surface friction coefficient (i.e., the larger the tangential force) the larger is the plastic zone. But the shape of the plastic zone appears to be unaffected by the surface friction coefficient.

Zywicz and Parks [49] have proposed that for small-scale yielding (SSY) of an elastic/perfectly-plastic half region bonded to a rigid substrate, the asymptotic closed crack-tip stress state can be represented by a slip-line field which consists of two centered fans and two constant pressure state regions (Fig. 6.9). In the constant pressure state region, the shear strain should be small, of the order of the initial yield strain. In the region of the centered fan, however, the shear strain is singular as $r \rightarrow 0$. Thus larger shear strains are expected in centered fans near the crack tips.

In the present analysis, the interlayer (nickel) is not rigid but has a larger elastic modulus compared with the modulus of the substrate (brass), and the substrate is not elastic/perfectly-plastic but is slightly work-hardening (E_p= 0.01E). Nevertheless, in the interest of comparison and simplicity, the interlayer-substrate structure can be treated as a rigid upper region bonded to an elastic/perfectly-plastic region. The shape of the plastic zones in Fig. 6.8 suggests that the Zywicz-Parks SSY slip-line field in Fig. 6.9 can also well represent the asymptotic stress state of a closed interface crack in large-scale yielding. Fig. 6.10 shows the shear strain distributions $\gamma_{r\theta}$ at three radial distances from the right crack tip. The largest positive and negative shear strains $\gamma_{r\theta}$ occur at $\theta = 360$ degree and $\theta = 235$ degree, which correspond to the direction of local maximum plastic zone radii and to the directions of the centered fans in the slip-line field of Fig. 6.9. In the regions that correspond to the constant pressure region in the slip-line field, the shear strains are very small. Fig. 6.10. shows that as $r \rightarrow 0$, the shear strain $\gamma_{r\theta}$ in the fan region increases drastically, while in the constant pressure regions remains constant and small.

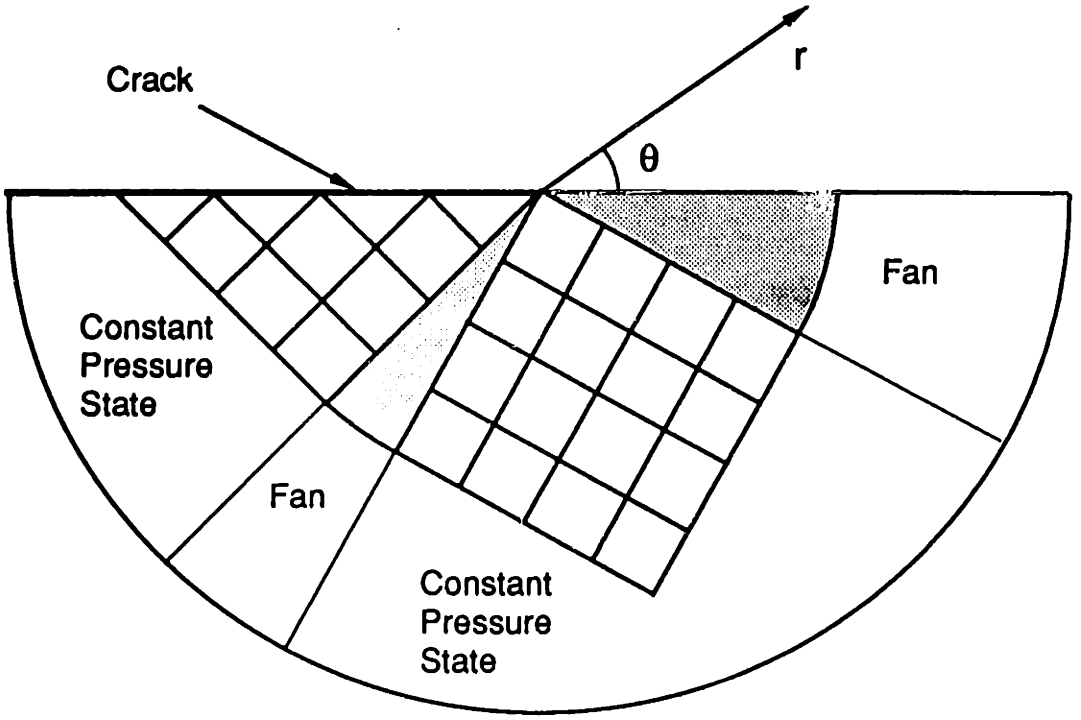

Fig. 6.9 Slip-line field at a closed interfacial crack between a rigid upper region and an elastic/perfectly-plastic bottom region [49]

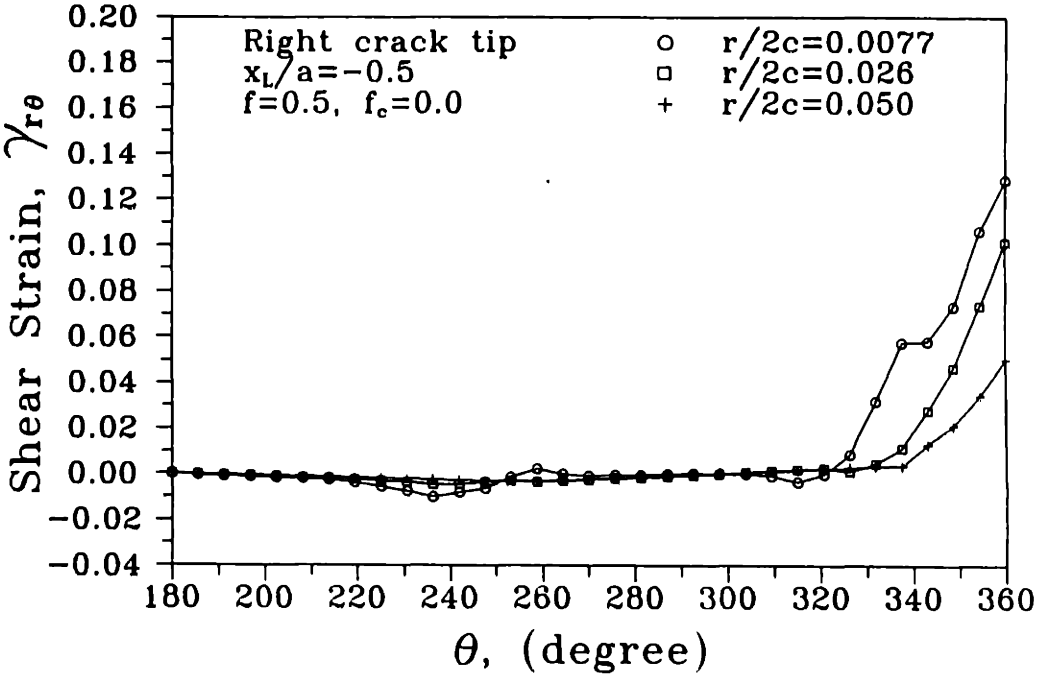

Fig. 6.10 Circumferential variation of shear strains near the right crack tip

4.3 Relative sliding displacement of crack faces

For a traction-free crack, Rice [44] has shown that the singular shear strains in the centered fan region lead to a non-zero crack tip displacement (CTD). For a closed crack tip, too, Zywicz and Parks [49] have shown that the centered fans would lead to a non-zero crack tip sliding displacement (CTSD) proportional to J/σ_{ys}, where σ_{ys} is the yield strength. However, the present finite element calculations show that the values of the J-integral evaluated within the plastic zone are strongly path-dependent. Thus CTSD cannot be estimated from the J-integral values. Accordingly, the crack sliding displacement (CSD) was calculated directly from the finite element analysis. Then the CSD curve versus the distance from the crack tip was extrapolated to $r=0$ to obtain CTSD.

Figs. 6.11a-11f show the CSD versus the normalized radial distance from each crack tip, x/2c, along the crack line for various surface friction coefficients and at various loading positions. CSD is defined as $CSD(x)=u^+(x)-u^-(x)$, where $u^+(x)$ and $u^-(x)$ are the horizontal displacements of the crack faces of the interlayer and of the substrate, respectively. The positive values of CSD indicate that the upper face of the crack is sliding past the lower face of the crack in the positive x-axis direction or the direction of the tangential force. The CSD is positive near both crack tips when the surface load is on the left-hand side of the crack ($x_L<0$), and negative when the load is on the right ($x_L>0$). The magnitude of CSD, as expected, decreases as x approaches zero. The largest value of CSD around the left tip occurs when $x_L/a=-1.5$, which corresponds to the position when the leading edge of the surface load is right above the left crack tip. Similarly, the largest value of CSD around the right tip occurs at $x_L/a=-0.5$ when the leading edge of the load is right above the right crack tip. The tangential force on the surface tends to further extend the sliding of the crack faces in the positive x direction. When $x_L<0$, the magnitude of CSD increases with the surface friction coefficient. When $x_L>0$, the magnitude of CSD decreases with the friction coefficient because the effect of tangential force offsets some of the negative values of CSD. The largest extrapolated CTSD for f=0.5 was about 80 Å for the left crack tip and 40 Å for the right crack tip.

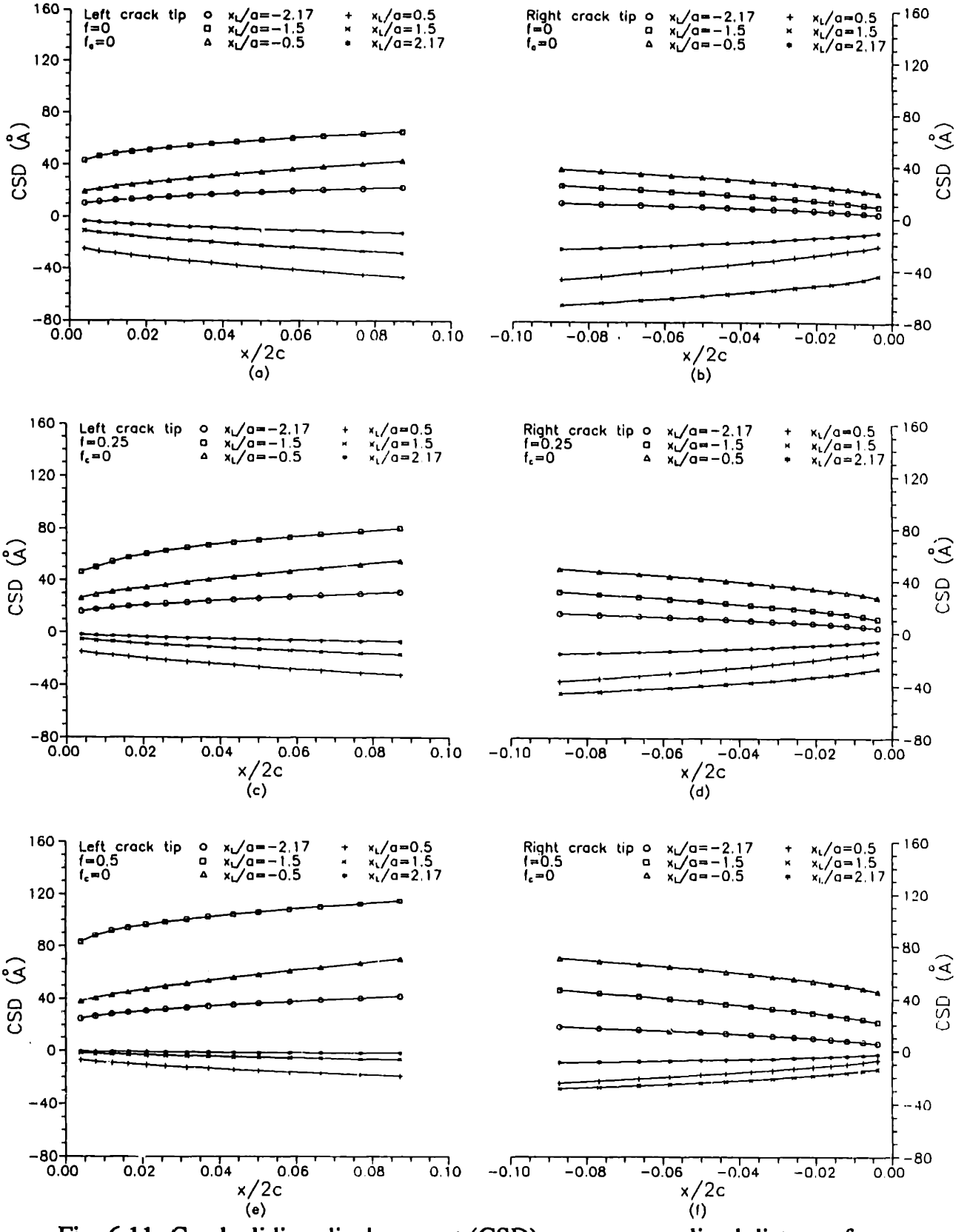

Fig. 6.11 Crack sliding displacement (CSD) versus normalized distance from the crack tips for various loading positions

4.4 *Effects of the crack face friction*

The finite element calculations have also shown that the interface crack stays closed throughout the loading process. Previously, the contact of the crack faces was assumed frictionless, i.e., the crack faces are subjected to the normal compression but are free to slide relative to each other. In reality, however, friction always exists between the crack faces. To model the frictional interface crack, a friction coefficient, f_c, was assigned to the interface elements along the crack line. Figs. 6.12a-6.12f show the plastic zones around the left and the right crack tips for various crack face friction coefficients. The loading position was at $x_L/a = -0.5$, and the surface friction coefficient, f, was equal to 0.5. Clearly, the plastic zones around the crack tips have been considerably reduced due to the presence of crack face friction. When $f_c = 0.5$, the plastic zones around the crack tips were only about 0.6% of the crack length. However, the crack face friction has only marginal effect on the shape of the plastic zones.

Since the crack face is not free of shear traction, the slip-line field in Fig. 6.8 has to be slightly modified. The crack face friction coefficient is assumed constant at every point of the interface, i.e., the ratio of shear stress to normal stress is constant. Within the plastic zone, let the normal compressive stress along the interface be a constant p_c, then the shear stress tangential to the interface is $\tau_{xy} = f_c p_c$. The resultant forces exerted on a small element ABC of the interface are balanced by the resolved components of the forces acting on the slip lines as shown in Fig. 6.13. Thus one set of slip lines (β-line) will intersect the interface at an angle φ ($\varphi \le \pi/4$). For the equilibrium of the element ABC, it follows

$$\cos 2\varphi = f_c p_c / k$$

and

$$\varphi = \frac{1}{2}\cos^{-1}\left(\frac{f_c p_c}{k}\right)_c \le \frac{\pi}{4} \qquad (6.18)$$

The modified slip-line field for an interface crack tip with crack face friction is shown in Fig. 6.6.13. The drawback of this slip-line field is that the normal compressive stress p_c must be known before the slip-line field can be constructed.

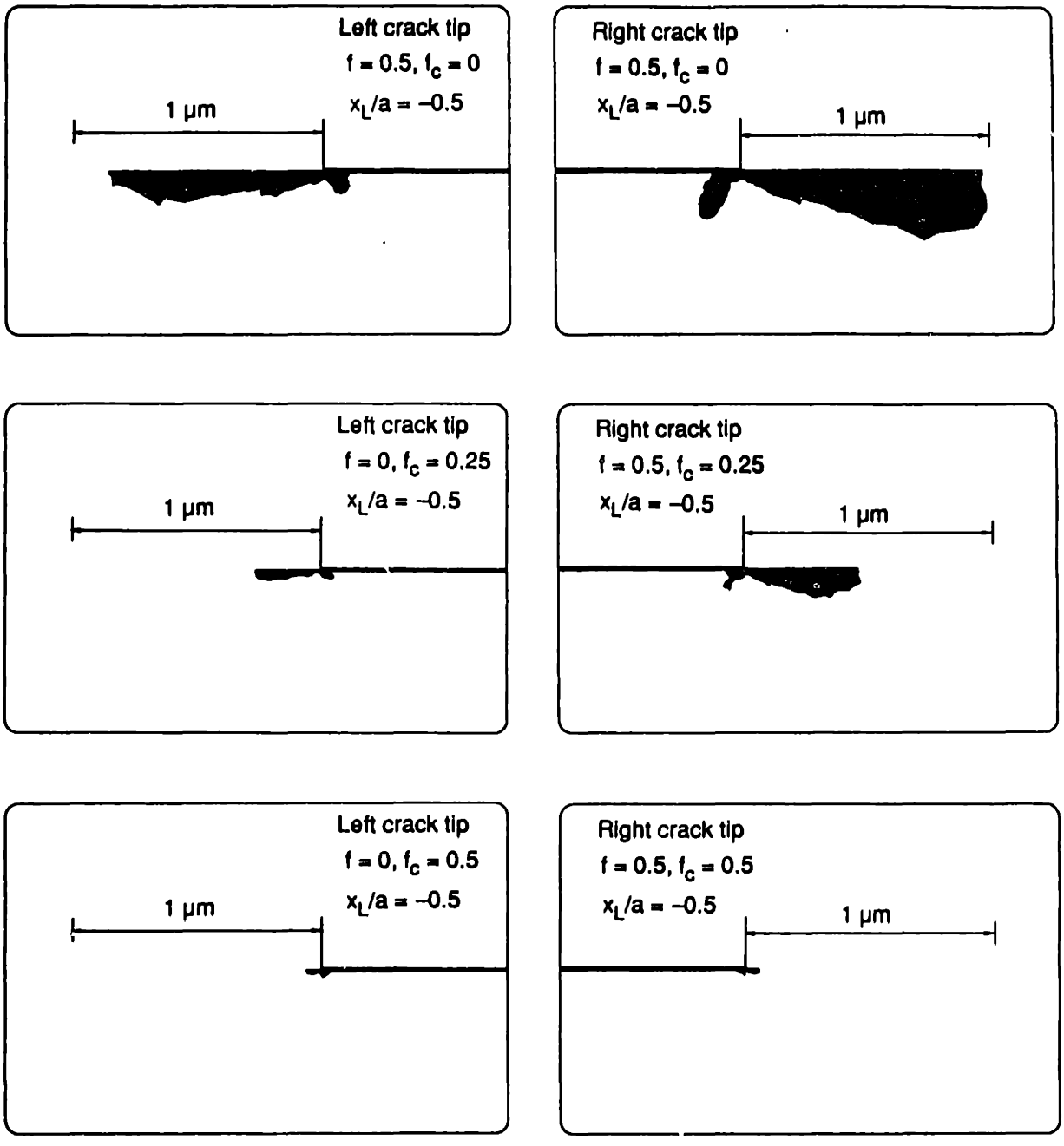

Fig. 6.12 Plastic zones around the crack tips for various crack face friction coefficients

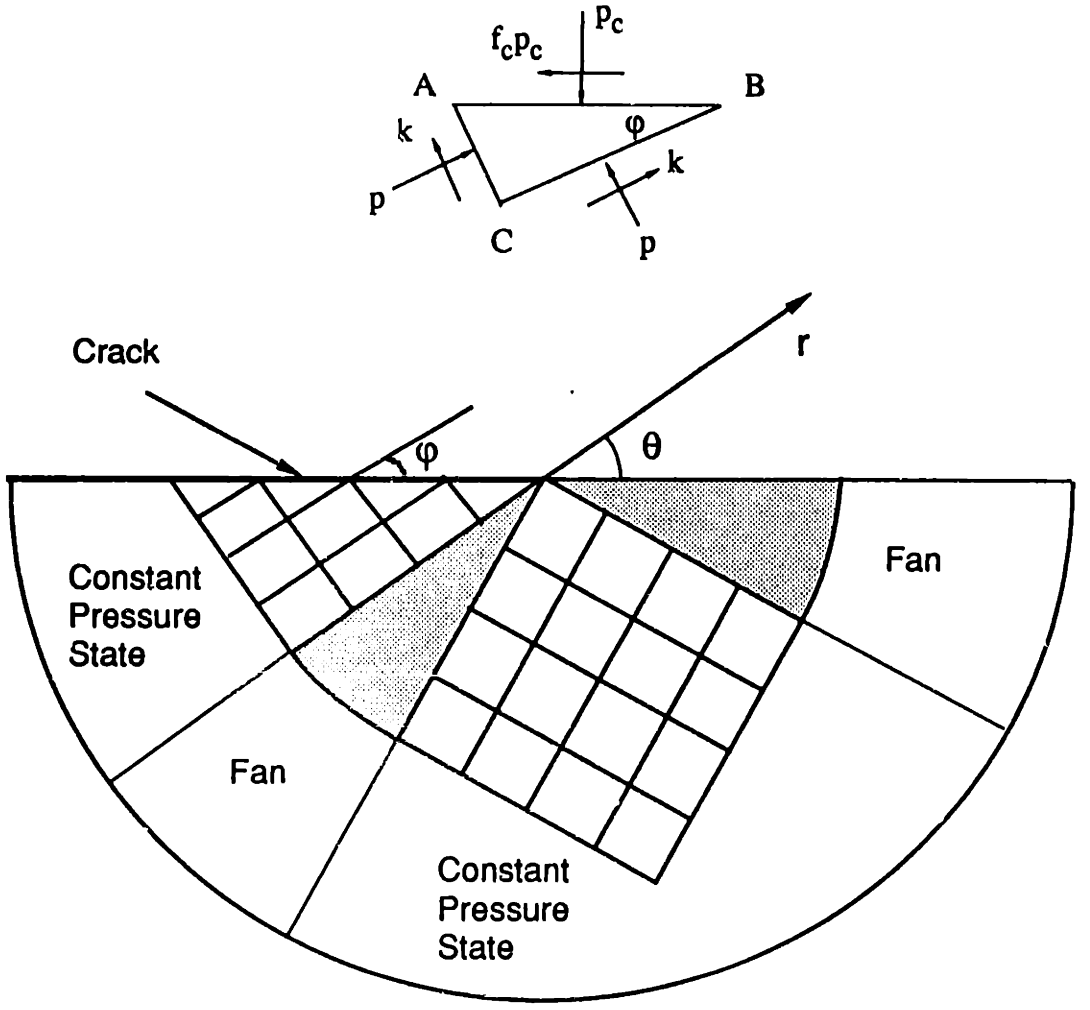

Fig. 6.13 Slip-line field at a closed frictional interfacial crack between a rigid upper region and an elastic/perfectly-plastic bottom region

Kim et al. [29] have shown in their elastic analysis of the interface cracking that the crack face friction significantly lowers values of stress intensity factor (K_{II}^c in the present notation) and the size of slipped region. Thus the crack face friction is expected to decrease the crack sliding displacement (CSD). Fig. 6.14 shows the CSD near both crack tips for various crack face friction coefficients. The surface friction coefficient was 0.5 and the loading position was at $x_L/a = -0.5$. Indeed, the crack face friction drastically reduced the CSD. For $f_c = 0.5$, the extrapolated values of CTSD are only a few angstroms.

4.5 Implications to fatigue failure of thin film systems

The finite element calculations have shown that the interface crack remains closed as the surface load moves over it. Hence the relative displacement of the crack faces has only the horizontal component, i.e., the CSD. McClintock [22] suggested that slip from the crack tip may be thought of as being produced by a dislocation leaving the tip. In the present study, the predominant mode of deformation is the slip along the plane in front of the crack, as shown in Fig. 6.15. A new surface, as shown by the dashed line, is generated. The crack growth is in the sliding direction, and the crack advances by a magnitude of the CTSD if there is no rewelding. This view was also adopted by Sin and Suh [27] in their estimate of subsurface crack growth.

As the surface load moves over the interface crack (from left to right), the value of CTSD changes from positive to negative. This implies that during the first half of the sliding cycle, the slip that the crack faces experience is not a simple forward motion. In fact, the crack faces first slide (relatively) in the direction of tangential force, then they slide backward as the surface loading moves away from the crack. In any event, the crack growth rate is no more than the largest CTSD under loading. Thus values of the CTSD are the upper bounds of the crack growth rate.

The largest CTSD in the present study is around 80Å for the frictionless crack faces. The value of CTSD reduces to a few angstroms when the crack face friction is taken into account. Thus it appears that the crack grows very slowly, or may not grow at all if a large friction exists between crack faces. A large crack face friction also facilitates the rewelding of the crack faces, which in turn reduces the

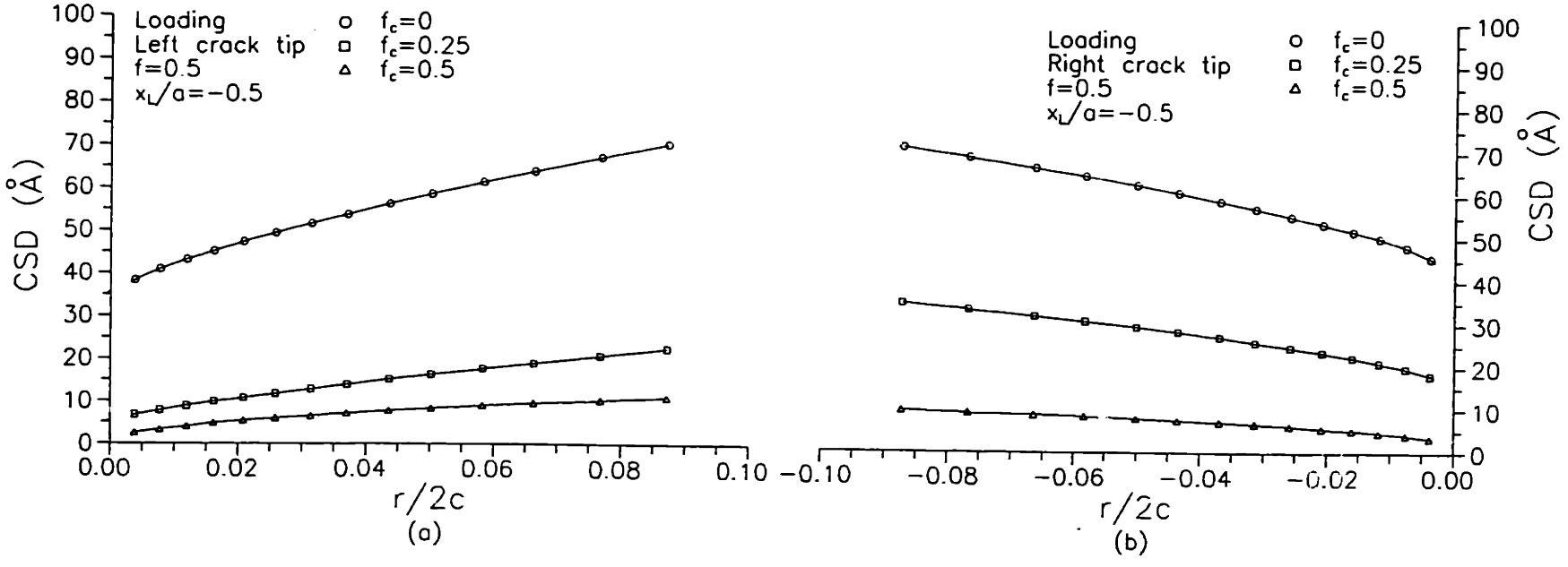

Fig. 6.14 Crack sliding displacement (CSD) versus normalized distance from the crack tips for various crack face friction coefficients

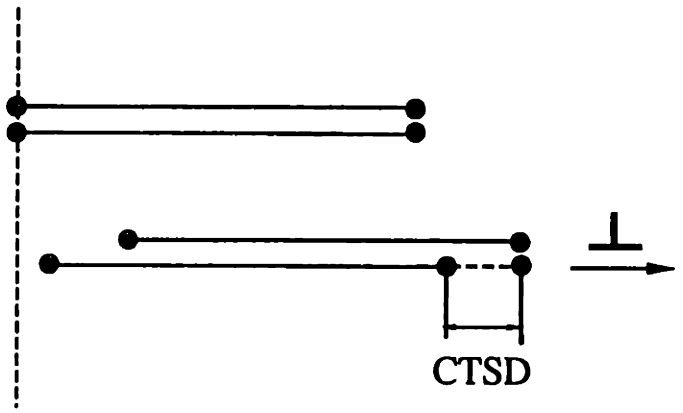

Fig. 6.15 Schematic of crack growth by dislocations emitted from the crack tip

crack growth rate. The experimental observations indicate, however, that cracking or debonding does indeed occur along the interfaces and that delamination takes place as a result of repeated surface loading. Possible explanation for the discrepancy is that the friction coefficient between crack faces is indeed small. Thus the crack does grow but slowly. Another explanation is that the interface ahead of the crack tips is not infinitely strong as assumed in the finite element analysis. Thus the crack may grow much faster than predicted by the CTSD calculations. More experiments and analytical investigations are needed to fully understand the mechanisms of interface crack extension in sliding contacts.

Neverthelss, the surface friction and the crack face friction are the two key controlling parameters for the size of plastic zone around crack tips. Larger plastic zones in front of the crack tip result in larger values of CTSD. Thus to reduce the crack growth effectively, the surface friction coefficient must be reduced and the crack face friction be increased. In the multi-layer contact systems, the surface friction coefficient or the sliding friction coefficient is determined by many parameters, such as coating thickness, compatibility of the contacting top layers, hardness of the top layer and the substrate, lubrication conditions at the contact interfaces, and so on. The crack face friction, however, is a relatively unknown phenomenon because it is difficult to directly measure the crack face friction. Nevertheless, one of the novel methods to increase the crack face friction is to increase the roughness of crack faces. This method has been shown to be successful in the fracture testing of a tension field [53]. Whether this approach is valid for the compression dominated crack problem needs to be explored.

5. Conclusions

A finite element analysis of interface cracking under sliding contact was conducted. The following conclusions can be drawn from the analysis.

(a) In tribological problems, the contact zone behind crack tip is large. Thus the closed crack tip model must be used in modeling interface cracking.

(b) The elastic solutions of interface cracking are not suitable if one of the materials is soft and ductile. The plastic zone at the crack tips are too large to be ignored. The J-integral approach is also questionable due to the frictional crack faces.

(c) The plastic deformation around the crack tips extends primarily in two directions as predicted by the Zywicz-Parks slip-line field for closed interface cracks. The shape of the plastic zone can also be well represented by that slip-line field, although the plastic deformation is in the large-scale yielding regime.

(d) The crack tip sliding displacement (CTSD) is a fair indicator of interface crack growth. The CTSD is in the angstrom (Å) range and thus the crack grow rate is very small.

(e) CTSD is strongly affected by the loading position, the surface friction coefficient, and most importantly, the crack face friction. To reduce the crack growth rate effectively, the surface friction must be reduced and the crack face friction increased. In terms of plastic zones in the front of crack tips and the CTSD value, increasing the crack face friction is more effective than decreasing the surface friction.

References

[1] Evans, A. G. and Hutchinson, J. W., "On the Mechanics of Delamination and Spalling in Compressed Films," *Int. J. Solids Structures*, Vol. 20, 1984, pp. 455-466.

[2] Hu, M. S., Thouless, M. D., and Evans, A. G., "The Decohesion of Thin Films from Brittle Substrates," *Acta Metall.*, Vol.36, 1988, pp. 1301-1307.

[3] Drory, M. D., Thouless, M. D., and Evans, A. G., "On the Decohesion of Residually Stresses Thin Films," *Acta Metall.* Vol. 36, 1988, pp. 2019-2028.

[4] Cao, H. C., Thouless, M. D., and Evans, A. G., "Residual Stresses and Cracking in Brittle Solids Bonded with a Thin Ductile Layer," *Acta Metall.*, Vol.36, 1988, pp. 2037-2046.

[5] Chai, H. Knauss, W. G., and Babcock, C. D., "Observation of Damage Growth in Compressively Loaded Laminates," *Expl. Mech.*, 1983, pp. 329-337.

[6] Tian, H., Saka, N., and Rabinowicz, E., "Friction and Failure of Electroplated Sliding Contacts," Submitted to *Wear*.

[7] Tian, H., Saka, N., and Rabinowicz, E., "Fretting Failure of Electroplated Gold Contacts," Submitted to *Wear*.

[8] Suh, N. P., "The Delamination Theory of Wear," *Wear*, Vol.25, 1973, pp. 111-124.

[9] Jahanmir, S. and Suh, N. P., "Mechanics of Subsurface Void Nucleation in Delamination Wear," *Wear*, Vol. 44, 1977, pp. 17-38.

[10] Fleming, J. R. and Suh, N. P., "Mechanics of Crack Propagation in Delamination Wear," *Wear*, Vol. 44, 1977, pp. 39-56.

[11] Fleming, J. R. and Suh, N. P., "The Relationship Between Crack Propagation Rates and Wear Rates," *Wear*, Vol. 44, 1977, pp. 57-64.

[12] Suh, N. P., Tribophysics, Prentice-Hall Inc., Englewood Cliffs, NJ, 1986, pp.

[13] Rosenfield, A. R., "A Fracture Mechanics Approach to Wear," *Wear*, Vol. 61, 1980, pp. 125-132.

[14] Hills, D. A. and Ashelby, D. W., "On the Determination of Stress Intensification Factors for a Wearing Half-Space," *Eng. Fract. Mech.*, Vol. 13, 1980, pp. 69-78.

[15] Hills, D. A. and Ashelby, D. W., "On the Application of Fracture Mechanics to Wear," *Wear*, Vol. 54, 1980, pp. 321-330.

[16] Keer, L M., Bryant, M. D., and Haritos, G. K., "Subsurface Cracking and Delamination," *Solid Contact and Lubrication*, AMD Vol. 39, 1980, pp. 79-95.

[17] Chang, F. K., Comninou, M., and Sheppard, S., and Barber, J. R., "The Subsurface Crack Under Conditions of Slip and Stick Caused by a Surface Normal Load," *J. Appl. Mech.*, Vol. 51, 1984, pp. 311-316.

[18] Hearle, A. D. and Johnson, K. L., "Mode II Stress Intensity Factor for a Crack Paralle to the Surface of an Elastic Half-Space Subjected to a Moving Point Load," *J. Mech, Phys, Solids*, Vol. 33, 1985, pp. 61-81.

[19] O'Regan, S. D., Hahn, G. T., and Rubin, C. A., "Driving Force for Mode II Crack Growth under Rolling Contact," *Wear*, Vol. 101, 1985, pp. 333-346.

[20] Tzou, D. Y. and Sih, G. C., "Crack Growth Prediction of Subsurface Crack in Yielded Materials," *J. Appl. Mech.*, Vol. 52, 1985, pp. 237-238.

[21] Sheppard, S., Barber, J. R., and Comninou, M., "Short Subsurface Cracks Under Conditions of Slip and Stick Caused by a Moving Compressive Load," *J. Appl. Mech.*, Vol. 52, 1985, pp. 811-817.

[22] McClintock, F. A., "Plastic Flow Around a Crack Under Friction and Combined Stress," *Fracture 1977*, Taplin, D. M. R., ed., Vol. 4, ICF4, Waterloo, Canada, 1977, pp. 23-38.

[23] Rosenfield, A. R., "A dislocation Theory Approach to Wear," *Wear*, Vol. 72, 1981, pp.97-103.

[24] Rosenfield, A. R., "Elastic-Plastic Fracture Mechanics and Wear," *Wear*, Vol. 72, 1981, pp.245-254.

[25] Bilby, B. A., Cottrell, A. H., and Swinden, K. H., "The Spread of Plastic Yield From a Notch," *Proc. Royal Soc. Series A*, Vol. 272, 1963, pp. 304-314.

[26] Otsuka, A., Tohgo, K, Kiba, T., and Yamada, S., "Mode II Fatigue Crack Growth Characteristics and Mechanism in Aluminum Alloy 7N01-T4 Weldments Under Mode II Loading, " *Proc. 6th Int. Conf. Fracture*, New Delhi, 1984, pp. 1671-1678.

[27] Sin, H. -C. and Suh, N. P., "Subsurface Crack propagation Due to Surface Traction in Sliding Wear," *J. Appl. Mech.*, Vol. 51, 1984, pp. 317-323.

[28] Bastias, P. C., Hahn, G. T. and Rubin, C. A., "Finite Element Modelling of Subsurface Mode II Cracks Under Contact Loads," *Engineering Fracture Mechanics*, Vol. 33, 1989, pp. 143,152.

[29] Kim, S. H., Keer, L. M. and Cheng, H. S., "Loss of Adhesion of a Layer Bonded to an Elastic Half Space Caused by a Concentrated Contact," *Tribology Transaction*, Vol. 33, 1990, pp. 53-59.

[30] Dundurs J., Discussion, *J. Appl. Mech.*, Vol. 36, 1969, pp. 650-652.

[31] Suga, T., Elssner, E., and Schmander, S., "Composites Parameter and Mechanical Compatibility of Metal Joints," *J. Composite Materials*, Vol. 22, 1988, pp. 917-934.

[32] Rice, J. R., "Elastic Fracture Mechanics Concepts for Interfacial Cracks," ASME Trans., *J. Appl. Mech.*, Vol.55, 1988, pp.98-103.

[33] Hutchinson, J. W., "Mixed Mode Fracture Mechanics of Interface," *Scripta Met.*, in press.

[34] Williams, M. L., "The Stresses Around a Fault or Crack in Dissimilar Media," *Bulletin of the Seismological Society of America*, Vol. 49, 1959, pp 199-204.

[35] England, A. H., "A Crack Between Dissimilar Media," *J. Appl. Mech.*, Vol.32, 1965, pp 400-402.

[36] Erdogan, F., "Stress Distribution in Bonded Dissimilar Materials With Cracks," *J. Appl. Mech.*, Vol. 32, 1965, pp 403-410.

[37] Sih, G. C. and Rice, J. R., "The Bending of Plates of Dissimilar Materials with Cracks," *J. Appl. Mech.*, Vol. 31, 1964, pp 477-482.

[38] Rice, J. R., and Sih, G. C., "Plane Problems of Cracks in Dissimilar Media," *J. Appl. Mech.*, Vol. 32, 1965, pp 418-423.

[39] Park, J. H. and Earmme, Y. Y., "Application of Conservation Integrals to Interfacial Crack Problems," *Mech. Mater.*, Vol. 5, 1986, pp. 261-276.

[40] Hutchinson, J. W., Mear, M., and Rice, J. R., "Crack Paralleling an Interface Between Dissimilar Materials," *J. Appl. Mech.*, Vol. 54, 1987, pp. 828-832.

[41] Shih, C. F. and Asaro, R. J., "Elastic-Plastic Analysis of Cracks on Bimaterial Interfaces: Part I--Small Scale Yielding," *J. Appl. Mech.*, Vol. 55, 1988, pp 299-316.

[42] Shih, C. F. and Asaro, R. J., "Elastic-Plastic Analysis of Cracks on Bimaterial Interfaces: Part II--Structure of Small-Scale Yielding Fields," *J. Appl. Mech.*, Vol. 56, 1989, pp 763-779.

[43] Suo, Z. and Hutchinson, J. W., "Interface Crack Between Two Elastic Layers," *Int. J. Fracture*, in press.

[44] Rice, J. R., "A Path Independent Integral and Approximate Analysis of Stain Concentration by Notches and Cracks," *J. Appl. Mech.*, Vol. 35, 1968, pp. 379-385.

[45] Zywicz, E. and Parks, D. M., "Elastic Yield Zone Around an Interfacial Crack Tip," *J. Appl. Mech.*, Vol. 56, 1989, pp. 577-584.

[46] Comninou, M., "The Interface Crack," *ASME Trans., J. Appl. Mech.*, Vol. 44, 1977, pp 631-636.

[47] Comninou, M., "The Interface Crack in a Shear Field," *J. Appl. Mech.*, Vol. 45, 1978, pp 287-290.

[48] Comninou, M. Schmueser, D., "The Interface Crack in a Combined Tension-Compression and Shear Field," *J. Appl. Mech.*, Vol. 46, 1979, pp 345-348.

[49] Zywicz, E. and Parks, D. M., "Elastic-Plastic Analysis of Frictionless Contact at Interfacial Crack Tips," *Int. J. Fracture*, in press.

[50] Parks, D. M. and Zywicz, E., "Elastic/Perfect-plastic Small Scale yielding at Bi-Material Interfaces," *Proc. ICF7*, eds. Salama, K. et al., Vol. 4, Pergamon, 1989, pp. 3081-3088.

[51] Tian, H. and Saka, N., "Finite Element Analysis of Two-Layer Half-Space: Sliding Contact," Submitted to *J. Tribology*.

[52] Tian, H. and Saka, N., "Finite Element Analysis of Two-Layer Half-Space: Normal Contact," Submitted to *J. Tribology*.

[53] Oh, T. S., Rodel, J., Cannon, R. M. and Ritchie, R. O., "Ceramic/Metal Interfacial Crack Growth: Toughening by Controlled Microcracks and Interfacial Geometries," *Acta Metall.*, Vol. 36, 1988, pp. 2083-2093.

Chapter 7

Friction and Interfacial Delamination

7.1 Introduction

It was shown in chapters 2 and 3 that high surface friction coefficients in both sliding and fretting of electroplated gold contacts are responsible for progressive removal of gold coating and for the interfacial delamination of the nickel underplate from the brass substrate. The finite element analyses of a multilayer contact system in chapters 4 and 5 have shown that the surface friction coefficient and the nickel thickness are the two important parameters that control the interfacial stresses and strains. The finite element analysis of interface cracking in chapter 6 showed that the surface friction coefficient and the crack face friction have strong effects on the crack tip sliding displacement (CTSD), which is believed in the present study to be a valid indicator of interfacial crack growth rate. Thus the objectives of this chapter are to establish a fatigue model for interface delamination of thin film contact systems and to validate experimentally the main conclusions of the finite element analysis. Before the fatigue model and experimental evaluations are presented, the conclusions from the experimental investigation of contact failures and the finite element analysis are summarized in the following section.

7.2 Main Conclusions from the Previous Chapters

7.2.1 Sliding and Fretting Failures

Three stages can be distinguished in the sliding behavior of electroplated gold contacts based on the friction coefficient, and acoustic emission and Auger electron spectral analyses. In stage I, the friction coefficient increases monotonically, and a prow forms on the ball surface which is eventually rubbed off. In this stage, the

high adhesion characteristic of gold is responsible for the prow formation and for progressive coating removal from the ball. In stage II, the friction coefficient is more or less constant until wear particles are delaminated from the nickel-brass interface of the ball specimen. High friction stresses seem to induce and promote the interfacial delamination process. Plowing by the hard asperities of the nickel underplate results in high but stable friction coefficient. At the onset of stage III, friction coefficient starts increasing again, and wear particles are delaminated from the ball surface periodically, resulting in high and fluctuating friction coefficient as well as severe wear. Delamination occurs in one of the contact members, and severe plastic deformation takes place in the other.

Fretting failure of electroplated gold contacts can also be divided into three stages. In stage I, the gold coating on both contact surfaces is pushed out in the direction of fretting motion. Then accumulation of plastic deformation due to the fretting motion tears the gold coating apart, resulting in island-like gold patches in the contact. Nickel starts to appear on the surface at the contact center due to the extrusion of the gold coating. In stage II, tensile stresses at the edge of the contact region and high shear stresses at the nickel/brass interface, due to the high friction on the surface, result in the initiation of surface and subsurface interfacial cracks. As fretting continues, these cracks propagate and thin wear sheets are removed from the nickel/brass interface. In stage III, the brass substrate is exposed to the atmosphere, and oxidation of the brass substrate takes place. Thin plates of oxide-covered wear debris are detached from the surface due to the fretting wear process. These wear particles accumulate at the contact interface due to the small relative motion between the contact surfaces, and the contact resistance starts to increase.

The electrical contact resistance is low as long as metal-to-metal contact exists at the contact spot. In sliding tests, electrical contact resistance remains low throughout the tests even if the nickel underplate and brass substrate are exposed. Similarly, in fretting tests, the nickel underplate and the brass substrate are exposed long before any increase in contact resistance is noticeable. Thus in the accelerated laboratory tests, the electrical contact resistance is not a reliable indicator of sliding and fretting failure of electroplated gold contacts.

High surface friction is one of the main causes of sliding and fretting failures. Lubricated sliding and fretting tests indeed confirm this view. Lubrication reduces the friction considerably and keeps the sliding and fretting systems in the early stage of failure (stage I in both cases). Thus low surface friction is an essential requirement for delaying failures of the thin film contact systems in both sliding and fretting situations.

7.2.2 Finite Element Analysis

Normal Contact

A finite element analysis of a rigid cylinder indenting an elastic-plastic two-layer half-space is conducted. For elastic loading, the contact pressure distributions of indented multi-layer media with a soft top layer and a hard interlayer are bounded by parabolic and elliptic distributions. Under high elastic-plastic loadings, however, the pressure distribution is flatter and the peak pressure moves slightly away from the contact center. Higher center pressure and smaller contact width are obtained with thicker interlayers. Stress discontinuities occur at the interfaces since perfect bonding between layers is assumed. The maximum stress jumps are obtained for an intermediate thickness of the nickel interlayer. Interfacial stresses and strains at the top layer-interlayer interface are not greatly affected by the interlayer thickness. At the interlayer-substrate interface, however, the highest shear stress and strains are produced when the interlayer thickness is of intermediate value.

The interlayer thickness strongly affects the location where yielding initiates. Plastic deformation initiates in the substrate when a thin, hard interlayer is used. As the interlayer thickness increases, both the top layer and the substrate are subjected to plastic deformation. For very thick interlayer, however, only the top layer deforms plastically. Generally, it is undesirable for one of the materials at interfaces to be in the plastic regime, especially at the interlayer substrate interface. Therefore the interlayer thickness should be so chosen that plastic deformation does not reach the interfaces under the designated normal load.

Sliding Contact

A finite element analysis of the sliding contact of a two-layer elastic-plastic half-space has also been conducted. Surface deformation and profile are strongly affected by the friction coefficient. The surface material is deformed along the sliding direction. A small hump is observed at the leading edge of the contact when the friction coefficient is large. The location of initial yielding strongly depends on the friction coefficient as well as the normal load. Yielding initiates in the substrate for a small friction coefficient if the normal load is large enough. When $\mu \geq 0.3$, yielding initiates on the surface (and in the substrate as well if the normal load is larger). Whenever the surface yields, it always occurs near the trailing edge of the contact. Whenever yielding initiates in the subsurface, however, it occurs at the leading region of the contact. The tangential force is the primary cause of the uncontained plastic deformation of the top layer (gold). Normal stresses and strains (σ_{yy} and ε_{yy}) along the interfaces are not greatly affected by friction. By contrast, the horizontal and shear stresses and strains (σ_{xx}, ε_{xx}, and τ_{xy}, ε_{xy}) along the interfaces are strongly influenced by the friction coefficient. For frictional loading, σ_{xx} in the trailing region of the contact is tensile, and is compressive in the leading region of the contact. The magnitudes of shear stress and strain along both interface increase significantly with the friction coefficient.

Three criteria have been developed for the initiation of interfacial cracks: energy criterion, the local strain criterion, and the local stress criterion. Among the three, the local shear strain criterion seems to be relevant to the compression-dominated contact problems. When the interfacial shear strain exceeds a critical value, it is likely that debonding or microcracking occurs. Thus the interfacial stresses and strains should be minimized as much as possible. It is apparent from the FEM analysis that when the friction coefficient is less than 0.3, the interfacial shear stresses and strains are not much different from the case of normal indentation. But they become significantly large when the friction coefficient is larger than 0.3, and then the interfacial failure is likely. Thus the sliding friction of a multi-layer contact system should be kept below 0.3. In the unlubricated sliding and fretting tests, the surface friction coefficient is larger than 0.3, usually above 0.6. Large interfacial shear stresses and strains due to the high surface friction result in interfacial

failures after a number of sliding or fretting cycles. The lubricated tests, by contrast, generally yield low friction coefficient about 0.2, and interface failure is greatly delayed. Thus the conclusions drawn from the finite element analysis are consistent with the experimental findings.

Interfacial Cracking in Sliding Contacts

A plane strain finite element analysis of interface cracking in sliding contacts is conducted. A closed crack tip model is considered because the contact zone behind the crack tip is large relative to the crack length. In the present study the elastic solutions of interface cracking are not suitable because the plastic zone at the crack tips are too large to be ignored. The J-integral approach is also unsuitable due to the frictional crack faces. The plastic deformation around the crack tips extends primarily in two directions as predicted by a slip-line field. The shape of the plastic zone can also be well represented by that slip-line field. The crack tip sliding displacement (CTSD) is a valid indicator of interface crack growth rate. CTSD is in the angstrom (Å) range, and thus the crack growth rate is small. CTSD is strongly affected by the loading position, the surface friction coefficient, and most importantly the crack face friction. In terms of plastic zones in the front of crack tips and the CTSD value, increasing the crack face friction is more effective than decreasing the surface friction.

7.3 The Fatigue Model for Interfacial Delamination

One of the important observations in the elastic analysis of interface cracking is that the calculated values of the stress intensity factor ΔK_{II} are so small that ΔK_{II} is far below the threshold value for crack growth. However, the length of interface crack in the present study is only 6 μm, relatively small compared with cracks in conventional fracture mechanics. It is now well known that the behavior of small cracks is quite different from the predictions of linear elastic fracture mechanics (LEFM) of long cracks. Small cracks in general tend to grow not only at stress intensities below the large crack ΔK_{th}, but also at an average rate significantly higher than the extrapolation of the Paris' regime [1]. Fig. 7.1 is a schematic showing behavior of small cracks (SC) versus large cracks (LC). Thus the threshold value for long cracks are not valid for small cracks.

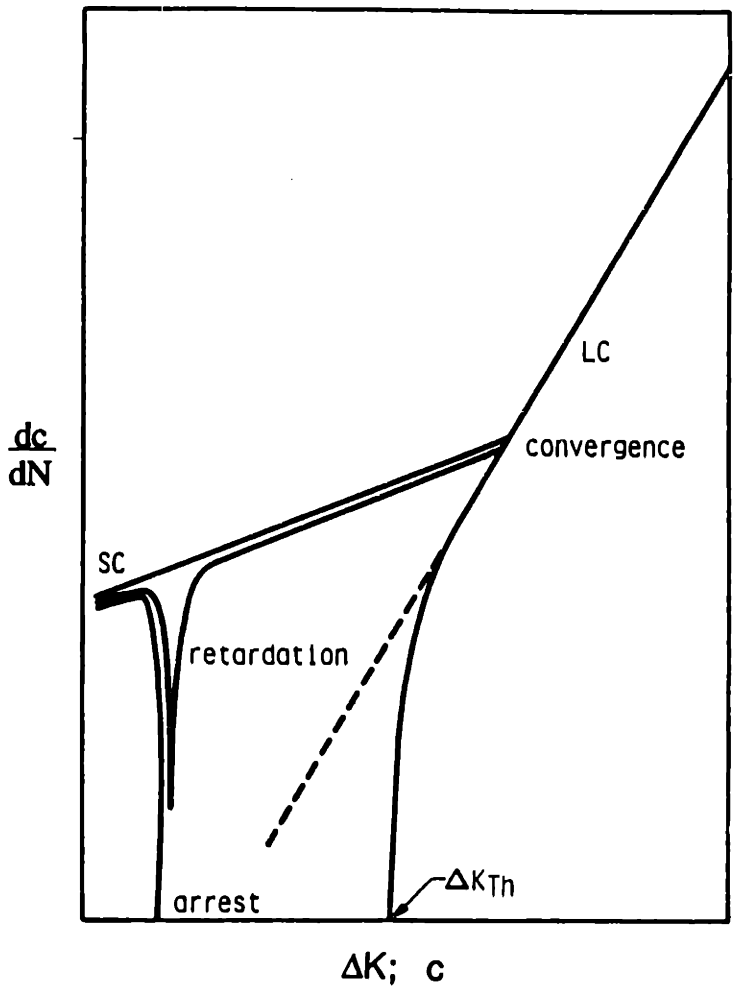

Fig. 7.1 Schematic showing behavior of small cracks (SC) versus large cracks (LC). Small cracks grow at a rate above the extrapolation (dashed line) of the LC Paris' regime, and are subject to arrest and retardation [2]

McClintock [3] suggested that the crack advances by the crack tip sliding displacement (CTSD) if there is no re-welding. This view was also adopted by Sin and Suh [4] in their estimate of subsurface crack growth. Assuming no re-welding occurs, the crack growth rate, dc/dN, can be written as:

$$dc/dN = \Delta CTSD \tag{7.1}$$

Thus the crack growth behavior can be discussed on the basis of ΔCTSD.

Fig. 7.2 shows the variations of CTSD with loading positions for various surface friction coefficients. When the leading contact edge is right above the left crack tip, the value of CTSD reaches a maximum (Fig. 7.2a, x_L/a=-1.5). The same result is obtained for the right crack tip (Fig. 7.2b, x_L/a=-0.5). For a given loading position, the CTSD increases with the surface friction coefficient and decreases with the crack face friction coefficient at both crack tips (Fig. 7.3). It appears that increasing the crack face friction coefficient is more effective in reducing CTSD than reducing the surface friction coefficient. Thus low surface friction and high crack face friction are desirable for delaying interface crack growth.

The initial crack length $2c_i$=6 μm, and the crack grows up to $2c_f$ to form a wear particle. The values of $2c_f$ are estimated from the micrographs of worn surfaces, about 90 μm and 60 μm for sliding and fretting tests, respectively. Assuming that $\Delta CTSD_{\text{per cycle}} \approx 2Max[(CTSD)_{\text{left crack tip}} + (CTSD)_{\text{right crack tip}}]$, the number of cycles for interfacial delamination is then given by (from the Eqn. 7.1)

$$N_f = (c_f - c_i) / \Delta CTSD \tag{7.2}$$

Table 7.1 compares the FEM calculations and experimental data for the number of cycles for interfacial failures in both sliding and fretting tests. It appears that the FEM analysis overestimates the failure life of sliding tests and underestimates the failure life of fretting tests. However, the total sliding distance to failure for both sliding and fretting tests is almost the same (eight and nine meters, respectively).

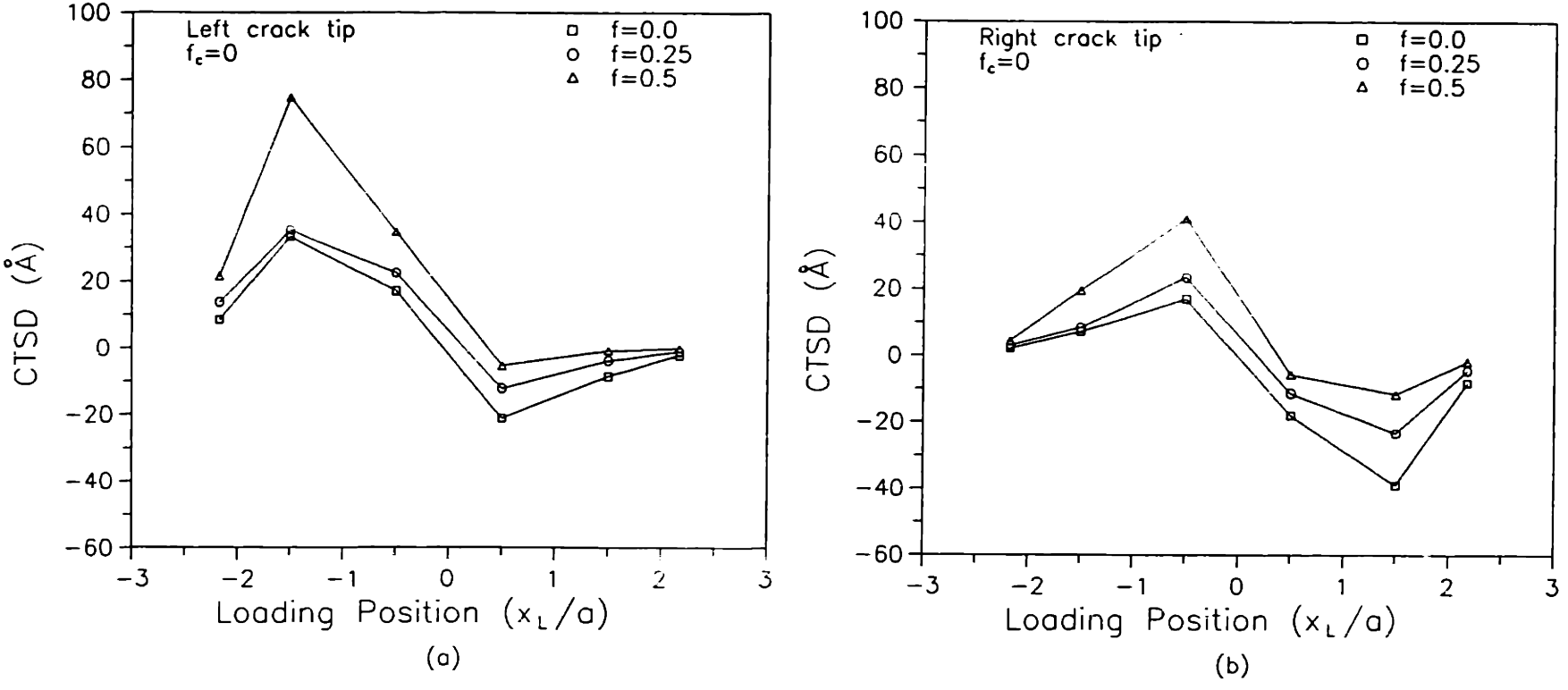

Fig. 7.2 Variations of CTSD with loading positions for various surface friction coefficients

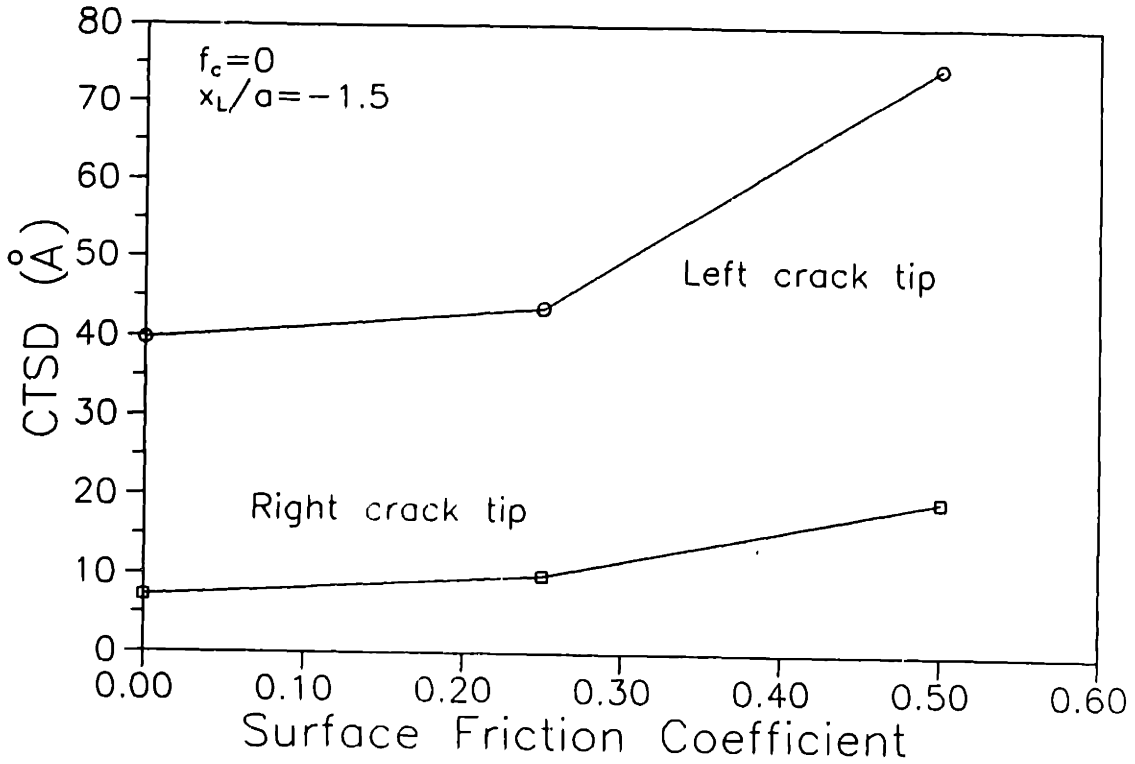

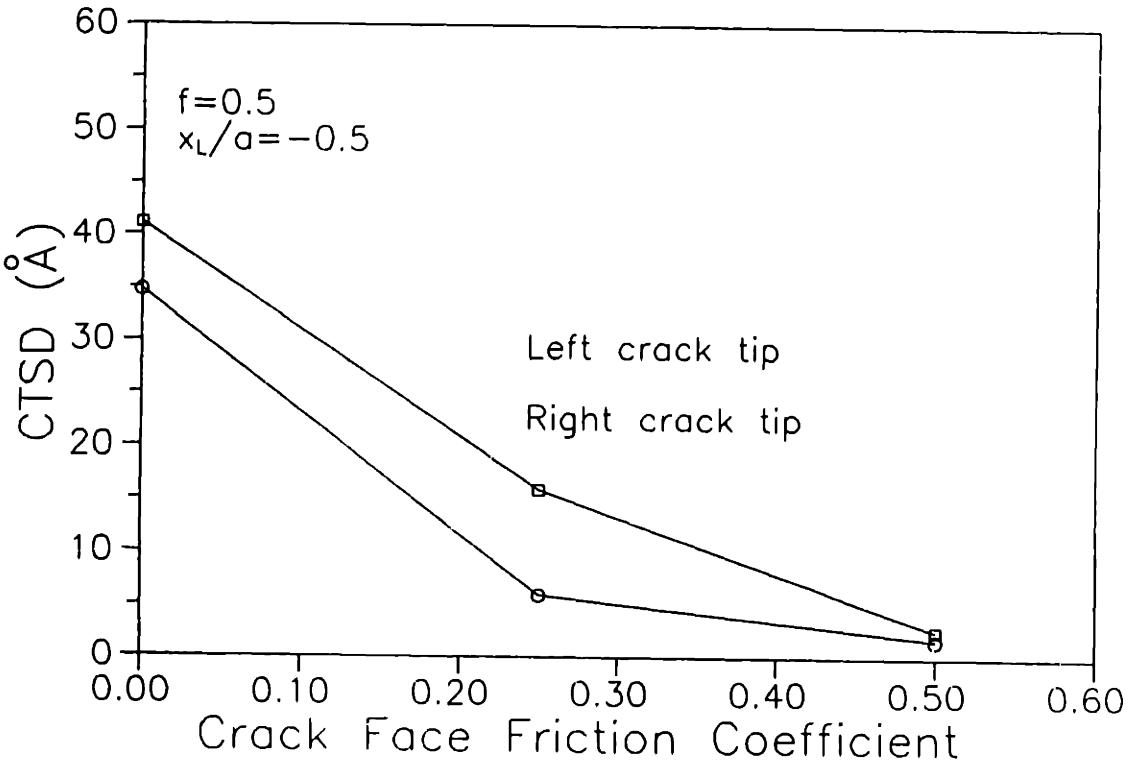

Fig. 7.3 Variations of CTSD with (a) surface friction coefficient and (b) crack face friction coefficient.

Table 7.1 : FEM calculations and experimental data

	FEM Calculations				Experimental			
	$2c_i$	ΔCTSD	$2c_f$	N_f	Stroke length	Frequency	Sliding distance	N_f
Sliding	6 μm	220 Å	90 μm	1,909	20 mm	0.1 Hz	8 m	200
Fretting	6 μm	220 Å	60 μm	1,227	30 μm	80 Hz	9 m	150,000

$$\Delta CTSD \approx 2Max[(CTSD)_{\text{left crack tip}} + (CTSD)_{\text{right crack tip}}]$$

$$dc/dN \approx \Delta CTSD$$

$$N_f = (c_f - c_i) / \Delta CTSD$$

7.3 Experimental Evaluations

The finite element analysis of interface cracking tells us that the surface friction coefficient should be reduced and the crack face friction coefficient should be increased to delay interfacial delamination. Accordingly several approaches have been tried and the experimental evaluations are presented.

7.3.1 Effects of metallurgical compatibility

One obvious solution to reduce surface friction is to use lubricants. The experimental results in chapters 2 and 3 show, not surprisingly, that lubrication is very effective in reducing sliding and fretting friction coefficients, and that interface delamination is considerably delayed. When lubrication is not preferable, one should consider the compatibility of sliding contact materials. Metal pairs which are metallurgically incompatible show less friction and wear [5]. To assure high corrosion resistance and low contact resistance in electrical contacts, however, noble metals must be used. The noble metals which are incompatible with gold are: osmium, iridium, rhenium, ruthenium, and rhodium. Adhesion and friction can be reduced if one of these noble metals is used as a coating on one of the contacts [6].

Fig. 7.4 shows the friction coefficient versus sliding cycles when a plated ruthenium plate was replaced by the electroplated gold plate. The thickness of ruthenium was 2 μm. The sliding friction coefficient was about 0.4 to 0.5 throughout the test. Since ruthenium is incompatible with gold, the relative low sliding friction coefficient was expected. Fig. 7.5 is the micrograph of the ball surface after sliding against ruthenium for 400 cycles. It appears that no delamination has occurred because of relatively low sliding friction coefficient.

7.3.2 Effects of surface roughness

For various reasons, gold is the preferred material for the top layer in electrical contacts. Besides using incompatible sliding pairs, the other options for reducing sliding friction efficient of thin film systems aim at the hardness of coating and substrate, coating thickness, surface roughness and so on. For example, undulated surfaces have been shown to be effective in reducing fretting and sliding friction in both dry and boundary lubricated tests [7-9]. The main function of the

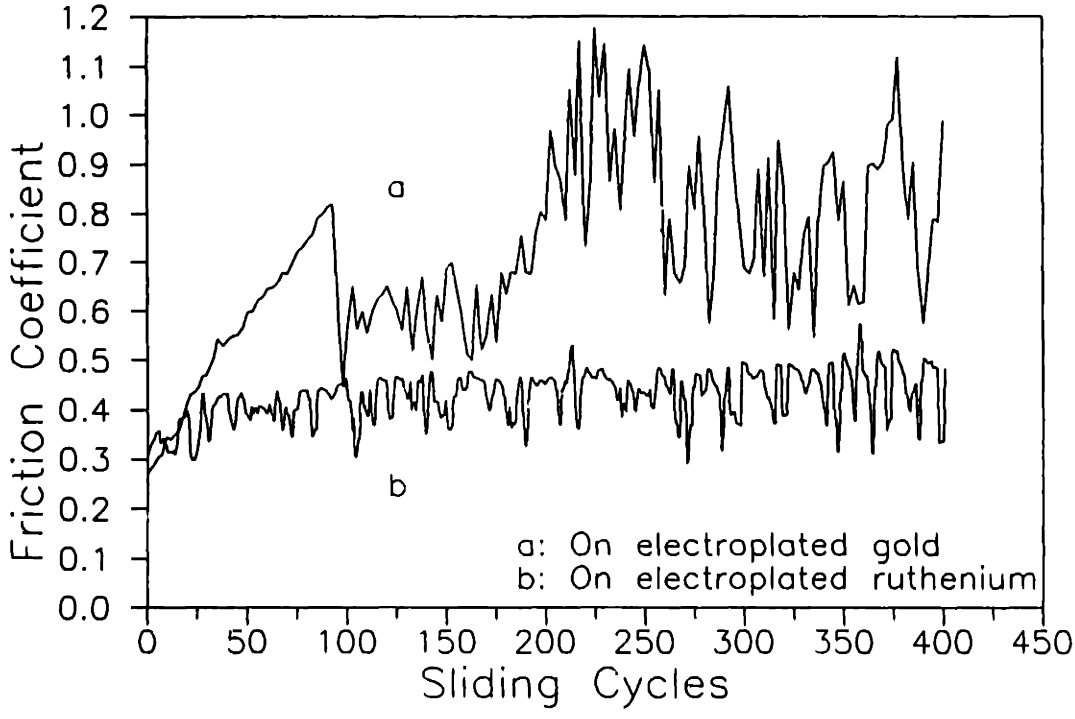

Fig. 7.4 Friction coefficient versus sliding cycles for gold plated brass balls sliding against electroplated gold and ruthenium plates.

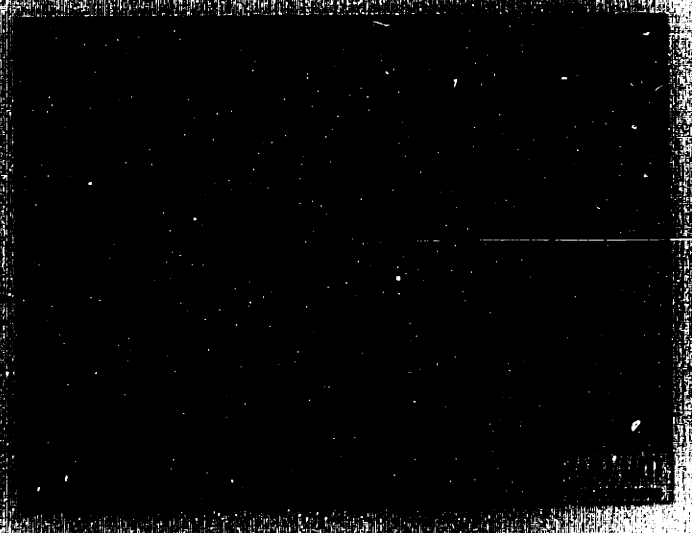

Fig. 7.5 Micrograph of the ball surface after sliding against electroplated ruthenium plate for 400 cycles

undulated surfaces is to trap wear particles so that the plowing component of friction is minimized. Besides minimizing plowing, the undulated coating surfaces might reduce the size of adhered junctions and the tendency of prow formation of gold contacts.

Accordingly, the effect of surface roughness on sliding friction of thin film systems was investigated. Since the thickness of the gold coating is only in a few micrometers, it is difficult to produce rough surface after electroplating. Thus the substrates were first scratched by using an abrasive paper in one direction (the sliding direction is perpendicular to the grooves). Then the rough substrates were electroplated with nickel and then with gold. The schematic of rough surface design of thin film systems is shown in Fig. 7.6. The substrates were scratched using different grades of abrasive papers, and the surfaces with various roughness were obtained after electroplating.

Fig. 7.7 shows the surface profiles of the plate specimen with various roughnesses. The substrate material was Beryllium-Copper. Fig. 7.7a is the profile of the plate surface after electroplating and the substrate was not scratched. Figs. 7.7b and 7.7c are the surface profiles of the plate specimens whose substrates were abraded with grades 220 and 60 abrasive paper, respectively. The thicknesses of electroplated nickel and gold were about 5 μm and 2 μm, respectively. Brass balls, 1.5 mm in diameter, electroplated with nickel and gold, were used as sliders. The thicknesses of gold and nickel were 2.5 μm and 1.5 μm, respectively. The normal load was 1 N (100 gram), and the other experimental conditions were the same as in the sliding tests in chapter 2.

Fig. 7.8 shows the friction coefficients versus the sliding cycles for various rough surfaces. Fig. 7.9 shows the micrograph of the ball and plate surfaces after sliding on plates of various surface roughnesses for 400 cycles. For the plate surface with a RMS value of 0.5 μm , the initial friction coefficient was about 0.3, and increased gradually to about 0.8. The interfacial delamination did occur and the brass substrate was exposed after 400 cycles. For RMS of 1.2 μm, by contrast, the friction coefficient started at about 0.35, increased gradually up to 0.45, and then stayed at this value till the end of the test (400 sliding cycles). The micrograph of

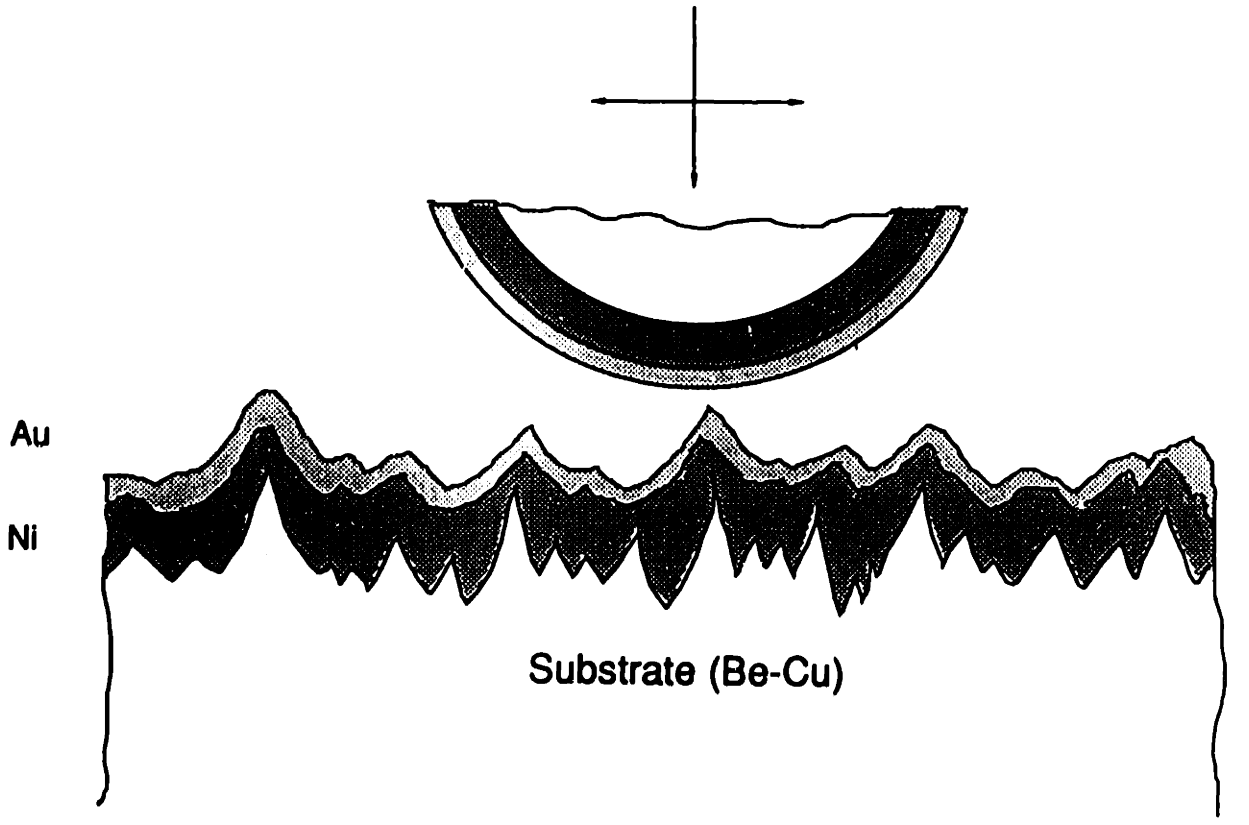

Fig. 7.6 Schematic of rough surface design for thin film systems

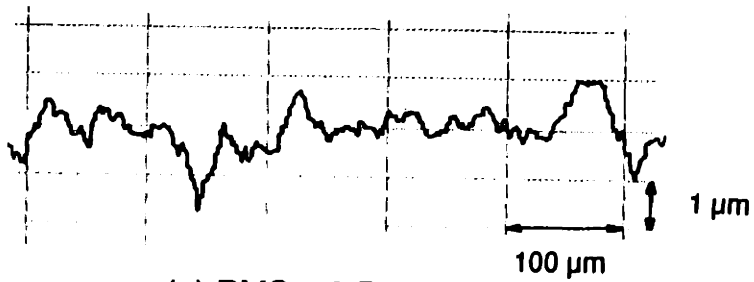

(a) RMS = 0.5 μm

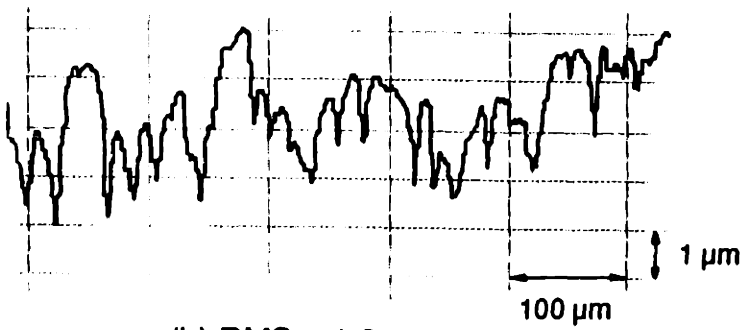

(b) RMS = 1.2 μm

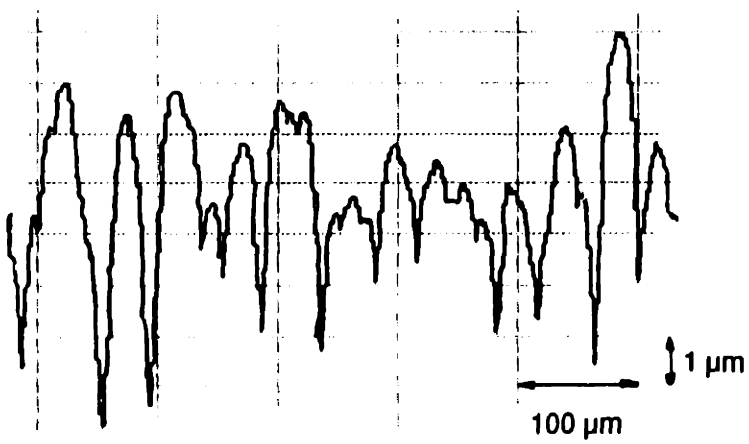

(c) RMS = 2.5 μm

Fig. 7.7 Surface profiles of abraded and electroplated plate specimens

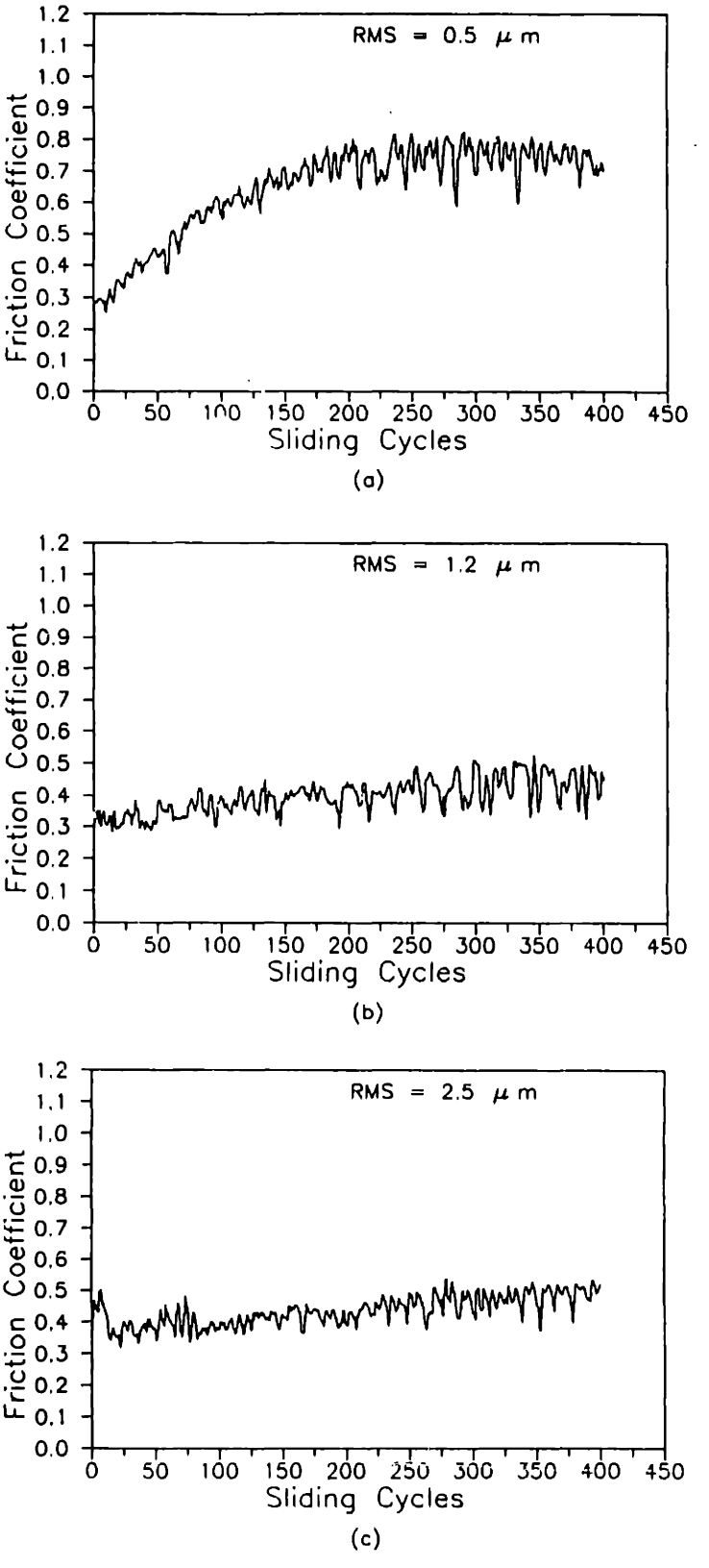

Fig. 7.8 Friction coefficient versus sliding cycles for plate specimens with various roughness.

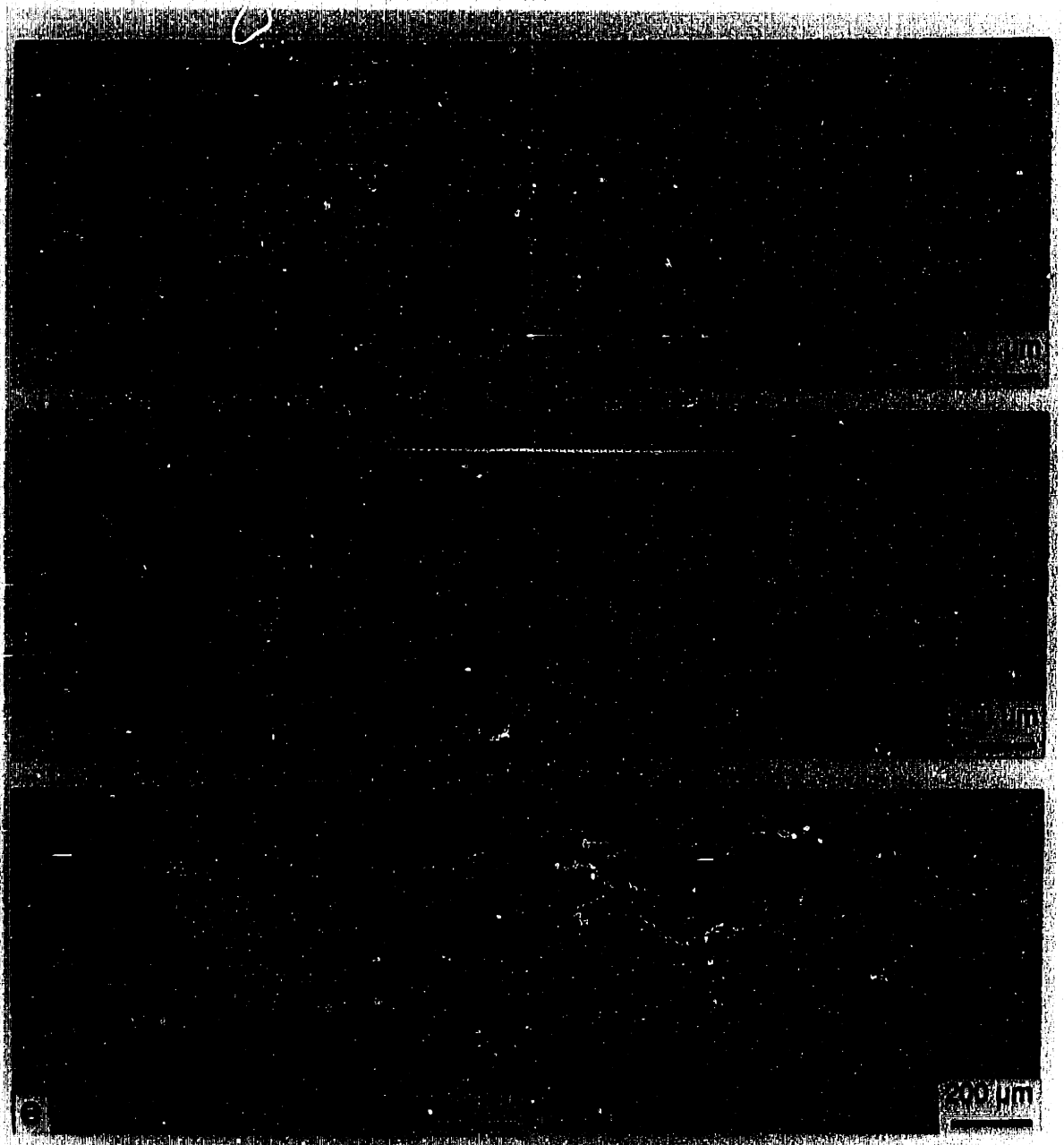

Fig. 7.9 Micrographs of worn surfaces after 400 sliding cycles: (a) ball specimen slid against plate (RMS=0.5 µm), (b) plate specimen (RMS=0.5 µm), (c) ball specimen slid against plate (RMS=1.2 µm), (d) plate specimen (RMS=1.2 µm), (e) ball specimen slid against plate (RMS=2.5 µm), and (f) plate specimen (RMS=2.5 µm)

the ball surface shows that the gold coating stayed on the bal surface and that nickel appeared only at one spot within the contact area. For RMS of 2.5 μm, the initial friction coefficient was about 0.4, increased up to 0.6, and then decreased to a steady state value of 0.45. The micrograph shows that a small wear particle has formed near the contact center of the ball specimen.

It is apparent that surface roughness has a strong effect on sliding friction of electroplated gold contacts. The plate surface with a RMS value of 1.2 μm seems to reduce the sliding friction coefficient significantly and delay the interfacial delamination effectively.

7.3.3 Effects of diffusion annealing

The sliding and fretting failures are primarily due to the excessive plastic deformation of the top layer (gold) and interfacial delamination. While the plastic deformation is caused by high surface friction, interfacial delamination strongly depends on interfacial strength (or toughness) and the crack face friction. Strong interface bonding can delay failures even with high surface friction. Thus both interfaces (between top layer and underplate; between underplate and substrate) should be strengthened. One way to increase interfacial strength is to choose metallurgically compatible materials on both sides of the interface because bonding is strong for compatible materials. Another way is to diffusion anneal the specimens after coating so that the atoms from each side can diffuse across the interface. The objective is to make a diffuse or graded interface in terms of composition and mechanical properties.

It was shown in chapter 2 that failure of sliding pairs is due to to poorly bonded interface between nickel and brass substrate. Accordingly, it was decided that diffusion annealing be used to strengthen the interfaces by means of interdiffusion between gold and nickel atoms, and between nickel and copper/zinc atoms. Since failure occurred on the ball specimen, only the ball specimen was subjected to diffusion annealing.

Brass balls, 1.5 mm in diameter, electroplated with 1.5 μm gold over 2.5 μm nickel underplate were used as sliders. Brass plates electroplated with 1.5 μm gold

over 5 μm nickel underplate were slid against the sliders. Diffusion annealing was conducted in an argon atmosphere at 350 °C for four hours.

Fig. 7.10 shows that friction coefficient and contact resistance plotted against sliding cycles for a diffusion annealed ball specimen slid on the plate specimen. The initial friction coefficient was about 0.3 as before. After a few cycles, it started increasing, up to 0.55 after about 200 cycles. Instead of increasing further as in the case of untreated ball specimens, the friction coefficient reached a steady state value of about 0.4. The contact resistance was below 10 mΩ throughout.

Fig. 7.11 shows the micrograph of the ball specimen after 500 sliding cycles. Only a few black contact spots in the contact zone appeared. Auger spectrum (Fig. 7.12) at area 1 shows major peaks of O and Ni, which indicates that gold coating was removed at that spot, and the spectrum of rest of contact zone (area 2) was not different from that of unworn area (area 3). Thus gold coating stayed on the substrate fairly well up to 500 sliding cycles except in a few spots. Thus it may be concluded that strong adhesion between gold and nickel, and between nickel and brass after diffusion annealing contributed to reducing sliding friction and delaying the interfacial delamination.

Another explanation for the effect of diffusion annealing is that diffusion annealing makes the interface a relatively homogeneous layer. Now even if a crack exists inside the layer (along the original interface), the crack face friction coefficient will be high according to compatibility theory of friction. Thus the crack growth rate will be very small and the interfacial delamination will be delayed.

As discussed before, a nickel underplate is used for two primary reasons. First, sliding and fretting wear resistance can be increased by "hardening" the two-layer system with a nickel underplating [9]. Second, a nickel layer between gold and brass is used as diffusion barrier because diffusion can occur when connectors are exposed to elevated temperatures (200-500 °C) during soldering, brazing, etc. [11]. The nickel underplate is used to avoid diffusion of Cu or Zn toward the gold surface. However, the effectiveness of nickel as a diffusion barrier has been questioned over the years because nickel also diffuses into gold and forms NiO on gold surface at temperatures above 200 °C [12-16].

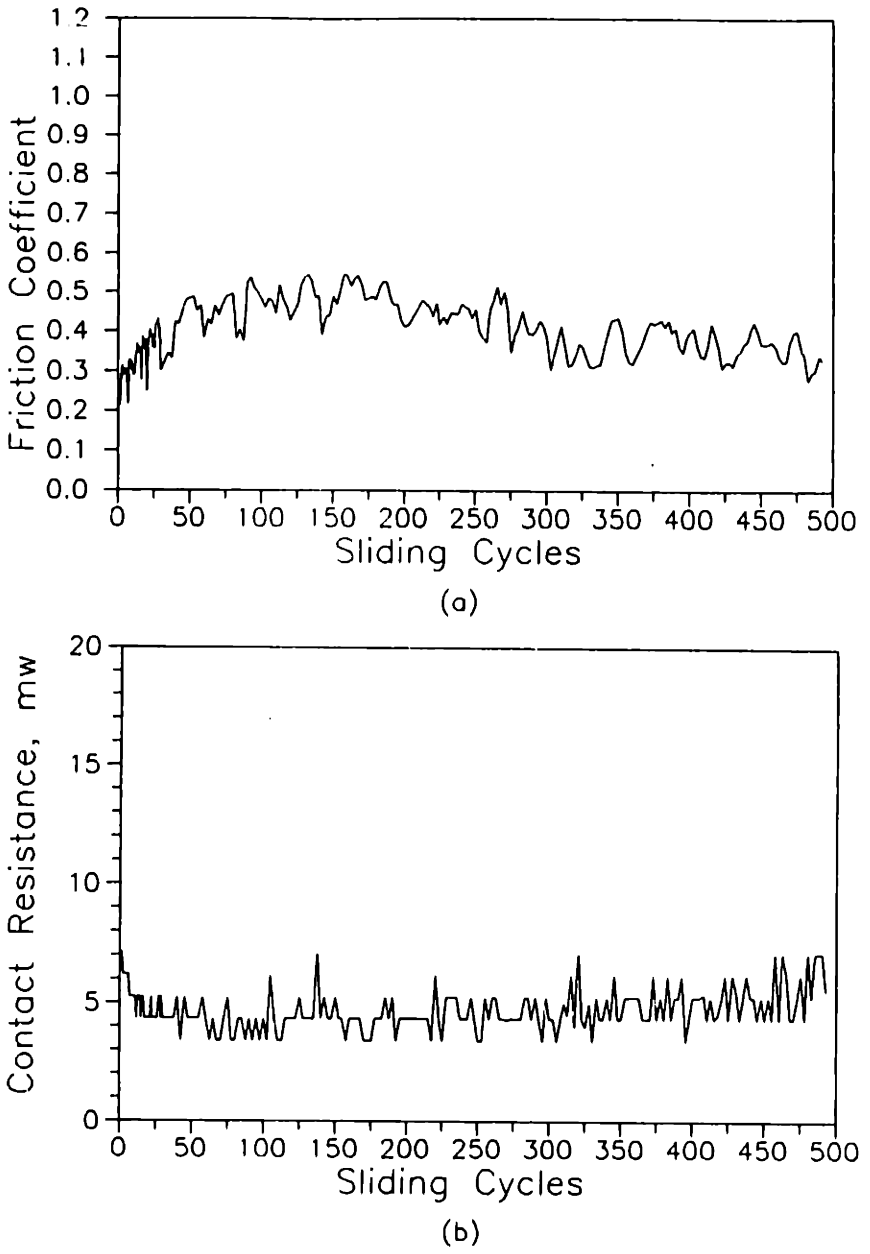

Fig. 7.10 Friction coefficient and contact resistance versus sliding cycles. The ball specimen was heat-treated at 350 °C for four hours.

Fig. 7.11 Micrograph of the ball surface after 500 sliding cycles.

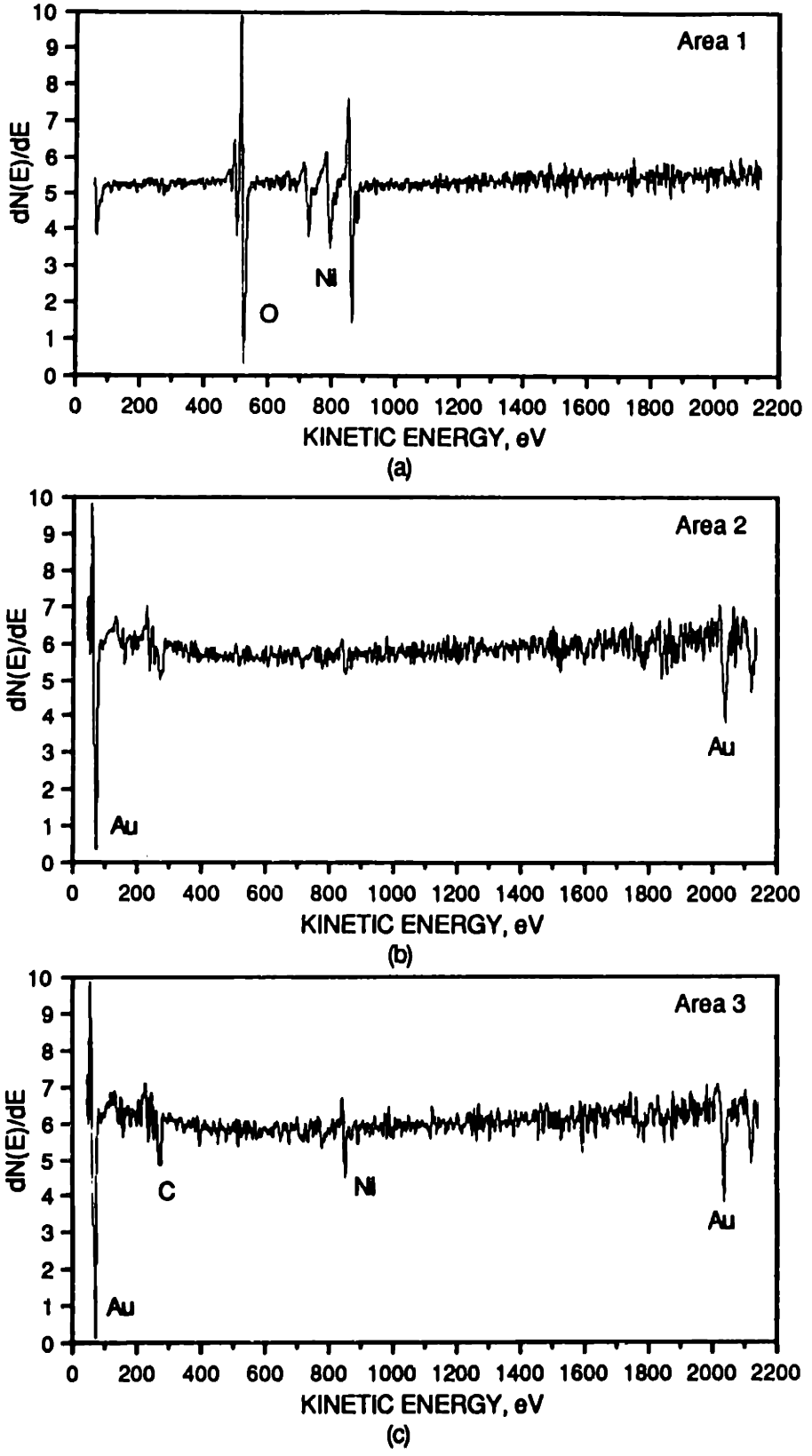

Fig. 7.12 Auger spectra of the ball surface: (a) area 1, (b) area 2, and (c) area 3

All these investigations, however, dealt with very thin gold films (about 0.1 μm). In electrical connectors, the thickness of gold film is about 1.25 μm, and nickel is unlikely to diffuse through gold at 350 °C. The following is an estimate of the concentration of Ni in the interdiffusion zone after diffusion annealing at 350 °C for 4 hours. The plane at original interface is called the Matano interface, and the interdiffusion flow is described by Fick's second law:

$$\frac{\partial C}{\partial t} = \frac{\partial}{\partial x}\left(D\frac{\partial C}{\partial x}\right) \tag{7.2}$$

where C is the concentration of gold or nickel, D the corresponding intrinsic chemical diffusion coefficient. If it is assumed that D is independent of composition, then Equation. (7.2) becomes

$$\frac{\partial C}{\partial t} = D\frac{\partial^2 C}{\partial x^2} \tag{7.3}$$

Since the thicknesses of gold coating and nickel underplate are about the same, and nickel is not expected to emerge to the gold surface, a semi-infinite solution to Equation (7.3) is obtained as:

$$C(x) = \frac{1}{2}\left[1 - \text{erf}\left(\frac{x}{2\sqrt{Dt}}\right)\right] \tag{7.4}$$

From reference [11], the interdiffusion coefficient of gold and nickel at 350 °C is 1.5×10^{-16} cm^2/sec. Substituting for t (14,400 s.) and D into Equation (7.4), we get the concentration curve of nickel after the diffusion anneal (Fig. 7.13). Indeed nickel diffuses only 0.1 μm into gold. Thus diffusion annealing is effective in strengthening the interfaces without contaminating the gold surface.

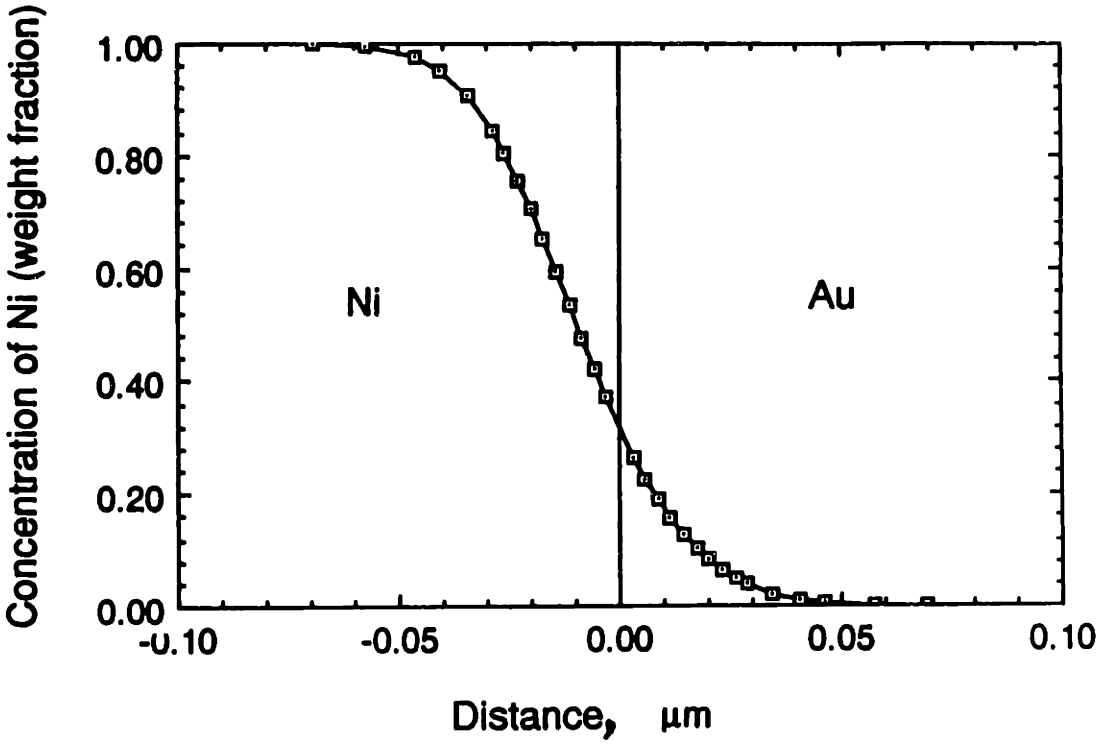

Fig. 7.13 Concentration of Ni about the Au-Ni Matano interface after diffusion annealing at 350 °C for four hours

References

[1] Ritchie, R. O. and Lankford, J., "Overview of the Small Crack Problem," *Small Fatigue Cracks*, Ed. by Ritchie, R. O. and Lankford, J., The Metallurgical Society, Inc., Warrendale, PA, 1986, pp 1-5.

[2] Lankford, J. and Davidson, D. L., "The Role of Metallurgical Factors in Controlling the Growth of Small Fatigue Cracks," *Small Fatigue Cracks*, Ed. by Ritchie, R. O. and Lankford, J., The Metallurgical Society, Inc., Warrendale, PA, 1986, pp 51-71.

[3] McClintock, F. A., "Plastic Flow Around a Crack Under Friction and Combined Stress," *Fracture 1977*, Taplin, D. M. R., ed., Vol. 4, ICF4, Waterloo, Canada, 1977, pp. 23-38.

[4] Sin, H. -C. and Suh, N. P., "Subsurface Crack propagation Due to Surface Traction in Sliding Wear," *J. Appl. Mech.*, Vol. 51, 1984, pp. 317-323.

[5] Rabinowicz, E., "The Influence of Compatibility on Different Tribological Phenomena," *ASLE Trans.*, Vol. 14, 1971, pp. 206-212.

[6] Barber, S. A. and Rabinowicz, E., "Material Selection for Noble Metal Slip Rings," *Proc. Holm Conference on Electrical Contacts*, Illinois Inst. of Technology, Chicago, IL, 1980, pp. 33-40.

[7] Saka, N., Liou, M. J. and Suh, N. P., "The Role of Tribology in Electrical Contact Phenomena," *Wear*, Vol. 100, 1984, pp 77-105.

[8] Tian, H. Saka, N. and Suh, N. P., "Boundary Lubrication Studies on Undulated Titanium Surfaces," *Tribology Trans.*, Vol. 32, 1989, pp 289-296.

[9] Saka, N., Tian, H. and Suh, N. P., "Boundary Lubrication of Undulated Metal Surfaces at Elevated Temperatures," *Tribology Trans.*, Vol. 32, 1989, pp 389-395.

[10] Antler, M., "Survey of Contact Fretting in Electrical Connectors," *IEEE Trans.* Vol. CHMT-8, 1985, pp 87-104.

[11] Antler, M., "Gold-Plated Contacts: Effect of Heating on Reliability," *Plating*, Vol. 57, 1970, pp 615-621.

[12] Hall, P. M. and Morabito, J. M., "Diffusion Problems in Microelectronic Packaging," *Thin Solid Film*, Vol. 53, 1978, pp 175-182.

[13] Tompkins, H. G. and Pinnel, M. R., "Relative Rates of Nickel Diffusion and Copper Diffusion through Gold," *J. of Applied Physics*, Vol. 48, 1977, pp 3144-3146.

[14] Swartz, Jr., W. E., Linn, J. H., Ammons, J. M., and Kovac, M. G., "An X-ray Photoelectron Spectroscopy Study of the Diffusion of Iron, Nickel and Cobalt through Gold Films," *Thin Solid Films*, Vol. 114, 1984, pp 349-356.

[15] Chao, Y. -K., Kurinec, S. K., Toor, I., Shillingford, H., and Holloway, P. H., "Porosity in Thin Ni/Au Metallization Layers," J. *of Vac. Sci. Technol.*, Vol. A5(3), 1987, pp 337-342.

[16] Kurinec, S. K., Toor, I., Chao, Y. -Y., Shillingford, H., Holloway, P., Ray, S., and Beckham, K., "Effects of Heat Treating Au/Ni Thin Film Composites in Various Ambients," *Thin Solid Films*, Vol. 162, 1988, pp 247-255.

Limitations of the Present Study and Suggestions for Further Work

The compatibility theory of friction developed by Rabinowicz suggests that sliding friction is relatively high when sliding pairs are identical or compatible materials. In the current study, initial contact surfaces are identical materials, i.e., gold against gold. The initial friction coefficient is about 0.3, but it increases monotonically as sliding and fretting continue. The increase in friction during this period is believed due to the increasing adhesion between gold contacts and due to prow formation. The dominant mechanism of initial friction, however, is not entirely clear, and no analytical model is available to explain the frictional behavior for this period. This aspect needs to be further explored.

In the present study of fretting failures, fretting amplitudes are chosen to be larger than the minimum fretting amplitude for gross slip. The fretting amplitude remains constant for each test, and only one frequency (80 Hz) is used for all fretting tests. In practice, however, the fretting amplitude and frequency due to vibration and thermal expansion could be changed in unpredictable patterns and sequences. The amplitude and frequency are certainly two important factors to fretting life and failure mechanisms. How they affect fretting failures individually and jointly remains to be studied. Moreover, the measurement of electrical contact resistance is traditionally considered as a failure criterion of fretting tests. The experimental observations have shown, however, that the substrate is exposed long before any increase in contact resistance is noticeable in the accelerated laboratory tests, though the contact resistance can give some qualitative measure of contact failures. Thus a better failure criterion or testing procedure needs to be established to obtain reliable assessment of fretting failures.

It is assumed in the finite element analyses that thin layers and substrates are homogeneous and isotropic. Interfaces between layers are assumed to be the zero-thickness mathematical interfaces. These assumptions are certainly not true for real thin film systems. Microstructure, grain size, grain orientation, composition, and porosity of the deposited thin films affect the mechanical properties and the inter-

facial bonding, which in turn affect the stress states and interface cracking. The present interface model assumes continuity of displacements but abrupt changes of mechanical properties across the interface. Whether these assumptions truly represent actual interfaces remains to be studied. Also as thickness of the layers becomes very small, the continuum mechanics approach may not be valid any more. The critical thickness needs to be determined for developing more accurate models for thin film systems.

In mechanics, and in the present study, friction force is treated as a tangential force acting on the surface. However, the physical meaning of the friction implies that plastic deformation or other kind of irreversible processes take place wherever friction exists. Thus for all contact problems, the contact surfaces are always subjected to plastic deformation when the sliding friction exists. Of course the extent of surface plastic deformation depends on the magnitude of the friction. Plastic deformation could be only on an asperity scale if the friction force is small, but plastic deformation could expand to the whole film thickness if the friction is large enough. In the analysis of interface cracking with high crack face friction, the plastic zone at crack tip is so small that the small scale yielding requirement is satisfied, and it appears that the elasticity theories of interface cracking can be used. However, the finite element model treats the crack face friction simply as a tangential force acting on the crack faces. What really happens is that the crack faces along the whole crack length are subjected to plastic deformation to some extent. Thus modeling friction by the finite element method is rather complicated. How to incorporate the physical implications of friction into a mechanics model of friction is a challenging task.

The present finite element analyses of sliding contacts with and without an interface crack actually deal only with the static aspects of the sliding contact. That is, the stress and strain states are determined only for normal and tangential loadings at various positions on the surface. The time factor is ignored. More importantly, the residual stresses from the current loading are not taken into account when the surface loading is applied at the next position is applied. Preferably, a continuous loading scheme should be used in the finite element analysis. It will be interesting to examine the stress and strain histories in the one sliding or fretting

cycle. Thus a better failure criterion and a better estimate of crack growth rate can be obtained from the finite element analysis.

The effects of crack length on plastic zones and CTSD have not been studied in this thesis. Obviously the crack growth rate is not a simple function of the crack length. Since the crack remains closed in the present problem, as in most tribology problems, the normal compression and the crack face friction facilitate rewelding of the crack faces. This brings additional complexity to the problem. Whether the crack grows faster when the crack is short or long remains to be studied. Another important aspect of interfacial delamination is that the interface crack has to branch and break through the surface to form a wear particle. How long does it take for a interface crack to break through the surface needs to be studied.

The crack tip modeling is an important issue, especially for a closed crack in the elastic-plastic regime. In the present study, the nodes at the crack tip have independent displacement. Thus some overlapping is expected to occur among these crack tip nodes. Obviously this violates the geometry compatibility. Another way to model the crack tip is to tie all the nodes belonging to the upper region together and the nodes belonging to the bottom region together. Which model can more accurately represent the interface crack tip behavior needs further study.